TRANSPORT STUDIES IN

LASER PLASMA INTERACTIONS

BY

Jonathan David Hares

Imperial College

London

A thesis submitted for the degree of Doctor of Philosophy

of the University of London and for the Diploma

of Membership of the Imperial College

(November 1980)

TRANSPORT STUDIES IN LASER-PLASMA INTERACTIONS

ABSTRACT

This thesis reports an experimental investigation of the important energy transport mechanisms in high intensity laser-matter inter-actions at $1.06 \mu m$ and $0.53 \mu m$. The range of thermal, suprathermal and radiation transport is directly measured by means of X-ray spectroscopy. The technique of layered target $K\alpha$ spectroscopy is described paying particular attention to previously ignored satur-ation and radiation pumping effects. The observation of radiation pumped $K\alpha$ emission confirms the presence of significant radiation preheat.

A non-linear regime of suprathermal electron transport is identified in which the charge neutralising return current induces a sufficient electric field to impede the suprathermals and hence reduce the preheat range. This effect is potentially useful in reducing preheat in laser-fusion schemes.

The intensity and pulse length scaling of the energy coupling into preheat have been measured and the form of the preheating distrib-ution function determined. It was observed that the fractional coupling into preheat decreases with increasing pulse length for the same mean intensity.

The measurements of thermal and suprathermal transport are compared with numerical simulations and departures from simple linear theory observed.

CONTENTS

LIST OF TABLES

LIST OF SYMBOLS

c — Velocity of light

G — Radiative Gaunt factor

h — Plank's constant

I — Intensity

k — Boltzman's constant

m_e — Electron mass

m_A — Atomic mass

T_H — Fast electron temperature

ϵ — Dielectric constant

θ — Angle

k — Coefficient of thermal conductivity

λ — Wavelength

μ — Absorption coeffient

ν — Frequency

ρ — Density

ACKNOWLEDGMENTS

FOR MY PARENTS

CHAPTER 1

1.1   Introduction

The attainment of a controlled thermonuclear fusion reaction
poses many technological and scientific problems. The ignition of
such a reaction requires the competing conditions of high temperature
and large density-duration product. Modern pulsed laser technology
has provided a possible route to ignition. In 1972 Nuckolls et al (1)
proposed a mechanism in which a high power laser is used to compress
a small fuel-containing sphere to the extent that thermonuclear burn
occurs. Since then much experimental and theoretical effort has been
invested in laser fusion with accompanying triumphs and set-backs in
the progress.

At this stage no suitably energetic laser driver exists for a
practical reactor but much of the relevant physics can be studied
using currently available lasers. Indeed thermonuclear burn, although
not self-sustaining, does occur for various experimental configurations.
It is interesting to note that the highest resultant thermonuclear energy
production is~1joule to date (for an input laser power of 20TW and
50ps duration).

The small time and length scales of the interaction place
stringent requirements on diagnostic equipment, much of which has been
developed specifically for the purpose. In particular X-ray spectroscopy
has shown itself to be an invaluable tool, indeed very little, other
than X-rays, escapes the dense core of the target, appart from reactionproducts.

There are abundant physical processes determining the behaviour
of laser targets but two important questions one might pose are;
i) How much laser energy is absorbed? and ii) Where does it go? Much
evidence exists to the effect that at high intensities, $(I \lambda^2 \gg$
$10^{14} w.cm^{-2} \mu m^2$, where λ is the driver wavelength in microns) a large
fraction of the absorbed light is coupled into anomalously energetic
(fast) electrons (2,3,4,5,6). These electrons have a large range in
the target and are able to preheat the fuel core before thermonuclear
burn occurs. The preheat raises the adiabat along which the fuel is

compressed and reduces the final density (7,8). This makes ignition harder to attain, so questions i) and ii) are particularly pertinent with respect to fast electron production and transport.

Ideally (in the absence of fast-electrons) the target is compressed by the reaction of the outwardly ablating thermal plasma, driven by the laser. Theoretical evidence suggests a strong wavelength dependence on the mass ablation rate (9,10), as well as fast electron production (11,12), with everything becoming more favourable for fusion at shorter wavelengths. However at the current stage of laser development the efficiency, ease of construction and power output of a laser go down rapidly with its wavelength so one would like to know if at the available wavelengths (in our case $1.06\mu m$ and $0.53\mu m$) the answers to i) and ii) are favourable to fusion.

With regard to fast electrons, an extensive study (with $1.06\mu m$ illumination) is presented in which both the form and intensity scaling of the fast electron distribution is determined (3). This study supercedes previous work (e.g. with hard X-rays (2)) in that it has yielded direct fast electron range and energy content measurements, virtually independent of any model assumptions. In the aforementioned case the conclusions are strongly dependent on the chosen form of the fast electron distribution function.

Transport experiments have been performed using a frequency doubled ($0.53\mu m$) beam. The mass ablation rate has been measured in both spherical and plane target irradiations and the results are contrasted with existing work at $1.06\mu m$. Results are interpreted in terms of the one dimensional hydrodynamic simulation MEDUSA and it is concluded that thermal conduction is less than diffusive theory predicts.

In the remainder of Chapter 1 some fundamental laser-fusion scaling laws are presented, with the emphasis on preheat and mass ablation.

Chapter 2 gives an account of fast electron energy deposition and the production of characteristic radiation. The layered target fast-electron detector technique is described and the effects of saturation and radiation pumping of the K_α emission are demonstrated. It is shown how the K_α yields from layered targets may be predicted for arbitrary preheating

distributions.

Chapter 3 contains the results of a series of experiments presenting quantitative information on the intensity scaling of the fast electron preheat range and energy deposition. The results are discussed in Chapter 4 and an experiment which has measured the dependence of preheat on pulse length is described.

The novel preheat reduction technique of resistive inhibition is described in Chapter 5 and an experiment confirming the effect is reported (13). A one-dimensional Monte-Carlo numerical simulation is compared with the results.

Chapter 6 deals with mass ablation experiments performed with 0.53μm illumination. The results are analysed in conjunction with the hydrodynamic simulation MEDUSA and are compared with earlier work at 1.06μm. Enhanced radiative preheat with the shorter wavelength is observed.

Chapter 7 deals with the overall energy balance and the application of resistive inhibition to fusion targets. Final comments are made on the likely development of laser-fusion.

1.2 Laser-fusion - simple considerations

i) Exploding pushers

There are two distinct classes of laser-fusion experiments; the exploding pusher and the ablative compression. In the exploding pusher mode a short ($\lesssim$ 100ps) high intensity pulse irradiates a microballoon target. The intensity is such that the fast electron range, λ_e, is larger than the target thickness (wall thickness). The entire target, including the fuel fill, is bathed in fast electrons and is uniformly heated. The pulse length is short compared with the hydrodynamic time-scale so the evolution of the target can be described by considering the relaxation of the uniformly high energy deposition (pressure) after the laser pulse has ended. The dense wall of the microballoon explodes with approximately half of the mass travelling inwards. This motion stagnates when the core material reaches a sufficiently high pressure to decelerate the inwardly directed mass.

Various models have been proposed to explain the observations of temperature, density and neutron yield as functions of absorbed energy, aspect ratio of target (radius divided by shell thickness) and fuel fill density. Two successful models are (14) and (15,16). The main assumptions and results are tabulated in Figure 1.2.1. The most success-ful feature of (15,16) is the prediction of neutron yields over a wide range of intensity.

Both models exhibit the same essential feature of little final density (ρ_f) dependence on absorbed energy i.e.:

$$(14) \quad \Rightarrow \quad \rho_f = \quad \propto \left(\frac{R}{\Delta R} \right)^{-1} \qquad 1\cdot 2\cdot 1$$

where $\propto$ is an empirically determined constant and $R/\Delta R$ is the aspect ratio, and:

$$(15,16) \quad \Rightarrow \quad \rho_f = 2\cdot 2 \, \rho_s^{0\cdot 6} \, \rho_{go}^{0\cdot 4} \qquad 1\cdot 2\cdot 2$$

where ρ_s is the shell density and ρ_{go} is the initial fuel fill density. Physically this is because the fuel fill is subjected to the same fast electron preheat as the exploding shell, (since $\lambda_e > \Delta R$). This preheat raises the gas temperature and hence the pressure against which it is compressed. This in turn reduces the final density.

It is thus difficult to reach high densities in this mode. The immediate usefulness of exploding pusher targets lies in the large neutron yields ($\sim 10^7$) which are obtained for moderate laser energies ($\sim 100J$). These arise from the high core temperatures achieved (up to $6keV$ for $\sim 200J$ absorbed(8)). To reach the high densities required for a breakeven fusion reaction ($\sim 1000x$ solid(7)) a more sophisticated target design is required in which, for example, the fuel is screened from preheating effects. In a conventional target experiment at 20TW (17) a neutron yield of $\sim 10^{10}$ was obtained in a short pulse target interaction. However, much doubt exists about the value of the exploding pusher mode of operation for fusion.

DENSITY SCALING LAWS FOR EXPLODING PUSHER TARGETS

Model	Result	Assumptions
(15) Storm	$\rho_F = 13 \frac{\Delta R}{R}$ $(\rho_p = 2.5)$	empirical constant 13 obtained from fitting experimental data
(16) Rosen & Nuckolls	$\rho_F = (1 + 1.9 \frac{\Delta R}{R\rho_o})^2 \rho_o$	at peak compression glass shell density ρ_g is distributed as 1) $\rho_g(r=R_F) = \rho_F$ 2) $\rho_g(r) = \rho_F (\frac{R_F}{r})^{3/2}$ 3) $\frac{1}{4}$ of shell mass inside R_o
(14) Ahlborn & Key	$\rho_F = 3.8 \, \rho_o^{0.4}$	contact surface velocity u_2, peak pressure P_F related to specific absorbed laser energy E/M_p as u_2^2, $P_F \sim E/M_p$

Figure 1.2.1 A summary of the features of the exploding pusher models of (14), (15) and (16). (Reproduced from (8)).

ii)   Ablative compression

An alternative approach is the ablative compression. The pulse
length is matched to the hydrodynamic time-scale of the compression and
the intensity is sufficiently low that the fast electron range is less
than the target thickness. Mass is ablated from the surface of the
target for the duration of the compression, accelerating the shell
inwards by the rocket effect. Pressure amplification at the core
occurs because of the high velocities to which the shell is accelerated.
Of prime consideration is the pressure and mass ablation rate in the
interaction region. As high a pressure as possible is required.
Unfortunately as the intensity increases,fast electrons become important
and the absorbed energy is not directed into the ablation process.
The ablation pressure saturates for $I\lambda^2 \gg 10^{14} w.cm^{-2}.\mu m^2$.
In figure 1.2.2 ablation pressure as a function of intensity is shown,
collected from several sources (8), for $1.06\mu m$ incident light.
Theoretical models (11,12) and some experiments (11,18) indicate that
fast electron phenomena scale as $(I\lambda^2)$. At shorter wavelengths one
might expect the ablation pressure to saturate at a higher value.
Moreover the critical density (i.e. the highest electron density capable
of supporting wave propagation at the incident wavelength) is higher, so
the laser energy will be absorbed in a denser region leading to a higher
pressure.

The Chapman Jou$_g$et (CJ) deflagration model assumes that a steady
state exists in which the shock wave velocity,$\mathcal{V}_s$ and the thermal front
velocity, $\mathcal{V}_T$ (the thermal front being carried by electron thermal
conduction) are equal, the density in front of· the shock is solid and
behind is critical. The implied steady-state density/pressure profile
propogates into the target at a velocity $\mathcal{V} = \mathcal{V}_s = \mathcal{V}_T$. An
important result is that the pressure is proportioned to $\left(1/\lambda\right)^{2/3}$.
Consideration of a rocket type acceleration of the shell leads to an
optimum ratio between the ablated mass (exhaust mass) and the accelerated
mass (4:1)(8).The distance over which the shell is accelerated, while
$\sim$ 80% of the mass is being ablated, determines the aspect ratio of the
target. This is given by:

$$\frac{R}{\Delta R} = (80\%)^2 \frac{\rho_s}{\rho_a} \qquad\qquad 1.2.3$$
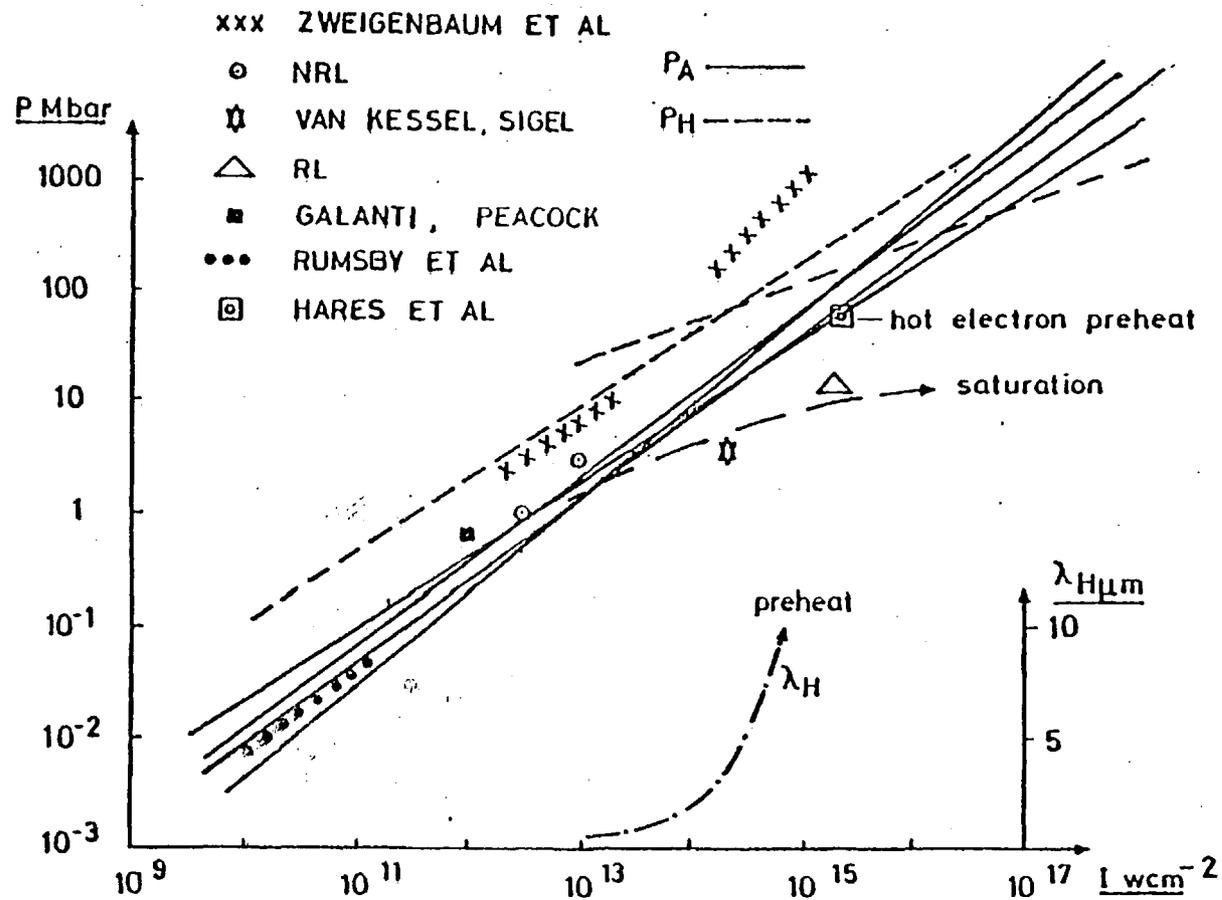
Figure 1.2.2 Ablation pressure as a function of laser intensity for 1.06μm illumination. (Reproduced from (8)).

where ρ_s is the shell density and ρ_a the ablated density. Since ρ_a (essentially the critical density) is much less than ρ_s a high aspect ratio is desirable.

The acceleration of a high density shell by a low density ablation plasma , leads to the possibility of growth of the Rayleigh-Taylor instability (19) which becomes more acute for large aspect ratio. For a fixed final shell velocity (determined say by the requirements for fusion) a lower aspect ratio may be used with shorter wavelength. This follows from the intrinsically higher pressure obtained (experiment and : theory) with short wavelengths, the higher operating intensity such that fast electron preheat is not important (i.e. $I\lambda^2 \lesssim 10^{14} \omega.cm^{-2}.\mu m^2$) and the higher ablation density, ρ_a , resulting from the higher critical density for shorter wavelength.

A further consideration in an ablative compression is the temporal structure of the laser pulse. In the simple case of a 'top-hat' pulse, the instantaneous application of pressure to shell drives a shock wave into the fuel, thus preheating it. To avoid this the pressure (via intensity) time profile must be tailored to provide an ideal adiabatic compression (20).

iii) Fast electron driven ablative compressions

A compromise between preheat and ablative compression is being investigated at the Los Alamos Scientific Laboratory (L.A.S.L.). A CO_2 ($\lambda = 10.6\mu m$) laser is used to drive a target in which the shell is thicker than the fast electron range. The preheat pressure generated in this shell exceeds the ablation pressure and drives the unheated part of the shell inwards by an ablative type expansion of the heated material. The fast electron range is large, typically tens of microns, so a large aspect ratio implies a large target. The motive for using 10.6μm illumination is the relative ease of construction and high efficiency ($\sim$ 10%) of the CO_2 laser. However, large targets have a large energy requirement and preheating effects are difficult to suppress when fast electrons play a dominant role.

The pure ablative compression with a short wavelength laser seems to offer the most favourable solution, nonetheless many problems remain,

particularly;

i) Rayleigh-Taylor instability limiting aspect ratio

ii) Efficiency of laser light absorption

iii) Efficient production of short wavelength laser pulses

iv) Reduction of core preheating effects. (Both radiative and fast electron)

v) Generation of temporally structured laser pulses

vi) Production of sufficiently high ablation pressure (linked to iii)).

Active research is being carried out in all of the above areas. The experiments to be described here are inspired by ii), iv) and vi).

1.3

i) Transport phenomena

There is strong evidence that the thermal transport of energy away from the absorption region is inhibited with respect to predictions based on diffusive transport theory. Several simulations, both 1D and 2D, have been performed, and experimentally observable parameters, such as optical transmission (18, 21) X-ray thermal continuum emission (11, 22), reflectivity (18), ion emission (23) and X-ray line emission (22) predicted (24). In all of these predictions (except (24)), an anomalously reduced peak thermal heat flux was required to match predictions with experiment. In (24) it was claimed that the inclusion of the ponderomotive force was sufficient to explain many experimental observations. However the majority of the data were for $10.6 \mu m$ illumination for which ponderomotive effects are large. The importance of the effect is governed by the relative magnitude of the local plasma pressure and the ponderomotive force. The ponderomotive force density is given by (24):

$$F = \frac{\omega_p^2}{\omega_{LASER}^2} \nabla I \left[2c \left(1 - \frac{\omega_p^2}{\omega_{LASER}^2} \right)^{0.5} \right]^{-1} \qquad \text{1.3.1}$$

where ω_p is the local plasma frequency, $\left(\frac{4\pi n_e e^2}{m_e} \right)^{1/2}$

In the region of interest, i.e. the absorption region, the density is equal to the critical density i.e. $\omega_p = \omega_{laser}$. Thus the pondermotive force is proportional to I. The local plasma pressure will vary as density, i.e. the critical density, which is proportional to λ^{-2}. Thus the importance of pondermotive effects goes as $I\lambda^2$. From (24) strong density profile modification occurs for $I\lambda^2 > 10^{15}$ w.cm$^{-2}\mu$m^2. For 1.06 μm illumination this implies $I \simeq 10^{15}$ w.cm^{-2}. However much data interpreted in (22) is at 1.06 μm with $I \simeq 10^{14}$ w.cm^{-2}. Clearly pondermotive effects cannot explain the apparently reduced thermal conductivity here. Moreover, in (22) the burn depth of the thermal front is measured by observation of X-ray emission from the target substrate, overlaid with a variable thickness isolating layer. The thickness of the overlay required to supress thermal emission from the substrate gives the thermal penetration depth which has been interpreted by means of a 1D hydrodynamic simulation. A reduction of the peak thermal flux by a factor of 20-30 was required to reproduce observations. Ponderomotive effects could possibly explain a reduced ablation rate but not a reduced thermal penetration depth.

It is thus apparent that an anomalous flux reducing mechanism exists. Several proposals have been made for such a mechanism, e.g. magnetic field generation (25) and ion acoustic turbulence (26,27). No significant differences between plain and spherical burn rates exist (22) thus gross magnetic fields can be ruled out. Ion acoustic turbulence can be driven by either a sufficiently high thermal flux (27) or fast electron neutralising return currents. These will be discussed later in the light of experimental measurements. In (26) the thermal conductivity in a preformed underdense plasma, heated by a CO_2 laser, was inferred by means of ruby laser scattering. The conductivity was observed to saturate at 2-5% of the free-streaming limit and enhanced ion scattering at a wave number of $2k_0$ indicated an ion-acoustic turbulence level of $\sim$ 9%, sufficient to strongly inhibit thermal conduction. Ion acoustic turbulence is widely believed to be an important mechanism for thermal inhibition.

Various approaches have been made to the treatment of fast electron transport. The most favoured source of fast electrons (11,12,28), resonance absorption, generates electrons directed towards the laser. In the low density 'coronal' region the local density scale length becomes comparable to the fast electron Debye length and space charge effects dominate the transport.

A sheath is formed, defined by the position at which fast electrons turn around in their self-consistent electric field. This electric field is able to accelerate ions to high velocities (up to the electron sound speed) with the distribution of the fast ions being similar to that of the fast electrons. (Other workers (29,30) have suggested that local high temperatures resulting from thermal flux inhibition are responsible for fast ion production). Indeed the fast ion spectrum has been used to diagnose the fast electron spectrum (31) although this is rather indirect.

The transport of   electrons in the solid target material is essentially classical (32) (except in very low density materials – to be discussed in detail later) and is described adequately by classical scattering and energy deposition formulae. In the majority of laser-plasma simulations, fast electron transport (when included) is described by a multigroup diffusion formulation. It is particularly important to correctly predict the fast electron transport and hence preheat in compression simulations because of the profound effect it has on final density in high density compression schemes.

ii)   Fast electron production mechanisms

It is currently accepted that fast electrons are dominantly produced by the mechanism of resonance absorption (28). Laser energy penetrates into the plasma and at the surface defined by the local plasma frequency being equal to the laser frequency (the critical density surface) the laser energy is resonantly coupled into plasma oscillations. In the presence of a density gradient these oscillations, or stationary waves, break -   and result in the release of energetic electrons. The mechanism relies on the existence of parallel components of electric field and density gradient. The assumption that the density gradient is normal to the target surface leads to an optimum angle of incidence for resonance absorption. This is given as:

$$\left(k_0 L\right)^{2/3} \sin^2 \theta = 0.6 \qquad\qquad 1.3.2$$

where k_0 is the vacuum wave number and L the density scale length

in (33), for p polarised light. Such a peak has been observed
experimentally (34,35) with the fast ion emission and cold electron
temperature maximising at a specific, acute, angle of incidence. However,
fast particle production is still observed in normal incidence irradiations
(35). It is likely therefore that the critical density surface is rippled
so there will always be components of density gradient parallel to the
electric field (36). Refraction of the incident light occurs in the large
density gradient. The illumination is turned around before it reaches
the critical density surface and coupling to plasma oscillations occurs
via tunnelling. The path of a typical ray is shown in figure 1.3.1.
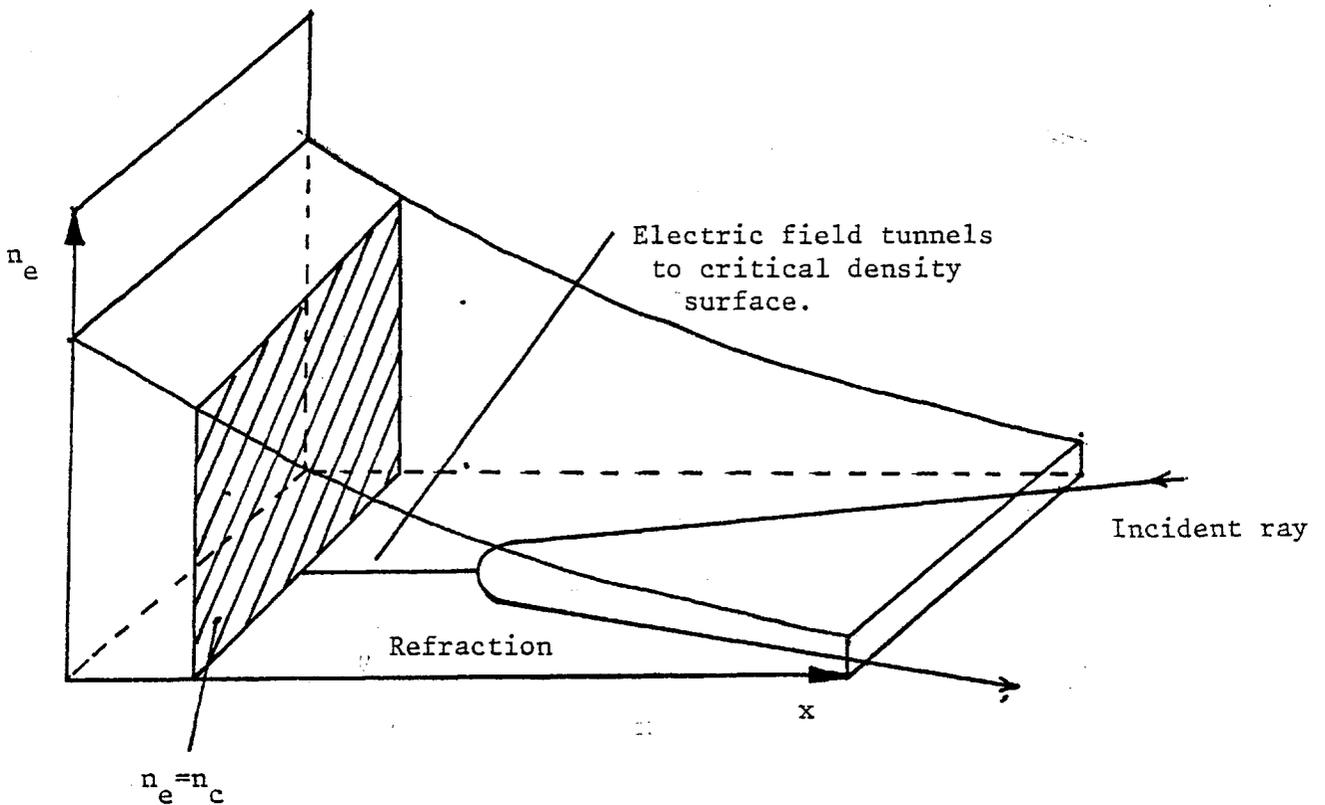
Figure 1.3.1 The diffracted path of a ray of light close
to the critical density surface.

We will now examine a simple model and its prediction of scaling of
fast electron energy with wavelength and intensity. In (11) and (12) the
problem is tackled by attributing energy balance to fast electrons and
momentum balance to thermal electrons. The fast electrons carry away the
absorbed energy at their thermal velocity thus:

$$\propto] \quad = \quad \tfrac{1}{2} \beta \, n_H \, m_e \, v_{TH}^3 \qquad\qquad \underline{1 \cdot 3 \cdot 3}$$

where α is the absorption fraction, $\overline{v}_{TH}$ the thermal velocity
and β a numerical factor arising from the form of the distribution
function. It is then assumed that the laser penetrates to a point at
which the thermal electron pressure balances the radiation pressure,
so:

$$(2 - \alpha) \frac{I}{c} = (2 - \alpha)\frac{\mathcal{E}^2}{8\pi} = n_u T_c \qquad 1\cdot 3\cdot 4$$

In (11) the average fast electron energy(and hence kT_H) is taken as
the product of electric field, $\mathcal{E}$, and density scale length, L.

$$kT_H = \mathcal{E} e L \qquad 1\cdot 3\cdot 5$$

where L is obtained from a numerical particle simulation. The
empirical scaling law:

$$T_H \simeq 13 \left(I\lambda^2 \right)^{1/3} T_c^{1/3} \qquad 1\cdot 3\cdot 6$$

(with T_H and T_c in units of keV and $I\lambda^2$ in $10^{16} W.cm^{-2}\mu m^2$)
follows. In (12) consideration of the reduced density scale length.
leads to:

$$T_H \propto \mathcal{E}_{VACUUM} \cdot L^{1/2} \qquad 1\cdot 3\cdot 7$$

giving a scaling law for T_H of:

$$T_H \propto \left(I\lambda^2 \right)^{0.26} \qquad 1\cdot 3\cdot 8$$

a lower exponent than (11). Also in (12) a numerical particle
simulation was performed in two dimensions for which the hot

temperature is described by the empirical relation:

$$T_H = 20 T_c^{0.25} (I\lambda^2)^{0.39} \qquad 1.3.9$$

where units are as in equation 1.3.6 Thus all the models presented are in at least qualitative agreement with $T_H \propto (I\lambda^2)^\gamma$ with $\gamma \simeq 0.3$, and some weaker dependence on the cold temperature T_c .

It is apparent, from its regular occurence, that the parameter $(I\lambda^2)$ is of some importance in wave plasma interactions. For a fixed plasma temperature the ratio of plasma pressure to light pressure at the critical density surface is determined only by $(I\lambda^2)$, also the quiver velocity of a particle in an E.M. wave is determined by the same parameter - hence its fundamental importance.

It is difficult to theoretically obtain the form of the fast electron spectrum. Simplistically one would expect the wave-breaking process of resonance absorption to produce bursts of mono-energetic electrons,however much evidence exists to the effect that the distribution is Maxwellian (2,37,38). Recently in (39) a randomising mechanism has been identified, via a numerical particle simulation, by which a Maxwellian spectrum of fast electrons is generated. The random nature of the 'spikey' electric field is seen to drive a spectrum of resonant oscillations, leading to a wide range (roughly Maxwellian) of electron energies. A simpler mechanism for the production of a spectrum of energetic electrons is the random time at which electrons enter the resonant region. Electrons entering at a time close to the peak of the electric field will aquire a large energy, those entering at other times will aquire lower energies. It is difficult however to explain the production of electrons of energy up to 1MeV as have been experimentally observed(40).

CHAPTER 2

THE LAYERED FLUOR TARGET PREHEAT MEASUREMENT TECHNIQUE

In this chapter the fundamental processes of fast electron energy deposition and $K\alpha$ production are discussed. The layered fluor target electron detection technique is introduced and its ability to measure absolute energy deposition is demonstrated. The shortcomings of existing work are discussed.

A simple analysis sufficient for target design is carried out and the previously ignored radiation pumping and saturation of the $K\alpha$ emission are identified and observed. It is shown how the $K\alpha$ yields from layered targets may be predicted for arbitrary preheating distributions.

2.1 The laser facility

The experiments reported in this chapter were performed at the Science Research Council Central Laser Facility at the Rutherford Laboratory. The laboratory uses a neodymium glass rod driver and two disc amplifiers. The system can be configured in various ways to produce pulses of 50ps to several nanoseconds duration, with a peak power up to 0.5 TW. The experiments described here used a single beam of this laser. The system is described in some detail in (22,p1.1).

The beam could be focussed to a diameter of $\sim 30\mu m$ by a f/1 Sorro lens, although in general the target was moved from the optimum focus to vary the intensity.

The prepulse level was monitored on each shot and an acceptable prepulse level was taken to be $\leqslant 5 \times 10^{-6}$ of the main pulse energy.

Far and near field telemicroscopes in the target area facilitate alignment and focussing of the target. A C.W. $1.06\mu m$ beam is propogated down the main beam path to enable alignment between the target area CW laser and the main laser. A diffusion pump produces an ultimate pressure of 10^{-6} Torr although a working pressure was 10^{-5} Torr.

2.2   Electron energy deposition

As an energetic electron passes through matter, it loses energy by collisions with stationary atoms and by emitting X-radiation as it undergoes random accelerations along its path (Bremsstrahlung). Secondary X-radiation is produced by the radiative decay of excited and ionised atoms within the stopping medium. For electron energies $\lesssim$ a few hundred keV, the bulk ($> 99\%$, (41)) of the energy dissipation is collisional. The linear, non-relativistic, energy deposition rate is calculated in (42). The semi-quantum mechanical calculations assume that the bound electrons, and their available excited state, are hydrogenic. The electron energy loss rate is given by;

$$\left(\frac{\partial E_e}{\partial s}\right) = \frac{-2\pi e^4 Z n_A}{E_e} \ln\left(\frac{2E_e}{\overline{IP}}\right) \qquad \underline{2.2.1}$$

where n_A is the atomic density and $\overline{IP}$ is the average ionisation potential. This is given by (42) as an acceptable extention for non hydrogenic atoms of moderate Z. This is the the Bethe-Bloch linear energy deposition rate. The form is the same as that for electron energy deposition in a plasma:

$$\left(\frac{\partial E_e}{\partial s}\right) = \frac{-2\pi e^4 n_e}{E_e} \ln \Lambda \qquad \underline{2.2.2}$$

where n_e is the electron density and $\ln\Lambda$, the Coulomb logarithm, has an argument equal to the ratio of maximum to minimum impact parameters for the electron-electron collisions. The argument of the logarithmic term in equation 2.2.1 is similar since the minimum impact parameter (usually the De-Broglie wavelength) is related to the electron energy, E_e, and the maximum impact parameter (the largest distance at which the electron will interact with an ion) is determined by the ionisation potential, IP, i.e. the lowest discrete energy deposition.

Consider an electron incident normally on a solid, homogeneous target. The linear range of the electron can be calculated by integration of equation 2.2.1. This is the residual range, r_A. As the electron passes into the

target it will be scattered and its trajectory will deviate from a straight path.

Solid target material.

Total path given by integration of linear energy deposition rate.

e^-

Collisions weight energy deposition to a range less than r_A.
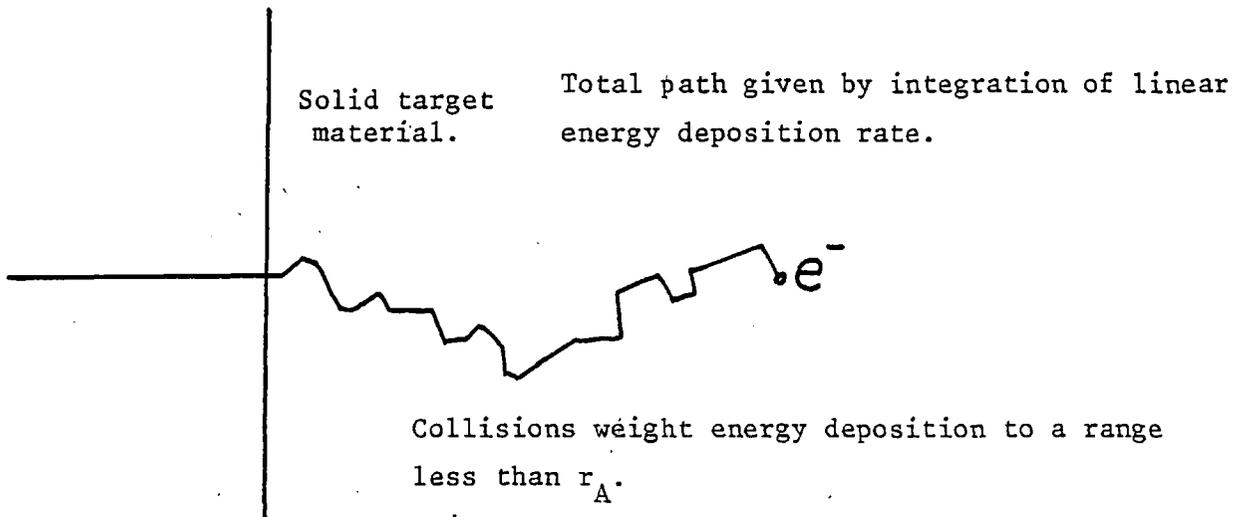
Figure 2.2.1 The effect of scattering on an electron penetrating matter.

This is illustrated in figure 2.2.1. Spencer (43) has performed extensive numerical calculations on fast electron scattering and energy deposition. A typical result is illustrated in figure 2.2.2, compared with a linear integration of equation 2.2.1. The range is significantly reduced from r_A and the energy deposition increased over the linear rate.

As mentioned previously, a small fraction of the electron energy is emitted as primary X-radiation. Consideration of the acceleration and resulting radiation of the randomly colliding electron leads to the well known Bremsstrahlung equation for the radiation emitted by an electron per unit path length per unit energy:

$$\left(\frac{\partial^2 E_e}{\partial h\nu \, \partial s} \right)_{RAD} = \frac{8 \, Z^2 n_A e^6 G}{3 \, h \, m_e c^3 \, E_e} \qquad 2.2.3$$

where m_e is the electron mass and G is the radiative Gaunt factor.

Result of Spencer's calculations for aluminium with E_e=25keV.

Figure 2.2.2 An example of Spencer's calculations (43) for 25keV electrons normally incident on aluminium.

Mass depth (mg.cm^{-2}).
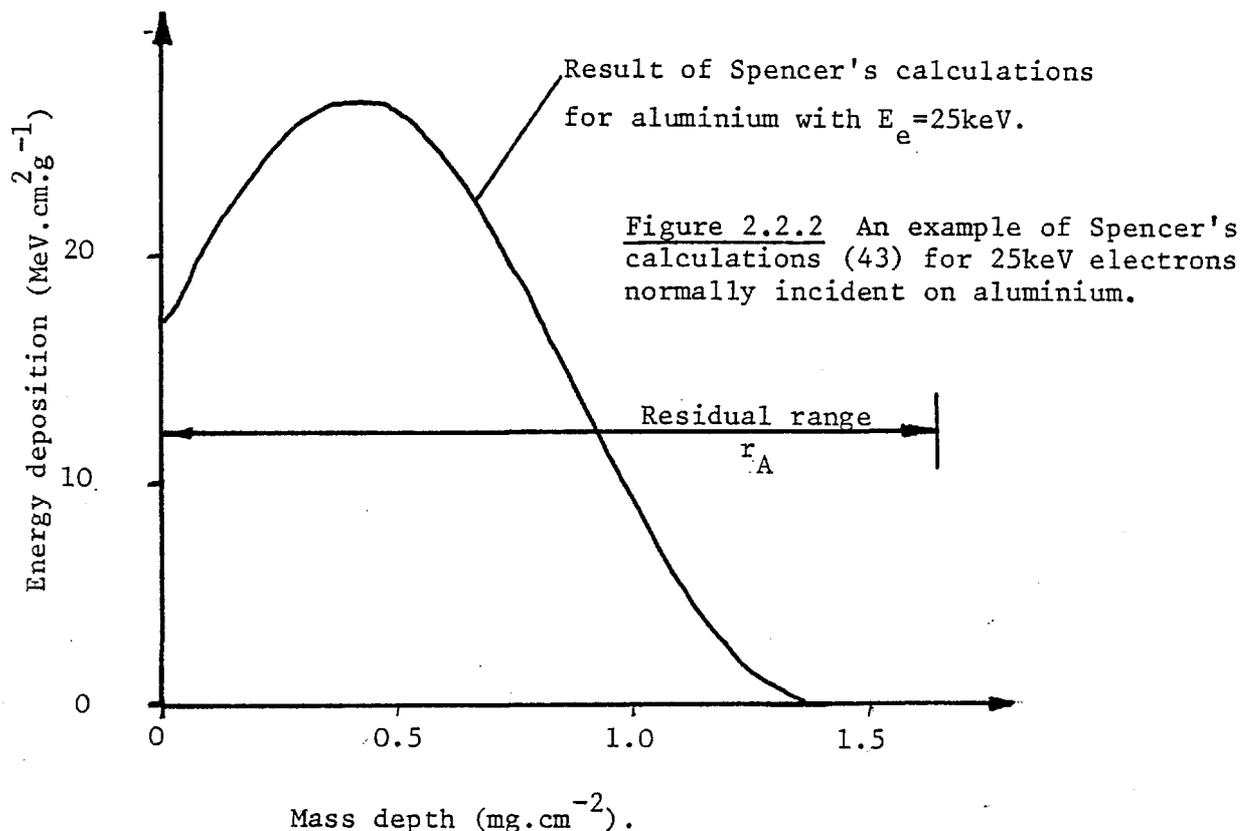
In (41) the collisional and radiation energy loss for electrons is tabulated. Typically, the radiation yield per unit path length is 10^{-3} of the total energy deposition (E_e = 20keV, target is Al). The spectrum is flat from $h\nu$ = 0 to E_e, beyond which it is zero. This is in good agreement with experiment (44).

There are several components to the secondary radiation resulting from the relaxation of ionised states in the target. If the electron energy is greater than the K shell ionisation potential, E_{KI}, then a significant component of the emission will arise from transitions from the higher shells into the K shell.

2.3 The production of Kα radiation

A Kα photon is emitted by a K ionised ion when an L shell electron decays radiatively into the K shell vacancy. The configuration for potassium

is $1s^1 2s^2 2p^6 3s^2 3p^6 4s^1 - 1s^2 2s^2 2p^5 3s^2 3p^6 4s^1$. The emitting element, or fluor, can be ionised by an incident photon or electron of energy $\gg E_{KI}$. Photons are very efficient at producing K ionisations. Figure 2.3.1 shows the mass attenuation coefficient of a typical element (K) in the region of the K absorption edge. Photons of energy $> E_{KI}$ are able to cause K ionisations. Photons of energy $< E_{KI}$ are unable to K ionise and hence excite the absorption mechanism. This threshold for K ionisation is the reason for the existence of the absorption edge.
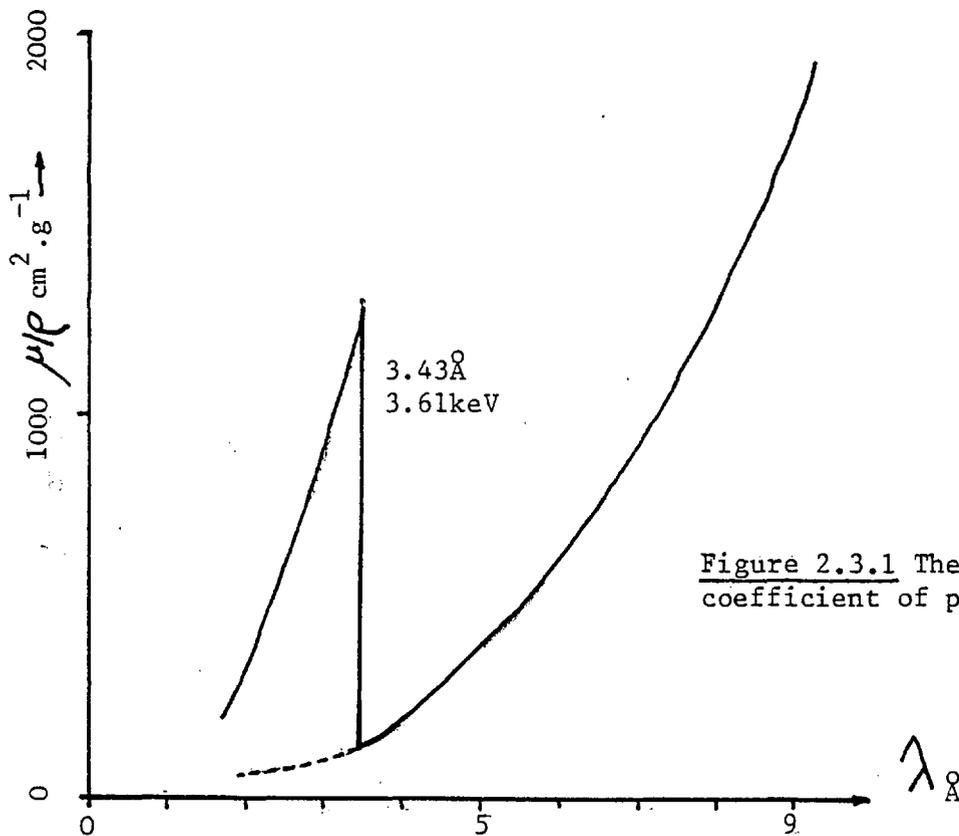
Figure 2.3.1 The mass attenuation coefficient of potassium from (50).

Photo-ionisation cross sections generally vary as $\lambda^{-\alpha}$ where $\alpha \simeq 3$ (45). The non K shell absorption in figure 2.3.1 is extrapolated as λ^{-3} to short wavelengths. The K shell absorption varies in a similar way so the fraction of absorbed photons which lead to K ionisations is constant for $h\nu > E_{KI}$. This fraction is given by (46):

$$\frac{n_{KI}}{n_{PHOTONS, ABS.}} = 1 - \frac{1}{J_R} \qquad \underline{2.3.1}$$

where J_R, the jump ratio, is the ratio of μ/ρ above to below the absorption edge. The fraction $(1 - 1/J_R)$ is of order unity and is plotted in figure 2.3.2 as a function of Z.
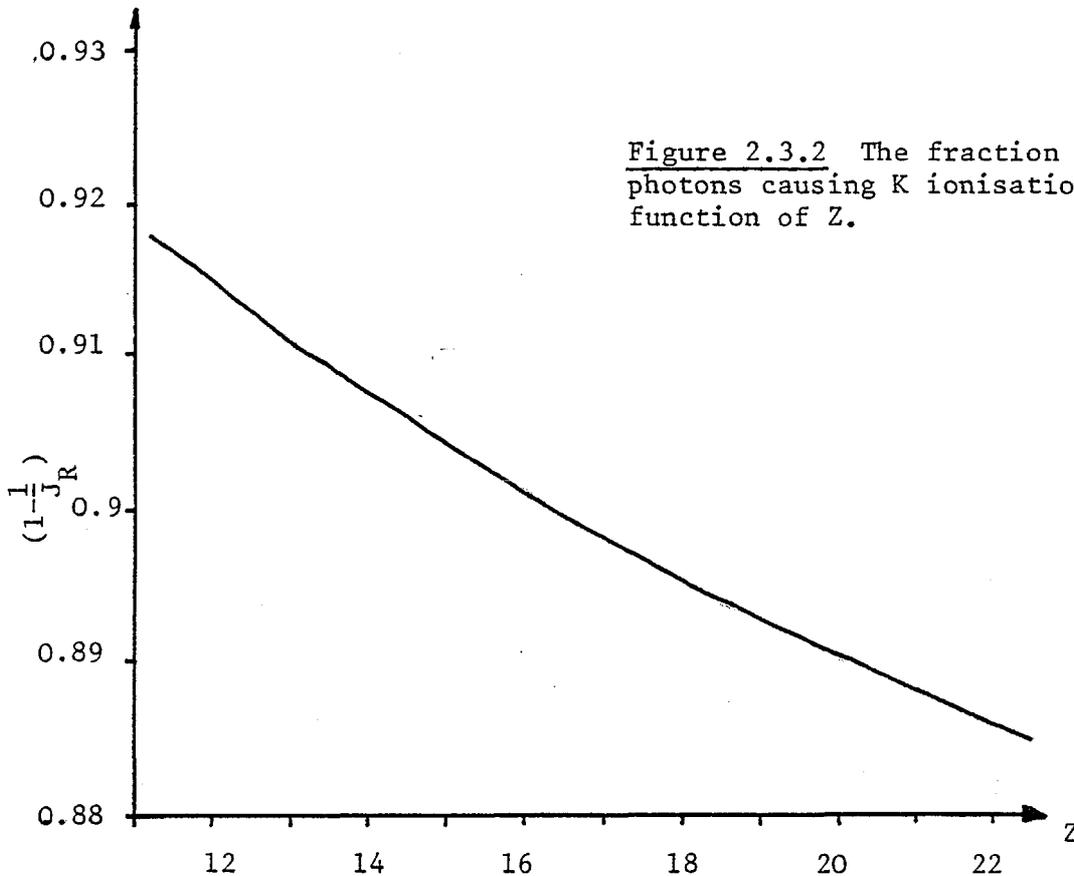
Figure 2.3.2 The fraction of absorbed photons causing K ionisations as a function of Z.

Electrons on the other hand are very inefficient at producing K ionisations. The majority of the energy deposition is into outer shell ionisation. The ratio of energy deposition into K shell ionisation to total energy deposition, R (E_e), is calculated as follows. Along a path ds in a medium of density ρ and atomic mass m_A, an electron will produce n_{KI} K ionisations:

$$n_{KI} = \sigma_K(E_e) \frac{\rho}{m_A} \qquad 2\cdot3\cdot2$$

where $\sigma_K (E_e)$ is the cross section for K ionisation for an electron of energy E_e in the fluor. Along the same path the electron will deposit a total energy dE_e given by:

$$dE_e = \left(\frac{\partial E_e}{\partial s}\right) ds \qquad 2.3.3$$

where $\partial E/\partial s$ is obtained from 2.2.1. Each K ionisation deposits an energy E_{KI} so the ratio $R(E_e)$ is given by:

$$R(E_e) = \frac{\sigma_K(E_e) \; E_{KI} \; \rho}{m_A \left(\frac{\partial E}{\partial s}\right)} \qquad 2.3.4$$

A fraction, ω, of the K ionisations results in the emission of a $K\alpha$ photon. Competing deexitation mechanisms reduce ω, the fluorescence yield, from unity. In (47) ω is calculated considering non radiative decay of electrons from the L shell into the K shell vacancy, as the principal competing deexitation mechanism. For this transition the excess energy is carried by an Auger electron emitted from the L shell. The configuration is $1s^1 2s^2 2p^6 3s^2 3p^6 4s$ – $1s^2 2s^2 2p^4 3s^2 3p^6 4s + e^-$. The calculation gave the fluorescence yield as:

$$\omega = \left(1 - \frac{const.}{Z^4}\right) \qquad 2.3.5$$

The assumption has been tested experimentally by measurement of the intensity of the Auger electrons for each of the possible transitions (48) and it was found for $Z < 30$ that Auger emission from the L shell accounts for $>70\%$ of the relaxation from a K ionised state.

The principal competing radiative decay is the emission of a $K\beta$ photon where the K shell vacancy is filled from the M shell. The configuration is $1s^1 2s^2 2p^6 3s^2 3p^6 4s$ – $1s^2 2s^2 2p^6 3s^2 3p^5 4s$ for potassium. The intensity of $K\beta$ emission is less than the $K\alpha$ intensity ($X \sim 30\%$ for each of the fluors used here). Experimentally, no $K\beta$ emission was observed because of the rapid removal of M shell electrons by the preheat.

Experimental measurements (49) have produced more accurate values for ω than 2.3.5. In (50) selected experimental data is used to fit a semi-empirical form for ω to give values accurate to better than 10% over a wide range of Z. ω as a function of Z is plotted in figure 2.3.3.
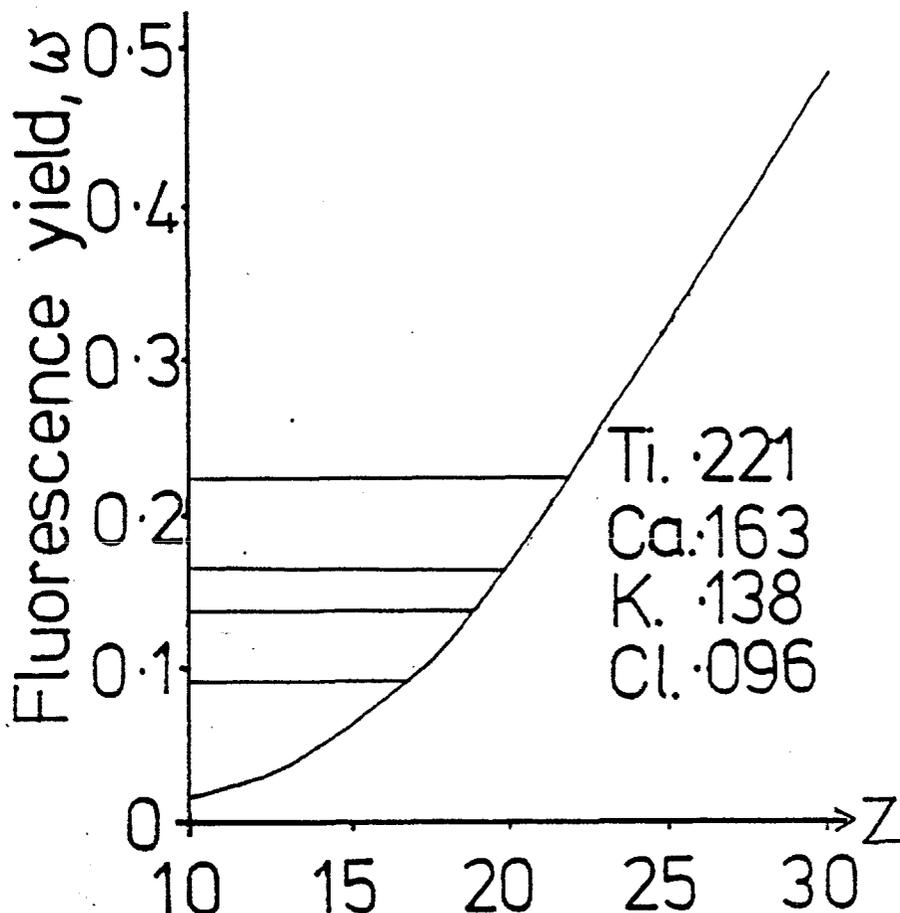
Figure 2.3.3 The K_α fluorescence yield as a function of Z (50).

We will now compare K_α production by electrons and photons in a typical laser target situation. Consider a thin layer of fluor, dx thick, on which electrons of energy E_e are incident. If the layer is thin compared with the electron range, Γ_A, and the total deposited energy is E then the K_α yield is:

$$Y = \frac{E_\omega \; E_{K\alpha} \; R(E_e)}{E_{KI} \; 4\pi} \qquad 2.3.6$$

For photon pumped $K\alpha$ emission, where the absorbed energy is E_p and the photon energy is $h\nu$, the $K\alpha$ yield is:

$$Y = \frac{E_p}{4\pi} \frac{E_{K\alpha}}{h\nu} \left(1 - \frac{1}{J_R}\right) \omega \qquad \underline{2.3.7}$$

Figure 2.3.4 compares the $K\alpha$ production efficiencies for photons and electrons for likely conditions.

Fluor is Cl (17). $E_{K\alpha}$ =2.62keV. E_{KI}=2.82keV	
Photons	Electrons
Photon energy =3keV*. ω =0.098 J_R=9.8 $Y_{phot} = E_{phot.} \times 6.1 \times 10^{-3} sr^{-1}$	Electron energy =10keV ω =0.098 σ_K=3.31 x 10^{-21}cm^2 $\frac{1}{\rho}\left(\frac{\partial E}{\partial s}\right)$ =1.62 x 10^4keV.cm^2.g^{-1} $Y_{elec.} = E_{elec.} \times 7.0 \times 10^{-5} sr^{-1}$
*Since in an experiment the X ray emission will be exponentiating rapidly the largest contribution will be just above(in energy) the K absorption edge.	

Figure 2.3.4 A comparison of the efficiency of $K\alpha$ production by photons and electrons.

2.4 The layered target technique

The fast electron energy is dissipated in several ways. Roughly half (4) is coupled into fast ions, a small fraction goes into characteristic X-ray emission and the remainder is deposited as preheat within the target. There are several techniques by which the fast electron spectrum may be diagnosed.

Other workers have used X-ray continuum (2,4,37,51,52) and fast ion velocity measurements(4,31,53)as a diagnostic of the fast electron spectrum. In each of the analyses however the inferred total energy carried by the fast electrons is sensitive to the assumed distribution function. In addition, neither method offers spatial resolution of the preheated area, nor provides direct preheat range measurements.

Two alternative techniques are the observation of fast electron induced $K\alpha$ emission and X-ray absorption spectroscopy of the preheated material. The latter will be discussed in sub-section 3.3.

For suitably chosen elements the $K\alpha$ fluorescence will be large in the presence of fast electrons (54). Such elements will be referred to as fluors. The K ionisation cross-section (50) and the classical linear electron energy deposition rate have similar functional dependences on electron energy. Hence the ratio of $K\alpha$ yield to total energy loss is a weak function of E_e if $E_e > E_{KI}$. This leads to the desirable result that the $K\alpha$ yield is proportional to the preheat energy, almost independent of the distribution function. This is illustrated in figure 2.3.5, in which $R(E_e)$, the instantaneous ratio of energy deposition into K ionisation to total energy deposition, is plotted as a function of electron energy, for potassium.
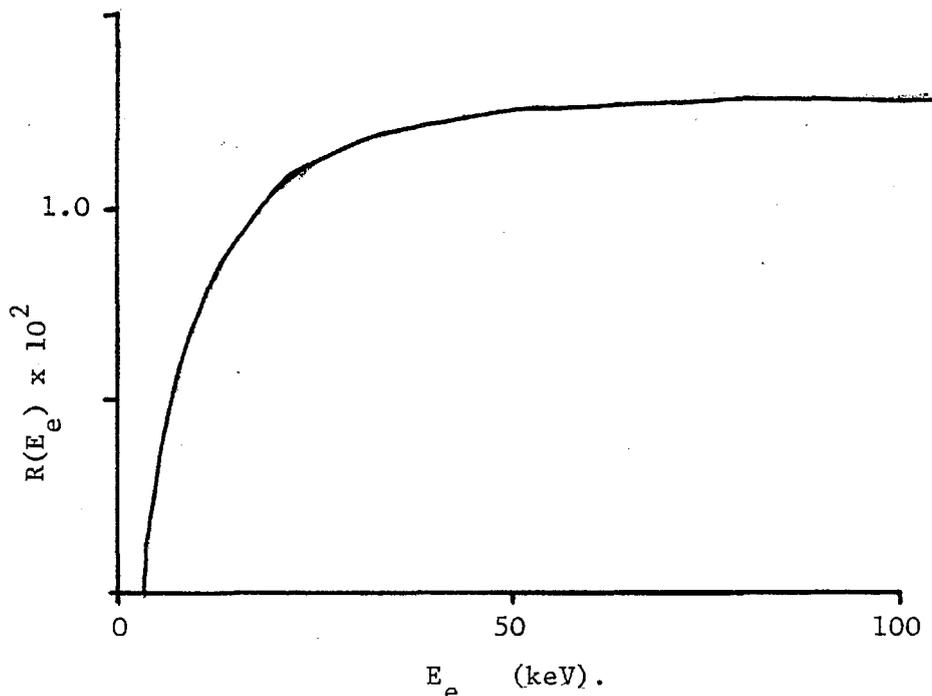
Figure 2.3.5 The fraction of electron energy deposited into K ionisations.

The total energy deposition rate is obtained from (41) and the K ionisation cross section from (50), in which it is given as:

$$\sigma_K(E_e) = \frac{7.92 \times 10^{-20} C}{E_e \, E_{KI}} \ln\left(\frac{E_e}{E_{KI}}\right) cm^2 \qquad 2.4.1$$

$$C = 0.85 + 0.0047 Z$$

In (42) a quantum mechanical formulation gives σ_K proportional to $E_e^{-1} \ln (E_e/B)$ where $B \sim E_{KI}$. The theory is essentially the same as in Bethe's linear energy deposition rate, this being a sum over all ionisation cross sections. This is the reason for the similar functional dependence of σ_K and $\partial E_e/\partial s$. The empirical equation 2.4.1 has been checked experimentally (55), and was found to be accurate to within 6%.

It is clear from figure 2.3.5 that, for electron energies greater than $\sim$15keV, $R(E_e)$ is nearly constant. Thus if the fast electron distribution is incident on a homogeneous fluor and the resultant $K\alpha$ yield is $N_{K\alpha}$ photons, then the energy content of the preheating distribution is given to first order by:

$$E_{PH} = \frac{N_{K\alpha} \, E_{KI}}{\omega \, R_{MAX}} \qquad 2.4.2$$

where R_{MAX} is the value of $R(E_e)$ in the plateau region and ω is the fluorescence yield.

Each K ionisation event deposits an energy E_{KI} in the fluor. A fraction, ω of these ionisations result in the emission of a $K\alpha$ photon of energy $E_{K\alpha}$, which is slightly less than E_{KI}. We will define the ratio of energy carried by $K\alpha$ photons to that deposited into K ionisation as the corrected fluorescence yield:

$$\omega' = \omega \, \frac{E_{K\alpha}}{E_{KI}} \qquad 2.4.3$$

Equation 2.4.2 thus becomes:-

$$E_{PH} = \frac{4\pi Y}{R_{MAX}\,\omega'} \qquad\qquad 2.4.4$$

where Y is the Kα yield in J.sr^{-1}

It is important to note that 2.4.4 gives an absolute minimum value for the preheat energy. Any real distribution will contain electrons for which R(E) is below the plateau. These electrons deposit more energy for a given Kα yield than 2.4.4 suggests.

Thus a single fluor target can give a good measure of the preheat energy content, by its Kα yield. If some reasonable assumption is made about the distribution function, $N(E_e)$, such as suggested by the hard X-ray continuum, a more accurate E_{PH} may be calculated by using $R(E_e)$ averaged over the distribution:

$$\bar{R} = \frac{\int_0^\infty N(E_e)\,E_e\,R(E_e)\,dE_e}{\int_0^\infty N(E_e)\,E_e\,dE_e} \qquad\qquad 2.4.5$$

and the total preheat energy is:

$$E_{PH} = \frac{4\pi Y}{\bar{R}\,\omega'} \qquad\qquad 2.4.6$$

It is desirable to measure the range of fast electrons. A technique therefore has been applied in which tracer layers of different fluors are situated within the target (56). Each layer samples the energy deposition at a specific depth within the target. An accurate reconstruction of the preheat energy deposition profile (and, as we will see later, of the distribution function) can thus be made.
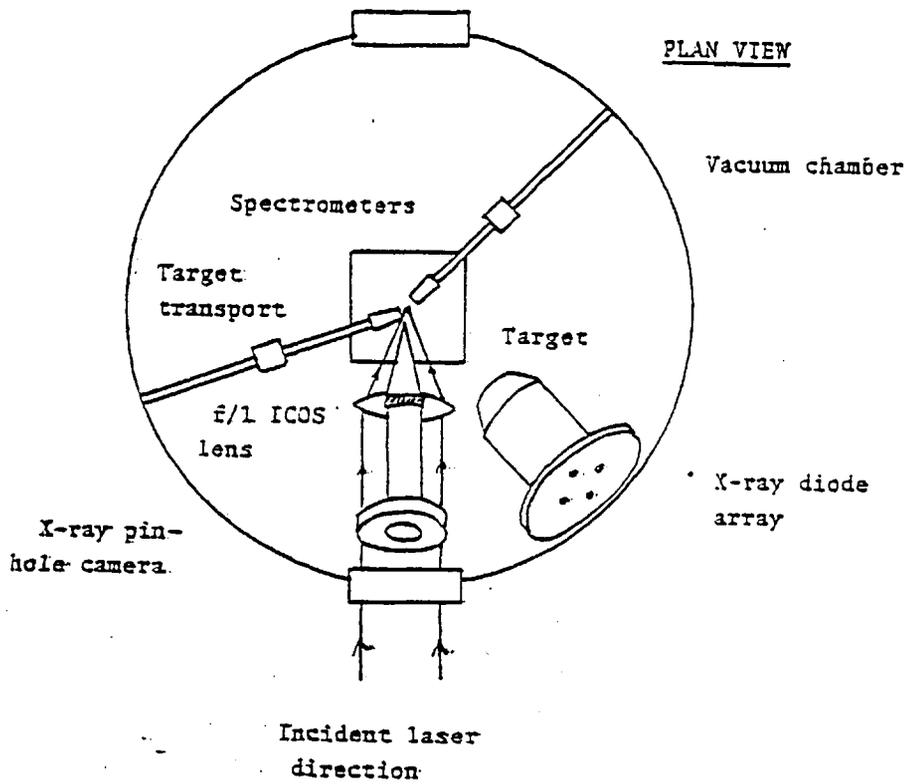
Figure 2.5.1 The experimental layout in the target chamber.
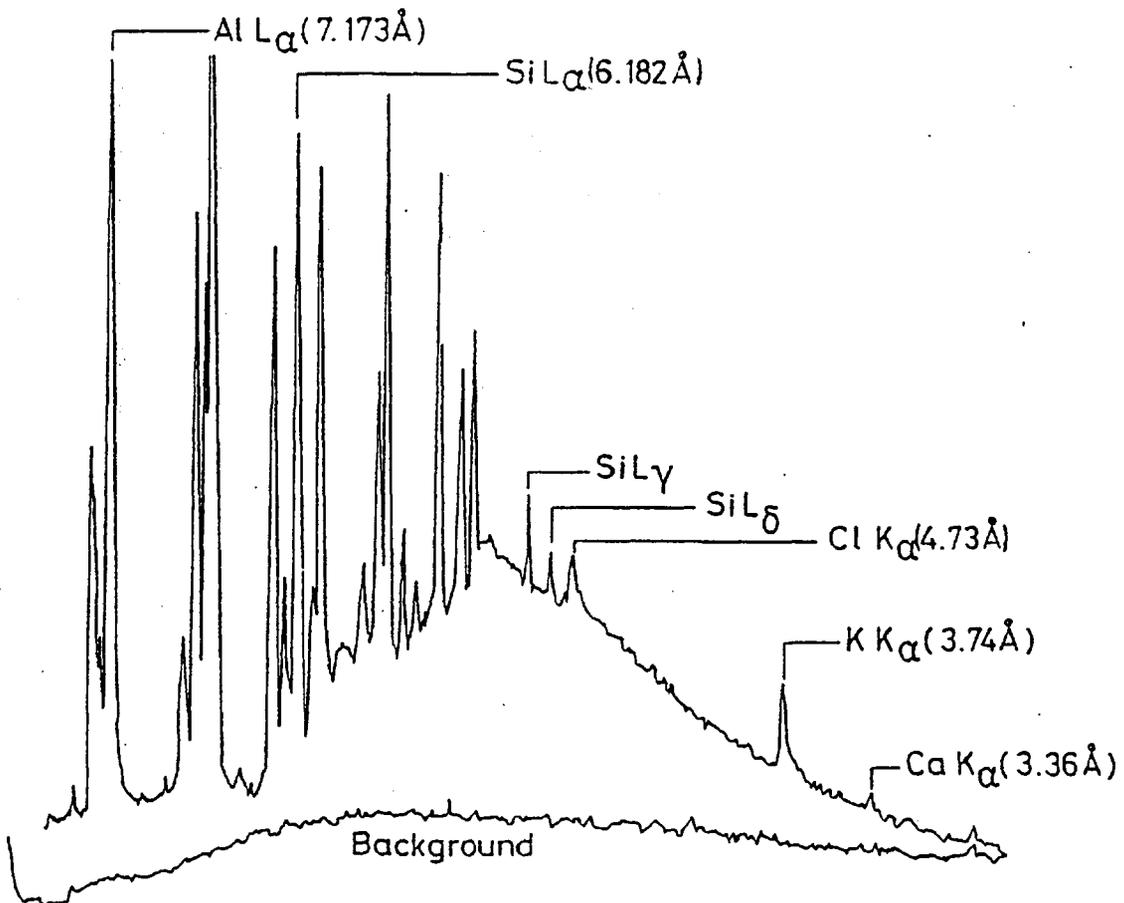
Figure 2.5.2 A typical spectrum recorded on the front (MK I) spectrometer.
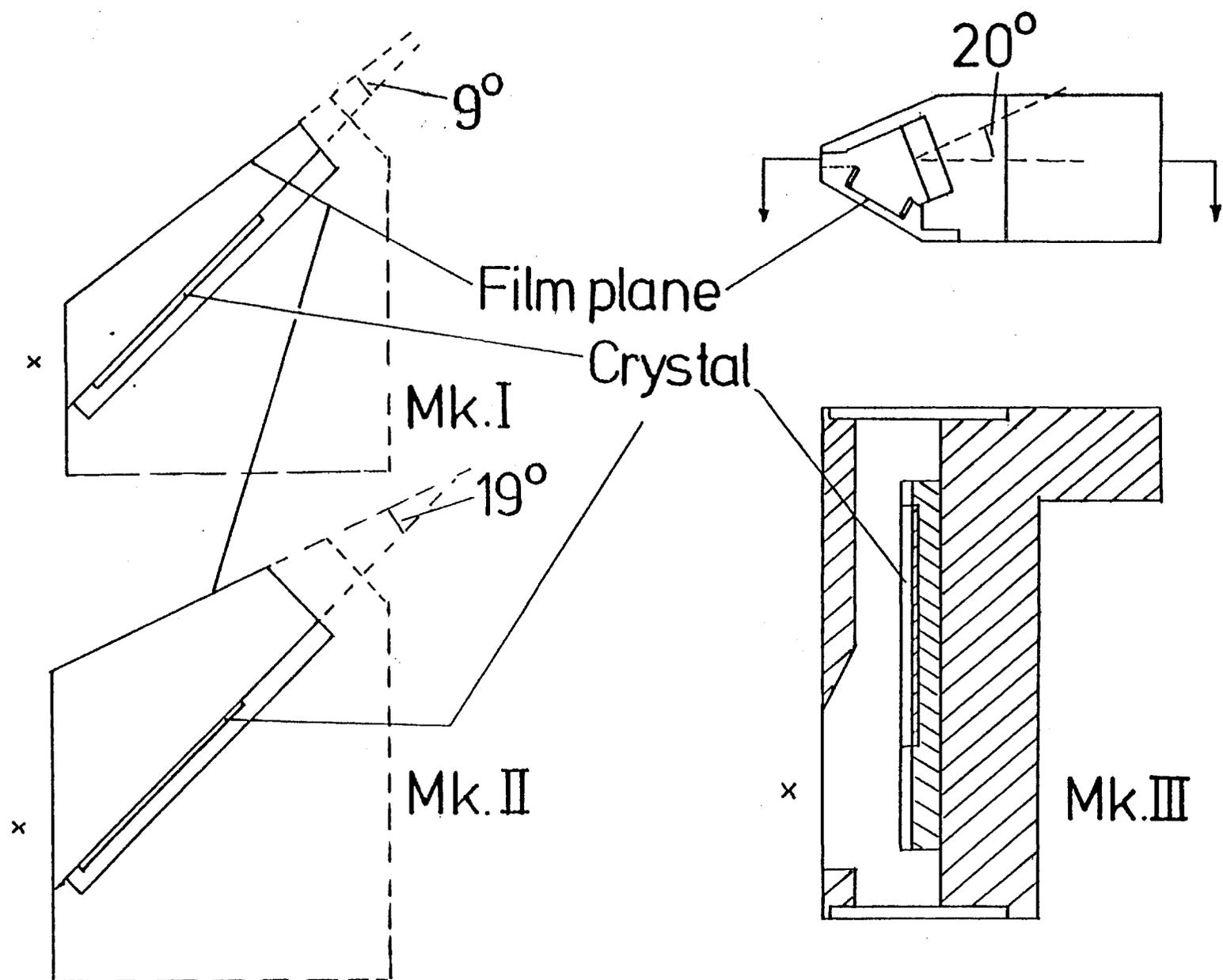
Figure 2.5.3   The geometry of the spectrometers.

2.5   The diagnostics

The prime diagnostics used in the layered target experiments were three miniature space-resolving, time-integrating flat crystal spectrometers. In most experiments two spectrometers were used in the target chamber. This allowed a double check on energy, especially as one could be used in the more sensitive space integrating mode. Some targets were strongly attenuating to X-rays so $K\alpha$ emission was viewed through as little absorbing material as possible i.e. the front spectrometer viewing the front fluor etc. The positioning of the spectrometers with respect to a target is shown in figure 2.5.1. Figure 2.5.2 shows a microdensitometer tracing of a typical spectrum recorded on the Mk. II spectrometer.

The proximity of the spectrometer entrance slits to the plasma resulted in the filter fluorescing under the impact of energetic particles. The Mk. III was configured such that there was no line of sight from the slit to the film. The geometry of the spectrometers is shown in figure 2.5.3 and the performance is described in the appendix. In this experiment pentaerythritol (PET) crystals were used with a 2d (2x crystal plane spacing) of 8.74Å. The crystals have been calibrated in reflectivity (22) and the film used (Kodirex) has been calibrated in sensitivity (57) hence the spectrometers give absolute. intensity measurements. The calibration curves are shown in the appendix. The energy content of a particular line is given by (see appendix):

$$\gamma = \frac{FS \; r \; A}{R_c \; T} \quad J.sr^{-1} \qquad \qquad \underline{2 \cdot 5 \cdot 1}$$

where r is the distance from the source to the film (via crystal), FS is the film sensitivity ($J.ND^{-1}.cm^{-1}$), R_c is the Bragg reflection integral (sr), T is the X-ray transmission along the source-film path and A is the area under the line on the microdensitometer tracing (ND. cm), with any appropriate film non-linearity corrections having been made (see appendix).

This expression is for the spectrometer operating in the space integrating mode i.e. slit width > source size. If spatial resolution

is required a narrow slit ($12\mu m$ or $25\mu m$) can be placed on the
spectrometer. In this case equation <u>2.5.1</u> becomes (see appendix):

$$Y = \frac{r\ A}{FS\ R_c\ T} \frac{(\text{source size})}{(\text{slit width})} \frac{(r_1 + r_2)}{r_1} \qquad \underline{2 \cdot 5 \cdot 2}$$

where r_1 is the distance from the slit to the film, along the X-ray
path and r_2 is the distance from the source to the slit along the same
path.

Subsidiary diagnostics were a X-ray pin-hole camera and a X-ray
pin diode array. The pinhole camera was operated with two copper
substrate pinholes of $3\mu m$ and $6\mu m$ diameter. The filters used were
$25\mu m$ Be and $125\mu m$ Be with transmission cut-off energies of 1.3keV
and 2.5 keV respectively. The overall magnification onto the film
was 4 and the spatial resolution was 5 - $10\mu m$, depending on the film
being used.

The pin diode array consisted of four pin diodes situated $\sim$ 60cm
from the target. Interchangeable filters were screened from energetic
electrons by a magnet. The hardest channel had a filter of $150\mu m$ Ni
with $1/e$ transmission at 35 keV. However at such high energies the
diode response is low, since the absorption in silicon is low. The
peak response is thus at somewhat lower energy (see sub-section 3.2).

2.6 Saturation effects

As fast-electrons deposit energy in the fluor it heats up and
becomes ionised. This results in a shift of the spectral position of
the $K\alpha$ emission. As outer shell electrons are removed, their screening
effect on the inner shells is reduced and the $K\alpha$ emission shifts to
shorter wavelength (58).

This effect becomes large only when electrons are removed from
the L shell. Figure 2.6.1 shows the theoretical spectral position

of the Kα emission as a function of ionisation stage for potassium (58).

POTASSIUM
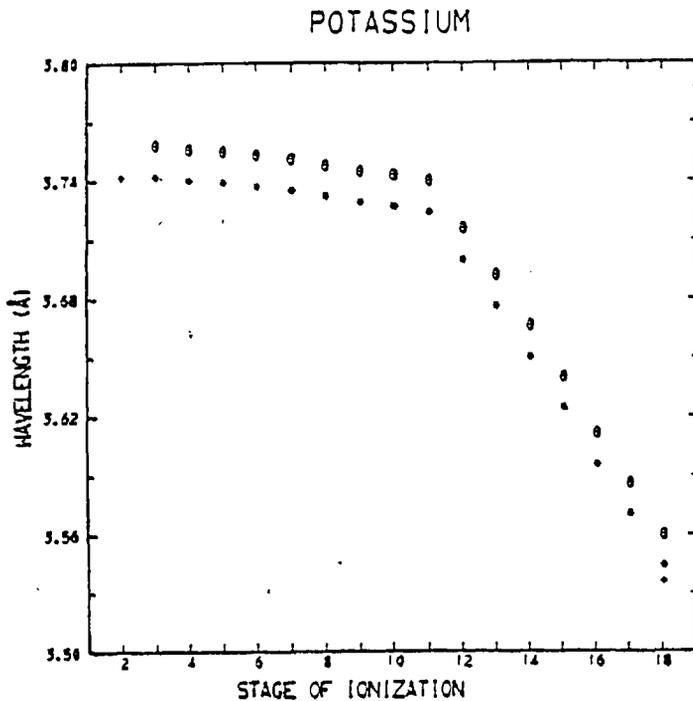
Figure 2.6.1 The spectral position of K Kα emission as a function of ionisation stage (58).

The shifted components of the Kα emission will be undetected when the shift becomes large, because the emission will be spectrally spread out and lost in the noise of the film. Therefore a saturation level for each component of the Kα emission can be predicted. The fractional population density of each ionisation state I, F_I $(\mathcal{E}_d)$ is a function of energy density $\mathcal{E}_d$. Components of the Kα emission arising from states up to (Z-10) will be detected. From 2.4.6 the saturation Kα yield will be:

$$Y_{SAT} = \omega' R(E_e) \int_0^{\mathcal{E}_{d\,max}} \sum_{I=1}^{Z-10} F_I(\mathcal{E}_d)\, d\mathcal{E}_d \cdot \underline{\frac{V}{(Fluor\ volume)}} \qquad 2\cdot6\cdot1$$

The integrand is the instantaneous fraction of the fluor which can emit detectable Kα radiation. We will reduce this integral to a sum. Let the fluor be present as a compound, FC_N in which F is the fluor. The molecular weight is M_n. We will assume that if the average charge

state of any element is $\bar{Z}_x$ then there will only be two species of X with significant populations; $I = INT(\bar{Z}_x)$ and $I = INT(\bar{Z}_x + 1)$, where INT $(\bar{Z}_x)$ is the highest integer less than $\bar{Z}_x$. We will further define FRAC $(\bar{Z}_x) = \bar{Z}_x - INT(\bar{Z}_x)$. Thus up to $\bar{Z}_F = Z_F - 10$ the integrand will have value unity so :

$$Y_{SAT} \left(up\ to\ \bar{Z}_F - 10 \right) = \omega' R(E_e) V \mathcal{E}_d \left(up\ to\ \bar{Z}_F - 10 \right) \qquad 2 \cdot 6 \cdot 2$$

We will now assume that from $\bar{Z} = N$ to $\bar{Z} = N + 1$, Z is linearly dependent on $\mathcal{E}d$, thus:

$$Y_{SAT} \left[(\bar{Z}_F - 10) \rightarrow (\bar{Z}_F - 9) \right] = \tfrac{1}{2} \omega' R(E_e) V \mathcal{E}_d \left[(\bar{Z}_F - 10) \rightarrow (\bar{Z}_F - 9) \right] \qquad 2 \cdot 6 \cdot 3$$

so the total saturation yield is :

$$Y_{SAT} = Y_{SAT} \left[(\bar{Z}_F - 10) \rightarrow (\bar{Z}_F - 9) \right] + Y_{SAT} \left(up\ to\ \bar{Z}_F - 10 \right) \qquad 2 \cdot 6 \cdot 4$$

Since the fluors are present in compounds, we must redefine $R(E_e)$:

$$R_{COMP}(E_e) = \frac{\sigma_K(E_e) E_{KI}}{m_F \tfrac{1}{\rho} \left(\frac{\partial E_e}{\partial s} \right)_F + N m_c \tfrac{1}{\rho} \left(\frac{\partial E_e}{\partial s} \right)_c} \qquad 2 \cdot 6 \cdot 5$$

For a given element of average charge state Z the energy density is given by:

$$\mathcal{E}_d = n_A \left\{ \sum_{I=1}^{INT(\bar{Z})} IP(I) + FRAC(\bar{Z}) IP(INT(\bar{Z}+1)) + \tfrac{3}{2} kT_e (\bar{Z}+1) \right\} \qquad 2 \cdot 6 \cdot 6$$

For a compound with fluor average charge $\bar{Z}_F$, $\bar{Z}$ and $\bar{Z}_c$ are fixed by the equation of state. Thus:

$$\mathcal{E}_d = n_m \left\{ \sum_{I=1}^{INT(\bar{Z}_F)} IP_F(I) + FRAC(\bar{Z}_F) IP_F(INT(\bar{Z}_F+1)) + N \left[\sum_{I=1}^{INT(\bar{Z}_c)} IP_c(I) + \right. \right.$$

$$\left. \left. FRAC(\bar{Z}_c) IP_c(INT(\bar{Z}_c+1)) \right] + (1+N)(\bar{Z}+1) \tfrac{3}{2} kT_e \right\} \qquad 2 \cdot 6 \cdot 7$$

From equation 2.6.4 we see that the total yield is given by:

$$Y_{SAT} = V\eta_m \omega' R_{COMP}(E_e) \left\{ \mathcal{E}_d (\bar{Z}_F = 0 \rightarrow \bar{Z}_F - 10) + \right.$$

$$\frac{1}{2} \mathcal{E}_d \left(\bar{Z}_F = (\bar{Z}_F - 10) \rightarrow (\bar{Z}_F - 9) \right) \right\}$$

$$= V\eta_m \omega' R_{COMP}(E_e) \left\{ \mathcal{E}_d (\bar{Z}_F = 1 \rightarrow \bar{Z}_F - 9) - \right.$$

$$\frac{1}{2} \mathcal{E}_d \left\{ \bar{Z}_F = (\bar{Z}_F - 10) \rightarrow (\bar{Z}_F - 9) \right\} \quad \underline{2.6.8}$$

The first term is given by 2.6.7. To simplify the second term, two assumptions will be made; i) ionisation potentials scale as Z^2 and ii) $\delta Z_c \simeq \delta Z_F$. Assumption ii) is valid if $Z_F \simeq Z_c$. Thus:

$$\mathcal{E}_d \left(\bar{Z}_F = (\bar{Z}_F - 10) \rightarrow (\bar{Z}_F - 9) \right) = V\eta_m \left\{ IP(\bar{Z}_F - 9) + N \cdot FRAC(\bar{Z}_c) \right.$$

$$\times \left(\frac{\bar{Z}_c}{\bar{Z}_c + 1} \right)^2 IP_c (INT(\bar{Z}_c + 1)) + (N+1) k \left((\bar{Z} + 1) T_e^- - \bar{Z} T_e' \right) \quad \underline{2.6.9}$$

Where T_e^1 is the temperature at $Z_F = Z_F - 10$. Now by combining 2.6.7, 8 and 9 and centring T_e and Z at $Z_F = Z_F - 9.5$ we obtain:

$$Y_{SAT} = V\eta_m \omega' R_{COMP}(E_e) \left\{ \sum_{I=1}^{Z_F - 10} IP_F(I) + N \sum_{I=1}^{INT(\bar{Z}_c - 1)} IP_c(I) + \frac{1}{2} IP_F(\bar{Z}_F - 9) \right.$$

$$+ \frac{N}{2}(1 - FRAC(\bar{Z}_c)) IP_c(INT(\bar{Z}_c)) + \frac{N}{2} FRAC(\bar{Z}_c) \left(\frac{Z_c}{\bar{Z}_c + 1} \right)^2 IP_c(INT(\bar{Z}_c + 1))$$

$$+ (N+1) k (\bar{Z} + 1) T_e \quad \underline{2.6.10}$$

An LTE equation of state can be used to relate Z and T_e. Using the algorithm of (59) to solve the Saha equation gave the saturation yields per atom shown in figure 2.6.2. The saturation yield is a function of density via the density dependence of the Saha equation.

Figure 2.6.2 The saturation electron pumped $K\alpha$ yield per atom as a function of Z.
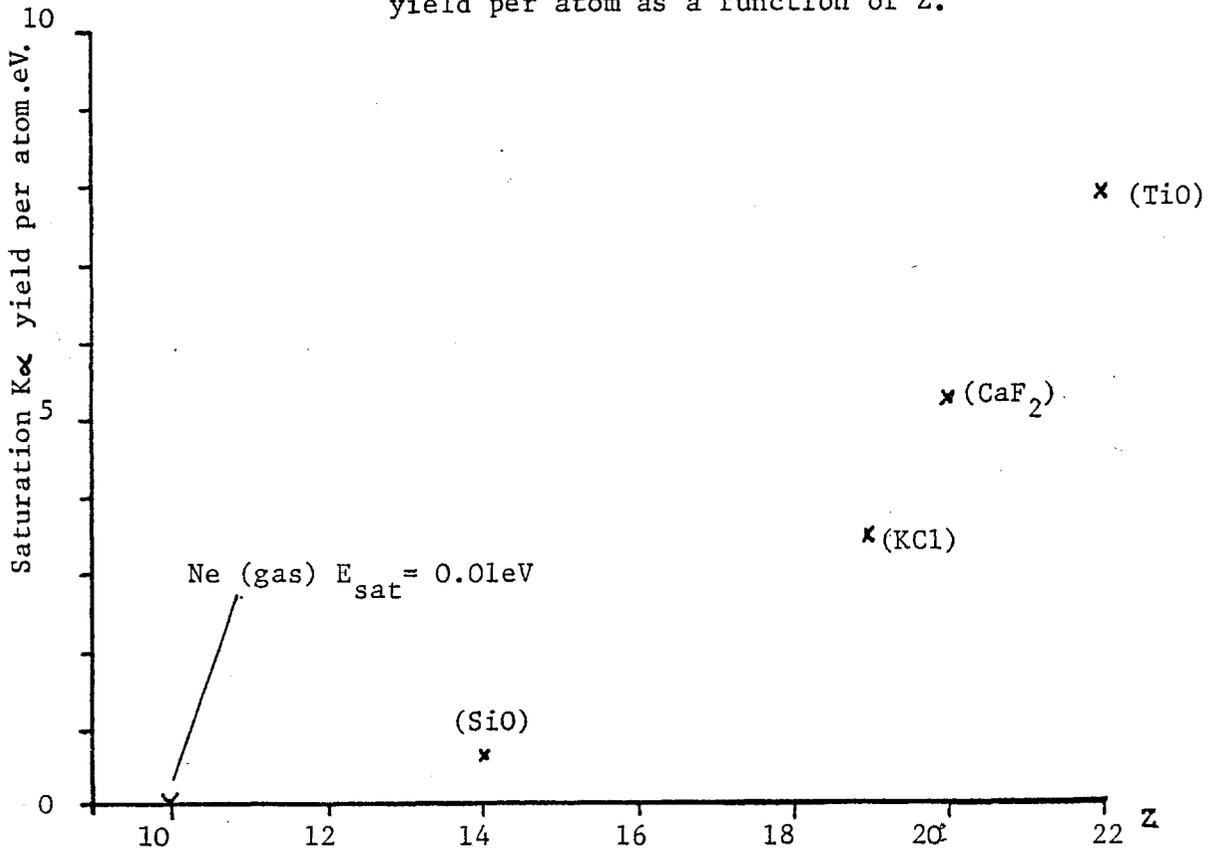
It is necessary that the saturation energy for the relevant volume of fluor material is greater than the fast electron energy deposition, if the $K\alpha$ yield is to give a reliable measure of preheat. This implies using a high Z fluor such that:

$$Z_{FLUOR} > 10 \qquad\qquad \underline{2 \cdot 6 \cdot 11}$$

The lowest energy fast electron which is detectable has energy E_{KI}. The typical suprathermal energy is kT_H so:

$$E_{KI} < kT_H \qquad\qquad \underline{2 \cdot 6 \cdot 12}$$

So far it has been assumed that the fluorescence yield is independent of the-state of the fluor. As the fluor becomes ionised, one might expect ω to increase, since the number of electrons which participate in competing transitions is reduced. However, as demonstrated in (48), the dominant transitions all originate from the L-shell therefore no great change in ω is to be expected until the L shell is disturbed. This is

confirmed by the behaviour of ω as a function of Z. Radiative transition rates generally scale as Z^4 (45). Non-radiative decay rates however are Z independent. If the total non-radiative (Auger) rate is A_{NR} and the total $K\alpha$ radiative decay rate is $A_{K\alpha}$ then (neglecting other radiative transitions):

$$\omega = \frac{A_{K\alpha}}{A_{K\alpha} + A_{NR}} \qquad 2.6.13$$

If all electrons contribute to the total Auger rate then A_{NR}, being a sum of non Z dependent contributions for each electron, will be Z dependent. Conversely, if only L shell electrons participate significantly in Auger transitions then A_{NR} will be Z independent for a full L shell. The fluorescence yield will thus be:

$$\omega = \frac{Z^4}{Z^4 + const.} \qquad 2.6.14$$

and a plot of $(1 - \omega).Z^4$ vs ω will yield a straight line. This plot is shown in figure 2.6.3.

It is evident from this figure that the Auger rate is not dependent on ionization stage for $\bar{Z} < Z - 10$. As previously stated, the radiative transition rate is dependent on Z^4. The charge seen by electrons in the K shell only suffers screening from tightly bound electrons, i.e. those inside the L shell. The radiative rate will therefore also be independent of ionisation state for $Z < Z - 10$. This condition is the same as the saturation condition described above and therefore does not affect our analysis.
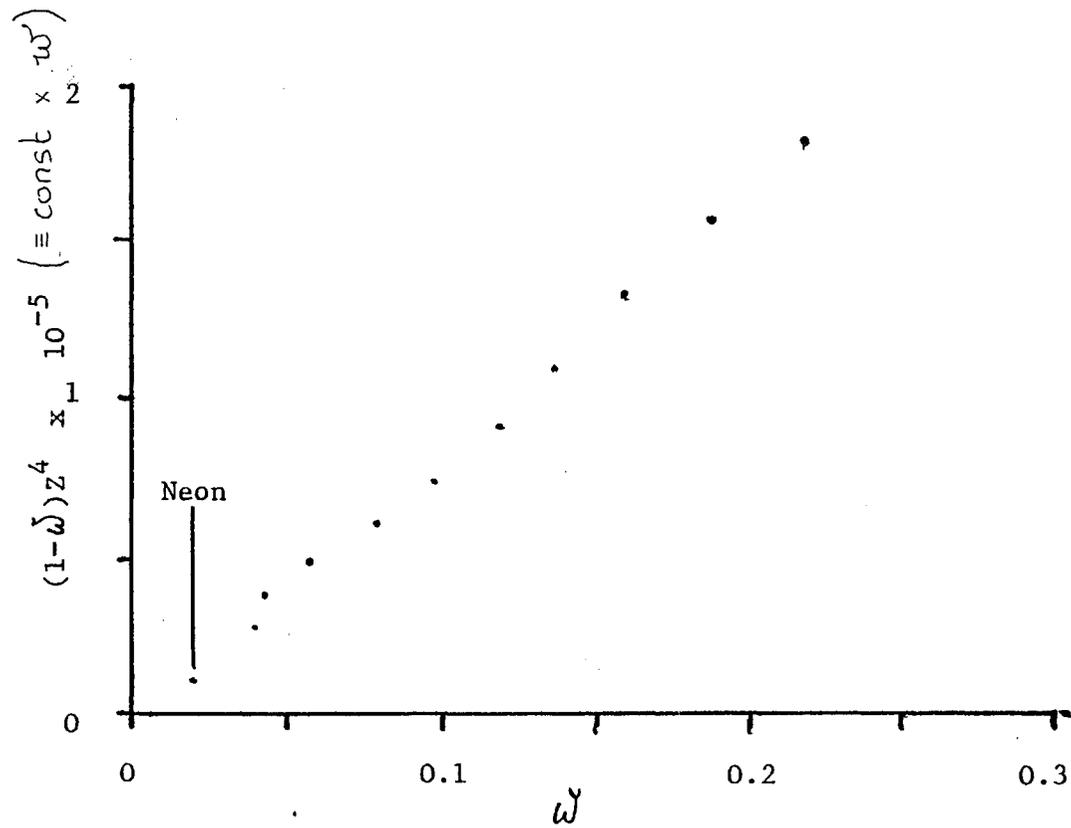
Figure 2.6.3. The function $(1 - \omega)Z^4$ as a function of ω.

2.7 Radiation pumping

It is apparent from figure 2.5.2 that there is significant
energy in the recombination continuum of the ablation plasma. If
E_{KI} is too low there is a danger that the $K\alpha$ emission will be
dominantly pumped by X-rays as opposed to fast electrons. This can
be avoided by using a fluor of as high as Z, and hence E_{KI} as
possible. Increasing E_{KI} reduces the amount of X-ray energy above the
K absorption edge and thus reduces the radiation pumping.

The continuum emission shown in figure 2.5.2 is typical of all
the laser shots with an aluminum plasma. It is conveniently represented
by:

$$\frac{\partial I}{\partial h\nu} = I_\nu = I_o \exp\left(-h\nu/kT_c\right) \qquad \underline{2.7.1}$$

where T_c is the thermal plasma temperature, $0.5 \pm 0.1 \text{KeV}$ and $I_o = (6.0 \pm 1.0) \times 10^{-2} \text{ Jsr}^{-1} \text{ keV}^{-1}$.

From equation $\underline{2.4.12}$ the $K\alpha$ yield induced in a solid fluor target
by X-rays in the range $h\nu \rightarrow h\nu + dh\nu$ will be:

$$dY = 2\pi I_o \exp\left(-h\nu/kT_c\right)\frac{dh\nu}{4\pi h\nu} E_{KI}\left(1 - \frac{1}{J_R}\right)\omega' \qquad \underline{2.7.2}$$

so the total $K\alpha$ yield induced by the continuum is:

$$Y = \frac{I_o E_{KI}}{2}\left(1 - \frac{1}{J_R}\right)\omega' \int_{E_{KI}}^{\infty} \frac{1}{h\nu} \exp\left(-\frac{h\nu}{kT_c}\right) dh\nu \qquad \underline{2.7.3}$$

neglecting absorption effects.

We will now evaluate the $K\alpha$ yield induced by the continuum emission
in order to select suitable fluors. In figure 2.7.1 equation $\underline{2.7.3}$ is
applied to the continuum $\underline{2.7.1}$ for various fluor elements.

Pumping continuum is			6.0 x 10^{-2} J.sr^{-1}.keV^{-1}		
Fluor (Z)	E_{K1} (keV)	E_K (keV)	ω^y	J_R	Yield (J.sr^{-1})
Chlorine 17	2.82	2.62	0.098	9.8	4.2 x 10^{-6}
Potassium 19	3.62	3.32	0.138	9.3	1.2 x 10^{-6}
Calcium 20	4.04	3.69	0.163	9.1	6.1 x 10^{-7}

Figure 2.7.1 A comparison of the susceptibility of various fluors to radiation pumping of Kα emission.

The minimum detectable Kα yield is 10^{-6} Jsr^{-1}, thus a significant radiation pumped yield will be induced in chlorine, however potassium and elements of higher Z are sufficiently imune to be useful as fast electron detectors. Radiation pumping considerations thus give:

$$ Z \geqslant 19 \qquad\qquad 2.7.4 $$

We will now perform a more general calculation of radiation pumping for a practical layered target, including absorption effects. Figure 2.7.2 shows the geometry of the calculation.

In consideration of the small depth and hence optical depth of the ablation plasma I_y is assumed isotropic.

The number of photons emitted into dhv dθ is:

$$ n_{ph} = \frac{I_v}{h\nu} dh\nu\, d\Omega $$

$$ = \frac{I_v}{h\nu} 2\pi \sin\theta\, dh\nu\, d\theta \qquad\qquad 2.7.5 $$

These are attenuated in the layers between the source and the fluor
by:

$$A(h\nu, \theta) = \exp\left(- \sum_{n=1}^{N} (t_n \mu_n (h\nu) / \cos\theta\right) \qquad 2.7.6$$

where $\mu_n (h\nu)$ is the scalar attenuation coefficient of the material
of layer n.
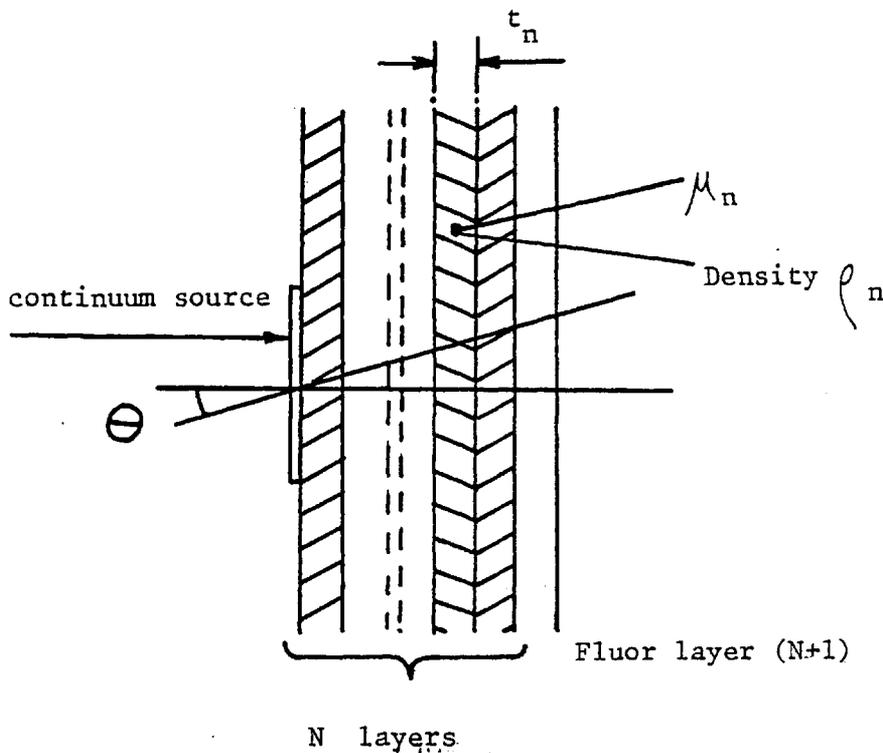
Figure 2.7.2 The geometry of the radiation pumping calculation.

A fraction, F, will then be absorbed by the fluor:

$$F(h\nu, \theta) = 1 - \exp\left(-t_{N+1} \mu_{N+1} (h\nu) / \cos\theta\right) \qquad 2.7.7$$

A fraction, B, of these photons will cause K ionisations in the
fluor layer which consists of elements I and II where I is the
fluor:

$$B(h\nu) = \left(1 - \frac{1}{J_R}\right) \cdot \frac{\mu_I (h\nu)}{\mu_I (h\nu) + \mu_{II}(h\nu)} \qquad 2.7.8$$

This fraction is a very weak function of $h\nu$, for $h\nu > E_{KI}$, since μ_I and μ_{II} in general exhibit λ^3 dependence.

The number of photons, which cause K ionisations in element I, absorbed in the fluor is:

$$N_{KI} = B \int_0^{\pi/2} \int_{E_{K\alpha}}^{\infty} A(h\nu,\theta) F(h\nu,\theta) I_\nu \sin\theta \, \frac{2\pi}{h\nu} \, dh\nu d\theta \qquad \underline{2.7.9}$$

Each K ionisation liberates $\omega \, E_{K\alpha}$ joules into 4π steradians. The total radiation pumped $K\alpha$ yield is thus:

$$Y = N_{KI} \, \omega \, E_{K\alpha} / 4\pi \qquad \underline{2.7.10}$$

2.8   Target design and fabrication

In consideration of equations 2.6.11, 2.6.12 and 2.7.4, potassium, calcium and titanium where chosen as fluor elements. The targets were fabricated by vacuum evaporation. Low melting point compounds containing the fluor elements were selected and their properties are given in figure 2.8.1

FLUOR ELEMENT	COMPOUND	DENSITY ($g\ cm^{-3}$)	MELTING POINT(°C)	$K\alpha$ ENERGY(keV)	$K\alpha$ WAVELENGTH($\overset{\circ}{A}$)
POTASSIUM (19)	KCl	1.98	770	3.32	3.74
CALCIUM (20)	CaF$_2$	3.18	1423	3.69	3.36
TITANIUM (22)	TiO	4.93	1750	4.51	2.75
POTASSIUM (19)	KBr	2.75	734	3.32	3.74

Figure 2.8.1   The fluors used in these experiments and some of their physical characteristics.

In order that each fluor layer samples a narrow part of the fast electron spectrum, the thickness of the layer, t, must be small compared with the total electron range:

$$t \;<\; \frac{kT_H}{\left(\dfrac{\partial E_e}{\partial s}\right)} \qquad\qquad \underline{2 \cdot 8 \cdot 1}$$

On the other hand the layer must be sufficiently thick that the $K\alpha$ yield is detectable with a good signal to noise ratio. We will now take T_H = 15keV and E_{PH} = 1Joule as typical values ([2]) to estimate the correct fluor thickness. Assuming that all the fast electrons have E_e = 15keV and that the fluor thickness is such that <u>2.8.1</u> is valid, the number of electrons passing through the fluor is:

$$n_e \;\simeq\; \frac{E_{PH}}{kT_H(eV).\,e} \qquad\qquad \underline{2 \cdot 8 \cdot 2}$$

Each electron will cause n_{KI} K ionisations:

$$n_{KI} \;=\; \sigma_K\,(kT_H).\frac{\rho}{m_m}\,t \qquad\qquad \underline{2 \cdot 8 \cdot 3}$$

where m_m is the molecular weight of the fluor compound. The $K\alpha$ yield is thus:

$$Y \;\simeq\; \frac{E_{PH}}{kT_H\,e}\;\frac{\sigma_K\,\rho\,t}{m_m}\;\frac{\omega\,E_{K\alpha}}{4\pi}$$

$$=\; \frac{E_{PH}\;\sigma_K\,\rho\,t\;\omega}{m_m\,4\pi}\;\frac{\overbrace{E_{K\alpha}}^{eV}}{\underbrace{kT_H}_{eV}}\; J.sr^{-1} \quad \underline{2 \cdot 8 \cdot 4}$$

If the sensitivity of the spectrometer is Y_{MIN} then:

$$t \;\simeq\; \frac{Y_{MIN}\;m_m\;4\pi\;kT_H}{E_{PH}\;\sigma_K\,\rho\,\omega\;E_{K\alpha}}\times 10 \quad (signal\!:noise) \qquad \underline{2 \cdot 8 \cdot 5}$$

Now $Y_{MIN} \simeq 10^{-6} Jsr^{-1}$ thus for each of the fluor compounds in figure 2.8.1:

Compound	$\sigma K(15keV)$	E_{KI}	t	$E/\frac{\partial E}{\partial s}$
KCl	$1.95 \times 10^{-21} cm^2$	3.62keV	2.65μm	6.3μm
CaF$_2$	$1.62 \times 10^{-21} cm^2$	4.04keV	1.58μm	3.9μm
TiO	$1.11 \times 10^{-21} cm^2$	4.98keV	0.74μm	2.5μm
KBr	$1.95 \times 10^{-21} cm^2$	3.62keV	2.97μm	4.5μm

Figure 2.8.2 A guide to the optimum fluor thickness.

In a two fluor layer target the temperature of the fast electron distribution can be obtained from the ratio of the two Kα yields (sub-section 2.10). For this ratio to be sensitive to changes in T_H, the separation of the fluors must be well matched to the fast electron range. The targets were fabricated by evaporating the various compounds onto a thin mylar substrate. The separation of the front and rear fluors can be set by choosing a suitable mylar thickness. In figure 2.8.3 the optimum separation is shown for various values of $\overline{E_e}$, the mean electron energy. This separation is obtained from (41) and is the total fast electron range for $E_e = kT_H$. N.B. The preheat range is approximated by the residual range. This is inaccurate due to scattering effects but will suffice for these approximate target calculations.

$\overline{E_e}$ (keV)	Range (taking Z = 13)*	Equivalent mylar thickness	Available mylar thickness
10	0.35 mgcm^{-2}	2.92μm	2μm
15	0.71 mgcm^{-2}	5.92μm	7μm
20	1.17 mgcm^{-2}	9.75μm	12μm
25	1.72 mgcm^{-2}	14.33μm	25μm
30	2.36 mgcm^{-2}	19.67μm	50μm

* A rough average of mylar and the fluor compounds

Figure 2.8.3 A guide to the fast electron filter thickness.

The front fluor layer contributes significantly to the electron range for low energies and is equivalent to $\sim 4\mu m$ mylar. However it was found in practice that targets sensitive to fast electrons with $kT_H = 5keV$ could be made using a $2\mu m$ mylar substrate and fluor layers as above. In view of the preceding calculations the following two-fluor layer targets were constructed (target type I)

$$0.1\mu m \ Al, \quad 1\mu m \ SiO, \quad 2\mu m \ CaF_2, \quad Mylar, \quad 5\mu m \ KBr$$

with mylar of $2\mu m$ and $7\mu m$ thickness.

The SiO layer acted as an isolator, protecting the fluor layer from the thermal ablation front, whose penetration depth is $0.1\mu m$ in 100ps (22). The aluminum provided a (previously) well characterised plasma (22) and provided burn depth information (see sub-section 6.1).

It was found that KBr was not a good fluor (i) due to the large attenuation of the emission by bromine and (ii) because of the large mass of the layer. In view of this, KCl was substituted and the following targets fabricated (target type II):

$$0.1\mu m \ Al, \quad 1\mu m \ SiO, \quad 2\mu m \ CaF_2, \quad Mylar, \quad 4\mu m \ KCl$$

$$7\mu m \ \text{and} \ 12\mu m \ mylar$$

These targets had the shortcoming that on viewing both $K\alpha$ emissions from the rear (the rear spectrometer being space integrating and hence more sensitive) the Ca $K\alpha$ emission was strongly absorbed by the KCl. This was because $E_{K\alpha}(Ca) > E_{KI}(K) > E_{KI}(Cl)$ thus KCl is highly attenuating to Ca $K\alpha$. There is however an advantage with this arrangement. The fluor which has the highest saturation yield, i.e. has the highest Z, is at the front where the energy deposition is largest.

One further advantage of KCl over KBr is that Cl $K\alpha$ is produced. From figure 2.7.1 it is apparent that the chlorine will be radiatively pumped and this provides a quantitative check on the work in sub-section 2.7.

To minimise target absorption when viewing from the rear the
layers must be arranged in order of increasing Z from front to rear.
This leads to the final type of two layer target (type III).

$$0.1\,\mu m \ Al \ , \quad 1\,\mu m \ SiO \ , \quad 3\,\mu m \ KCl \ , \quad Mylar \ , \quad 2.5\,\mu m \ CaF_2$$

$$2\,\mu m \ , \quad 12\,\mu m \ , \quad 25\,\mu m \ and \ 50\,\mu m \ Mylar$$

In order to measure the energy deposition throughout the target,
a three fluor layer target was fabricated (type IV). It was designed
for minimum absorption from the rear and consisted of:

$$0.1\,\mu m Al \ , \quad 1\,\mu m SiO, \quad 2\,\mu m \ KCl, \quad 2\,\mu m \ Mylar, \quad 3\,\mu m CaF_2 \ , \quad 2\,\mu m Al \ , \quad 0.8\,\mu m TiO$$

In all cases the targets were irradiated from the aluminum side.

2.9   The observation of Z related effects

(i)   Saturation

The saturation yield can be predicted from equation 2.6.10.   In
view of the high density, electron-ion equipartition is assumed so T_e and
T_i are equal.   Figure 2.9.1 shows a microdensitometer tracing of the $K \ K_\alpha$
emission recorded on the front spectrometer.   In this example a type III
target ($12\,\mu m$ Mylar) was irradiated at 3×10^{15} Wcm^{-2}.   The focal diameter
was $100\,\mu m$.   The predicted saturation yield is 1.7×10^{-5} Jsr^{-1}.   The shaded
area in figure 2.9.1 covers all the components up to ionisation stage
(Z - 10).   The energy carried by these components is $(1.4 \pm 0.1) \times 10^{-5}$ Jsr^{-1}.
This is in reasonable agreement with theory.

The positions of $K\alpha$ like emission from ([58]) should be compared
with the observed peaks.   The main peak appears to be at the position of
the K^{9+} $1s2s^22p^6$ - $1s^22s^22p^5$ transition. (The longest wavelength peak was
taken as the unionised component).   This is to be expected because the
ionisation potentials suddenly increase beyond K^{9+} .   As energy is
deposited, Z will increase rapidly to 9 and then stay there until sufficient
energy has been deposited to overcome the next (high) ionisation potential.
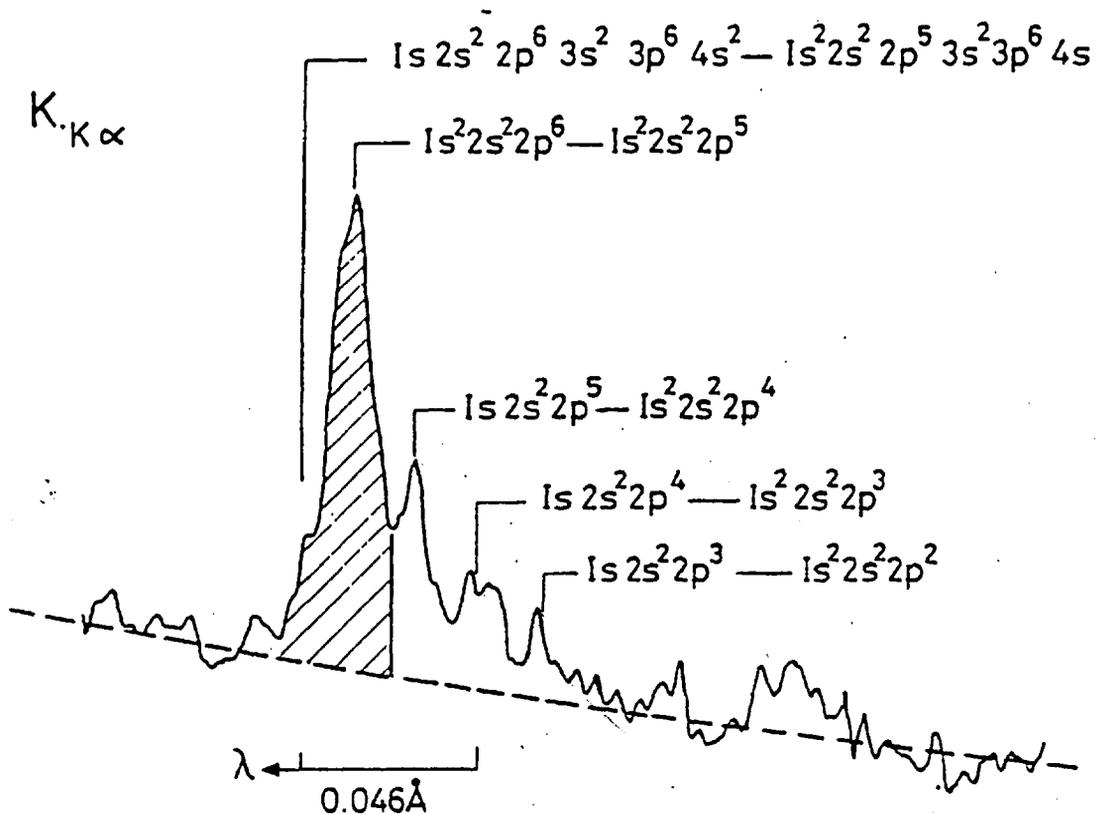The fluor will therefore have Z = 9 for a large part of the pulse.

$$Is\,2s^2\,2p^6\,3s^2\,3p^6\,4s^2 - Is^2 2s^2\,2p^5\,3s^2 3p^6\,4s$$

$$Is^2 2s^2 2p^6 - Is^2 2s^2 2p^5$$

$$Is\,2s^2 2p^5 - Is^2 2s^2 2p^4$$

$$Is\,2s^2 2p^4 - Is^2 2s^2 2p^3$$

$$Is\,2s^2 2p^3 - Is^2 2s^2 2p^2$$

$K_{\cdot K\alpha}$

λ

0.046Å

Figure 2.9.1 A microdensitometer tracing of the K K$_\alpha$ emission from target type III. Also shown are the positions of the K$_\alpha$ like transitions from (58).

(ii) Radiation pumping

.The recombination continuum, I_v, is not a strong function of the focussing conditions. To observe radiation pumping, a target(typeII) with a 25μm mylar substrate was irradiated at a position 400μm away from best focus. At this position the focal diameter was large ($\sim$ 350μm) and the intensity low ($\sim$ 2 x 10^{14}wcm^{-2}). The fast electrons were insufficiently energetic to penetrate to and activate the rear fluor layer. This was corroborated by the absence of any detectable K K$_\alpha$emission. The Cl K$_\alpha$ emission however was (1.3 $\pm$ 0.1) x 10^{-6}Jsr^{-1}, The recombination continuum was measured to have I_0 = (6.0 $\pm$ 1.0) x 10^{-2} Jsr^{-1}keV^{-1} and kT$_c$ = (0.5 $\pm$ 0.1)keV. Equations 2.7.9 and 2.7.10 predict a radiation pumped Cl K$_\alpha$yield of 1.7 x 10^{-6}J.sr^{-1}, for this target and continuum intensity. There is reasonable agreement with experiment. The predicted radiation pumped K K$_\alpha$yield is 0.3 x 10^{-6}J.sr^{-1} to be compared with the observed upper limit of 10^{-6}J.sr^{-1}. However on some shots where the KCl layer was at the front, the radiation pumped K K$_\alpha$ yield was significant (up to 30% of the

electron pumped yield on low intensity shots). In all cases this yield
was evaluated and allowed for in the preheat analysis. The CaK_α and
Ti K_α radiation pumped yields were at all times negligible.

In (60) and (61) K_α emission is interpretted as originating
from fast electron pumping. In (60) a study with 10.6μm illumination
at 3 x 10^{13}w.cm^{-2} yielded the range and effective temperature of the fast
electrons using Si and Cu as fluors. We would estimate that SiK_α emission
would be significantly radiation pumped. However, Cu is of sufficiently
high Z that CuK_α will originate from electron pumping only.

In (61) Ne K_α emission from a neon filled microballoon was reported.
Consideration of saturation effects would indicate that the reported yield of
of 2 x 10^{-4}J is $\sim 10^3$ times larger than the saturation yield for 10^{14}Ne
atoms (5 x 10^{-7}J). We conclude that the emission was either incorrectly
identified or completely radiation pumped.

2.10 Prediction of K_α yields and calibration of targets.

In order to accurately deconvolve the fast electron spectrum, it is
necessary to predict the K_α yields induced by various model fast electron
distributions.

Consider electrons incident on a solid fluor target. Their linear
motion (neglecting scattering) is described by:

$$\frac{\partial E_e}{\partial s} = \frac{2\pi e^4 Z n_A}{E_e} \ln\left(\frac{4 E_e}{\bar{I P}}\right) \qquad 2\cdot10\cdot1$$

the non-relativistic Bethe Bloch linear stopping formula (32), where S
is along the path of the electron. The total number of K ionisation
events produced along the path 0 to S_{max} will be:

$$N_{KI} = \int_0^{S_{MAX}} \sigma_K (E_e(s)) \, n_A \, ds \qquad 2\cdot10\cdot2$$

However for real targets, the fluor is not infinite and scattering effects must be included.

Spencer (43) has performed extensive numerical calculations on electron energy deposition. An example from his results is shown in figure 2.10.1.

These calculations were performed for monoenergetic electrons normally incident on homogeneous targets. We will adapt them to multimaterial targets. The energy deposition in the target due to an incident electron of energy E_o in a layer dx can be expressed as:

$$\left(\frac{\partial E_e}{\partial x}\right)dx = \frac{\partial E_e}{\partial s}\bigg|_{\substack{x=0 \\ E_e=E_o}} f(x) \quad g(E_e)dx \qquad 2\cdot10\cdot3$$

where f(x) is the ratio of actual path length of the electron passing through dx to dx, and g(x) is the linear electron energy deposition rate in dx divided by the initial energy deposition rate at E_o.

The non-relativistic linear energy deposition rate, $\partial E/\partial s$, is given by equation 2.2.1. Thus if $E_e(x)$ is the average electron energy in dx then:

$$g(x) = \frac{K\left(\ln E_e(x) - \ln \overline{IP}\right)}{K\left(\ln E_o - \ln \overline{IP}\right)} \qquad 2\cdot10\cdot4$$

and if $E_e(x) \gg \overline{IP}$

$$g(x) = \frac{\ln E_e(x)}{\ln E_o} \qquad 2\cdot10\cdot5$$

It is now assumed that the scattering (f(x)) and average energy ($E_e(x)$) in the target can be approximated by taking an average Z throughout it. This is reasonable since the scattering and stopping power of the target is not a strong function of Z and the overall effect on the fluor is the cumulation of scattering and energy deposition in each layer. Our targets have Z in the range 7 → 18.

Thus the energy deposition in a multilayer target by an incident electron is:
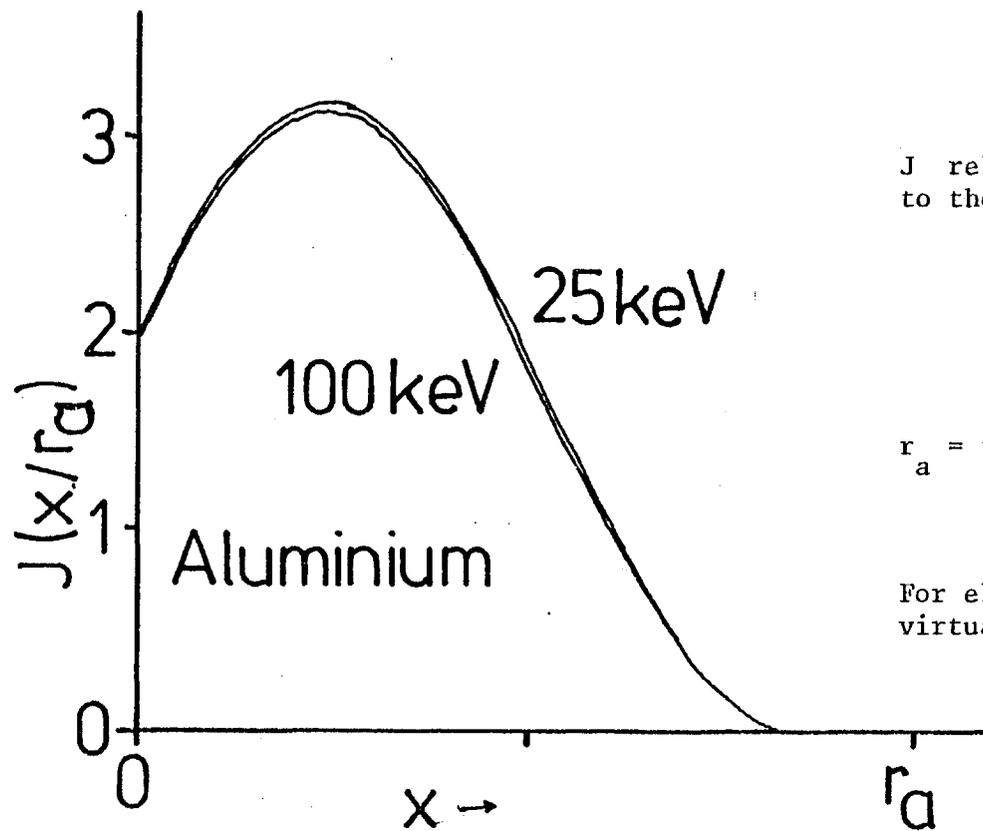
J relates the unscattered energy deposition rate to the real rate:

$$\frac{1}{\rho}\left(\frac{\partial E_e}{\partial x}\right)_x = \frac{1}{\rho}\left(\frac{\partial E_e}{\partial s}\right)_{E_e = E_o} \cdot J\left(\frac{x}{r_a}\right)$$

r_a = the total linear range in the absence of scattering

For electrons in the range E_o=10-200keV $J(x/r_a)$ is virtually indepdent of E_o.

Figure 2.10.1 A complete result from (43) for electrons of energy 25 - 100 keV incident on aluminium.

$$dE = \left.\frac{\partial Ee}{\partial s}\right|_{\substack{Z \\ E_o \\ X=0}} g_{\bar{Z}}(x)\, f_{\bar{Z}}(x)\, dx \qquad \underline{2 \cdot 10 \cdot 6}$$

which by Spencer's notation is:

$$dE = \frac{1}{\rho}\left(\frac{\partial Ee}{\partial s}\right)_{\substack{r_o \\ Z}} J_{\bar{Z}}\left(\frac{X}{X_{o\bar{Z}}}\right) \rho_{\bar{Z}}\, dx \qquad \underline{2 \cdot 10 \cdot 7}$$

$x_{o\bar{Z}}$ = integrated linear Bethe Bloch range.

Of the energy deposited by the electron, a fraction $R(E_e)$ goes into K shell ionisation. It should again be noted that for energies above ~ 15 keV the ratio is nearly constant.

Of the energy going into K ionisations a fraction ω' reappears as $K\alpha$ radiation, where ω' is the corrected fluorescence yield. The $K\alpha$ yield per electron is given by:

$$Y(E_o) = \frac{1}{4\pi} \cdot \frac{1}{\rho}\left(\frac{\partial Ee}{\partial s}\right)_{\substack{E_o \\ Z}} J_{\bar{Z}}\left(\frac{X}{X_{o\bar{Z}}}\right) \rho_{\bar{Z}}\, dx\, R(E_e)\, \omega' \qquad \underline{2 \cdot 10 \cdot 8}$$

In order to calculate $R(E_e)$, we must know the electron energy as a function of its depth in the target.

Along the path of the electron its energy will vary as:

$$E_e = E_o \left(\frac{r_A - s}{r_A}\right)^{\frac{1}{2}} \qquad \underline{2 \cdot 10 \cdot 9}$$

where r_A is the residual range. This weights the electron energy deposition towards the end of its path. The electron however is scattered, which reduces its energy deposition to a shorter range.
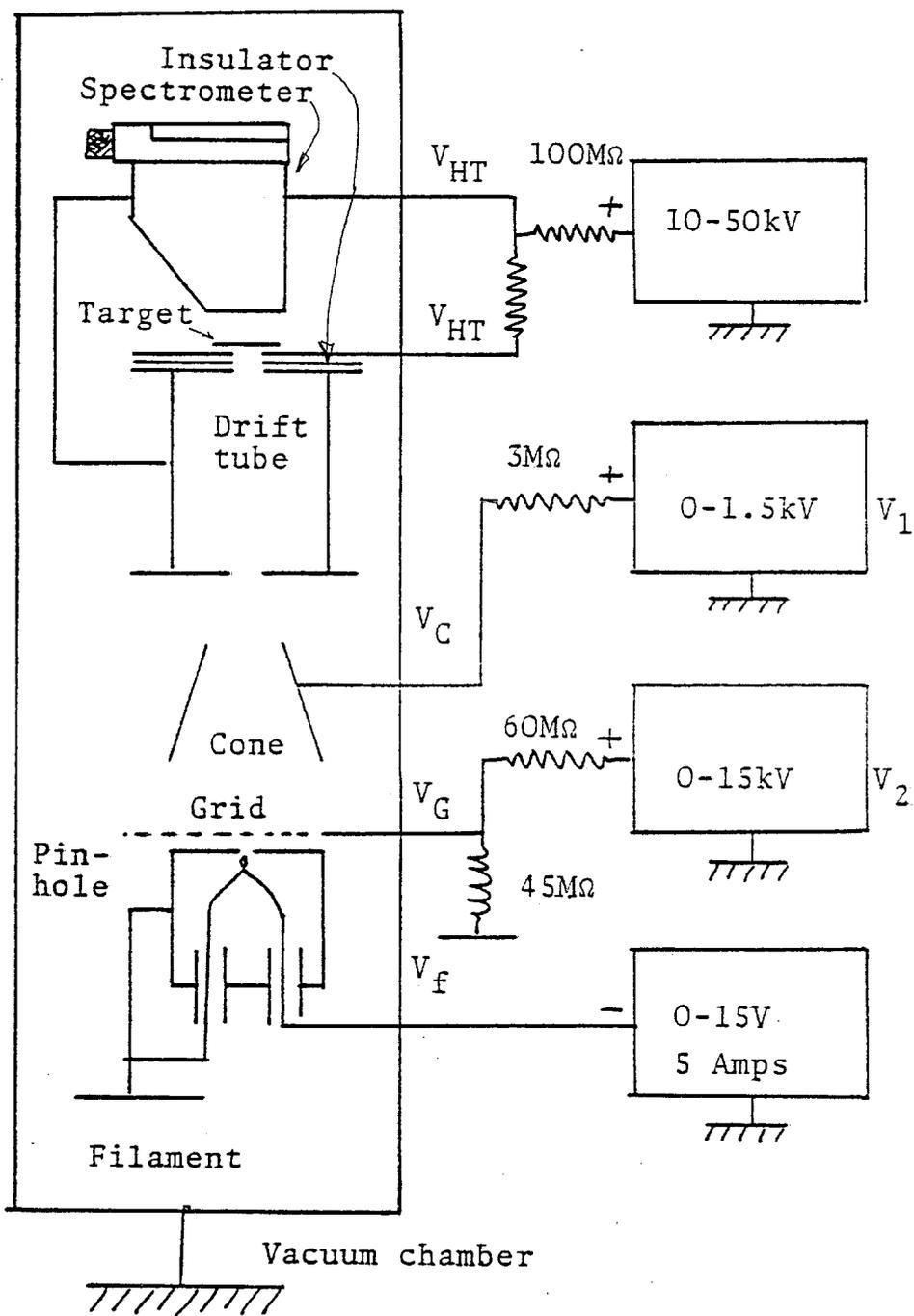
Figure 2.10.2 The layout of the calibration facility

Neon

10 MΩ   +VE

10 MΩ   10 MΩ

50 MΩ

0.1µF   200 kΩ

A   50µA

20 V
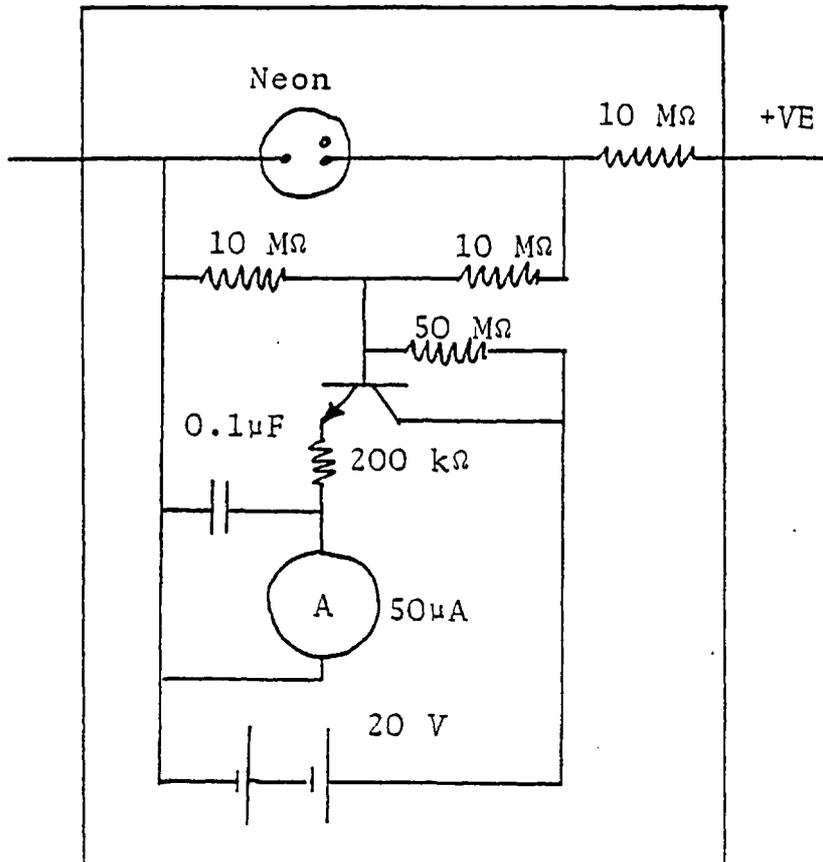
Typical operating voltages (keV)
$V_f=4V$, $I_f=3.5A$, $I_{HT}=0.1$ A

V_{HT}	V_1	V_2
10	0.30	5.0
20	0.65	6.0
30	1.05	6.0
40	1.25	6.0
50	1.70	6.0

Figure 2.10.3 The circuit diagram of the calibration facility.

As an approximation we take the electron energy to drop linearly to zero over the residual range, taken normally into the target. Any error in this assumption will have effect on the predicted yields only at low electron energies, because of the semi-constant behaviour of $R(E_e)$.

To reliably determine the yields at low energies, and quantitatively check the predictions at high energy, an electron beam target calibration facility was constructed. A DC electron gun was assembled, which provided $\sim 0.1 \mu$A with a 10 to 50 kV accelerating potential, focussed to a $300 \mu m$ diameter spot. The entire apparatus was contained in the bell-jar of a coating plant. Two mounts were provided, one each for the target and the spectrometer. A current pre-amplifier was included in the target beam return path to monitor the current incident on the target. The pre-amplifier had to float to the EHT voltage so it was battery operated and contained in a glass jar to avoid coronal discharge. It was calibrated against a voltage source and fixed resistor.

The layout of the calibration system and the circuit diagram are shown in figures 2.10.2 and 2.10.3 respectively. The facility was used to calibrate several of the target types.
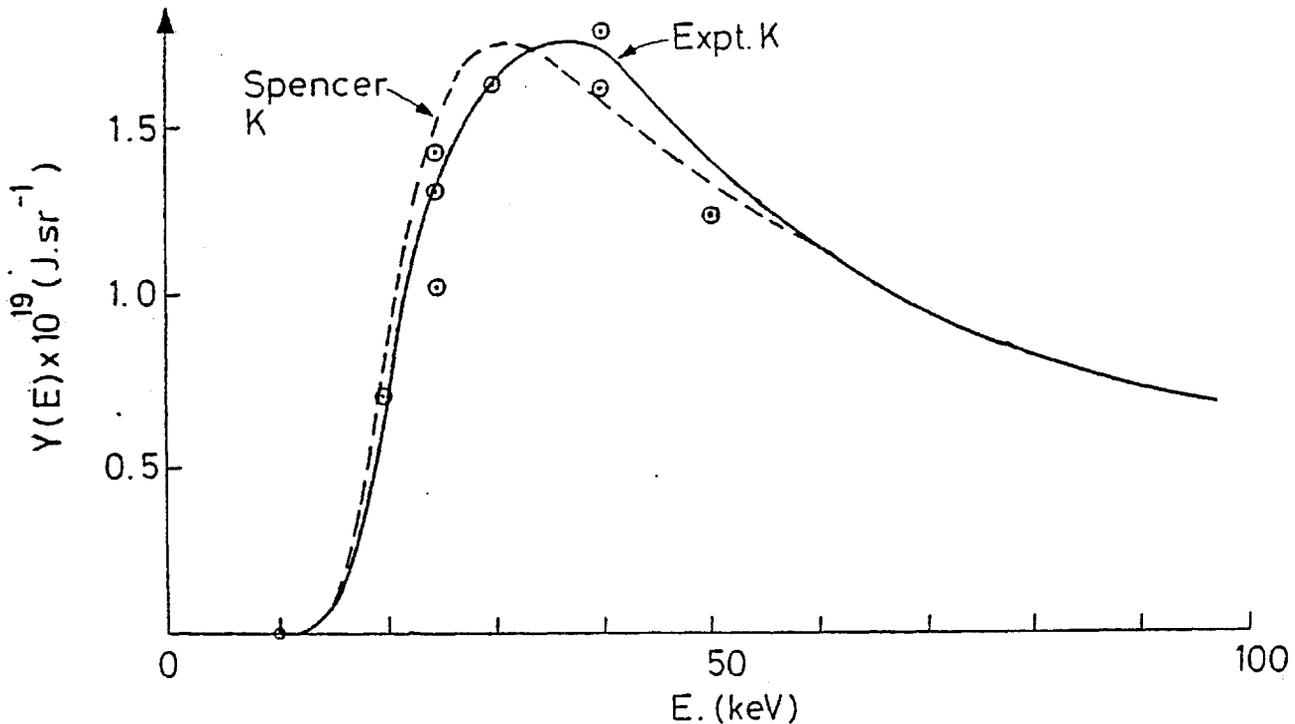
Figure 2.10.4 The K Kα yield per incident electron for type III targets.

No.	Type	Mylar thickness	Fluor
1	3	---	KCl
1	1	---	CaF_2
2	3	2	CaF_2
3	1	2	KBr
4	1	7	KBr
5	2	---	KCl
6	3	12	CaF_2
7	3	25	CaF_2
8	3	50	CaF_2

Figure 2.10.5 The complete results of the target calibrations

EXPERIMENTAL AND PREDICTED Ti Kα YIELD AS A FUNCTION OF DEPTH FOR $E_e = 29keV$

Figure 2.10.6 A check of the method of calculating the target response against experiment (44).

In figure 2.10.4, the predicted and calibration yields are shown for K K_α emission from target type III. The dotted line is the best yield, derived from experiment at low energy and theory at high energy. Figure 2.10.5 shows the best yields for all the target types.

The calibration yields and the predicted yields are in good quantitive agreement. This adds confidence to the absolute calibration of the spectrometers.

A further check on the calculations was obtained from (44). Here a layered target technique was used to determine the K_α yield per unit depth for 29keV electrons normally incident on a massive titanium target. This is illustrated in figure 2.10.6 with our calculation of the same. Note the good agreement.
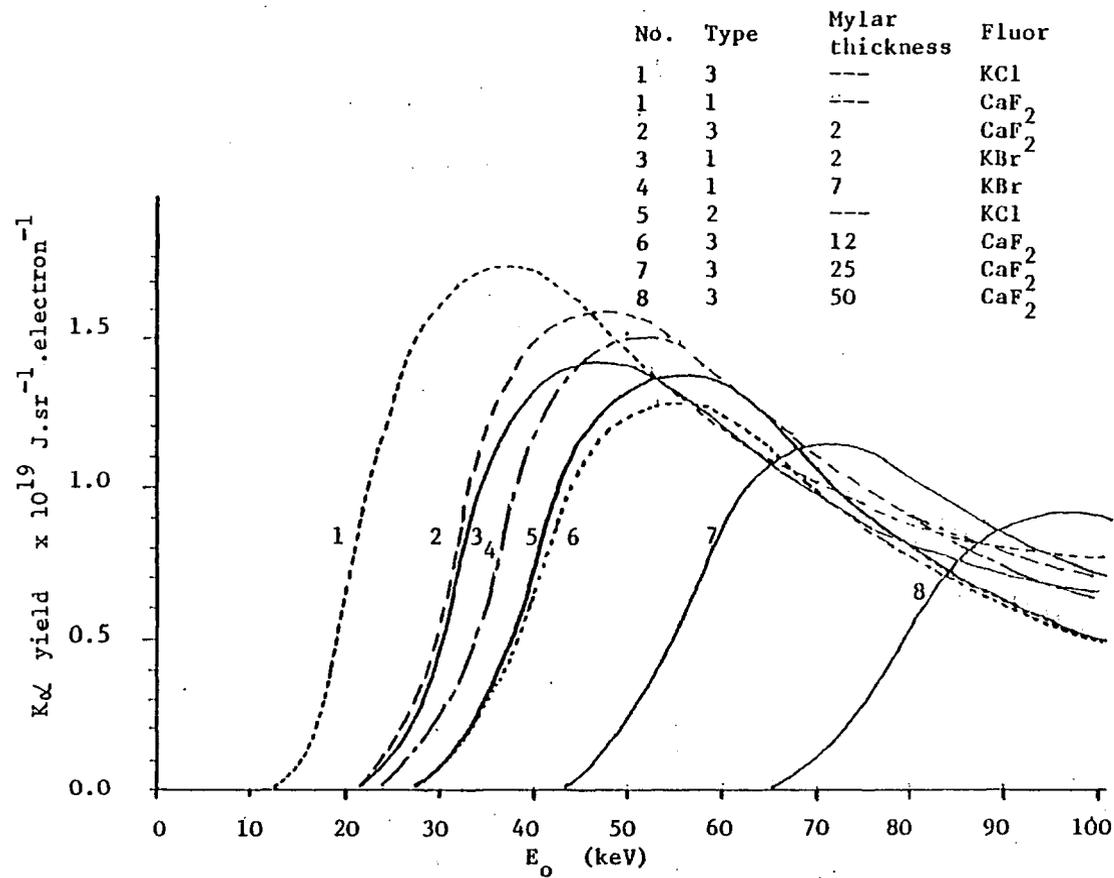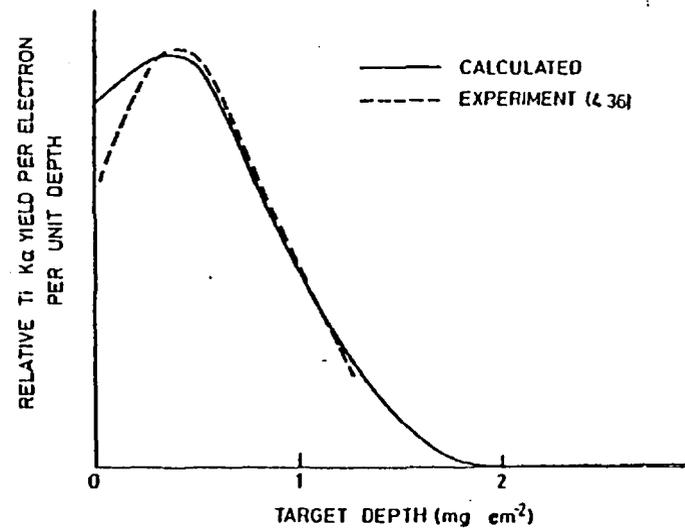
2.11 Equation of State (EOS)

For the saturation yield calculations we must know the ionisation stage and electron temperature in the solid preheated target as a function of specific energy deposition. The electron density in the solid material will be high even for a moderate state of ionisation, also the massive target will be optically thick to its thermal radiation (typically around 100eV) so one would expect a Local Thermodynamic Equilibrium model to apply (62).

The relative population of each of the ionisation states is given by a particular form of Saha's equation:

$$\frac{n_e \, n^z}{n^{z-1}} = \frac{2 \, F^z(T_e)}{F^{z-1}(T_e)} \left(\frac{m_e k T_e}{2\pi\hbar^2}\right)^{3/2} exp\left(\frac{IP(z-1)}{kT_e}\right) \qquad 2\cdot11\cdot1$$

where F^z is the partitition function for ion Z:

$$F^z(T_e) = \sum_n g_n \, exp(-E_n / kT_e) \qquad 2\cdot11\cdot2$$

g_n being the statistical weight of excited state n which is E_n above the ground state.

Applying 2.11.1 to each ionisation state leads to a series of non-linear algebraic equations which can be solved to arbitrary accuracy. In general one does not know the electron density, only the ion density and energy deposition. An iterative procedure is thus required. Moreover, due to the complex structure of the available excited states the partition function is very difficult to calculate. Clearly the complexity of the calculation is great so we will use a simplified form from (59).

We will first discuss the validity of L.T.E. in the solid target. From (2) coupled with the classical fast electron range (32,41) a typical energy deposition in a preheated solid target is $\sim 2 \times 10^6$ Jgm^{-1}. This represents an energy of ~ 1 keV per atom. Inspection of typical EOS results from (63) at solid densities suggests that this energy will be roughly equally shared between ionisation and kinetic energy. In KCl this leads to $\bar{Z} \sim 8$, $T_e \sim 100$ eV and $N_e \sim 2.5 \times 10^{23} cm^{-3}$. McWhirter (64) gives a necessary condition for LTE obtained by setting the collisional excitation rate much higher than the radiative rate:

$$n_e (cm^{-3}) > 1.75 \times 10^{14} \left(T_e (eV) \right)^{\frac{1}{2}} \left(E_1^{Z-1} (eV) \right)^3 \qquad 2.11.3$$

where E_1^{Z-1} is the excitation energy of the first bound state above the ground state of ion (Z - 1). Assuming the excited states to be hydrogenic,(a clear overestimate of E_1^{Z-1}) leads to:

$$n_e > 1.75 \times 10^{14} T_e^{\frac{1}{2}} \left((Z-1)^2 13.6 \cdot \frac{3}{4} \right)^3 \qquad 2.11.4$$

which is just about satisfied by the figures mentioned above. Since the RHS depends on E_1^{Z-1} to the third power and we have overestimated E_1^{Z-1} we can assume the condition is met. Moreover this equation applies to complete L.T.E. i.e. equilibrium between the excited states of each ion. We are only interested in the total ion populations, for which the validity criterion is less rigorous.

Equation 2.11.1 is not strictly correct. The ionisation potential of an ion in a plasma is reduced from that of a free ion by the screening effect of the free electrons. This reduction is given by the Debye energy (62,65), E_D (see sub-section 3.3).

In equation 2.11.1, IP(Z-1) is replaced by IP(Z-1) - E_D. Since E_D is a function of η_e the equation becomes even more difficult to solve.

If the situation exists that $E_D > IP(N)$, then ionisation stage N is unbound and its population is zero.

We will now discuss the approximation of (59). They make three assumptions; i) the partition function for two consecutive ionisation stages is the same, ii) the ionisation stage can be considered to be a continuous variable, m and iii) the ionisation potential is also a continuous function of m, I(m). Assumption ii) rests on the fact that at any one time the population density as a function of ionisation stage is sharply peaked, i.e. only one or two species have significant population at any one time.

They reduce the series of non-linear algebraic equations implied by 2.11.1 to:

$$I\left(\bar{m} + \tfrac{1}{2}\right) = kT_e \ln \frac{A\, T_e^{3/2}}{\bar{m}\, n} \qquad\qquad 2.11.5$$

where I is obtained by linearly interpolating between ionisation potentials and $A = 4\pi m_e k/h^2 = 6 \times 10^{21} cm^{-3} eV^{-3/2}$.

The pressure is given by:

$$P = n_i \left(1 + \bar{m}\right) kT_e \qquad\qquad 2.11.6$$

and the internal energy is:

$$\mathcal{E} = \frac{3}{2} n\left(1 + \bar{m}\right) kT_e + n Q(\bar{m}) \qquad\qquad 2.11.7$$

where $Q(I) = \sum_{N=1}^{L} IP(N)$ and $Q(\bar{m})$ is obtained by linear interpolation.

Figure 2.11.1 compares this simplification with the Sesame (63) equation of state look-up table. This table is a compilation of experimental observations and more complete theoretical E.O.S. calculations. Sesame provides

specific internal energy, $\mathcal{E}$, and pressure, p, as a function of density and temperature. Figure 2.11.1 shows $\mathcal{E}$ and p plotted against T_e for solid density aluminium for both Sesame and Zel'dovich and Raisers' approximation.
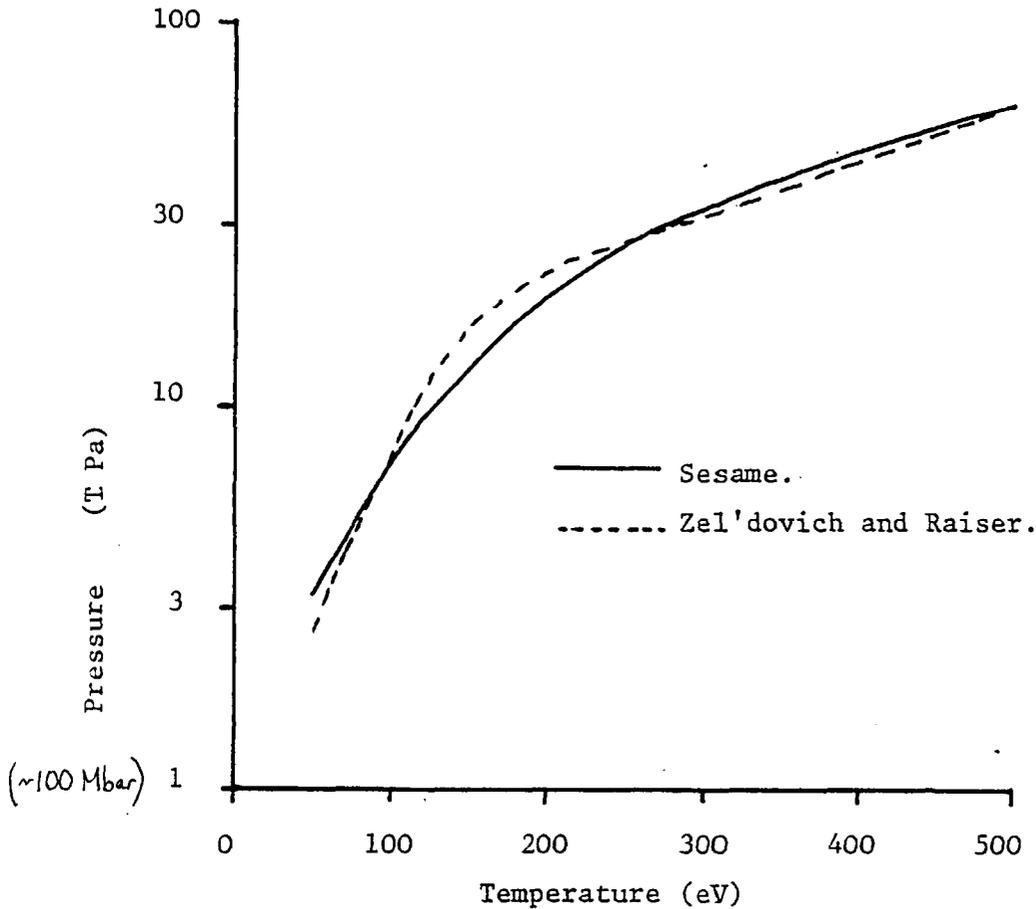

Figure 2.11.1 A comparison of the approximation of (59) with the EOS results of (63).

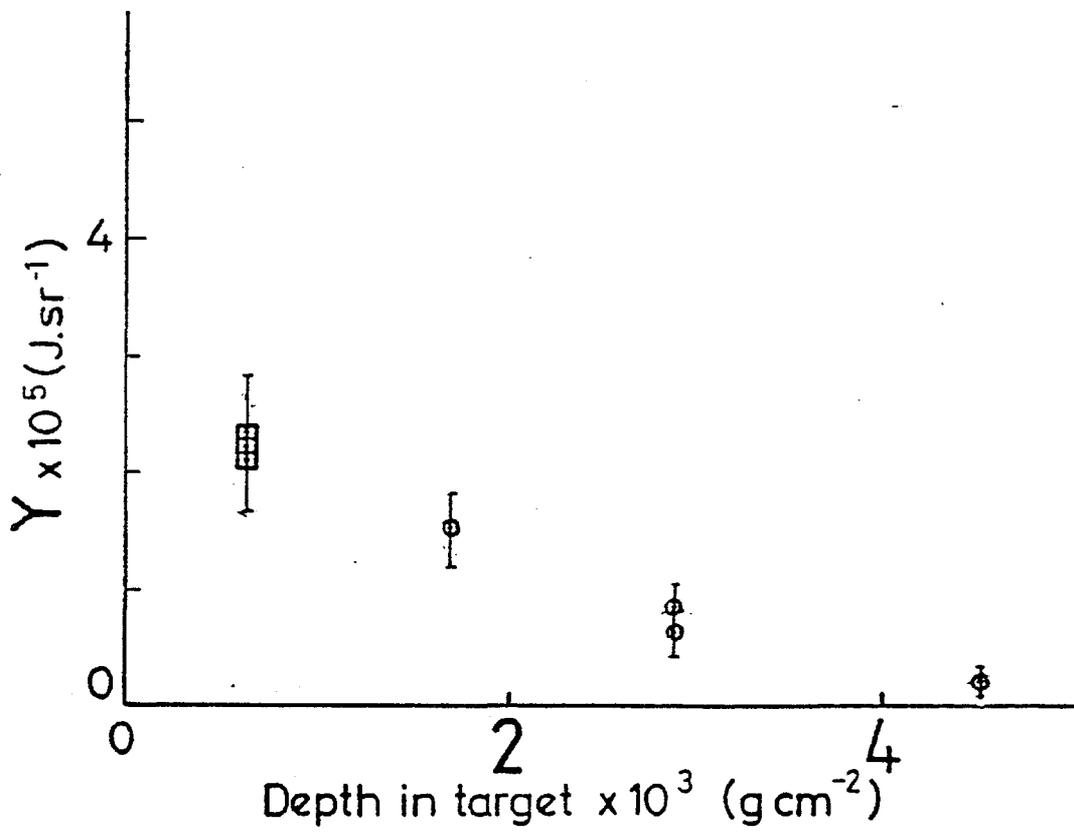The agreement is good, justifying the use of the approximation.

Figure 3.1.1   The K_α yield as a function of depth in the target (type III).

CHAPTER 3

RESULTS AND ANALYSIS OF THE FAST ELECTRON EXPERIMENTS

This chapter describes how the $K\alpha$ yields and the hard X-ray continuum can be used to determine the form of the preheating distribution function.

The intensity scaling of fast electron temperature and preheat coupling efficiency are measured. A corobarative measurement of preheat level is reported in which the spectral shift of the K absorption edge in the preheated material is used as a diagnostic of its state of ionisation.

3.1   The determination of the fast electron distribution function

i)   The $K\alpha$ yields

Figure 2.10.5 gives the $K\alpha$ yield per electron. The total yield from a distribution $n(E_e)$ is thus:

$$Y = \int_0^\infty n(E_e) \, Y(E_e) \, dE_e \qquad \underline{3 \cdot 1 \cdot 1}$$

Hard X-ray continuum measurements indicate that the fast electron spectrum is Maxwellian (exponential) but the dimension of the distribution is unclear (i.e. 1D, 2D etc.). For this reason a general distribution of the form:

$$n(E_e) = n_0 E_e^{N/2} \exp(-E_e / kT_H) \qquad \underline{3 \cdot 1 \cdot 2}$$

was used where N and T_H were fitting parameters, chosen to give overall consistency between each of the $K\alpha$ yields and the hard X-ray continuum.

To obtain as much information as possible on the form of the distribution all the available target thicknesses were shot with a fixed

intensity and hence distribution. For maximum sensitivity, target type III was used. The saturation yield for K Kα was at all times larger than the observed yield.

Figure 3.1.1 shows the Kα yield as a function of target thickness. The focal position was 150μm from best focus, so the focal diameter was 100μm. This was confirmed by the X-ray pinhole camera which recorded an emitting region of 100μm diameter. Figure 3.1.2 shows a typical pinhole picture and its microdensitometer tracing, from which the f.w.h.m. is 100μm. Taking account of reflection losses the incident energy was 25 $\pm$ 4 Joules and the pulse length 100ps, so the intensity was 3.2 $\pm$ 0.5 x 10^{15} w.cm.$^{-2}$.

The results of sub-section 2.9 were used to calculate the Kα yields as a function of target depth for values of kT_H from 5 to 30keV and N from 0 to 4. Some of these results are shown in figure 3.1.3. For each value of N there is a best value for kT_H to give a good experiment/theory fit. The best fits for each value of N however are not equally good. N = 3 appears to give yields closest to those recorded, although the N = 2 and N = 4 distributions do fit within the experimental error bars.

To demonstrate the insensitivity of the total preheat energy, E_{PH}, to the distribution we have calculated E_{PH} for each of the 'good fits' with N = 0 to 4. This is tabulated with the fitting parameters in figure 3.1.4. E_{PH} is obtained from:

$$E_{PH} = \int_0^\infty E_e \, n(E_e) \, dE_e$$

$$= \int_0^\infty n_0 \, E_e^{\frac{N+2}{2}} \cdot \exp(-E_e / kT_H) \, dE_e$$

$$= n_0 (kT_H)^{\frac{N+4}{2}} \cdot \Gamma\left(\frac{N+4}{2}\right) \qquad \underline{3.1.3}$$

For the case N = 3, E_{PH} is given by:

$$E_{PH} = n_0 (kT)^{7/2} \cdot \frac{15\sqrt{\pi}}{8} \qquad \underline{3.1.4}$$
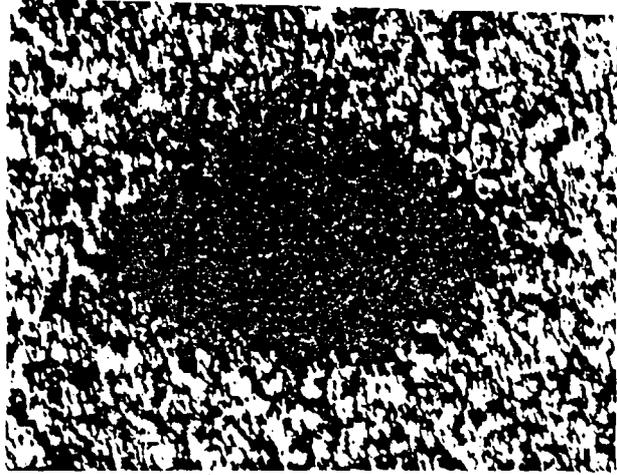
Figure 3.1.2 (a) An X-ray pinhole image (hν $\geqslant$ 2keV) on Kodirex film.

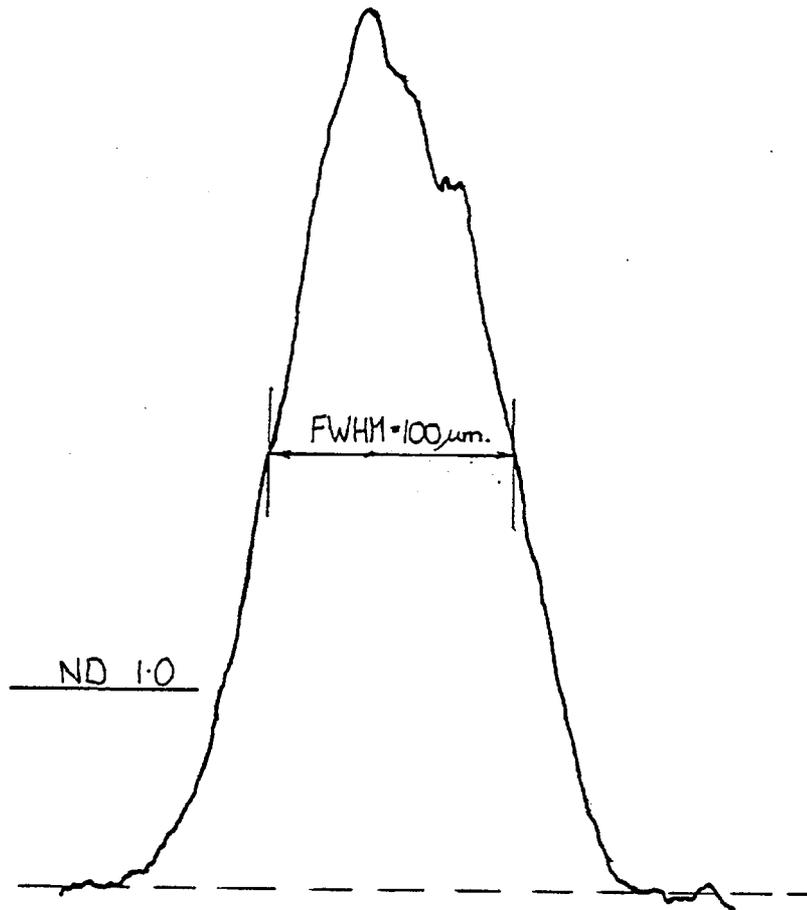FWHM $= 100 \mu m$.

ND 1·0

Figure 3.1.2 (b) A microdensitometer tracing of the above image.
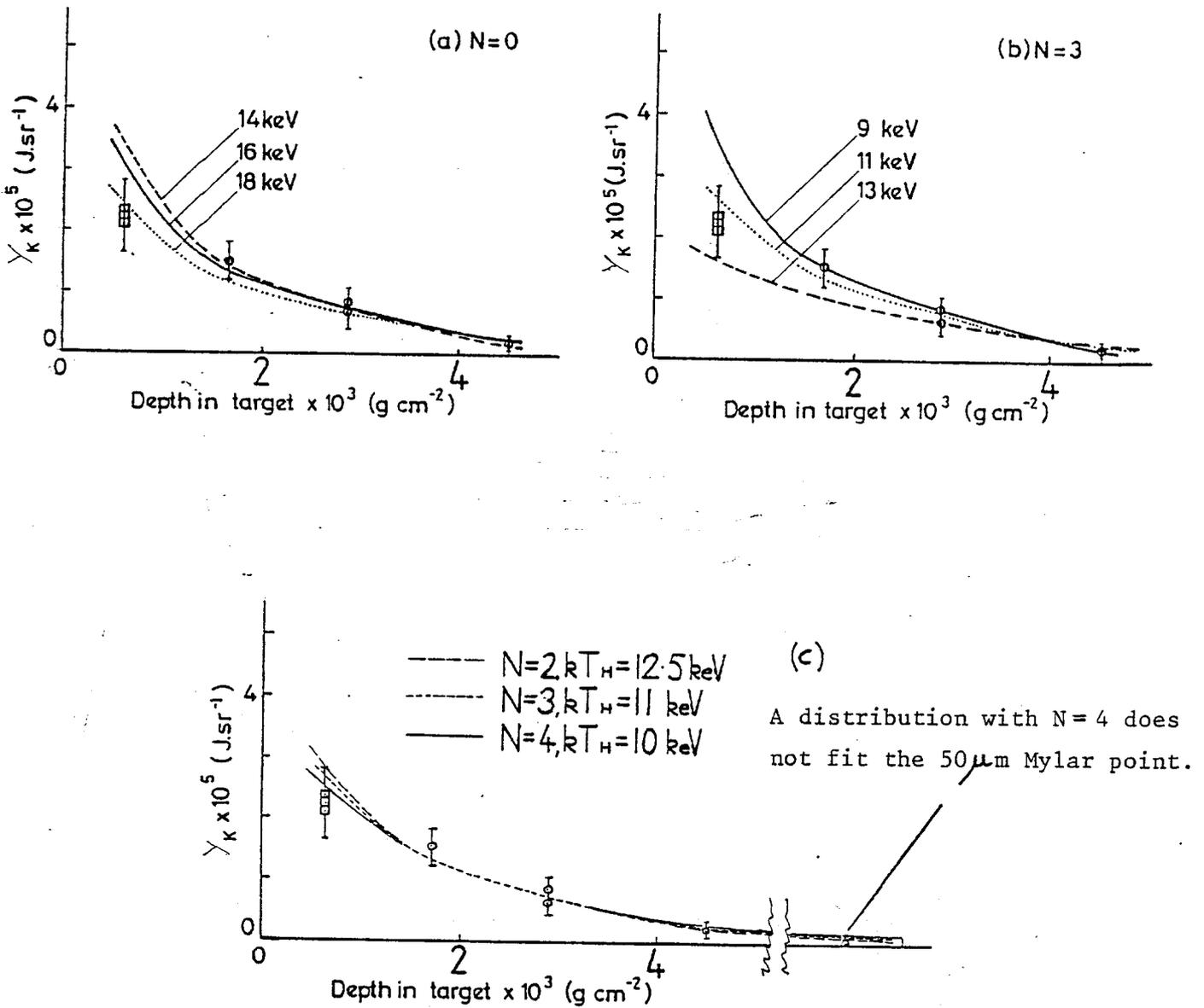
Figure 3.1.3 The predicted $K\alpha$ yields for various fast electron distributions together with the experimental yields.

$I = 3.2 \times 10^{15} \text{w.cm}^{-2}$,	$E_{INC} = 25 \text{Joules}$,	Target III	
N	kT_H (keV)	(electrons/keV$^{\frac{N + 2}{2}}$)	E_{PH} (J)
0	18	2.98×10^{13}	1.55
1	15	7.59×10^{12}	1.40
2	12.5	2.15×10^{12}	1.35
3	11	5.39×10^{11}	1.27
4	10	1.23×10^{11}	1.18

Figure 3.1.4 The total inferred preheat energy as a function of the assumed N.

From the $K\alpha$ data alone the preheat energy is $\sim 7\%$ uncertain due to uncertainty in the distribution ($N = 3 \pm 1$).

As a further check on the form of the distribution, a 3 fluor layer target (target type IV) was irradiated at a similar intensity. Because the spectrometers are unable to detect TiKαemission with PET crystals, the rear spectrometer was fitted with a germanium crystal (2d = 4.00Å CF PET 2d = 8.74Å) thus enabling it to detect K, Ca and TiKαsimultaneously. The front spectrometer was operated with a PET crystal and since both spectrometers detected K and Ca Kαit was possible to cross calibrate the germanium reflectivity with the PET, making allowance for target absorption. The yields are shown in figure 3.1.5. The predicted yields for N = 2,3, and 4 distribution are also shown. Again the best fit is for N = 3 although the N = 2 and 4 yields do lie within the error bars.
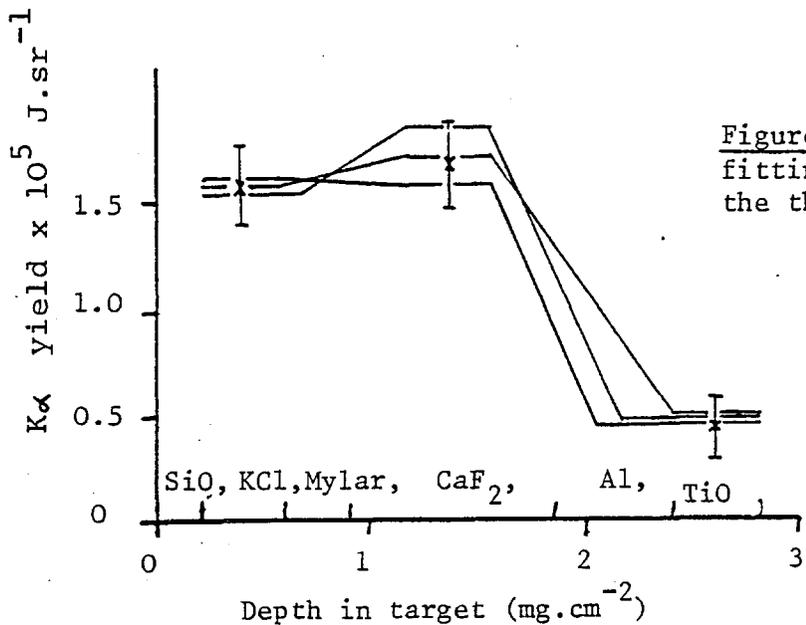
Figure 3.1.5 The results of fitting various distributions to the three-layer target yields.

N=3,T$_H$=13keV
N=4,T$_H$=11keV
N=2,T$_H$=15keV

ii) X-ray continuum

Each distribution function will give rise to different hard X-ray continuum emission. For the correct distribution this must be the same as that which is recorded by the pin diode array. We will calculate the Bremsstrahlung produced by each of the distributions.

For an electron of instantaneous energy E_e passing through material Z, the Bremsstrahlung emitted per unit path length per unit hν is ([66]):

$$\frac{d^2 I_\nu}{dh\nu\, ds} = N_{ATOMS} \cdot \frac{16 \pi^2 Z^2 e^6}{3\sqrt{3}\, c^3 m_e h E_e} \qquad J/J/cm$$

$$= 2.28 \times 10^{-33}\, N_A\, \frac{Z^2}{E_e} \qquad \underline{3.1.5}$$

for hν < E_e, and zero for hν > E_e. The Gaunt factor is assumed to be independent of electron energy.

The electron motion is determined by the Bethe Bloch formula 2.9.1 which numerically is:

$$\frac{\partial E_e}{\partial s} = 3.3 \times 10^{-37} \cdot \frac{Z \cdot N_A}{E_e} \ln\left(\frac{4 E_e}{IP}\right) \text{ erg.cm}^{-2}$$

$$\underline{3.1.6}$$

where $\overline{IP}$ is the average ionisation potential of material Z. Thus the total Bremsstrahlung emitted by an electron of energy E_o in the interval $h\nu - h\nu + dh\nu$ is:

$$I_\nu \, dh\nu = \frac{2.28 \times 10^{-33} \, Z}{3.3 \times 10^{-37}} \int_{h\nu}^{E_o} \frac{1}{\ln\left(\frac{4 E_e}{IP}\right)} dE_e$$

$$= 1.11 \times 10^{-5} \, Z \int_{h\nu}^{E_o} \frac{1}{\ln\left(\frac{4 E_e}{IP}\right)} dE_e \qquad \underline{3.1.7}$$

where E_e is in keV.

The total spectrum is then obtained by convolving the one electron spectrum with the distribution function:

$$I_\nu = A \int_{h\nu}^{\infty} n_0 E^{N/2} \exp(-E/kT_H) \int_{h\nu}^{E_e} \frac{1}{\ln\left(\frac{4 E_e}{IP}\right)} dE_e \, dE \qquad \underline{3.1.8}$$

This result may be compared with equations 14 and 15 of reference (2). It is essentially the same except that the Gaunt factor is assumed constant and the distribution has a slightly different normalising constant.

As a check equation 3.1.8 has been applied to the distributions inferred
in (2), and reproduces the X-ray continuum to which these distributions
were fitted.

The pin-diode array was used to record the X-ray continuum emission
in the range $h\nu$ = 10 - 30 keV. Unfortunately due to operating problems
(e.g. noise pick up) only two diode channels were available. The filters
on these channels were 250 μm Al and 150 μm Ni with 1/e transmission at
12keV and 35keV respectively. The falling spectral response of the diodes
however reduces the energy for peak sensitivity to 11keV and 32kev
respectively. (The filter thickness and the response of the diode have been
independently measured at AWRE, Aldermaston.) The continuum signal, as
recorded by these diodes on the two fluor layer fixed intensity shots, is
shown in figure 3.1.6. Also shown is the predicted continuum emission for
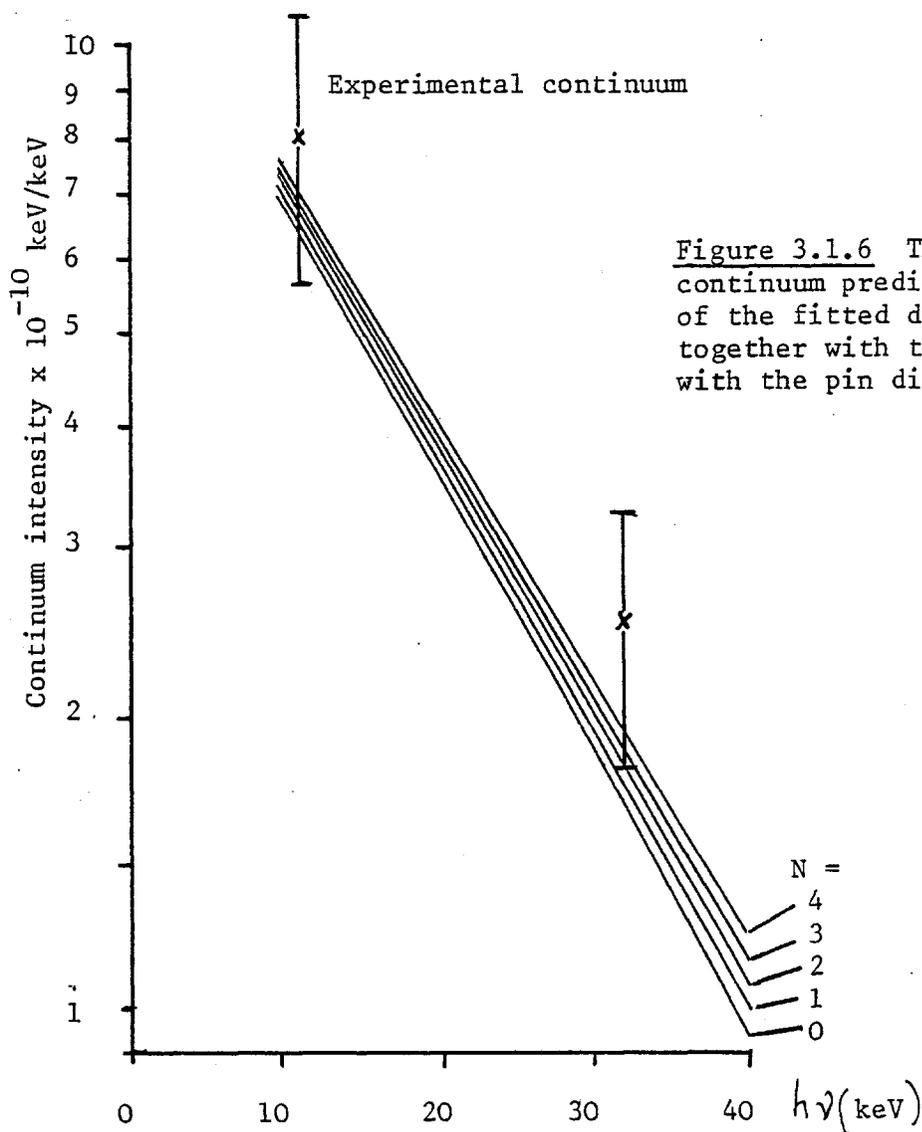each of the fitted distributions (see figure 3.1.4).

Figure 3.1.6 The hard X-ray
continuum predicted from each
of the fitted distributions
together with that recorded
with the pin diode array.

The energy span of the diode array was rather narrow so, from the diode measurements alone, the distribution cannot be chosen. The effect, on the continuum, of changing N (while keeping kT_H adjusted for optimum match to the $K\alpha$ yields) is greatest at high photon energies. This is because at high electron energies the distribution function is dominated by the exponential factor. The measurements up to 32keV, however, do agree well with predictions.

Other workers have made X-ray continuum measurements over a wider range of photon energies. In figure 3.1.7 the X-ray temperature is shown from many sources (2,11,37,38) analysed assuming an $N = 0$ distribution. The data were taken at photon energies up to 80keV. This is sufficiently high (i.e. several times kT_H) that the exponential factor would dominate over the $E^{N/2}$ factor in the distribution function. To first order one may therefore assume that the inferred T_H would not be a strong function of N. As can be seen in figure 3.1.4 the N dependence of T_H in the $K\alpha$ analysis is significant. This is because the $K\alpha$ technique is most sensitive to electrons around $k\,T_H$ i.e. in the region where the $E^{N/2}$ factor dominates. From figure 3.1.7 at an intensity of $3 \times 10^{15}\text{w.cm}^{-2}$ one would expect the X-ray continuum temperature to be 13 ± 2keV. The $K\alpha$ temperature is in agreement with this for $N = 1 - 3$.

The most reliable fix on N can be obtained from the distribution dependence of E_{PH}. Figure 3.1.4 shows the effect of N on E_{PH} for the $K\alpha$ analysis. In (2) the X-ray continuum up to 60keV from several short pulse, $1.06\mu m$ laser-target interactions has been analysed in terms of $N = 0$ and $N = 2$ distributions. The total fast electron energy on each shot was calculated for each of these distributions. In figure 3.1.8 the fractional coupling of the incident energy, E_{INC}, into preheat is plotted as a function of N for the X-ray analysis of (2) and for the $K\alpha$ analysis. This figure graphically illustrates the superiority of the $K\alpha$ technique over the continuum technique for measuring the preheat energy.

As can be seen in figure 3.1.8, a consistent value for E_{PH}/E_{INC} is only obtained for $N = 3$. We therefore conclude that this is the correct distribution and will apply it to all further $K\alpha$ analysis.

No analytic significance is implicit in the chosen form of the distribution function. It arises simply from an empirical fit to the
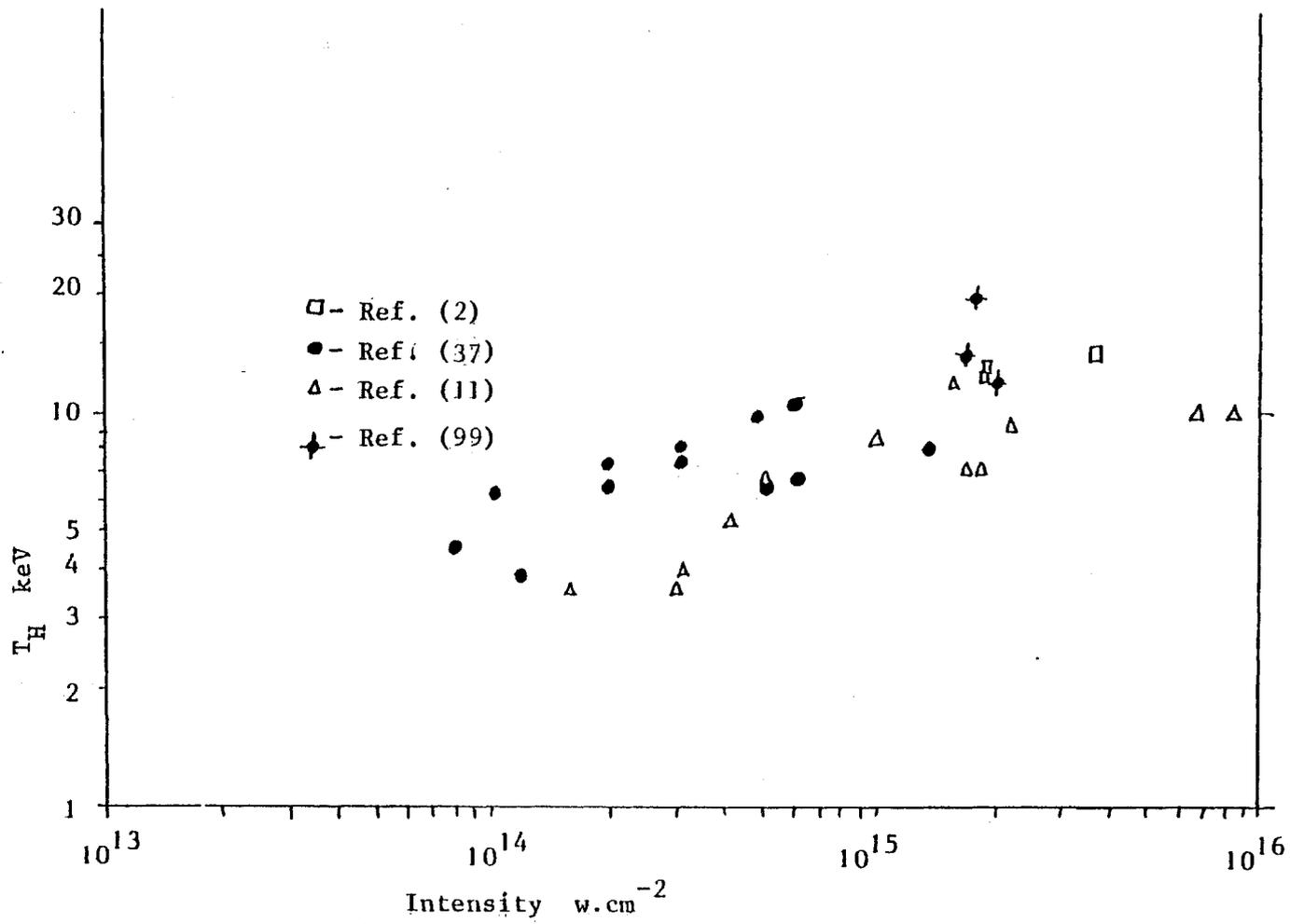
Figure 3.1.7 The fast electron temperature obtained from the hard continuum slope collected from many sources.

observed energy deposition and X-ray emission.

Figure 3.1.8 The fractional coupling into preheat as a function of N for the K_α analysis and for the continuum analysis of (2).

• - From figure 3.2.5

✗ - From ref. (2)

(y-axis label) E_{ph}/E_{inc} (%)

(x-axis label) Order of distribution function,N.
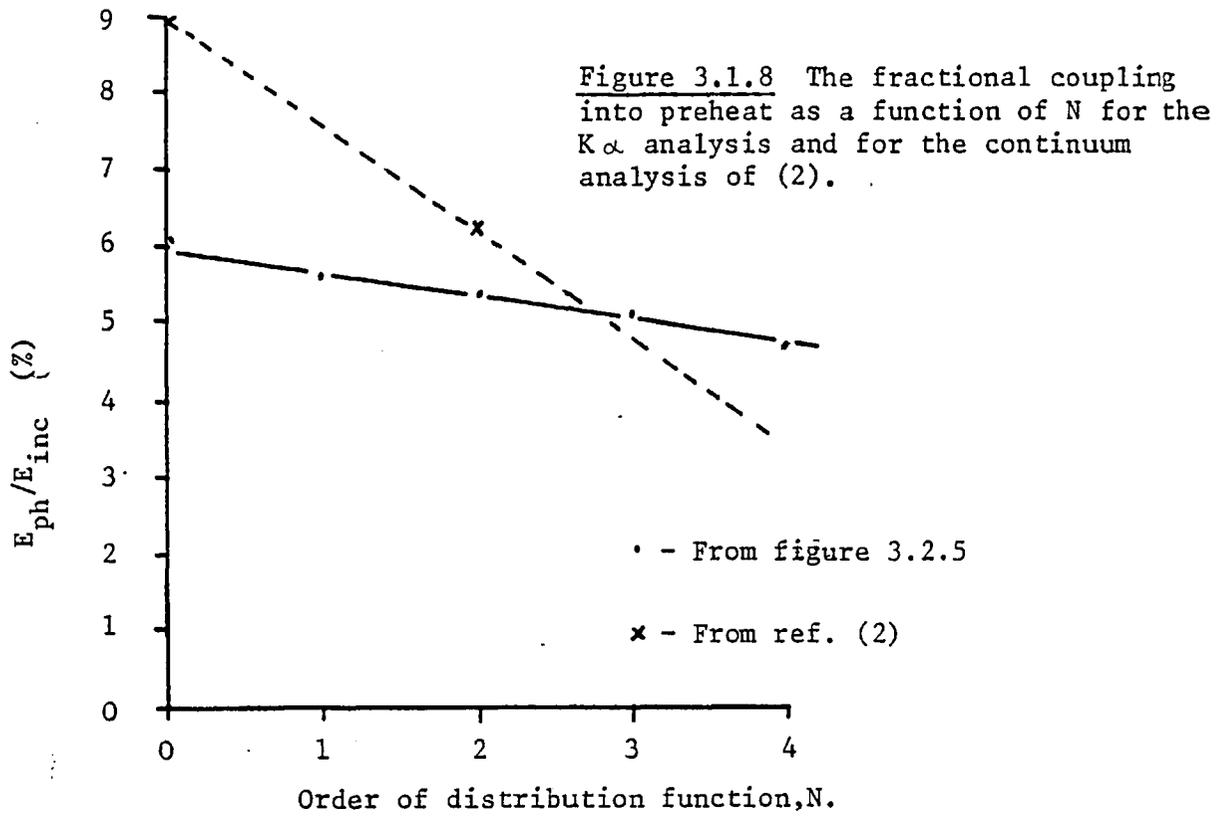
3.2   Intensity scaling of preheat coupling and temperature

In order to investigate the intensity scaling laws, targets types II and III were selected as being most immune to saturation effects. The MK III spectrometer was used at the rear with a PET crystal.

Twelve targets were shot and the intensity was varied from $0.5 \times 10^{15} w.cm^{-2}$ to $4 \times 10^{15} w.cm^{-2}$. In each case the size of the focal spot was determined from the X-ray pinhole camera. This was selected as the most reliable measure of spot size because the mechanics of the target alignment mechanism had a certain amount of jitter in the Z direction, this being reflected as uncertainty in the focal position. (NB. In the fixed intensity experiments (sub-section 3.1) a new, very precise transport mechanism was used which gave good, reproducible focussing).

Figure 3.2.1 shows the tabulated results from all the 'good' shots. As mentioned in subsection 2.6 there is a small radiation pumped K K_α yield. This has been calculated for each shot as in equations

SHOT	TARGET	ENERGY (J)	PINHOLE FWHM(μm)	INTENSITY 10^{15} w.cm^{-2}	YIELDS (10^{-5} J.sr^{-1})				RATIO K/Ca
					Ca	K	RAD.K	CORRECT K	
133	7^I MYLAR	14.7	140	0.95	1.3	0.54	0.10	0.44	0.34
138	3^I MYLAR	27.3	260	0.51	2.4	0.70	0.10	0.60	0.25
139	7^I MYLAR	26.6	94	3.83	2.4	1.5	0.10	1.40	0.58
1272	12^{II} MYLAR	17.0	75	3.85	1.86	1.0	0.12	0.88	0.47
1273	"	17.5	95	2.47	1.78	0.73	0.09	0.64	0.36
1274	"	10	120	0.77	1.68	0.28	0.05	0.23	0.14
1276	"	14.5	175	0.60	1.60	0.20	0.12	0.08	0.05
1277	"	18.0	130	1.36	1.52	0.43	0.09	0.34	0.22
1278	"	12.5	90	1.96	1.22	0.51	0.08	0.43	0.35

Figure 3.2.1 A summary of all the experimental results.

Figure 3.2.2 The ratio of rear to front $K\alpha$ yield as a function of T_H (N=3 distribution assumed) for each target type.
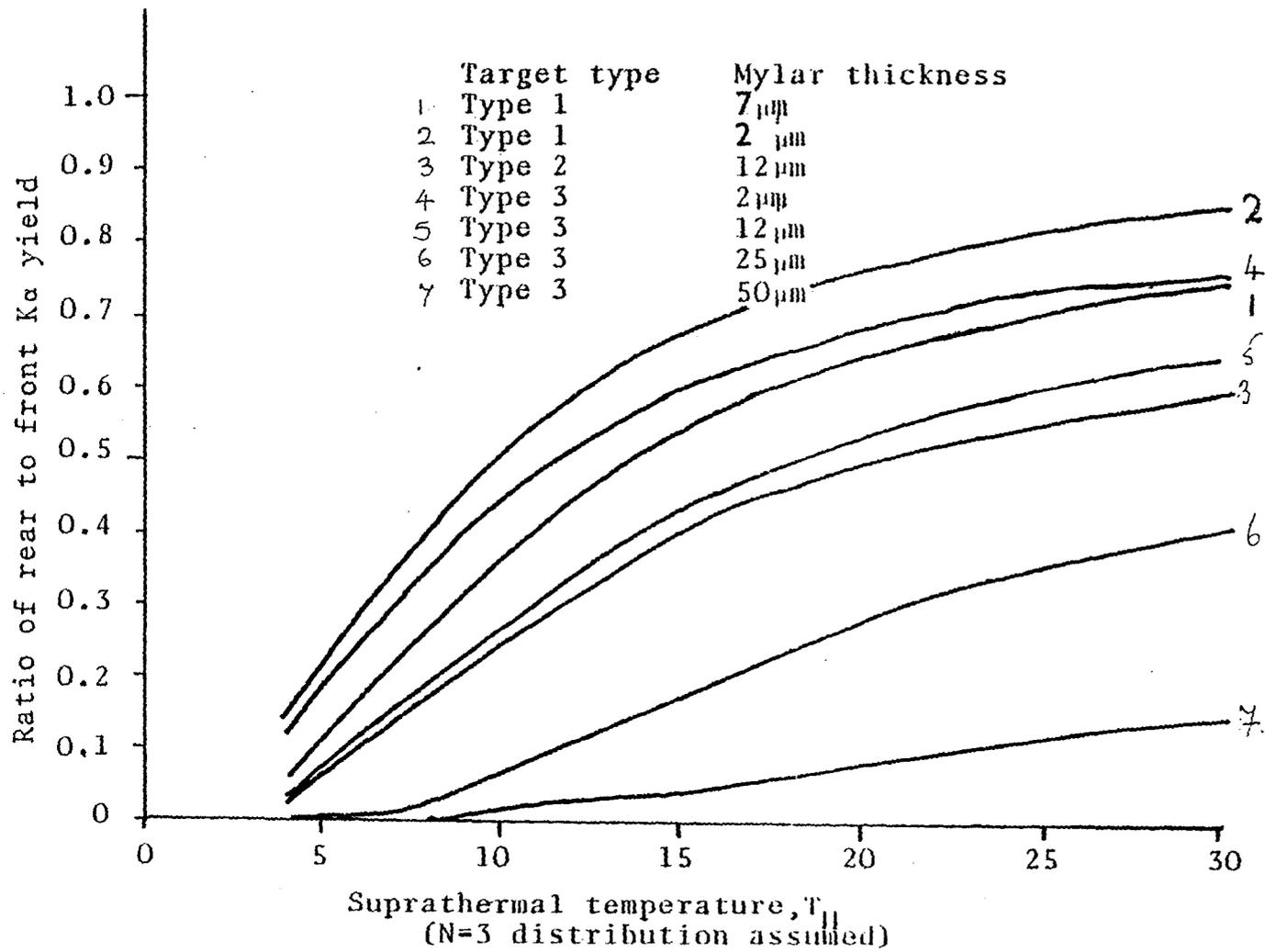
2.6.10 and 11 and is tabulated, with the corrected K Kα yield. From equation equation 3.1.1 and Y(E) (figure 2.9.5) the ratio of front to rear Kα emission can be found from:

$$\frac{Y_{FRONT}}{Y_{REAR}} = \frac{\int_0^\infty Y_{FRONT}(E_e) \, E_e^{N/2} \exp(-E_e/kT_H) \, dE_e}{\int_0^\infty Y_{REAR}(E_e) \, E_e^{N/2} \exp(-E_e/kT_H) \, dE_e} \qquad \underline{3.2.1}$$

This is shown in figure 3.2.2 as a function of T_H for each of the targets used. In all cases the N = 3 distribution is assumed.

T_H has been determined for each of the shots in figure 3.2.1. The other variable, n_0 , is determined from:

$$n_0 = \frac{Y}{\int_0^\infty E_e^{3/2} \exp(-E_e/kT_H) \, dE_e} \qquad \underline{3.2.2}$$

The total preheat energy is then calculated using 3.1.4. The incident energy (E_{INC}), intensity (I), T_H , n_0 and E_{PH} are tabulated in figure 3.2.3 and E_{PH}/E_{INC} and T_H are plotted against I in figures 3.2.4. and 3.2.5

A best fit to T_H gives the empirical relation:

$$T_H = A(I)^{0.47 \pm 0.1} \qquad \underline{3.2.3}$$

This will be discussed further in sub-section 4.2. No clear intensity dependence is evident in the preheat coupling efficiency. To remove any possible errors in the calculation of E_{PH} arising from the model distribution a lower limit on E_{PH} has been calculated. The absolute minimum energy deposited in a fluor layer is given by:

$$E_{MIN} = \frac{Y \, 4\pi}{w' \, R_{MAX}} \qquad \underline{3.2.4}$$

SHOT	E_{INC} Joules	I $10^{15} w.cm^{-2}$	n_o electrons $keV^{-7/2}$	T_H (keV)	E_{PH} (J) (Joules)	E_{ph}/E_{INC}
133	14.7	0.95	5.50×10^{11}	9	0.64	.044
138	27.3	0.51	8.13×10^{12}	5.5	1.69	.062
139	26.6	3.83	1.41×10^{11}	17	1.52	.057
1272	17.0	3.85	1.19×10^{11}	17	1.28	.075
1273	17.5	2.47	2.96×10^{11}	12	0.94	.054
1274	10	0.88	1.85×10^{12}	7	0.90	.090
1276	14.5	0.60	1.59×10^{13}	4.5	1.63	.112
1277	18.0	1.36	6.29×10^{11}	9	0.73	.041
1278	12.5	1.96	1.51×10^{11}	13	0.64	.051
4/2 (Fixed I)	25.0	3.2	9.4×10^{11}	11	1.27	.051
5/11 (Three layer)	21.7	2.8	3.78×10^{11}	13	1.30	.073
5/10	16.8	2.2	7.03×10^{11}	9	1.30	.077

Figure 3.2.3 The distributions fitted to each of the variable intensity shots.

This can be converted into energy deposition per unit mass by:

$$\frac{\partial E_{MIN}}{\partial m} = \frac{E_{MIN}}{\rho_{(FLUOR)} t_{(FLUOR)} A_f} \qquad 3.2.5$$

where A_f is the focal area.

The results shown in figure 3.1.1 suggest the manner in which $\partial E/\partial m$ should be interpolated between fluor layers. Figure 3.2.5 shows these yields converted into units of $J.gm^{-1}$.
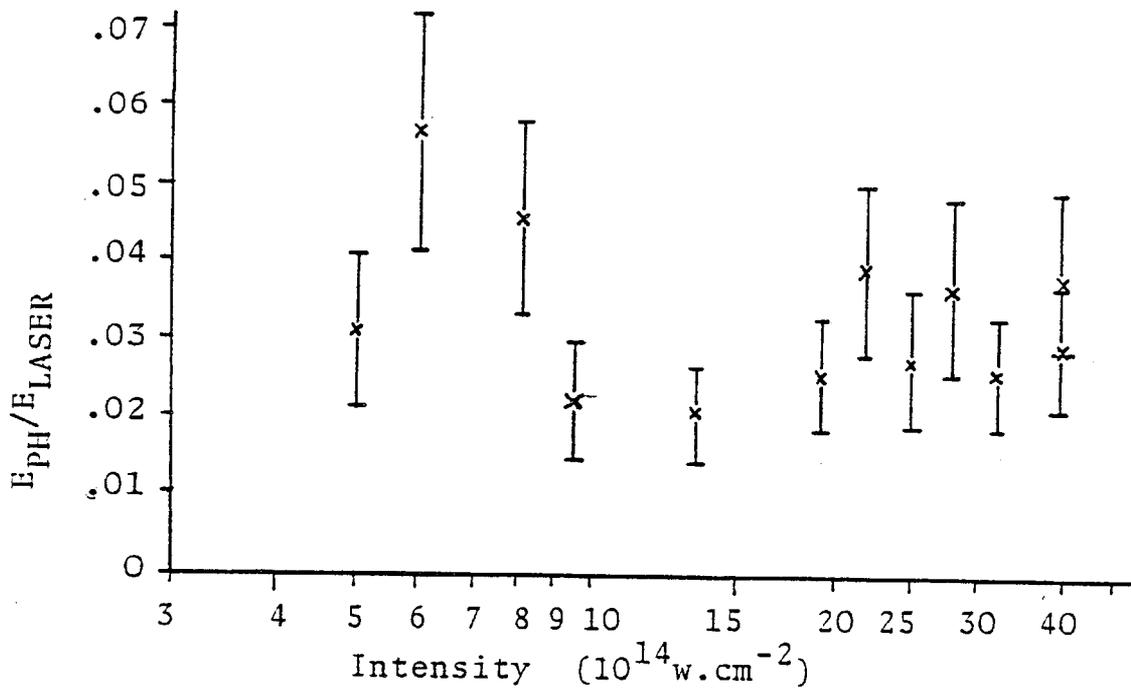
Figure 3.2.4 (a) Fractional coupling into preheat as a function of intensity
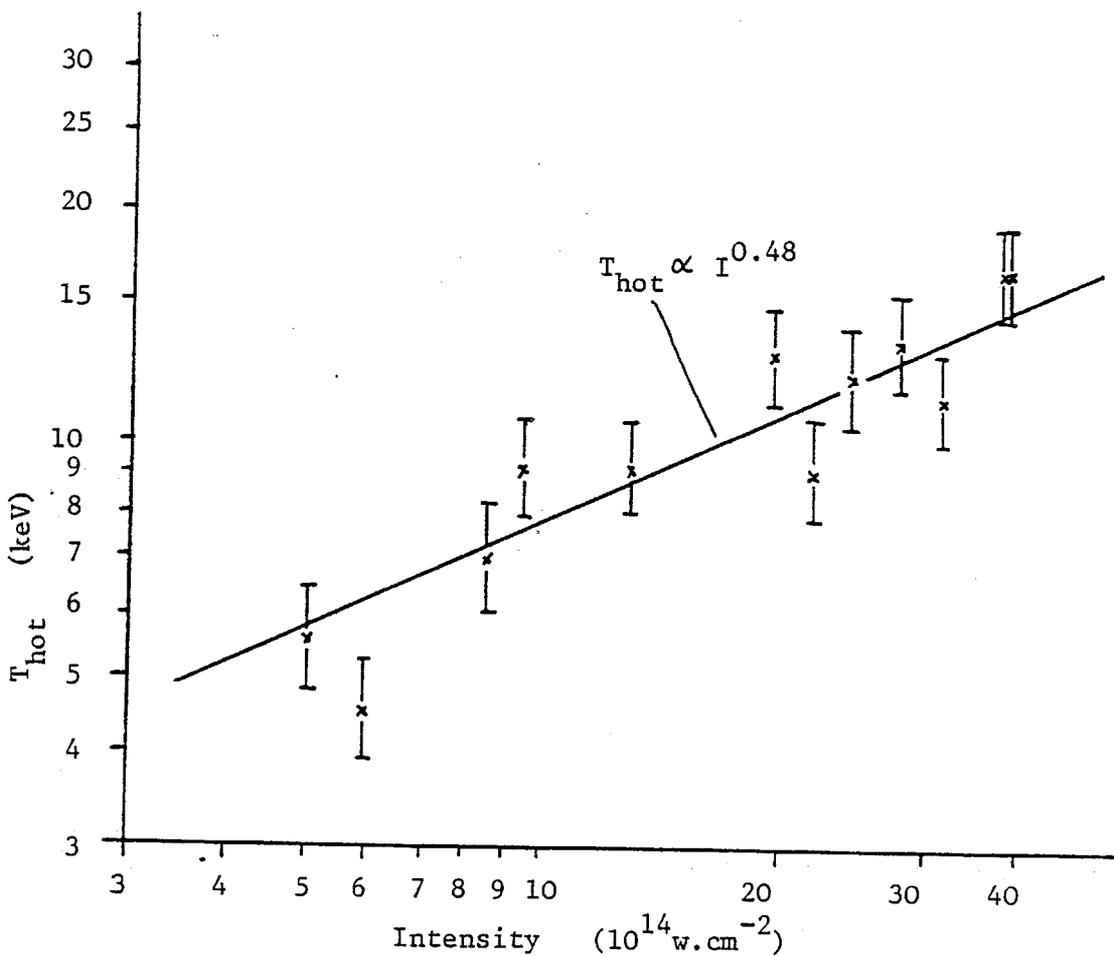
Figure 3.2.4 (b) T_H as a function of I (N=3 distribution assumed).
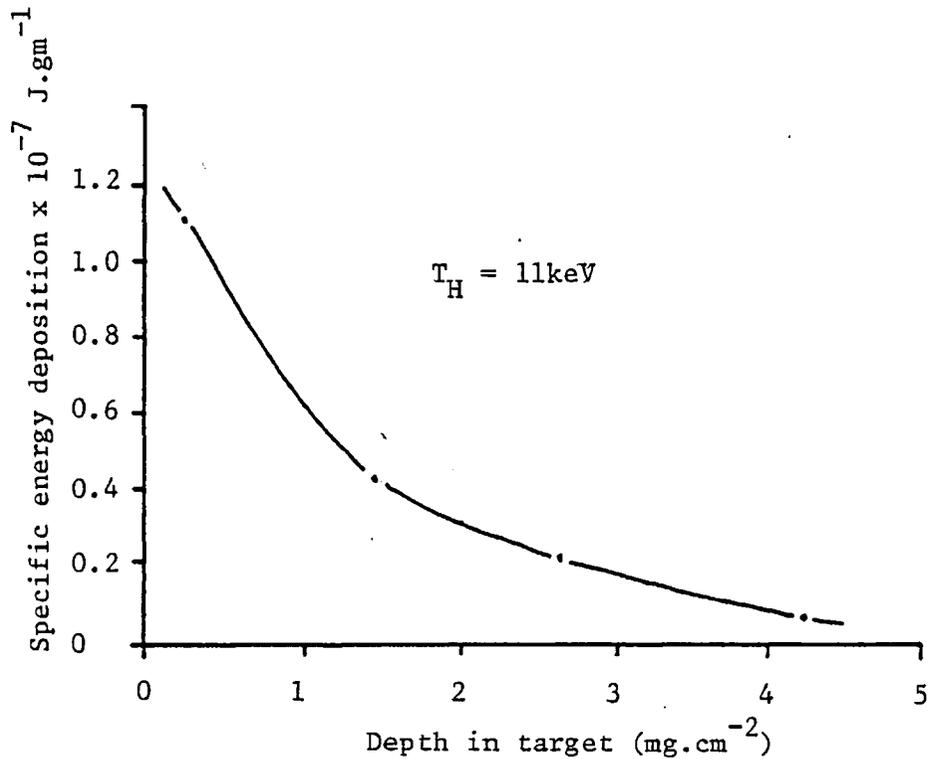
Figure 3.2.5 Specific energy deposition as a function of depth in the target.

The minimum preheat energy has been determined for each of the targets by graphically evaluating:

$$E_{MIN} = \int_0^t \frac{\partial E_{MIN}}{\partial m} \cdot A f \cdot \rho \cdot dt \qquad \underline{3 \cdot 2 \cdot 6}$$

where t is the target thickness.

It is not immediately clear what happens to electrons which completely penetrate the target. This will be discussed in sub-section 4.1. Assuming that the electrons are lost, the upper limit of 3.2.6 must be extended to ∞ thus:

$$E_{MIN, \infty} = \int_0^\infty \frac{\partial E_{MIN}}{\partial m} \cdot A f \cdot \rho \cdot dt \qquad \underline{3 \cdot 2 \cdot 7}$$
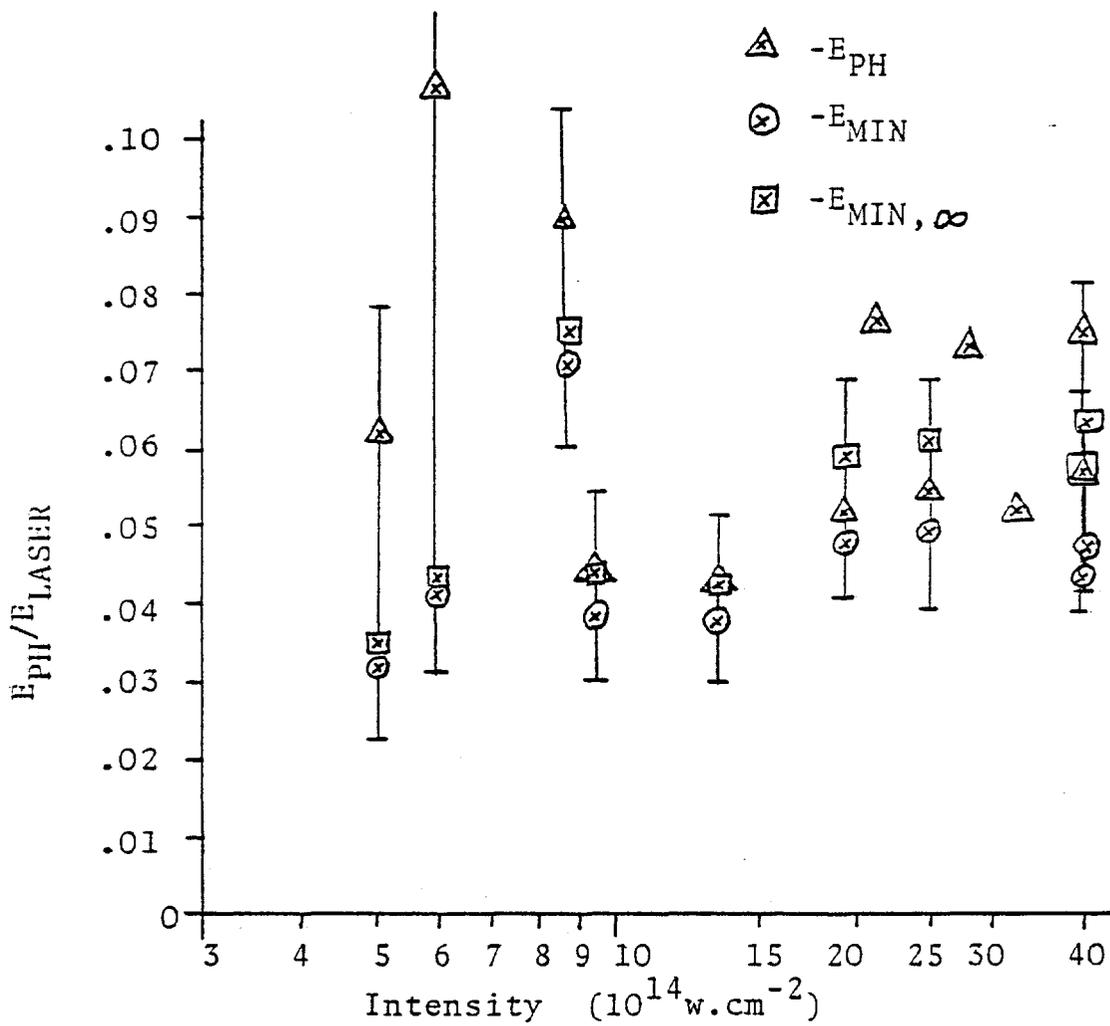
Figure 3.2.6 Fractional coupling into preheat (various assumptions) as a function of intensity.

E_{MIN}, $E_{MIN,\infty}$ and E_{PH} normalised to E_{INC} are plotted as a function of I in figure 3.2.6. The dependence of E_{PH} on the assumed distribution function is greatest for low T_H. This is because at low T_H the bulk of the energy is carried by undetected electrons. Therefore E_{PH} and E_{MIN} diverge at low intensity. The large error bars at low intensity arise from the correction due to radiation pumping (see figure 3.2.1). The overall error bar includes E_{PH} and E_{MIN} as absolute upper and low limits on the preheat. The fractional coupling shows no clear dependence on intensity, being $\sim 7\%$.

The range of the fast electrons is a strong function of intensity. A guide to this range is given by R_O, the characteristic preheat range. It is defined as the range at which the preheat has dropped to 10% of its value at the surface. The $K\alpha$ yield is converted into a specific energy deposition by:

$$\frac{\partial E}{\partial m} = \frac{4.\pi.Y}{\overline{R}(kT_H).\omega'.t_f.\rho_f} \qquad 3.2.8$$

where t_f and ρ_f are the thickness and density of the fluor layer.

Figure 3.2.5 is used to extrapolate to R_O, the range at the point where $(\partial E/\partial m)$ has dropped to 10% of its surface value. A plot of R_O vs I is shown in figure 3.2.7. This is discussed in sub-section 4.2.

$$R_O \propto I^{0.6}$$
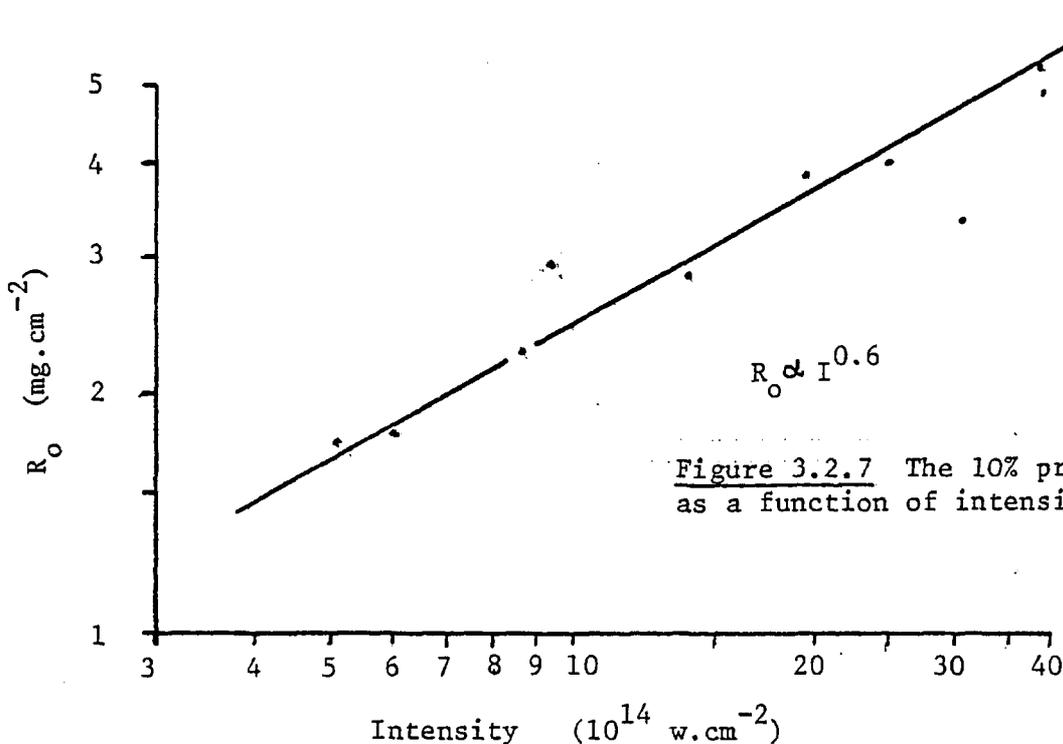
Figure 3.2.7 The 10% preheat range, R_O, as a function of intensity.

Intensity $(10^{14} \text{ w.cm}^{-2})$

3.3   The K absorption edge as a preheat diagnostic

The spectral position of the K absorption edge is defined by the energy required to remove a K-shell electron from the influence of the atom. As the absorbing material heats up, it becomes ionised. More energy is required to K ionise the absorber as its ionisation state increases. The removal of outer electrons reduces the screening of the inner shell potential, which increases, i.e. more energy is required to overcome it.

A K ionisation event is a transition of the form:- $1s\ 2s^2 2p^6.... \rightarrow$ $1s\ 2s^2 2p^6.... + e^-$.

If the atom/ion in the initial state is N times ionised, the energy of the configuration is given by:

$$E_I = \sum_{I=N}^{Z} IP(I) \qquad\qquad 3\cdot3\cdot1$$

House (58) has performed Hartree-Fock calculations on ionised atoms from C to Cu and has tabulated E_F for atoms with configuration $1s2s^2 2p^6$ ...... The K ionisation potential for ionisation state N, E_{KI}^N is simply:

$$E_{KI}^N = \sum_{I=N}^{Z} IP(I) - E_F^N \qquad\qquad 3\cdot3\cdot2$$

where E_F is the energy of configuration of the final state. There is a slight error in House's calculations which is accounted for by matching the unionised, experimentally well measured, K absorption edge to theory

by adjusting all the E_Fs by a fixed amount, δE_F:

$$\delta E_F = E_F^o - \left\{ \sum_{I=1}^{Z} IP(I) - E_{KI}_{(observed)} \right\} \qquad \underline{3 \cdot 3 \cdot 3}$$

where $E_{KI}(keV) = 12.399 / \lambda_{KABS} (A^o)$, so:

$$E_{KI}^N = \sum_{I=N}^{Z} IP(I) - E_F^N - \delta E_F \qquad \underline{3 \cdot 3 \cdot 4}$$

Figure 3.3.1 shows the wavelength of the K absorption edge plotted as a function of ionisation stage for Si. The shift in E_{KI} turns out to be $\sim\frac{1}{2}$ of the current ionisation potential. The contribution to the depression due to the Debye energy is not included in figure 3.3.1.

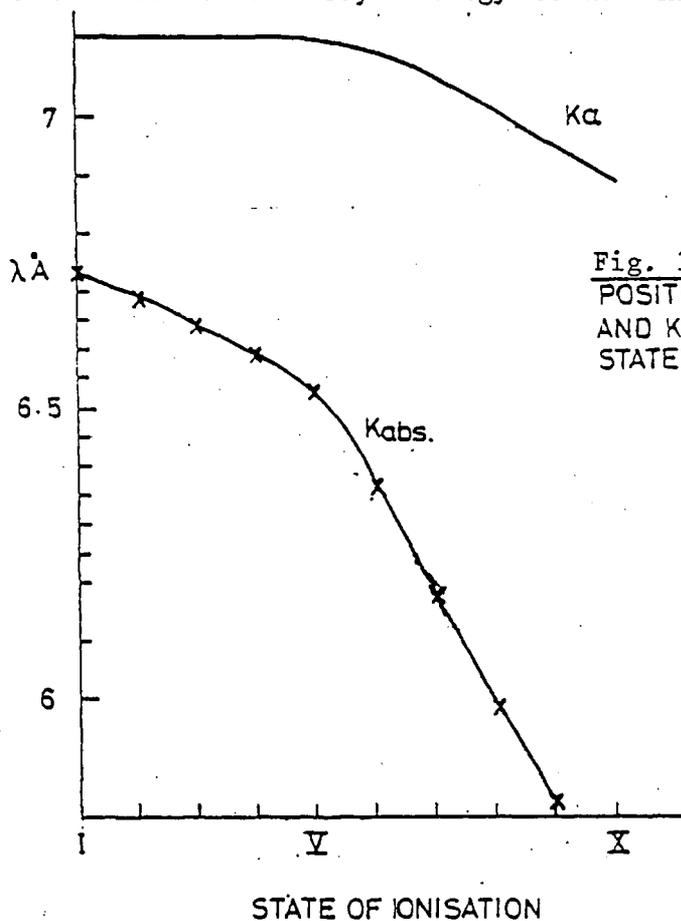Fig. 3.3.1
POSITION OF K_{abs}. EDGE
AND $K\alpha$ LINE FOR DIFFERENT
STATES OF IONISATION OF SILICON.

STATE OF IONISATION

An experiment was performed in which continuum emission was viewed through a layer of Si, which was subject to fast electron heating. The position of the K absorption edge of silicon was observed to shift, although this shift was reduced by ionisation depression effects.

The target consisted of $0.2\mu m$ Mg, $3.5\mu m$ SiO and $3.5\mu m$ Mylar. It was irradiated with 20J of incident energy in a $150\mu m$ diameter spot. The intensity was thus 1.1×10^{15} w.cm^{-2}. The geometry is as shown in figure 3.3.2.

In order that a significant amount of emission was present in the region of the absorption edge, a magnesium ablation plasma was selected. The hydrogen and helium like recombination continuum of Mg^{12+} and Mg^{11+} starts at 7Å (1.77keV), which is at lower energy than the Si K absorption edge at 6.73Å (1.84keV). The Mg^{11+} Ly and Lζ lines at 6.738Å and 6.580Å respectively provided and accurate calibration for λ (Si K_{abs}).

A microdensitometer tracing in the region of λ (Si K_{abs}) is shown in figure 3.3.3. The edge has clearly shifted to higher energy. This shift is 80 ± 30 mÅ . This shift initially suggests that the average charge state of Si is 3, however in the low temperature, high density Si plasma there are two effects reducing the effective E_{KI}. The first is the Debye depression. In a plasma, charges of a given sign will have an average excess of opposite charges around them. This leads to a mean potential distribution around the particle of:

$$V(r) = \frac{Ze^2}{r} \exp\left(-\frac{r}{\lambda_D}\right) \qquad 3.3.5$$

where λ_D is the Debye length. This is the maximum length over which particles are interacting and is given by:

$$\lambda_D = \left(\frac{kT_e}{4\pi (n_e + Z^2 n_i)e^2}\right)^{1/2} \qquad 3.3.6$$

If $\lambda_D < r_{ii}$, the inter-ionic separation ($r_{ii} = n_i^{-\frac{1}{3}}$) then the ion sphere model breaks down and we must take r_{ii} as the scale length (65). We will take the Debye depression as:

$$\min\left(\frac{Ze^2}{\lambda_D}, \frac{Ze^2}{r_{ii}}\right) \qquad 3.3.7$$

The ionisation potential is the energy required to remove an electron from the influence of the atom/ion. This is reduced since in the plasma a free electron still has average potential energy $-E_D$, so the energy required to raise it into the plasma is reduced by a corresponding amount.

Mg recombination continuum
source.

Spectrometer viewing
continuum through SiO
layer subjected to preheat.

Laser.

0.2 μm Mg,3.5 μm SiO,2 μm Mylar.
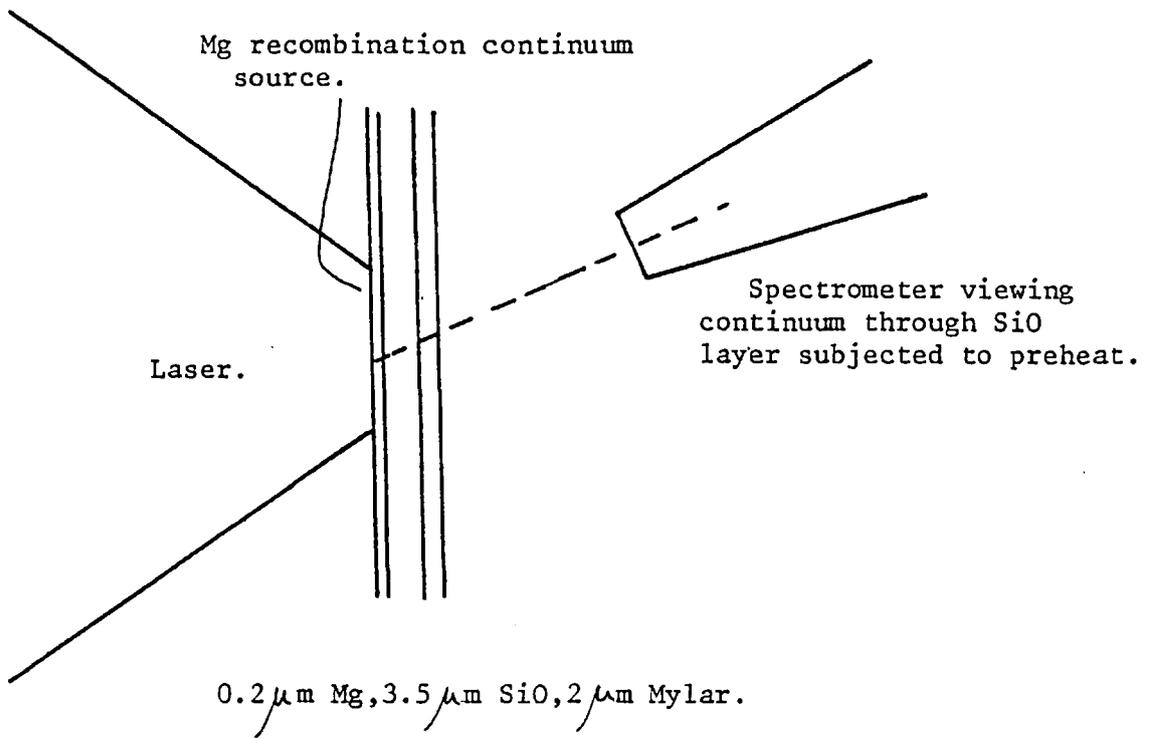
Figure 3.3.2 The geometry of the K absorption experiment.

Mg^{11+} Lγ

Si^{11+}
1'S.-2'S.

Mg^{11}Lδ

POSITION OF THE Si K$_{abs}$
EDGE IN A TARGET PREHEATED
BY FAST ELECTRONS
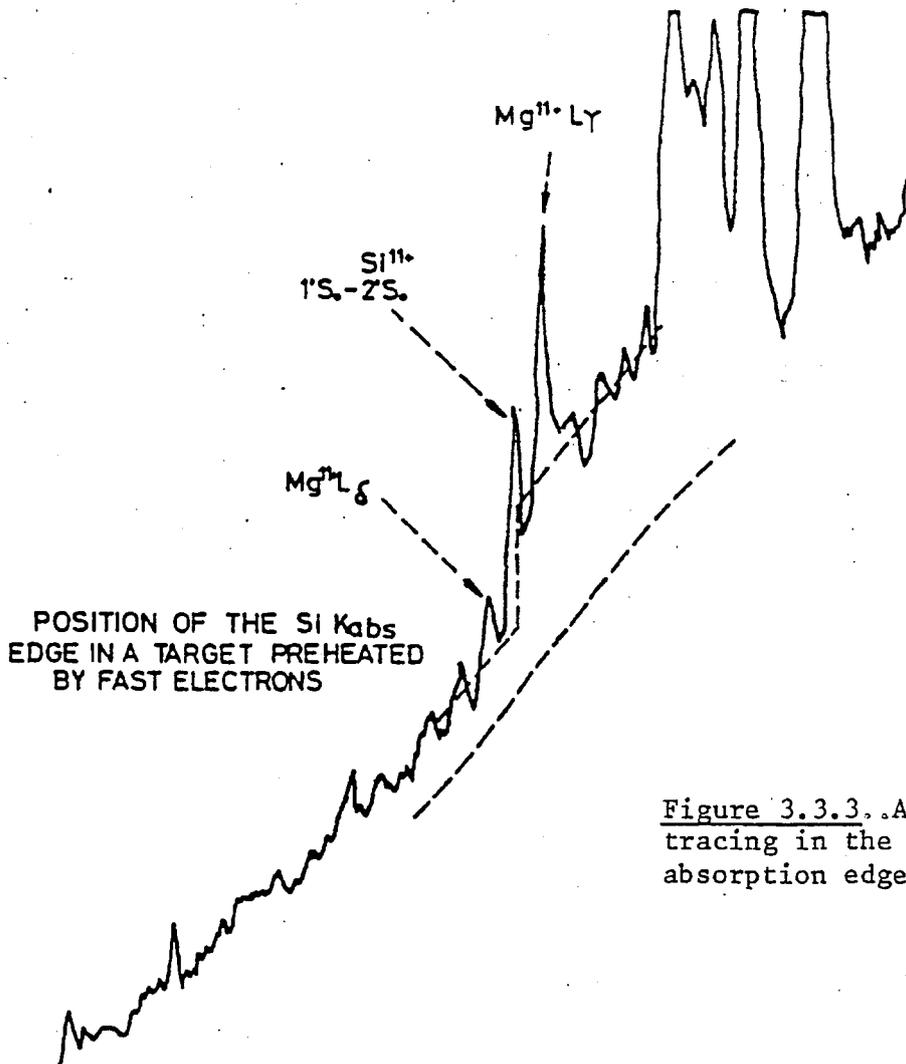
Figure 3.3.3. A microdensitometer
tracing in the region of the Si K
absorption edge.

The second mechanism for reducing the ionisation potential, which turns out to be more important in our regime, is described by the Inglis Teller limit (67). The effect is that stark broadening connects outer, vacant bound states with the continuum, reducing the effective ionisation potential. This is depicted in figure 3.3.4.
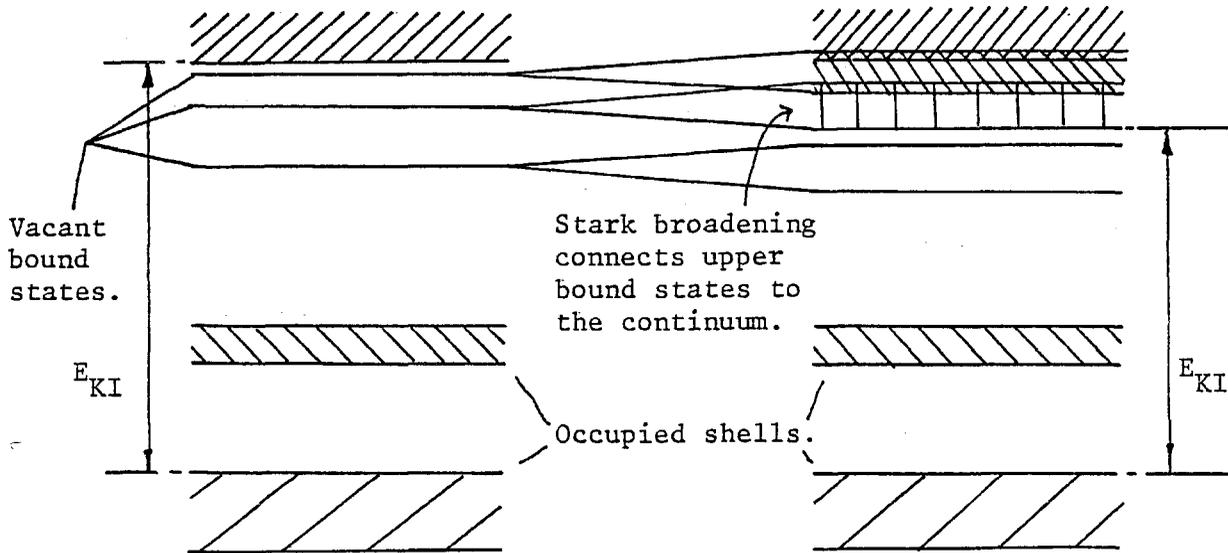
Figure 3.3.4 The mechanism of ionisation potential depression given by the Inglis Teller limit.

The Inglis-Teller limit assumes that all the vacant bound states are hydrogenic. This is not a bad approximation if the ion is fairly highly ionised and thus tightly bound, behaving like a point charge. We will accept this assumption if the ionisation energy of the theoretical hydrogenic state under consideration is less than the next ionisation potential of the original ion. Thus if the ion is initially ionised to charge state Z, and n_m is the principal quantum number of the hydrogenic bound state under consideration then for validity of the above assumptions:

$$IP(Z) \quad < \quad \frac{Z^2}{n_m^2} \cdot 13.616 \, (eV) \qquad 3.8.8$$

The Inglis-Teller limit is:

$$\frac{3 a_0 n_m^2 e F}{2 Z} = \frac{e^2 Z^2}{2 a_0 n_m^3} \qquad 3.3.9$$

$$(\text{Stark width}) \qquad\qquad (\tfrac{1}{2} \times \text{Energy level separation})$$

where a_0 = Bohr radius and F is the normal field strength given by $F = 3.7 \, e_0 N_{ch}^{2/3}$ (62).

$$N_{ch} = \begin{vmatrix} \dfrac{n_i + n_e \quad , \quad n_m < 40 / T_e (eV)}{n_i \qquad , \quad n_m > 40 / T_e (eV)} \end{vmatrix} \qquad 3.3.10$$

$$n_m = \sqrt[5]{\frac{Z^3}{N_{ch}^{2/3} \; 3.12 \times 10^{-16}}} \qquad 3.3.11$$

and

$$\delta E_{KI} = -\frac{Z^2 . 13.616}{n_m^2} \; (eV) \qquad 3.3.12$$

We will now check for numerical self-consistency between the observed shift, the previously determined energy depostion and our assumed equation of state.

From figures 3.2.6 and 3.2.7, of 20J of incident laser energy 1.2J will appear as preheat with a characteristic range of ~ 1.5 mgcm^{-2}. The L.T.E. equation of state (59), neglecting the ionisation depression, gives $T_e \simeq 100$ eV and Z = 7 for an energy deposition of 2×10^7J.cm^{-3}. The density of SiO is 2.13 gm.cm^{-3} so $N_i = 6 \times 10^{22}$cm^{-3} and $N_{ch} = 6 \times 10^{22}$ (from equation 3.3.10, as will be seen later). The Debye depression for this plasma is 36eV. Equation 3.3.11 gives $n_m = 3.7$ so the energy of the lowest 'average' unbound state is 49eV. This is the Inglis -Teller depression. Checking equation 3.3.8, (IP(7) = 303eV) $>$ ($-Z^2 . 13.6/ n_m^2 = 49$eV). Ths assumption of hydrogenic excited state is thus reasonable.

The total depression is therefore 49eV + 36eV = 85eV. A charge state of 7 in silicon will give a spectral shift of 530 m$\overset{o}{A}$ which is equivalent to 160eV. The predicted observed shift would thus be 75eV, however the recorded continuum is time averaged over the entire pulse so the average shift might be expected to be half this value; $\sim$ 36eV.

The observed shift was 80 $\pm$ 30 m$\overset{o}{A}$ which is equivalent to 22 $\pm$ 9eV. The observed shift in the K absorption edge is thus broadly consistent with the energy deposition inferred from the Kα yields. The similar magnitudes of the ionisation shift (to higher energy) and the ionisation depression (to lower energy) is a consequence of the particular density in this situation. The density dependence of E_D arose from the density dependence of the E.O.S. The overall shift is reduced from that in a plasma of small E_D and this reduces the usefulness of the diagnostic. Also a time dependent calculation is required to accurately predict the time integrated spectrum. However the consistency with the Kα analysis does reinforce our confidence in the calculated preheat energy depositions.

CHAPTER 4

A DISCUSSION OF FAST ELECTRON TRANSPORT AND THE EFFECT OF PULSE LENGTH
ON PREHEAT COUPLING

In this chapter fast electron transport in the various different
parts of the target is discussed and it is concluded that in the solid
part of the target, the transport is linear.

The results of the previous chapter are summarised and empirical
scaling laws for the preheat level and range are given.

An investigation into the variation of preheat coupling efficiency
with pulse length is described and the important result that for long
pulses the preheat is very low is reported.

4.1   Non-linear effects, spatial extent and reflexing

Non-linearities in the fast electron transport arise from the
generation of electric and magnetic fields. There are three regions of
interest in our plane targets which must be treated in different ways.
These regions are i)   interaction region, ii)   solid region and iii)
target rear.

We will discuss the interaction region first. Resonance absorption
accelerates electrons down the density gradient i.e. out of the target.
The electrons however carry charge with them and rapidly set up a large
electric field in such a direction as to slow them down. It is this field
which is, at least in part, responsible for the acceleration of energetic
ions. Ultimately the field turns around the electrons and they penetrate
the solid target surface. This leads to the possibility of spatial
spreading of the preheated area with respect to the interaction region.
The significance of this spreading will be determined by the magnitude
of the reflexing distance, relative to the focal diameter. We will estimate
this distance for typical conditions.

Let the fast electron distribution function be a simple exponential
(incorrect according to sub-section 3.1 but convenient for this order of
magnitude calculation) and the potential, a distance x from the surface,

be ϕ (x). We will assume that an outward travelling electron, of energy E_e, contributes to the density up to x, such that $e\phi$ (x) = E_e. The electron density takes the form (68):

$$n_e = n_o \exp\left(-e\phi \,/\, kT_H\right) \qquad \underline{4\cdot 1\cdot 1}$$

Coupling this equation with Poisson's equation in one dimension:

$$\frac{\partial^2 \phi}{\partial x^2} = \frac{-e\, n_e}{\mathcal{E}_o} \qquad \underline{4\cdot 1\cdot 2}$$

and solving, gives:

$$\phi = \frac{kT_H}{e} \ln\left(\left(\frac{e^2 n_o\, x^2}{2\, kT_H \mathcal{E}_o}\right) + 1\right) \qquad \underline{4\cdot 1\cdot 3}$$

This leads to a density scale length of:

$$L = \left(\frac{2\, kT_H \mathcal{E}_o}{e^2 n_o}\right)^{\frac{1}{2}} \qquad \underline{4\cdot 1\cdot 4}$$

This is the fast electron Debye length. We must now estimate n_o. Let the fraction of incident energy appearing as preheat be F_{ph}. The power density in fast electrons is:

$$P_{ph} = F_{ph} I \qquad \underline{4\cdot 1\cdot 5}$$

The average electron energy is kT_H so the current density is:

$$J_{ph} = \frac{e\, F_{ph} I}{kT_H} = \frac{F_{ph} I}{T_H\,(eV)} \qquad \underline{4\cdot 1\cdot 6}$$

Now:

$$J_{ph} = n_e \vec{v}_{th} e \qquad 4.1.7$$

but half the electrons are travelling out and half are travelling in so:

$$n_o \simeq 2 J_{ph}/\vec{v}_{th}e$$

$$= \frac{2F_{ph}I}{eT_H(eV)} \frac{m_e}{3eT_H(eV)} \qquad 4.1.8$$

$$\Rightarrow \quad L \simeq \left(\frac{2\varepsilon_o T_H^{5/2} e^{1/2}}{3^{1/2} m_e^{1/2} I F_{ph}}\right)^{1/2} \qquad 4.1.9$$

Taking typical values for the interaction parameters; $F_{PH} = 0.06$ (see figure 3.2.6), $I = 2 \times 10^{15} w.cm^{-2}$ and $T_H = 15keV$ we obtain $L = 0.3\mu m$. This is clearly very much smaller than the focal diameter so no spreading is to be expected. For electrons of energy $5kT_H$, (75keV) equation 4.1.3 gives a reflexing distance of $3.5\mu m$, still very small.

Such space charge effects will be important outside the surface where the background + ve charge density is less than the fast electron density:

$$Zn_i < n_{e,FAST} \qquad 4.1.10$$

This surface will move outwards under the influence of the fast electron pressure. We will obtain a scale length for this expansion. The ion equation of motion is:

$$\frac{\partial \vec{v}_i}{\partial t} \simeq \frac{1}{m_i n_i} \nabla p_{e,FAST} \qquad 4.1.11$$

If the scale length for the expansion is L then:

$$\nabla p_{e,FAST} \simeq \frac{n_{e,FAST} \, kT_H}{L} \qquad 4.1.12$$

and:

$$S = \frac{1}{2} a t^2$$

thus:

$$L \simeq \sqrt{\frac{Z \, kT_H}{2 m_i}} \, \Delta \tau \qquad 4.1.13$$

For a fast electron temperature of 15keV, $Z/A = 2$ and a pulse length of 100ps, $L \sim 50 \mu m$. This is of similar magnitude to the focal diameter, so there is a possibility of spreading, however this simple estimate does not demand it.

Experimentally, there was not evidence of spreading at the front surface. The $K\alpha$ emission was spatially resolved by means of a slit. A spatial tracing of the front Ca $K\alpha$ emission is shown in figure 4.1.1 together with a tracing of the pinhole picture at the same magnification. The spatial resolution of the spectrometer was degraded to $\sim 75 \mu m$ by the oblique viewing angle. The resolution is indicated. The pinhole camera images the thermal plasma, whereas the $K\alpha$ tracing is an image of the spatial extent of the reflexed fast electrons. The images are recorded to be the same size (see figure 4.1.1).

Moreover the hard-X ray continuum emission was consistent with the predicted fast electron distribution which suggests that there is no 'lost' emission due to spreading at the front.

In (69) hard X-ray emission ($h\nu > 17$ keV) was imaged in a short pulse microballoon experiment, and structure relating to the focussing conditions was observed. This is again consistent with our observation of no spreading in the extent of the $K\alpha$ emission.

In (70) fast electron pumped $K\alpha$ emission was reported from CO_2 ($\lambda = 10.6 \mu m$) laser target interactions at $I \sim 10^{13} w.cm^{-2}$. With thick (i.e. target thickness $>$ fast electron range) disc targets, $K\alpha$ emission was observed from the target rear. This was attributed to electrons orbiting, in their self-consistent electric field, around the target. At this intensity, 100 times less than our experiments,

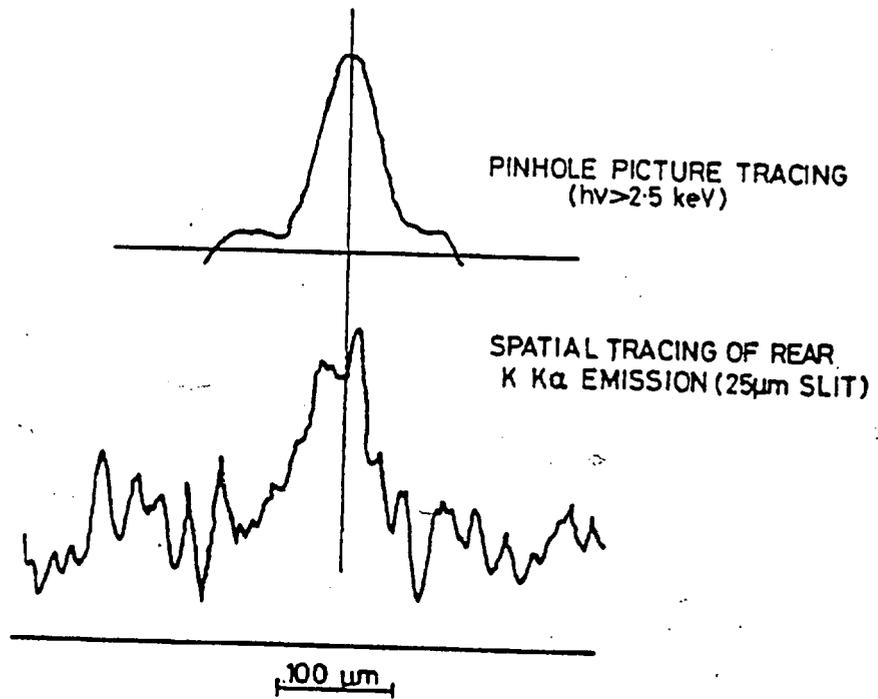**Figure 4.1.1** Microdensitometer tracings of the K Kα emission (spatial direction) and the pinhole image at the same magnification.
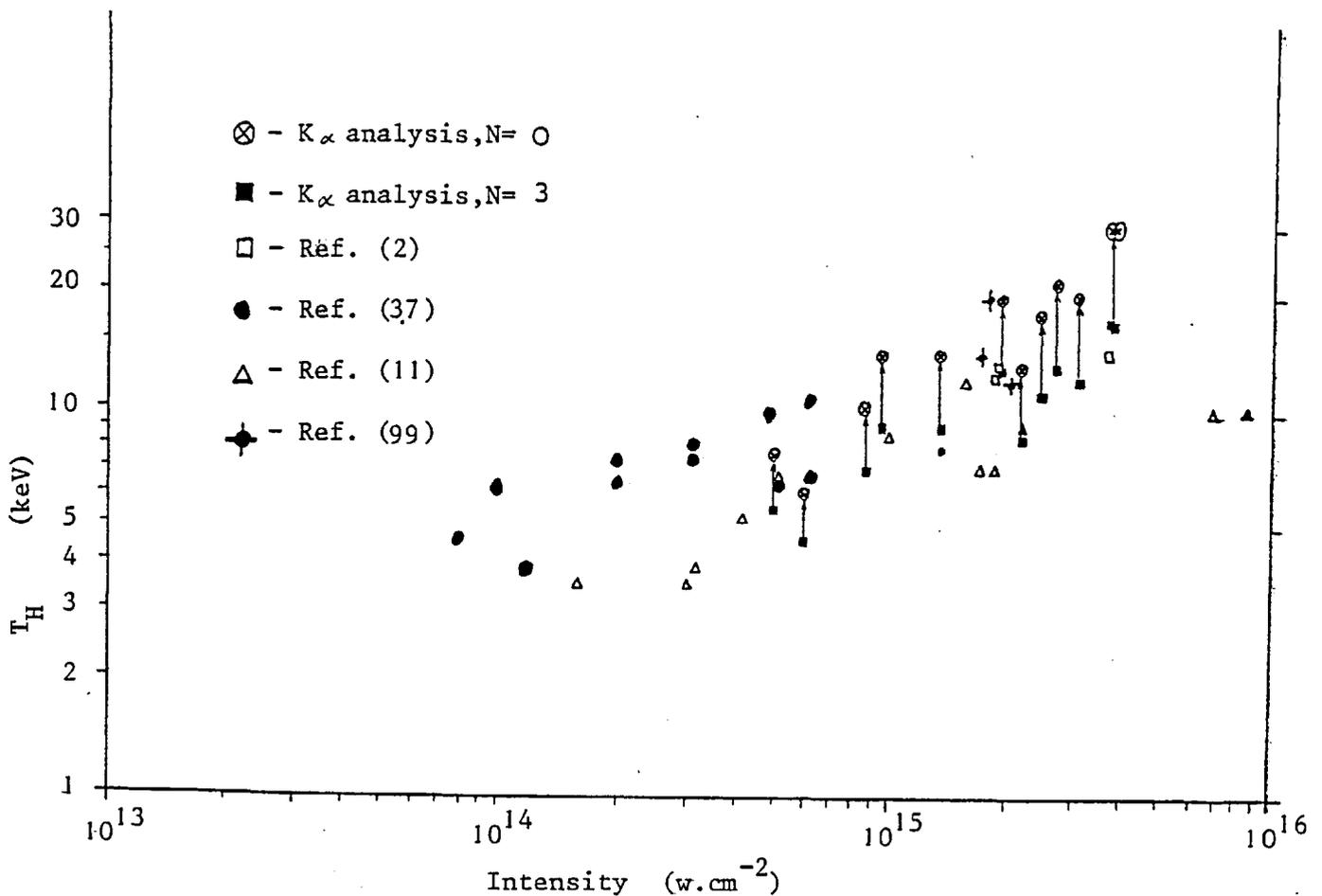
Figure 4.1.2 Collected X-ray continuum data and the suprathermal temperature determined from the Kα analysis.

the fast electron Debye length is large, so is the pulse length, and hence the plasma expansion scale length. Spatial spreading could thus be possible.

A different treatment is required for the solid target. Within the target we must have charge neutrality, i.e. $\nabla . \underline{j} = 0$. In one dimension this implies:

$$\dot{\underline{j}}_{TOT} = 0 \qquad\qquad 4 \cdot 1 \cdot 14$$

The penetrating fast electrons carry a current, $\underline{j}_H$, with them and this must be balanced by a return current of thermal electrons, $\underline{j}_c$, such that:

$$\underline{j}_H = - \underline{j}_c \qquad\qquad 4 \cdot 1 \cdot 15$$

This thermal return current will set up an electric field :

$$\underline{\mathcal{E}} = -\underline{j}_H \eta \qquad\qquad 4 \cdot 1 \cdot 16$$

where η is the resistivity of the solid density target (preheated thus ionised) material. If the classical range of the fast electrons is r_A (gm.cm^{-2}) and the density is ρ then the electric field will have significant influence on the fast electron transport if (see chapter 5):

$$\frac{\eta \underline{j}_H r_A}{\rho} \gg T_H (eV) \qquad\qquad 4 \cdot 1 \cdot 17$$

Taking equation of state parameters for the solid target from previous measurements ($n_e \sim 10^{23} \text{cm}^{-3}$, $T_e \sim 100\text{eV}$) we obtain a resistivity from Spitzer's (71) formula of $\sim 10^{-4} \Omega$ cm. For $T_H = 10\text{keV}$ the range is typically 2 mgm.cm^{-2}. This leads to a potential across the target, PD $\simeq$ 100 volts, completely insignificant. It is also apparent from the observed agreement between X-ray continuum emission and inferred distribution function, that electric fields are

unimportant. Any reduction in the classical electron range would result in a lower predicted temperature from the Kα yield ratio, since the analysis assumes only classical energy deposition.

This is an important point since it validates the use of classical energy deposition rates in the prediction of fast electron transport in solid targets. This has not been tested previously.

Figure 4.1.2 shows the 'Kα temperature' as a function of intensity together with collected X-ray data (11). The continuum temperature assumes an N = 0 (see sub-section 3.1) distribution, however the Kα temperature applies to an N = 3 distribution. Therefore the Kα temperature assuming N = 0 is also plotted for a more direct comparison. The Kα temperature is not reduced with respect to the continuum temperature so we may conclude that electric fields are small. (In chapter 5 we will see how the electric field may be increased to the extent that it dominates the transport).

The treatment of the rear is similar to that of the front. Electrons which penetrate the target will undergo space charge effects and will accelerate ions at the rear. The fast electron density will be considerably reduced on passage through the target. If the least energetic electron able to penetrate the target has energy E_{MIN}, then the number of electrons at the rear will be:

$$ n_{REAR} = n_{FRONT} \cdot \frac{\int_{E_{MIN}}^{\infty} n_e(E_e) \, dE_e}{\int_{0}^{\infty} n_e(E_e) \, dE_e} $$

$$ \simeq n_{FRONT} \cdot \exp\left(\frac{-E_{MIN}}{kT_H}\right) \qquad 4 \cdot 1 \cdot 18 $$

For target type II with 12μm mylar, E_{MIN} is, from (41), 50keV so for kT_H = 15keV: $n_{rear} \simeq 5\% \, n_{front}$. The distribution at the rear will be 'hotter' than at the front since electrons at the low energy end of the spectrum are more readily stopped than those of high energy. These two effects will increase the charge separation scale length (equation 4.1.9) but not sufficiently to make it comparable with the focal diameter.

The same equation for plasma expansion (equation 4.1.13) applies at the rear surface. Experimental observations suggest that electrons do not

reflex close to the rear of the target. If they did then the rear $K\alpha$ yield would effectively be doubled since electrons would traverse it twice. The fluor layer at the centre of the three fluor layer target would have been less subject to reflexed electrons and yet all three $K\alpha$ yields give a consistent fit to the distribution function determined by two fluor layer targets. In addition the $K\alpha$ temperature was consistent with the hard continuum emission.

This poses the problem of spreading at the rear but not the front. The fast electron density at the rear is certainly much lower than at the front surface. The problem is more complicated than our simple calculations assume, but the transport will depend in some non-linear way on the fast electron density, so a difference between front and back (on the relevant scale length) is to be expected. The local plasma conditions are very different. At the rear there is a very steep density gradient and the cold electron temperature is only a few tens of eV (from figure 3.2.5 and L.T.E equation of state). At the front the local temperature is 500eV and there is a long density ramp, through which plasma is streaming at the (500eV) thermal velocity. One would expect charge separation effects to become large where the local density gradient scale length becomes comparable with the fast electron Debye length (L in equation 4.1.4), i.e. when:

$$\frac{n_i}{\Delta n_i} \lesssim \left(\frac{2 k T_H \mathcal{E}_o}{e^2 n_{e,H}} \right)^{1/2} \qquad 4.1.19$$

At the front surface this equation may be valid at a density higher than $n_{e,H}/Z$ (see equation 4.1.10) so ∇p_e, FAST will be acting on a higher electron density than in 4.1.11 which will lead to a reduced expansion scale length. However at the rear surface the fast electrons will form a cloud extending λ_D away from the surface and will accelerate only sufficient ions to charge neutralise, i.e. equation 4.1.10 is valid.

Electrons at the rear of the target will have undergone scattering and their velocities will be nearly isotropic. This will enhance their dispersal via radial geometric effects.

4.2 Discussion

The results of chapter 3 can be summarised by:

$$\frac{\partial n_{e,H}}{\partial E_e} = A E_e^{3/2} \exp\left(-E_e / kT_H\right) \qquad 4.2.1$$

$$T_H = 7.8 \, (I)^{0.47 \pm 0.1} \, keV \qquad 4.2.2$$

$$R_o = 2.5 \, (I)^{0.6 \pm 0.1} \, mg.cm^{-2} \qquad 4.2.3$$

$$\frac{E_{PH}}{E_{INC}} = 0.06 \pm 0.03 \qquad 4.2.4$$

where I is in units of 10^{15}w.cm^{-2} and pulse length is 100ps. Equations 4.2.2 and 4.2.3 lead to:

$$R_o \propto (T_H)^{1.3 \pm 0.3} \qquad 4.2.5$$

This result is to be compared with the classical range of mono-energetic electrons. Although equation 4.2.5 applies to a distribution of electrons one would expect similar behaviour for R_o to the variation of classical range of a monoenergetic electron of energy kT_H. The residual range in aluminium (41) is plotted in figure 4.2.1 and can be seen to obey the empirical relation:

$$r_A \propto (E_o)^{1.7} \qquad 4.2.6$$

over the range 5 - 30keV.

Figure 4.2.1 The residual range
in aluminium as a function of
initial energy from (41).

$$r_a \propto E_o^{1.7}$$

Initial electron energy (keV)

Residual range (gm.cm^{-2})
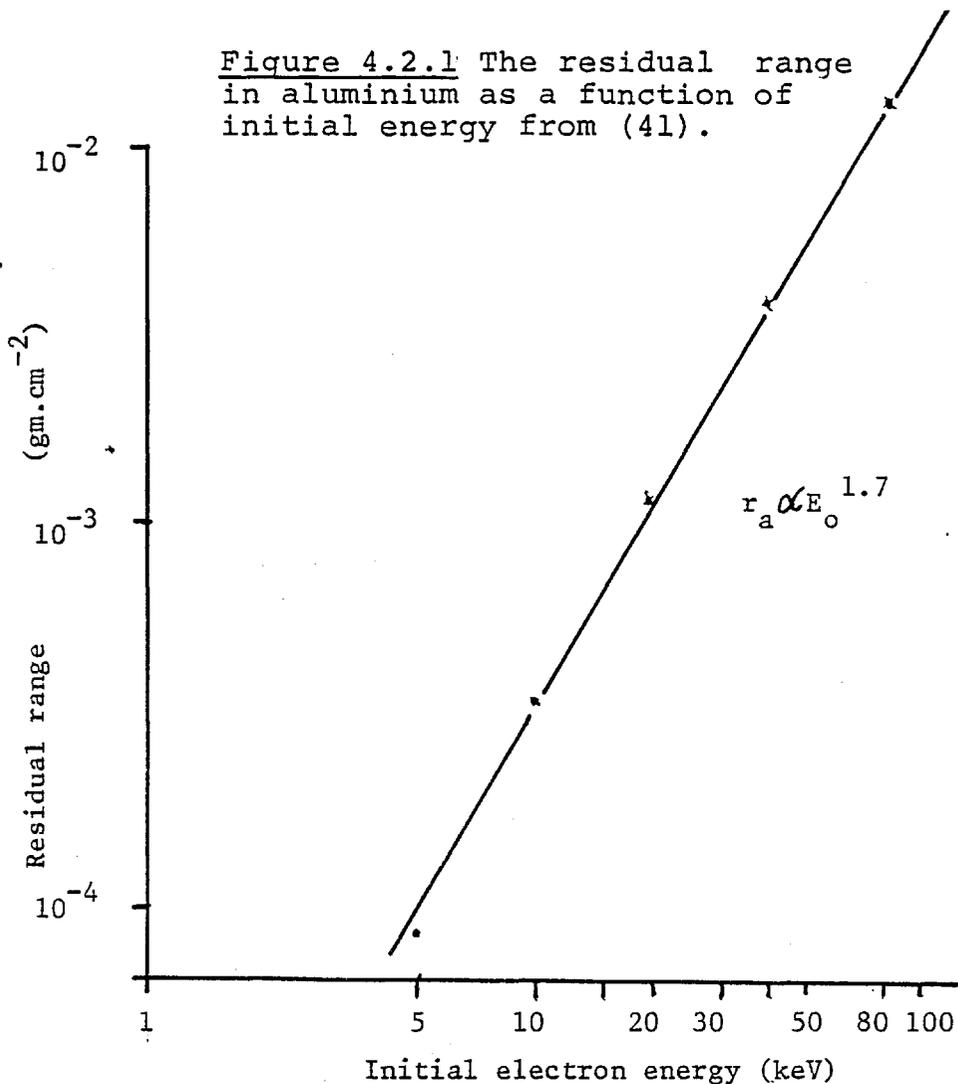
As mentioned in sub-section 2.10, the energy dissipation function
(the effect of scattering) is only very weakly dependent on E_o, so equation
4.2.6 applies to true energy deposition range. Equations 4.2.2 and 4.2.3
are thus consistent with the classical electron range.

The variation of R_o with I dictates the shell thickness for an
ablative compression at a given laser intensity .   The requirement
of a high pressure multiplication at the core (1.7) implies a large aspect
ratio. This makes a thin shell desirable which places a stringent limit
on laser intensity for preheat not to penetrate the shell. The laser energy
available restricts targets to $\sim 100\mu m$ diameter which in turn implies
a shell thickness of a few microns. From equation 4.2.3 the intensity
is limited to $\sim 10^{14}$w.cm^{-2}.

The onset of fast electron production coincides with saturation of

the ablation pressure since the absorbed energy is directed away from the ablation process. The intensity in an ablative compression is thus 'fixed' at $10^{14} w.cm^{-2}$. Unfortunately the saturation pressure is several orders of magnitude too low for an energy producing compression so shorter wavelength illumination is essential to an ablative laser-fusion scheme to escape preheat and pressure saturation.

The preheat pressure is roughly the preheat energy divided by the preheated volume, assuming the energy to be shared equally between kinetic energy and ionisation energy (typical of (63) at solid density).

Equations 4.2.2 - 4.2.4 lead to:

$$P_{PH} \propto I^{0.4} \tau_F \qquad 4.2.7$$

where P_{PH} is the preheat pressure and τ_F the duration of fast electron production. τ_F is limited to a few hundred picoseconds due to the production of a large density gradient scale length with a high reflectivity (e.g. Brillouin backscattering) and poor resonance absorption. The pressure has a rather weak dependence on intensity. The numerical results of chapter 3 (equations 4.2.1 - 4.2.4) yield the equation:

$$P_{PH}(MBar) = 0.98 \rho I^{0.4} (10^{15} w.cm^{-2}) \tau_F (p.s.) \qquad 4.2.8$$

where the preheated volume is taken to be the product of the focal area and the e^{-1} energy deposition range and $\tau_F \leqslant 100ps$.

Equations 4.2.7 and 4.2.8 apply to a target which is thick, compared with the fast electron range; $t_\rho > R_o$. This is the case in the fast electron driven ablative compressions of LASL (see sub-section 1.2) although equation 4.2.8 will be numerically different because of the different wavelength (10.6μm). The longer wavelength is more suitable for resonance absorption; principally because the requirement for a steep density gradient for efficient absorption is relaxed (33). This allows a longer pulse length and hence (see equation 4.2.8) a high pressure.

In the case of $1.06 \mu m$ illumination the pressure is rather low for fusion requirements at realisable intensities ($I < 10^{17} w.cm^{-2}$).

In thin target interactions ($t \rho < R_o$) space charge effects would be expected to turn around the fast electrons so they traverse the target several times (see previous section). As discussed in sub-section 3.1 the hard X-ray continuum emission from microballoon (2) and plane target interactions indicates similar coupling into preheat. The micro-balloon targets are thin to fast electrons. Bremsstrahlung emission arises from collisional electron energy deposition, one may conclude therefore that the electrons in the microballoon interactions traverse the target several times in order that they lose their energy collisionally. The preheat range becomes unimportant to the pressure since the energy is distributed throughout the target. Higher pressures might be obtained than in thick targets, but in the case of a spherical target the core is subject to the same energy deposition as the shell. The initial shell pressure, P_I, is simply:

$$P_I \simeq \frac{E_{INC} \quad 0.06}{4 \pi r^2 \, \delta r} \qquad\qquad 4.2.9$$

where the shell mass > fuel fill mass.

The Z dependence of preheat range is significant. Figure 4.2.2 shows the electron energy deposition as a function of depth in the target. It is plotted for various materials, with a fixed initial electron energy of 100keV. The depth of peak deposition goes down by a factor of 4 from plastic (CH) to lead.

The range shown in figure 3.3.7 is for an average Z of 13 within the target. To obtain the range in a material, Z, the range in figure 3.3.7 should be multiplied by the function in figure 4.2.3. This is the range within which half of the electron energy is deposited, normalised to that for Z = 13.

High Z layers have a significant reflectivity to electrons. This coupled with the higher specific energy deposition makes high Z layers the most suitable conventional way of screening from preheat. Moreover the high X-ray mass-attenuation coefficient enables them to screen against radiative preheat.
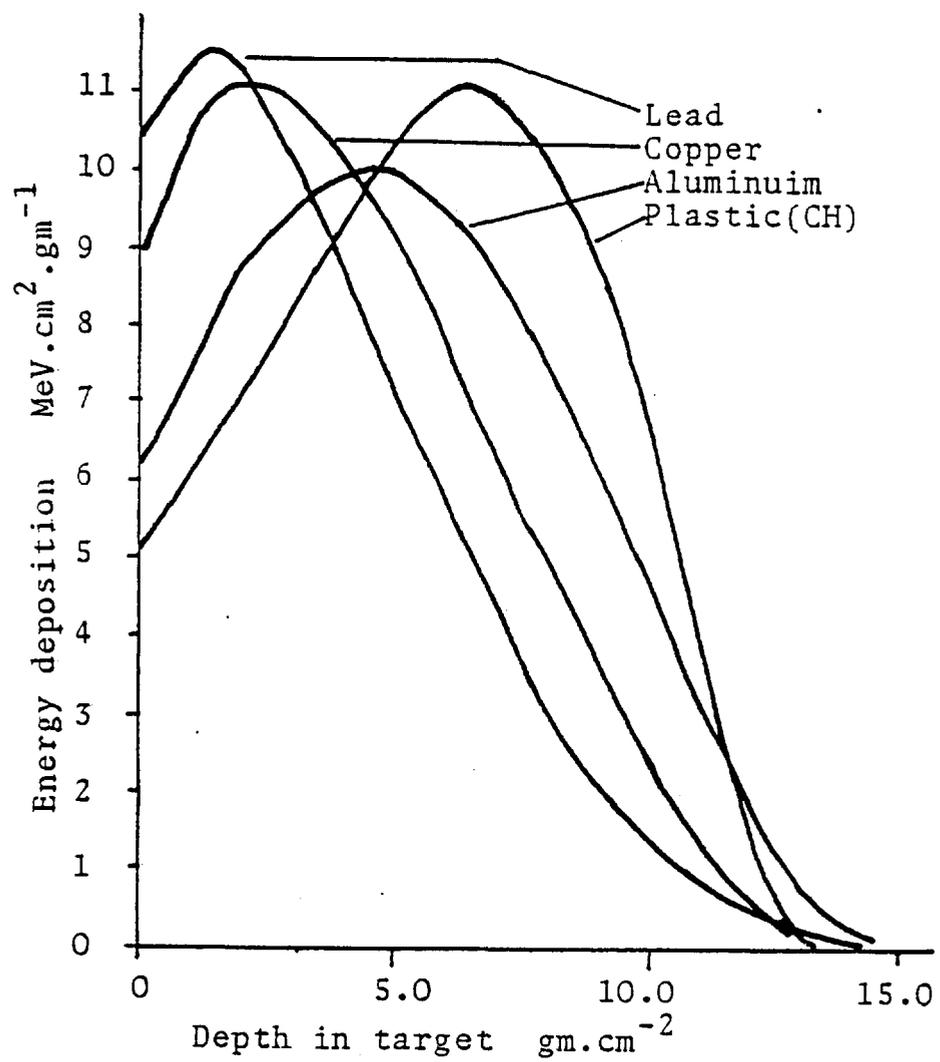
Figure 4.2.2 The effect of Z on energy deposition by 100keV electrons.

The graph shows a line plotted against "Z of stopping material" on the x-axis (with values 1, 5, 10, 13, 29, 50, 100) and values 0.5, 1.0, 1.5 on the y-axis. Text on the graph reads:

Obtained by integrating Spencer's results up to the point where $E_{deposited} = 0.5 \times E_o$.
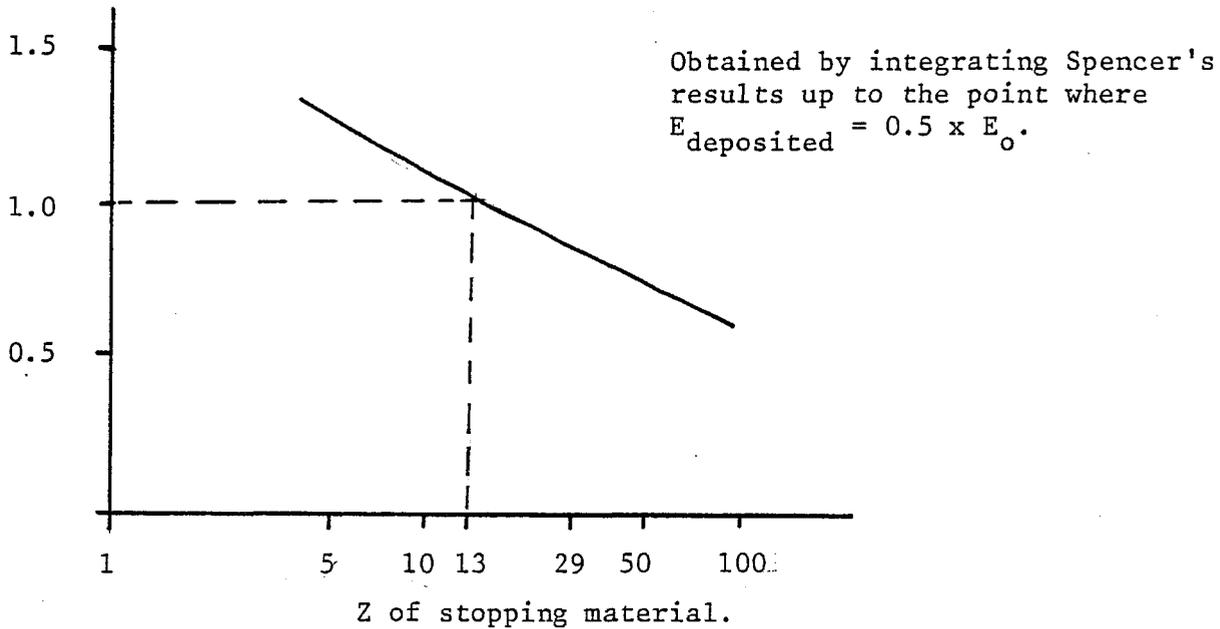
Figure 4.2.3 The preheat range conversion factor for a target of average atomic number Z.

4.3   Effect of pulse length on preheat

The variation of preheat coupling with pulse length is presented. Layered fluor targets have been irradiated with pulses from 70 to 200ps and single fluor targets (solid titanium and CaF_2) have been irradiated with pulses up to 1ns in duration.

The experimental configuration was the same as in chapter 2. In the case of single fluor targets only the front spectrometer was used, the crystal being germanium to enable detection of the Ti K_α emission.

The shortest pulse length available was   70ps. This was increased by inclusion of an etalon in the oscillator cavity. In this way pulses in excess of 200ps can be generated. For pulses of duration 1ns or more, the oscillator was set up to produce a single-mode pulse of duration ~60ns. A pulse of the desired length was then switched out electro-optically.

The intensity was determined from the incident energy, the pulse length (recorded by a streak-camera) and the focal spot size, assumed to be the same size as the X-ray emitting region recorded by the pinhole camera. Figure 4.3.1 shows the collected data from all the relevant shots. Note that with 1.3ns pulses on Ti and CaF_2 no clearly identifiable $K\alpha$ emission was observed, the coupling into preheat being very low.

SHOT	E_{INC} (J)	TARGET	I (10^{15} wcm^{-2})	PULSE LENGTH	$K\alpha$ YIELD(10^{-5} J.sr^{-1})			E_{PH} (J)	E_{PH}/E_{INC} %
					K	Ca	Ti		
20160480	33.8	TYPE III	5.7	75ps	FOGGED	1.12		2.2	6.47
01170480	19.8	(12μm Mylar)	1.5	"	2.80	0.38		1.53	7.73
02210480	24.8	"	1.9	"	4.95	1.36		2.37	9.54
05220480	20.4	"	1.5	"	2.08	FOGGED		0.99	4.85
01250480	13.9	"	1.0	"	0.78	0.45		0.96	6.93
03020580	20.9	"	1.7	150ps	1.43	0.20		0.80	3.89
14080580	22.4	"	7.5	"	3.51	0.64		1.80	8.02
16080580	21.0	"	3.6	"	0.98	0.49		0.74	3.52
02250380	4.8	SOLID T_i	0.61	400ps			<0.06	<.005	<.0.06
03250380	4.3	"	0.61	"			<0.08	<.006	<0.08
01240380	4.2	"	0.53	"			<0.06	<.005	<0.07
03051279	16.2	1μm KCl, T_i	0.16	1.3ns			<0.96	<.076	<0.47
01061279	50.4	"	2.0	"			<0.68	<.052	<0.10
03061279	69.6	SOLID T_i	2.7	"			<0.80	<.064	<0.09
04061279	55.8	"	2.2	"			<0.80	<.064	<0.11

Figure 4.3.1 A summary of the variable pulse length shots.

This is a significant result since it greatly relaxes the constraint on intensity due to preheat considerations. The effect is probably due to relaxation of the density gradient during the slow rising leading edge of the pulse. Resonance absorption relies on a steep density gradient, also a small density gradient leads to a long interaction distance up to the critical density surface in which backscattering (72,73) can occur, reducing the intensity at critical.

Other workers (74) have observed that a low energy pulse ($\sim$ few mJ) leading a short pulse by a few ns (a prepulse) greatly reduces fast ion emission, an effect consistent with the assumption about the density gradient.

In (75) momentum coupling into targets was measured as a function of pulse length and angle of incidence. With short pulses (60ps) the characteristic angle and polarisation dependence of resonance absorption was observed in the ratio of target momentum to specific energy. With long pulses (2.5ns) at a similar intensity (varied from 10^{14} - 10^{16}w.cm^{-2}) no such variation was observed. This was interpreted as showing resonant absorption to be absent with long pulses.

A simple consideration of the free expansion of the plasma into a vacuum in the absence of the ponderomotive force can yield the rise time of the pulse required to establish a sufficiently short density gradient scale length for resonance absorption.

From equation 4.1.13 the scale length of the expansion after time ΔT is:

$$L \sim \sqrt{\frac{Z k T_c}{2 m_i}} \, \Delta T \qquad 4\cdot3\cdot1$$

where in this case, the expansion is driven by the termal electron pressure. From sub-section 7.1 the density scale length for efficient resonance absorption is:

$$L \lesssim 2 \lambda_{LASER} \qquad 4\cdot3\cdot2$$

Inserting this value into 4.3.1 with canonical values for the inter-action parameters of : T_c = 500eV, Z = 10 and λ = 1μm gives $\Delta T \sim$ 20ps, a rather small value considering that fast electrons are produced with pulses of (at least) 200ps duration, and comparable rise time.

The illumination will in general be incident over a range of angles. In a linear density profile, $n_e = n_c (1 - \frac{x}{L})$ where L is the density scale length and x the distance from the critical density surface, radiation will

penetrate to a point x = L. sin Θ , Θ being the angle of incidence of a particular ray. For efficient coupling to the critical density surface the radiation must penetrate to within a few vacuum wavelengths, λ_o , of this surface so that tunnelling may occur (see sub-section 7.1). Taking an average angle of incidence of $\pi/4$ and setting $x \lesssim 2\lambda_{LASER}$ for efficient coupling leads to:

$$L \lesssim 3\lambda_{LASER} \qquad 4\cdot3\cdot3$$

Insertion into 4.4.1 gives:

$$\Delta T = \frac{\mathcal{T}_{LASER}}{4} \lesssim 3\lambda_{LASER}\sqrt{\frac{2\,m_i}{Z\,k\,T_c}} \qquad 4\cdot3\cdot4$$

for efficient resonance absorption, where $\mathcal{T}_{LASER}$ is the pulse length and $\mathcal{T}_{LASER}/4$ is roughly the rise time. The canonical plasma parameters of 4.3.2 give numerically $\mathcal{T} \lesssim 120ps$ in better agreement with observation.

Theoretical (24, 76, 77) and experimental (76) studies indicate that the ponderomotive force can be comparable to P_e and significantly modify the density profile. Physically the ponderomotive force can be thought of as swelling of the energy density, and hence pressure, of the incident radiation as it propogates through the plasma. The swelling arises since the group velocity, and hence energy transfer velocity, go to zero as n_e approaches n_c.

— The ponderomotive force per unit volume is given by (77):

$$F = \frac{(\epsilon - 1)}{8\pi} \nabla\langle(\delta E_x)^2\rangle \qquad 4\cdot3\cdot5$$

The gradient of $\langle\delta E_x^2\rangle$ will vary a L^{-1} and the volume over which the force acts is proportional to L, thus the net effect at critical is independent of the density gradient scale length.

This would suggest that the ponderomotive force is able to produce a steep density gradient regardless of the initial scale length, however after significant relaxation of the gradient there will be a delay before the ponderomotive force can steepen it. During this time

the sub-critical plasma will be further heated making it harder for the ponderomotive force to overcome $-\nabla p_e$, also the interaction length up to critical becomes large enabling Brillouin backscattering to reflect the radiation before it reaches critical.

If the peak intensity becomes sufficiently high that the vacuum radiation pressure, I/c, exceeds the plasma pressure then the profile will become steepened and resonance absorption will occur regardless of pulse length. This will occur at $I \sim 10^{16} \text{w.cm}^{-2}$ for $kT_c = 500\text{eV}$ and $n_e = n_c = 10^{21} \text{cm}^{-3}$.

Figure 4.3.2 shows the fractional coupling into preheat as a function of pulse length. The preheat energy in the two fluor targets was calculated as in sub-section 3.1 and in the single fluor targets as in sub-section 2.4 assuming $kT_H = 10\text{keV}$. The region of significant relaxation of the density gradient is indicated. In all of these shots the average intensity is a few $\times 10^{15} \text{w.cm}^{-2}$. The point (*) with a long (150ps) pulse at high intensity ($7.5 \times 10^{15} \text{wcm}^{-2}$) shows good coupling. This is in agreement with the predicted steepening when $I/c \gtrsim p_e$.
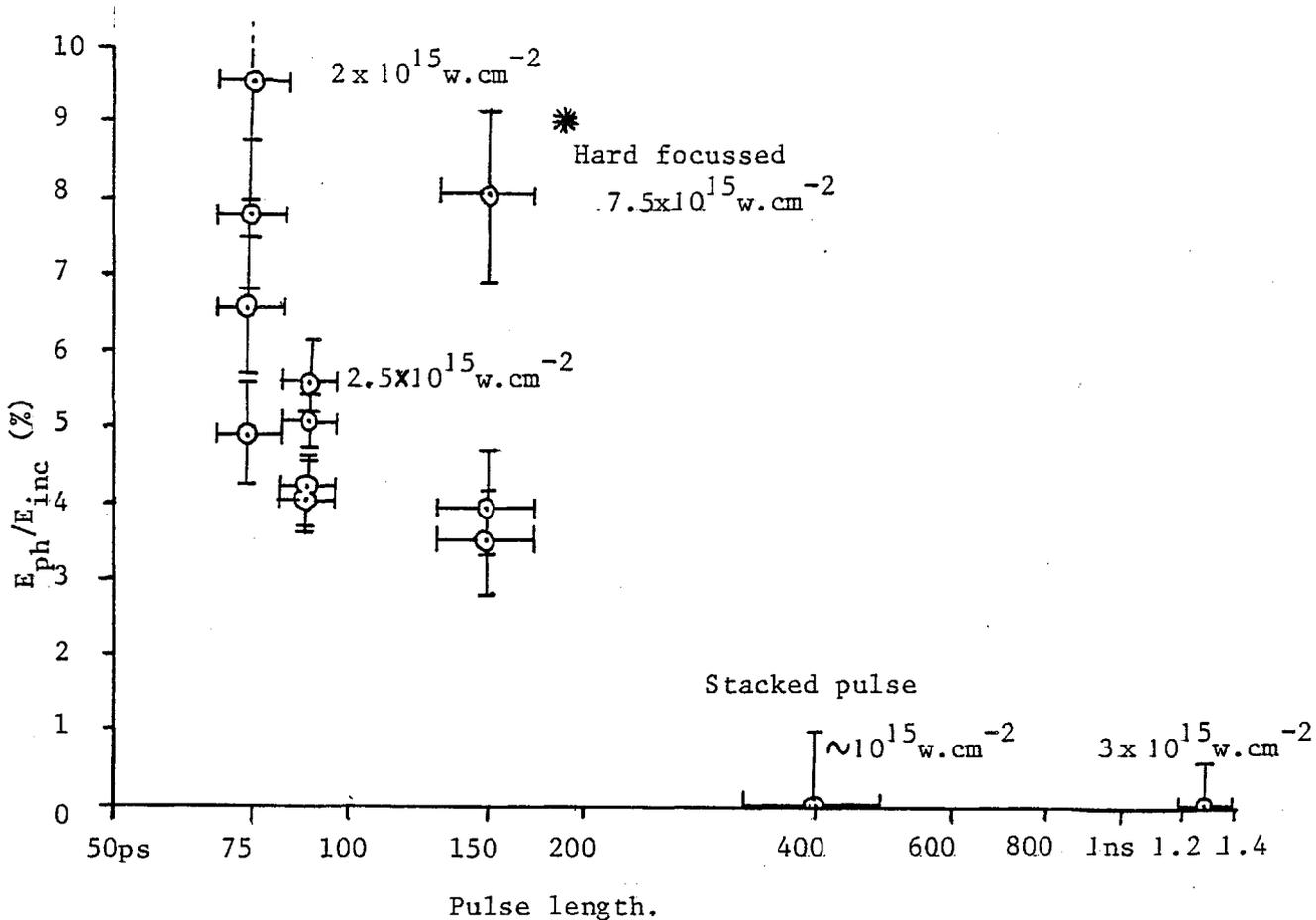

Figure 4.3.2 The fractional coupling into preheat as a function of pulse length.

CHAPTER 5

RESISTIVE INHIBITION

In this chapter it is shown how a non-linear effect, which is
referred to as resistive inhibition can reduce the fast electron preheat
range in special targets. An experiment is reported in which the
preheat range in low density gold is reduced by a factor of 2 - 3, over
solid gold.

A numerical Monte-Carlo transport simulation written by D.J. Bond
is used to quantify the effect. A higher than predicted inhibition is
interpreted as being due to anomalous resistance in the low density gold
(foam) resulting mainly from its density structure.

5.1   A simple description of the effect

Charge neutrality demands that $\nabla \cdot \mathbf{j} = 0$. In one dimension this
implies that a penetrating current of fast electrons, j_H, must be
balanced by a return current of thermal electrons, j_c. An electric
field is set up, by the fast electrons, of sufficient magnitude to drive
j_c through the solid target material. Fast electrons lose energy to
this field. If this energy loss-rate is of comparable magnitude to the
classical, collisional energy loss rate then the fast electron transport
will be inhibited with respect to linear theory (32). Figure 5.1.1
depicts the effect of the electric field.

We may compare the magnitude of the energy-loss mechanisms for a
typical laser target situation. The classical range of an electron, r_a
(mass per area), is obtained by integration of the Bethe-Bloch energy
deposition rate. This range is well tabulated (41). Scattering reduces
the electron range from the residual range, however for this estimate we
will ignore scattering. The energy loss of an electron to the self-
consistent electric field over this range is simply the product of the
electron charge and the total potential across the range r_a:

$$\Delta E_{e,field} \quad = \quad - e \, PD \qquad 5\cdot1\cdot1$$

Target

Fast electrons

carry current $\underline{j}_H$
balanced by:
return thermal

Laser

current $\underline{j}_c$

which produces
electric field $\underline{E}$,

impeding j_H
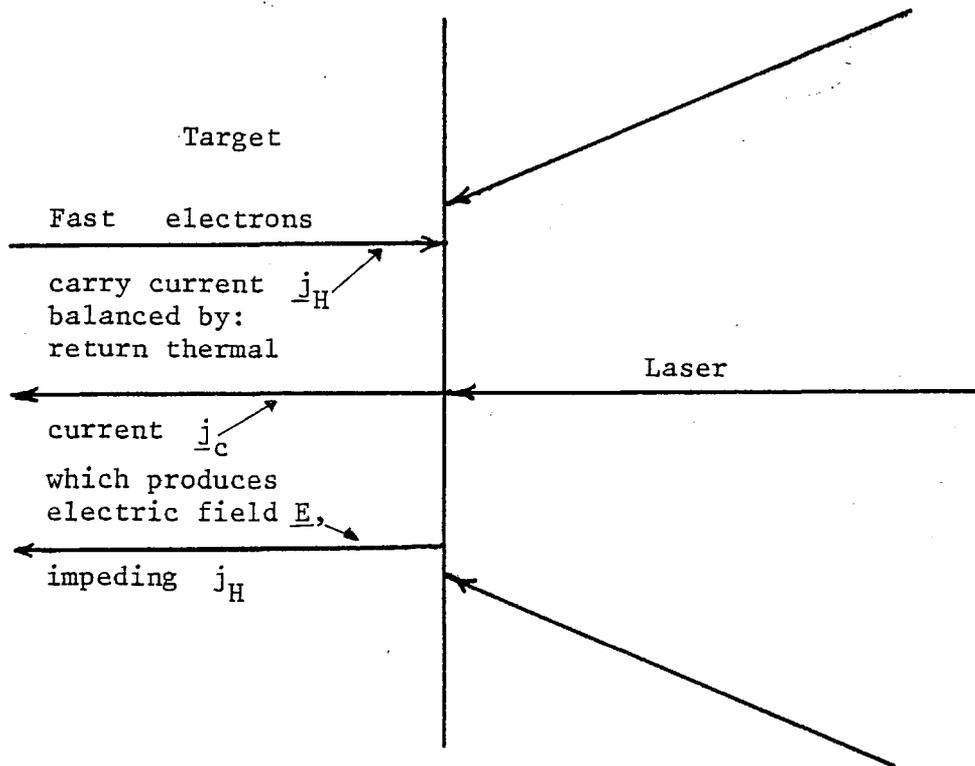
Figure 5.1.1   The mechanism of resistive inhibition

If the density of the target is ρ and the resistivity is η then:

$$PD = \underbrace{\frac{r_a}{\rho}}_{Distance} \cdot \underbrace{\eta j_c}_{Field} = -\frac{r_a}{\rho} \cdot \eta j_H \qquad 5\cdot1\cdot2$$

An electron will have a typical energy of kT_H so the electric field will play an important role if:

$$-\frac{r_a}{\rho} \cdot \eta j_H e \quad \gtrsim \quad kT_H \qquad 5\cdot1\cdot3$$

As discussed in section 4 the electric field is very small for solid density targets. It is possible however to specifically choose a target material such that the electric field is enhanced. Spitzer (71) gives the

resistivity of a plasma as:

$$\eta \propto \frac{\overline{Z}.\ln\Lambda}{T_e^{3/2}} \qquad \underline{5\cdot 1\cdot 4}$$

High Z elements have many loosely bound electrons and so reach
a high state of ionisation at a moderate temperature, and hence exhibit
a high resistivity. A low density material has a large classical
stopping distance (r_a/ρ) over which the electric field can act. More-
over in LTE the average state of ionisation varies inversely with
density (see sub-section 2.11) so a low density material will exhibit
a higher resistivity than a high density material.

It is possible to fabricate low-density gold layers at $\sim$0.6% of
the solid density. In such a layer one would expect resistive effects
to be greatly enhanced. In figure 5.1.2 solid and low density layers
are compared in terms of the total potential developed over the classical
electron range, at an incident intensity of 10^{15}w.cm^{-2}.

Interaction parameters:- $I = 10^{15}$w cm^{-2}, $T_H = 10$keV, $j_H = 5 \times 10^9$ Acm^{-2}		
TARGET MATERIAL	GOLD	
DENSITY	SOLID (19.3gcm^{-3})	0.6% (0.12gcm^{-3})
RESIDUAL RANGE $(E_e = 10$keV)	0.79 mg.cm^{-2}	
STOPPING DISTANCE	0.4μm	66μm
RESISTIVITY (L.T.E. AND SPITZER)	8.0 x 10^{-5}Ωcm $(T_e = 120eV$)	4 x 10^{-4} Ωcm $(T_e = 85eV$)
POTENTIAL	16V	13.2kV

Figure 5.1.2 A comparison of the effect of the resistive electric
fields in low and high density gold.

Evidently resistive effects will be important in low density gold. The mass of material required to stop fast-electron preheat will be reduced if resistive effects are significant and this could be beneficial to fusion target design.

5.2   Computer simulation of resistive inhibition

A Monte-Carlo numerical simulation was employed to predict the effect of the resistive electric field ([13]). For the purposes of the simulation the following assumptions were made:-

i) The interaction is adequately described in one dimension. The focal diameter is larger than the target thickness.

ii) No hydrodynamic motion

In 100ps the shock wave will not have traversed the target so no significant motion will have occured.

iii) Radiation thermal transport is ignored.

As seen in sub-sections 2.6 and 3.3 the fast-electron energy deposition is very much larger than radiation heating.

iv) At any instant there exists an equilibrium between the fast electron current and the electric field which can be solved as a time-independent problem.

The cross-target transit time for a 10keV electron is $\sim$2ps, (100μm thick) short compared with the pulse duration (100ps), hence an equilibrium will rapidly be established and maintained.

v) A L.T.E. equation of state applies (see sub-section 2.11)

vi) $T_e^{-3/2}$ resistivity applies ([71]).

The transport of the fast electrons at any one time is solved iteratively by a time-independent Monte Carlo transport calculation in slab geometry. Random Rutherford scattering ([78]) from Fermi screened nuclei and Debye shielded ions describe scattering events, between which electrons follow parabolic trajectories representing the effect of the electric field. A new electric field is determined from Ohm's law using a resistivity given by the equation of state for the local energy
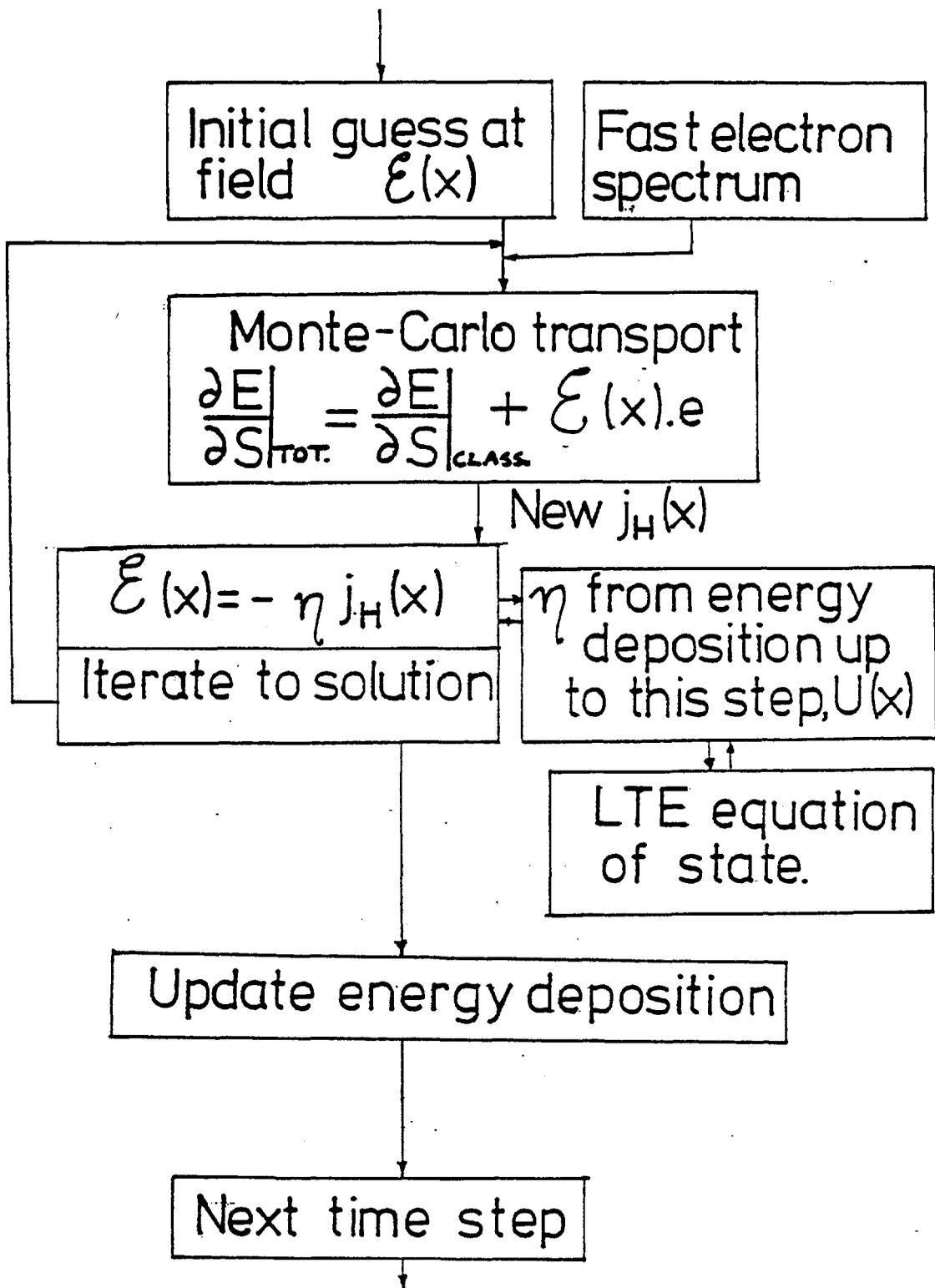
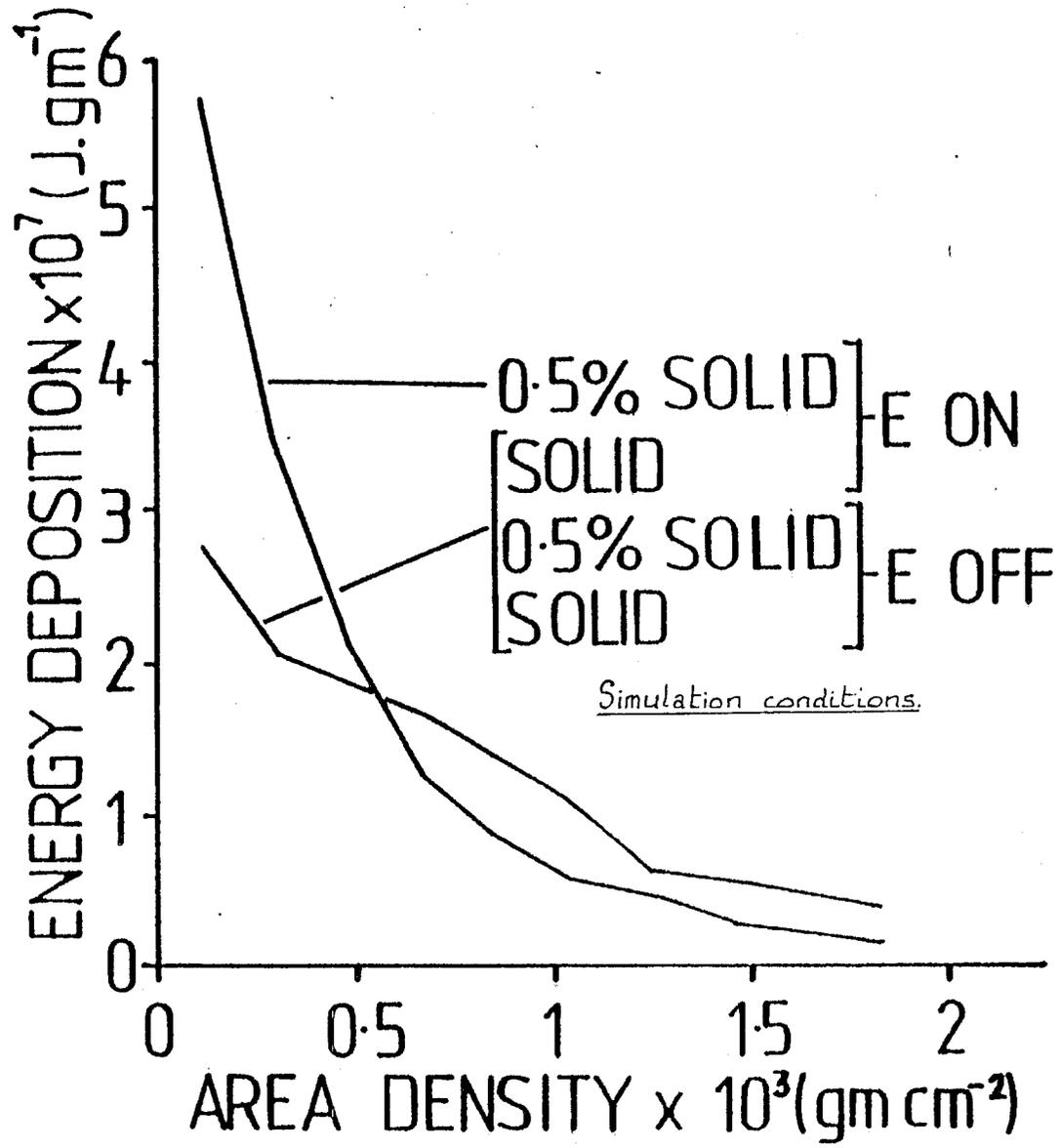Figure 5.2.1 The logic of the Monte-Carlo simulation.

Figure 5.2.2 A typical simulation result with a low density gold target.

deposition and Ohmic heating up to that time, and $j_c = -j_H$ is determined from the transport calculation. The electron transport is then iterated to find a consistent E and j_H. The collisional energy deposition is calculated using the continuous slowing down approximation accounting for bound electrons (32) and plasma electrons (79). A diagramatic representation of this procedure is shown in figure 5.2.1. In the absence of electric field effects this model reproduces other calculations (43).

The model was used to simulate a typical interaction. The parameters for this simulation (typical of the results of Chapter 3) where I = 3 x 10^{15} Wcm^{-2} and T_H = 14 keV with 8% of the incident intensity appearing as a fast electron distribution of the form;

$AE_e^{3/2} \exp(-E_e/kT_H)$.

The targets consisted solely of gold at solid density (19.3gmcm^{-3}) and 0.5% solid (0.097gmcm^{-3}). Figure 5.2.2 shows the energy deposition at the end of the laser pulse as a function of mass depth in target. The effective preheat range is reduced significantly in the low density gold. It should also be pointed out that approximately half of the energy deposition towards the rear of the target in the low density case is due to $\underline{J}.\underline{E}$ heating. This means that a thin layer of solid material at the rear of the gold would be subject to approximately half the specific energy deposition of the low density gold since $\underline{J}.\underline{E}$ heating would be small. The reduction in preheat over the solid gold target at the same mass depth would be large , approximately a factor of four, due to resistive inhibition up to the thin solid layer.

5.3   The experimental arrangement and results

In order to experimentally measure the effect of the resistive electric field,targets containing comparable layers of solid or low density gold were constructed. As in sub-section 2.2 layers of fluor materials were used to determine the fast electron range in low and solid density gold. The three types of target used were:

1) 0.1μm Al; 2μm Mylar; 3μm KCl; GOLD; 2μm CaF$_2$

2) 1.5μm Al; 3μm KCl; GOLD; 3μm CaF$_2$

3) 0.75μm Al; GOLD; 4μm CaF$_2$

In each case several targets were constructed with low and solid density gold layers with the overall area mass density of the target being matched to the fast electron range as determined in sub-section 3.2 (i.e. $\sim$ 2mgm.cm^{-2} for T$_H$ = 10keV).

The targets were irradiated from the aluminium side. On some shots a thin layer ($\sim$ 0.02μm) of KCl or CaF$_2$ was deposited on top of the Al to provide spectral calibration lines in the region of the Ca K$_\alpha$ emission. The attenuation of the K helium-like emission on passage through the gold layer provided an independent diagnostic of the area mass density of the low density gold layer.

Solid gold layers were made by vacuum evaporation and low density gold layers were made by slowly evaporating gold in an atmosphere of Argon (see appendix). This results in a foam-like structure on a very small scale-length ($\sim$ 1μm). The thickness of the low density layers was determined using a scanning electron microscope and the density by weighing. (A conventional crystal film thickness monitor as used for all the solid layers does not function with low density gold).

In target type i) the mylar provided a physical support (the substrate) and in types ii) and iii) this was provided by the aluminium. In all cases aluminium provided a flat and previously well characterised plasma. The KCl and CaF$_2$ were fast electron detectors and the gold was a variable density fast electron filter.

Target type 3) was constructed with a view to minimising the mass between the plasma and the gold layer, hence maximising the inhibition as discussed later. The gold layer makes the targets rather attenuating to the K$_\alpha$ emissions of interest so to avoid viewing the fluors through the gold two spectrometers were employed; one to monitor each of the front and rear emissions. As mentioned above the relative strengths of the K(1^1S_0 - 2^1P_1) line on the front and rear spectrometers provided an additional measurement of the area density of the gold layer. The thermal plasma is optically thick to K (1^1S_0 - 2^1P_1) emission. The source is not spherical so the emission is anisotropic. A correction was made, assuming the source

to be a disc. Figure 5.3.1 shows the layout of the target and
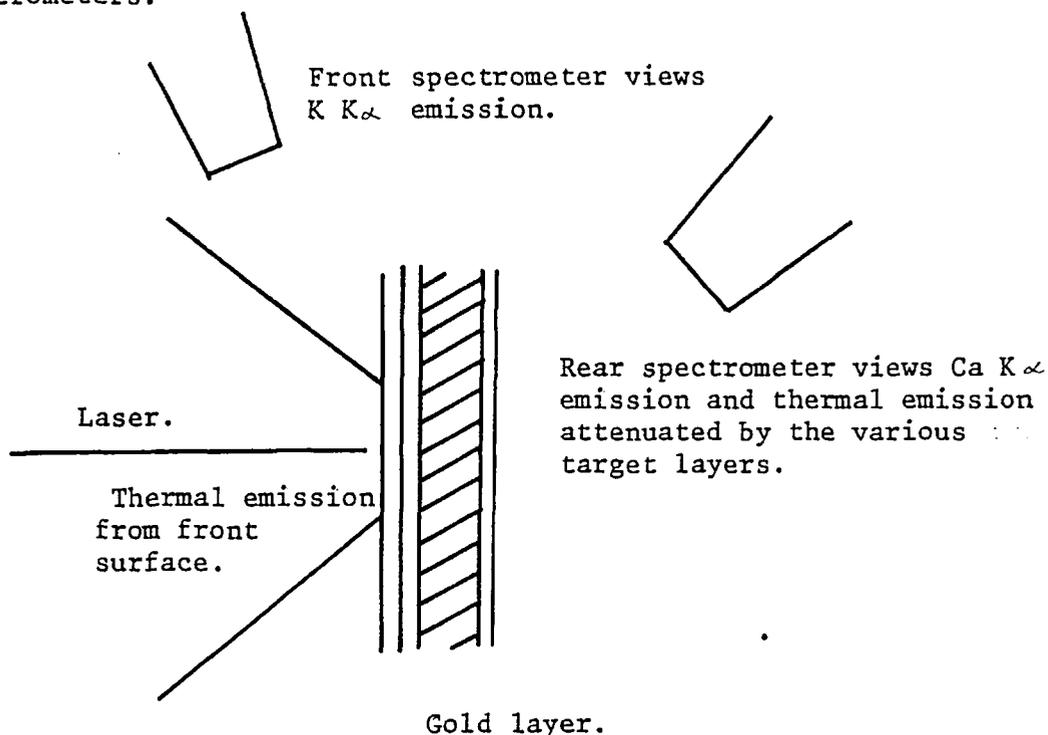spectrometers.

Figure 5.3.1   The experimental layout of the target and spectrometer.

Laser pulses of duration 75 - 200 ps and energy 10 - 30J
were focussed onto the targets with an f/1 lens. The intensity was
varied by means of a deliberate defocus and the focal spot size
confirmed by means of a X-ray pinhole camera. The intensity was
maintained around $2 \times 10^{15} w.cm^{-2}$ giving a fast electron temperature
of $\sim$ 10keV with characteristic preheat range $\sim 2mgm.cm^{-2} (\equiv 1\mu m$ solid
gold).

A summary of the shots is presented in figure 5.3.2. The front
spectrometer had a P.E.T. crystal (2d = 8.74Å) and the rear spectrometer
crystal was either P.E.T. or germanium (2d = 4.00Å). Germanium gave the
advantage of increased sensitivity (see appendix) but fogging problems
were aggravated since the exposed part of the film was brought nearer
to the source. Overall best performance was obtained with germanium.

On some shots an excessively thick layer of KCl on the front

| SHOT #	TARGET TYPE	OVERLAY ON Al.	COLD LAYER			CORRECTION DUE TO K Ly	LASER ENERGY (J)	PULSE LENGTH (p.s.)	INTENSITY 10^{15}w.cm^2	ENERGY 10^{-6}Jsr^{-1}	
			GOLD THICKNESS (μm)	SOLID EQUIV. (μm)	DENSITY (%)					K K$_\alpha$	Ca K$_\alpha$
06140679	1	10nmCaF$_2$	0.37		100	0	21.8	100p.s.	2.6	9.0	3.0
07140679	1	"	62	0.37	0.60	0	24.2	"	2.9	9.4	< 0.95
13140679	1	"	0.61	–	100	0	25.0	"	3.0	5.1	1.9
03150679	1	"	80	0.61	0.76	0	19.2	"	2.3	5.0	< 0.60
04250480	2	——	95	0.88	0.93	0	32.7	150p.s.	1.7	6.4	< 0.18
04020580	2	——	0.5	–	100	0	30.4	"	1.5	3.0	1.3
05020580	2	——	0.5	–	100	0	44.0	"	2.2	10.0	2.8
06020580	2	——	1.0	–	100	0	44.2	"	2.3	11.4	1.1
07020580	2	——	63	0.65	1.03	0	48.6	"	2.5	17.0	< 0.14
01060580	2	——	0.2	–	100	0	30.0	"	1.5	2.0	2.6
02060580	2	500nmKCl	1.0	–	100	0.30	40.3	"	2.1	5.5	0.25
03060580	2	"	0.5	–	100	0.33	38.0	"	1.9	5.0	1.5
04060580	2	150nmKCl	30	0.31	1.03	0.90	44.1	"	2.2	3.8	< 1.3
05060580	2	500nmKCl	1.0*	–	100	0.25	37.7	"	1.9	4.5	0.97
03070580	3	50nmKCl	120	0.78	0.65	0.23	41.0	"	2.1	–	0.58
04070580	3	"	90	0.46	0.51	0.35	42.2	"	2.1	–	1.7
05070580	3	"	40	0.24	0.60	0.25	36.1	"	1.8	–	5.0
07070580	3	"	55	0.22	0.40	0.32	38.6	"	2.0.	–	5.1
09070580	3	"	1.5	–	100	0	39.0	"	2.0	–	1.6
03080580	3	"	0.5	–	100	0.09	30.2	"	1.5	–	2.5
04080580	3	"	1.0	–	100	0	32.9	"	1.7	–	2.0
07080580	3	"	1.5	–	100	0	43.5	"	2.2	–	2.9
10080580	3	"	1.5	–	100	0	30.0	"	1.5	–	0.43
12080580	3	"	1.0	–	100	0	41.5	"	2.1	–	2.9

Figure 5.3.2. Complete data from low density gold experiments
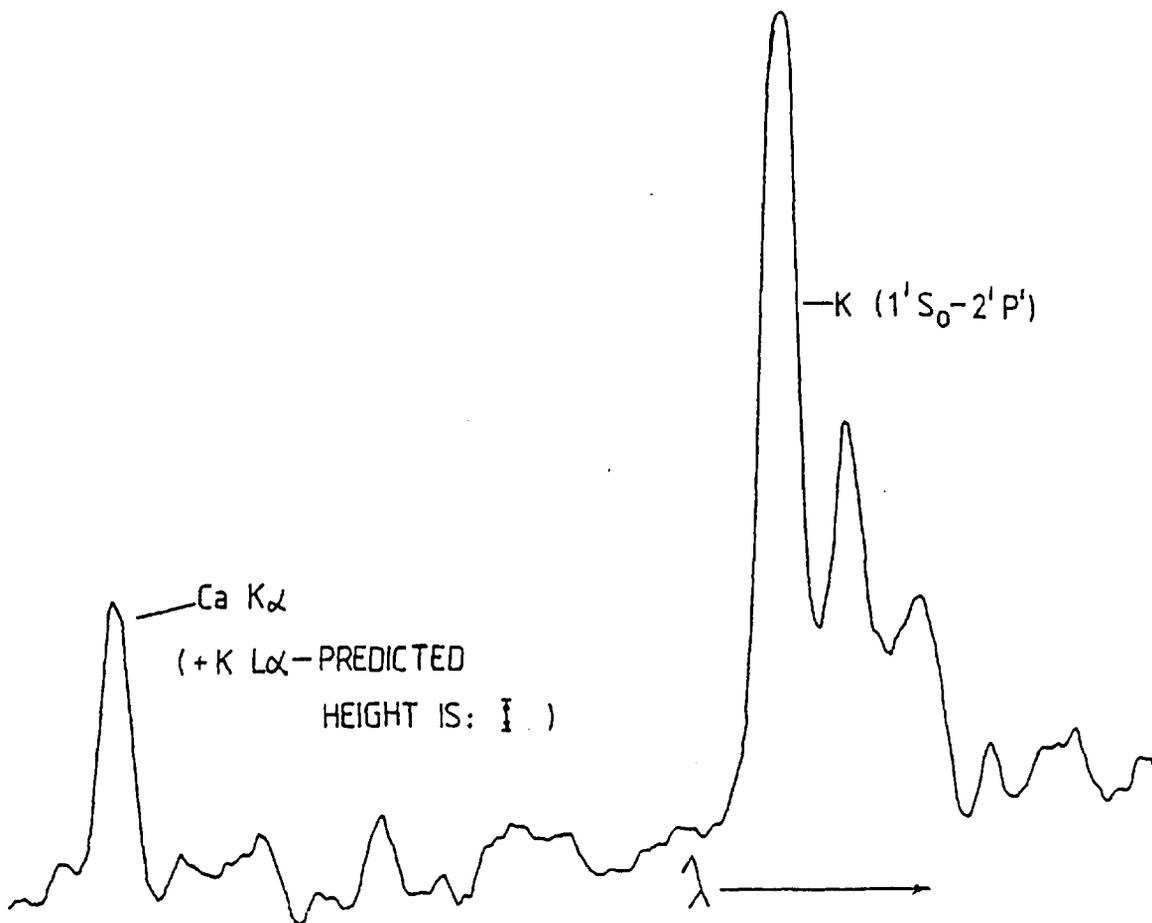
Typical rear spectrum.

Figure 5.3.3 Typical microdensitometer tracings of the spectra recorded on the front and rear spectrometers.
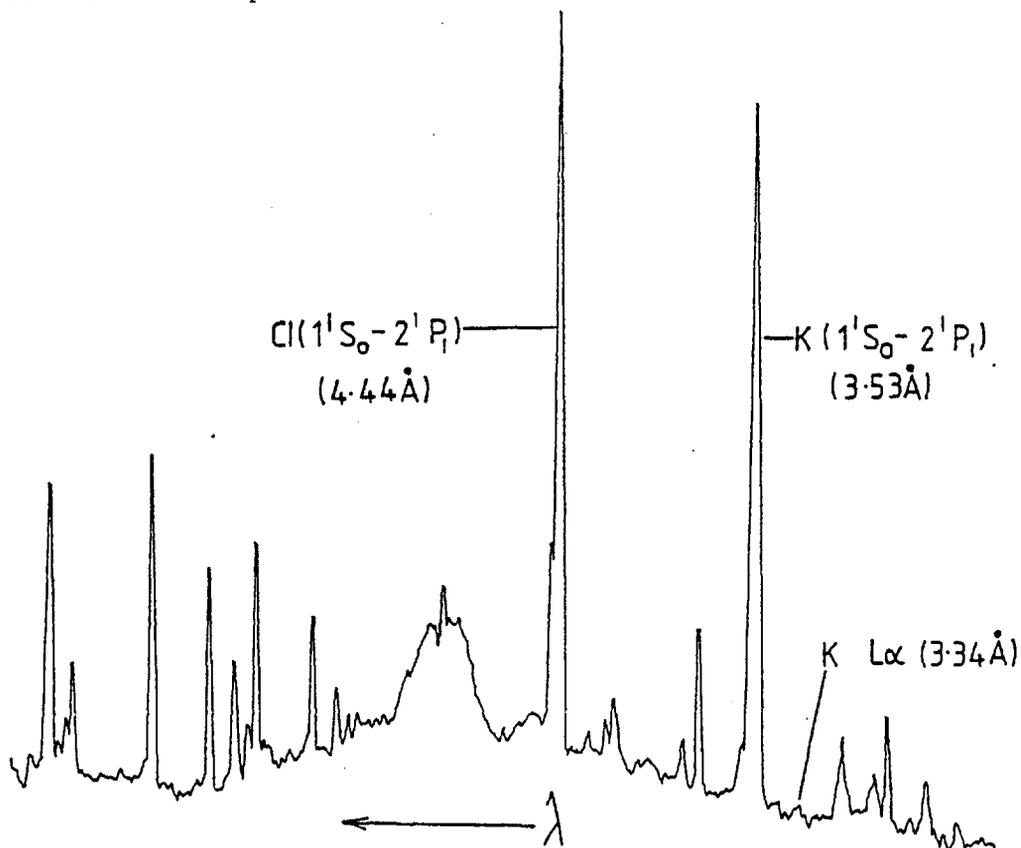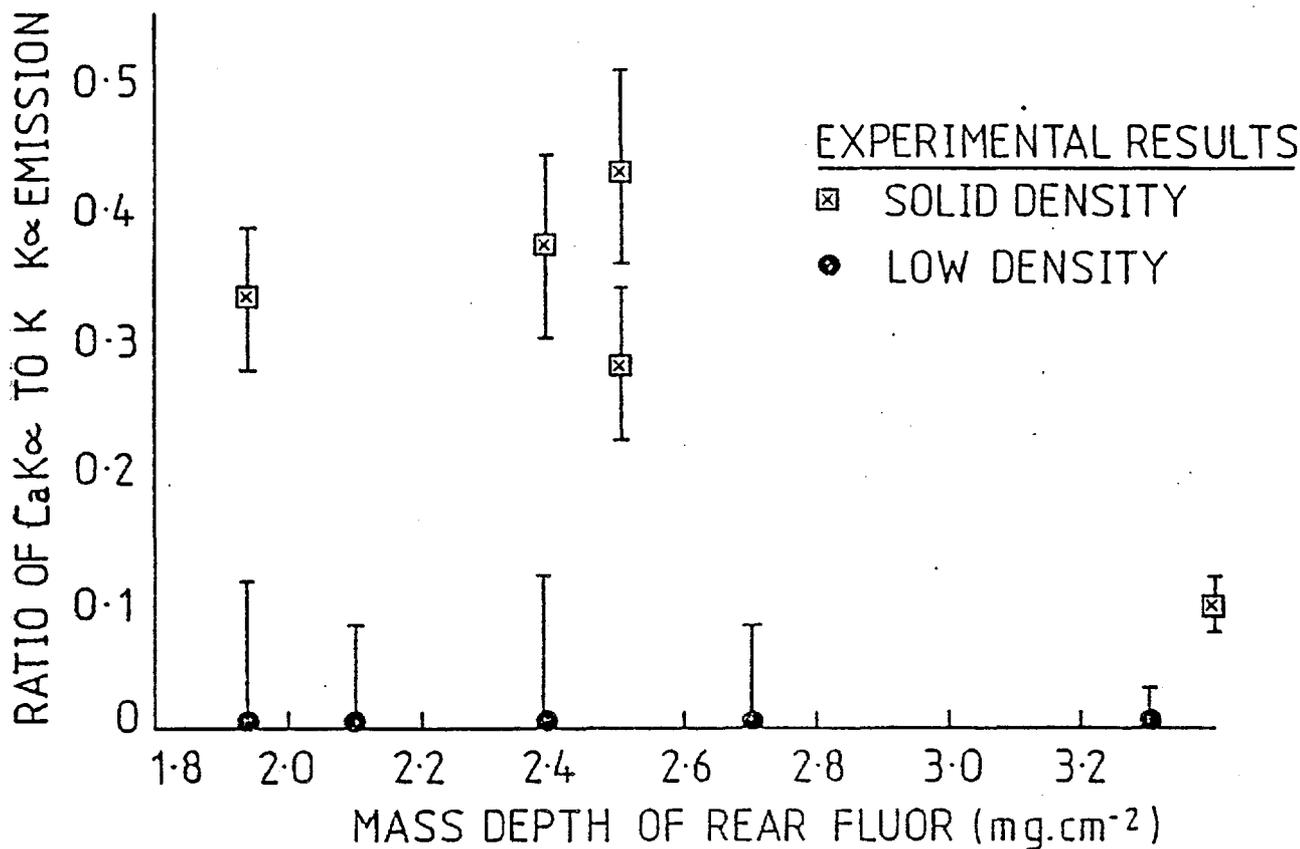

Typical front spectrum.

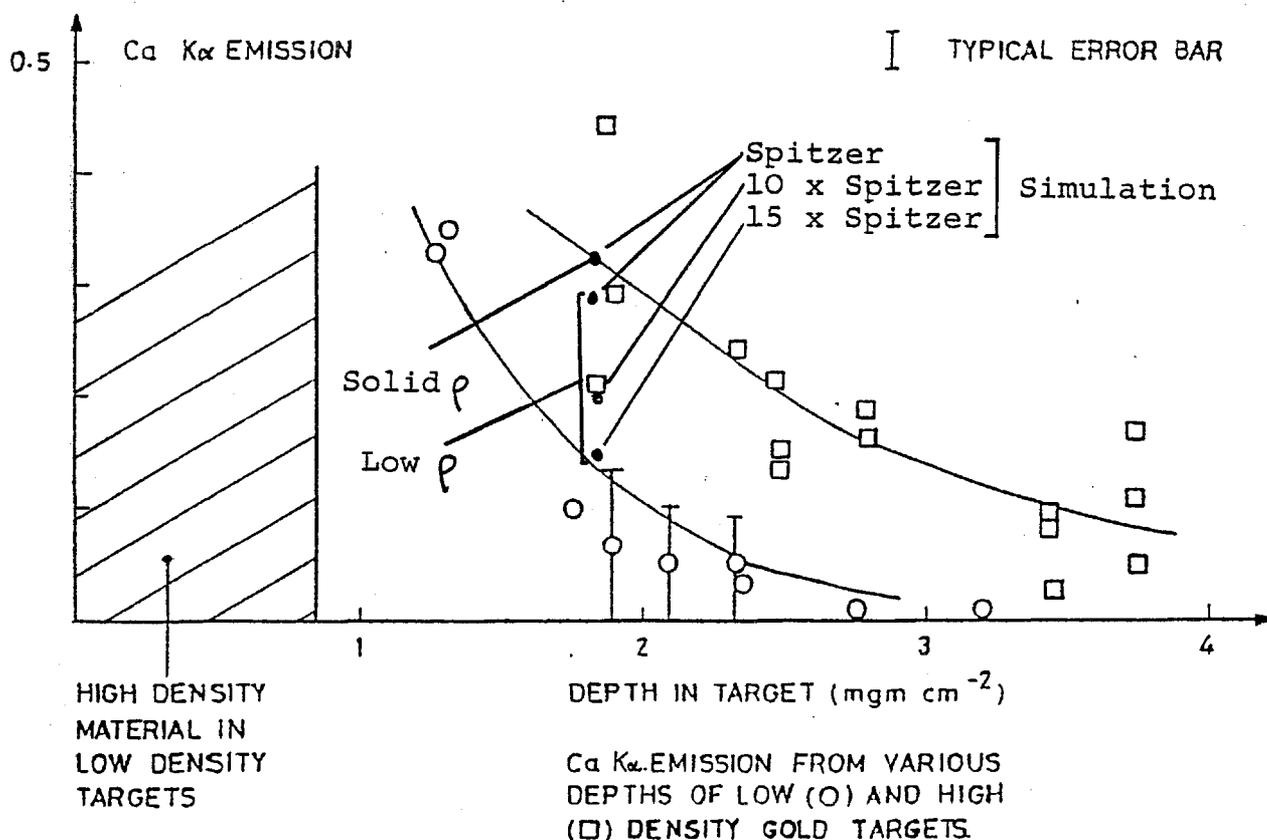Figure 5.3.4 The results of the shots onto two fluor targets

Figure 5.3.5 The results of all the shots in terms of the reduction in Kα yield due to the gold layer. Also shown are the results of the simulations.

coupled with a low area mass density of gold created the possible problem of confusion between the CaKα emission (3.36Å) and the K Lyα (3.34Å) line. To avoid this the intensity of the K Lyα emission on the rear spectrometer was calculated from its intensity on the front spectrometer and the attenuation. K Lyα emission was always accompanied by $K(I^1S_0 - 2^1P_1)$ emission (3.53Å). The relative intensities of the two emissions was calculated from the front spectrum. The intensity of the $K(I^1S_0 - 2^1P_1)$ emission from the rear spectrum thus gave an accurate value for the intensity of the K Lyα independent of the reflectivity of the crystal. This enabled an accurate correction to the Ca Kα yield to be made. The extent of the correction to the Ca Kα yield is indicated in figure 5.3.2. The figure is the fraction to be subtracted from the apparent Ca Kα yield. The CaKα yield tabulated is the corrected yield.

Typical microdensitometer tracings of the front and rear spectra are shown in figure 5.3.3 (shot number 03080580). The predicted height of the K Lyα emission is indicated. In this case the rear spectrometer used a germanium crystal.

The results of the two fluor layer shots are depicted in figure 5.3.4. The ratio of front to rear Kα emission is shown as a function of area mass density between the centres of each fluor layer. In all the low density shots the rear CaKα emission was undetected although on some shots rather large error bars result from a large K Lyα yield.

The combined results of all the shots are shown in figure 5.3.5. Here the rear Ca Kα emisssion normalised to the incident energy is shown plotted against the area mass density between the centre of the CaF_2 layer and the irradiated surface. The intensity is nominally the same ($\pm$ 40%) for each shot and is indicated. There is a clear difference between the low and solid density targets with the range in low density gold being substantially reduced.

5.4   Comparison with simulation and discussion

The numerical model described in sub-section 5.2 was used to simulate the single fluor target results. The simulation was initially run with solid gold targets (i.e. no electric field effects) in order to verify the validity of the assumed distribution function. This distribution was chosen using figures 3.2.4 and 4.3.2 to obtain the fractional coupling and suprathermal temperature appropriate to the intensity (2.0 x 10^{15}w.cm^{-2}) and pulse-length

(150ps). The incident distribution carried 1 Joule and kT_H was equal to 11 keV.

The results of the simulations are shown in figure 5.3.5 The K_α yield as a function of depth in the target is plotted for high and low density gold layers. The experimental yields are also shown. There is good agreement between prediction and experiment in the case of solid gold, however the simulation overestimates the K_α yields for low density targets. To obtain agreement between simulation and experiment the resistivity was empirically increased by a factor, f, this having no effect on the solid target simulations but reducing the K_α yield in the low density target simulations. Closer agreement was obtained for $f \geqslant 10$. This is also shown.

There are several possible causes for the apparently higher than Spitzer resistivity, principally:

i) The resistivity is wrong - the plasma has a very small 'log Λ', i.e. few particles per Debye sphere. Corrections to the Spitzer theory are of order $(\log\Lambda)^{-1}$, potentially significant.

ii) Voids in the gold are not dissipated in the duration of the pulse and contribute to the resistivity by reducing the effective area through which the current flows.

iii) The fast electron production time is less than the pulse length, leading to a larger j_H and hence a larger inhibition. NB. Increasing the resistivity by a factor f is numerically identical to reducing the pulse length by a factor f^{-1}.

The required value of f for consistency is rather large. It is not reasonable that Spitzer resistivity is so wrong. Hydrodynamic effects i.e. initial relaxation and then steepening of the density gradient at critical, can be expected to have some effect on the fast electron production time. In contrast to this in (80), the hard X-ray continuum was found to follow the laser intensity. The pulse length was ~ 300ps f.w.h.m. and the intensity $\sim 2 \times 10^{15}$w.cm^{-2}. With such a pulse length we would expect rather poor coupling into preheat (sub-section 4.4). The measurements of continuum intensity in (80) were relative and do not dispute this. One might postulate that the density profile did not become fully steepened and the observed continuum emission was characteristic of those absorption mechanisms not reliant on a steep density gradient, i.e. parametric decay (81), oscillating two-stream (84) or ion acoustic turbulence (85). If this be so then with a short pulse the fast electron flux will consist of a low level which is coincident with the main pulse and a dominant peak which exists only for the duration of the steep density gradient.

This duration will be dependent on the hydrodynamics of the interaction.

The assumption that $j_c = -j_H$ relies on the return current being unable to diffuse radially into the unheated gold. This can be considered to be a skin depth problem with characteristic frequency, γ equal to 2/pulse length. The skin depth in a conducting medium is:

$$\delta = \sqrt{\frac{\eta}{\pi \gamma \mu_0}} \qquad 5.4.1$$

Initially taking Spitzer resistivity:

$$\eta = 1.03 \times 10^{-2} \frac{Z}{T_e(eV)^{3/2}} \ln \Lambda \; \Omega cm \qquad 5.4.2$$

gives $\delta \simeq 5 \mu m$ for $T_e = 100eV$, $Z = 10$ and a pulse length of 150ps. A factor of 15 increase in the resistivity would increase this to $\sim 20 \mu m$. This is less than the focal diameter of $100 \mu m$ so we can assume $j_c \equiv -j_H$, especially since if the return current were to follow a different path from j_H, the predicted inhibition would be further reduced and the experiment/theory discrepancy larger.

The gold plasma is presumed homogeneous. As can be seen in figure 5.3.1 density structure exists in the low density layer on the scale of $\sim 1.0 \mu m$. As soon as the gold is heated it will start to expand and fill the voids. This will occur in a time given by the expansion velocity divided by the density structure scale length, L. This time is given by (see sub-section 4.2, equations 4.2.11 - 13);

$$\tau \simeq L \sqrt{\frac{2 m_i}{Z k T_e}} \qquad 5.4.3$$

which numerically is ($Z = 10$, $kT = 100eV$) $\simeq$ 50ps. The gold must initially be heated for the expansion to occur. A feedback situation may exist in which the initial density structure inhibits the conduction (and hence preheat) by space charge effects which in turn prolongs the existence of the density structure.

It is likely that all of the above effects contribute to the enhanced inhibition , although the density structure would seem to be the only mechanism capable of such a great increase in the resistivity. Initially the effect will be to reduce the effective area through which the current flows by a factor $\sim$ the ratio of the solid to low density to the two thirds power.The factor will aproach unity as the gold expands.

The important feature is that the inhibition _is_ great and hence potentially useful for preheat reduction.

CHAPTER 6

ABLATION STUDIES AT 0.53μm

This chapter describes a measurement of the thermal burn rate with 0.53μm illumination. The layered overlay technique, previously developed (22) for use at 1.06μm , was applied in spherical and plane geometries. The burn rate was found to be roughly. three times greater with 0.53μm illumination than with 1.06μm . The hydrodynamic simulation Medusa was used to model these results and it is concluded that inhibition of thermal flux is greatly reduced at the shorter wavelength.

As well as an increased burn depth, the recombination continuum emission was more intense than for 1.06μm . This was seen to significantly photoionise layered fluor targets.. A simple calculation is used to estimate the preheat level.

6.1 Previous work at 1.06μm .

As discussed in sub-section 1.3, much evidence exists to the effect that the thermal transport at high intensities is less than predicted by classical diffusive transport. Several experiments have been carried out at 1.06μm (21,22,23,51,84) but little data exists at 0.53μm . We will first describe some of the 1.06μm work, in particular a layered overlay technique which is applied in this 0.53μm experiment.

The main observables from which deductions have been made about the thermal conductivity are:

i) The continuum electron temperature in the X-ray luminous region (22).

ii) Ion velocity spectra from charge collectors (Faraday cups) and charge analysers (2 3).

iii) Time history of transparency of thin foils (21) and radial heat conduction (84).

iv) Density in X-ray luminous region from spectral line shapes of characteristic X-ray lines (22).

v) Burn depth measurements from relative strengths of characteristic X-ray emission in layered targets (22).

vi) Measurements of implosion velocity in spherical compressions (51).

In all cases the observables are compared with predictions based on numerical simulations. In general one or more free parameters within the simulation are varied to obtain consistent fits to experimental data.

In (24) however an attempt was made to model various experiments (at $1.06\mu m$ and $10.6\mu m$) without invoking a flux limit but including the ponderomotive force. Indeed in the examples cited, the ponderomotive force can reduce the ablation rate via density profile steepening sufficiently to explain the observations of foil transparency and ion velocity spectra, but it is difficult to see how the ponderomotive force could reduce the thermal wave velocity. In (22), the penetration of the thermal front is given by the thickness of overlay required to supress thermal X-ray emission from the massive substrate. In the simulations of such experiments a thermal flux limit of $\sim 3\%$ is required to explain the small burn depths, which could not be reproduced with only the ponderomotive force.

The most direct evidence for thermal inhibition is the radial size of the hot region in plain target interactions. In (84) a $50\mu m$ focal spot size was shown to produce a plasma of similar dimensions. Model simulation (using classical flux-limited thermal transport) predicted an emitting region considerably enlarged by radial conduction. Consistent simulations were obtained when a thermal flux limit was included. Figure 6.1.1 shows the X-ray micrograph profile and predictions of the same.

In (21), the radial burn velocity was determined by temporally resolving the radial evolution of the burn hole produced in a thin poly-styrene foil, by streaking the spatial extent of the transmission of a backlighting ruby ($0.69\mu m$) laser. Similarly a two dimensional numerical simulations predicted too large a hole and the reduced burn rate was attributed to ion acoustic turbulence.

Lastly in (22) the thermal penetration depth was directly measured by determining the Al overlay thickness required to supress the thermal X-ray emission from a thick underlying layer of Si (SiO). Figure 6.1.2
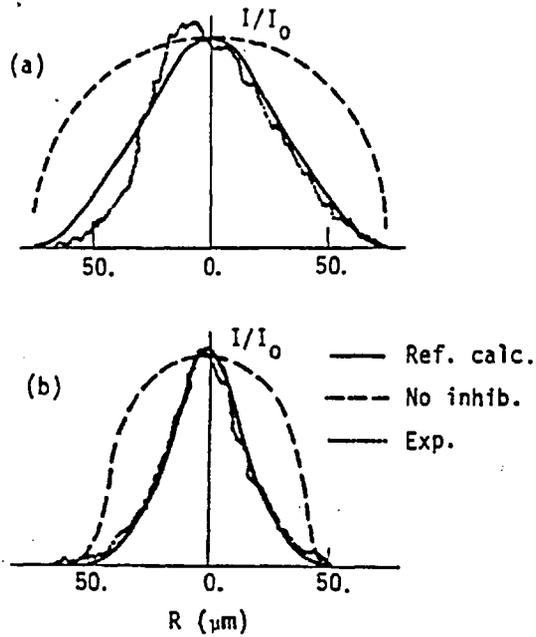
X-ray spatial profiles transverse to the beam
direction: (a) 80-μm spot size with 6.2-J, 60-psec
pulse; (b) 34-μm spot size with 11-J, 70-psec pulse.

Figure 6.1.1 The calculated and measured spatial extent of X-ray emission from a tight focussed laser plasma interaction (reproduced from 84).
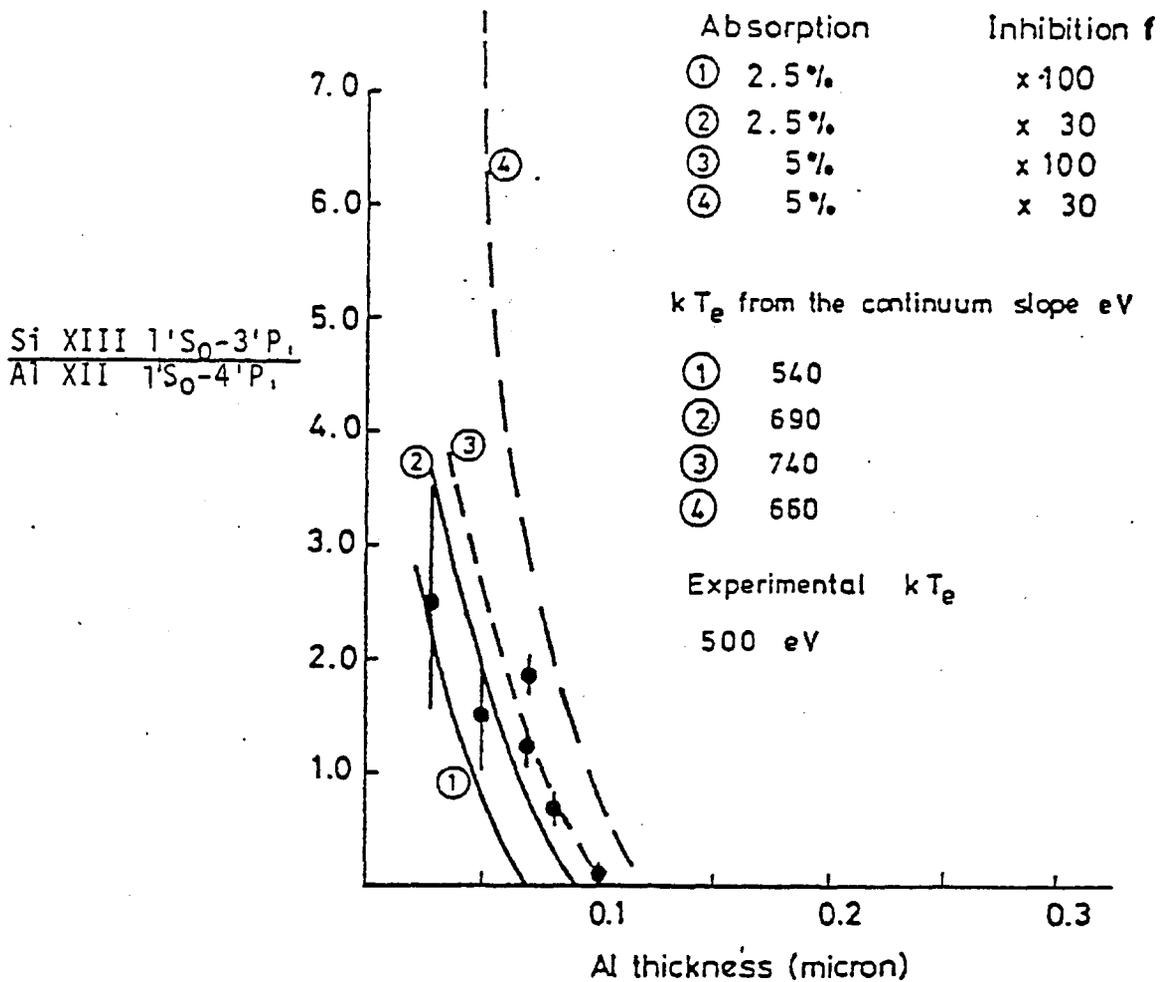

Figure 6.1.2 The ratio of Si to Al emission as a function of Al overlay thickness (reproduced from 22).
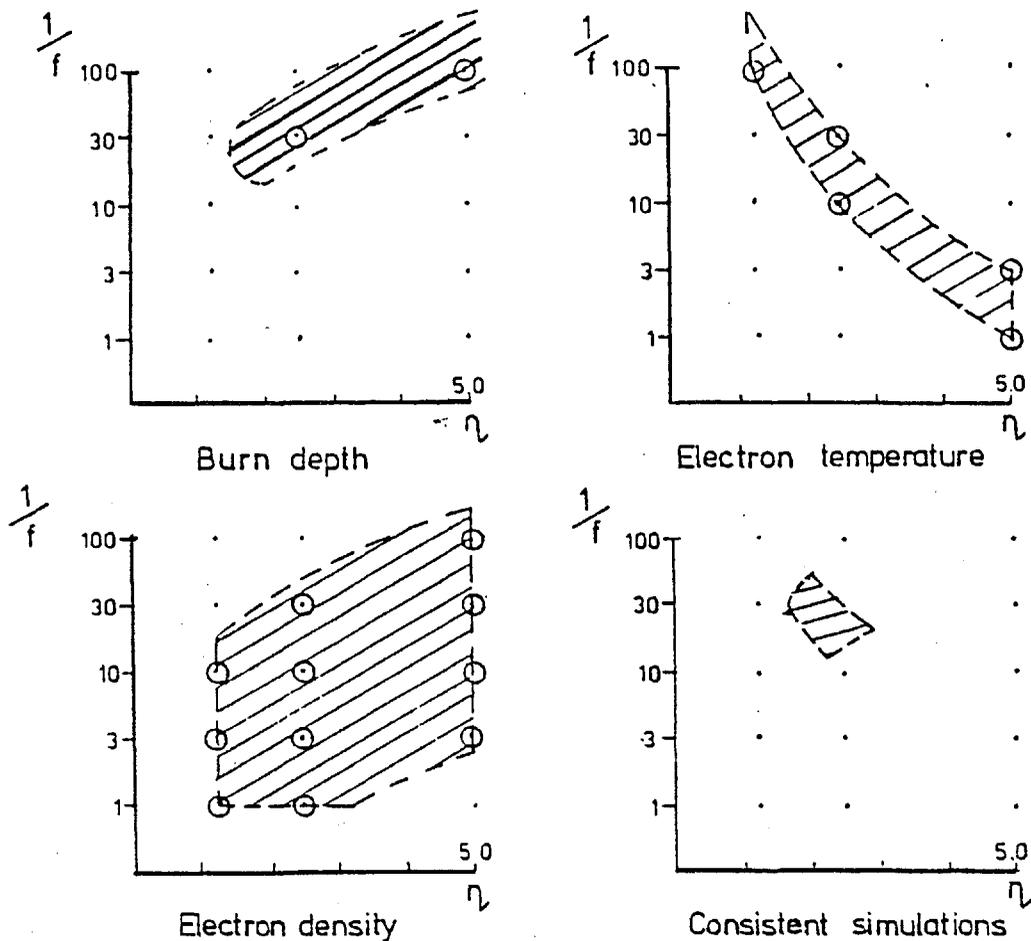
Figure 6.1.3 The results of fitting Medusa simulations to the burn depth experiment from (22).

shows the ratio of Si to Al emission as a function of Al overlay thickness. The experiment was performed in both spherical and plain geometry thereby eliminating any gross (i.e. on a length scale comparable to the spot size) magnetic field effects.

The experiment was interpreted via the 1D hydrodynamic simulation Medusa (85). The observables to which simulations were fitted were the Al/Si X-ray intensity ratio, the recombination continuum slope temperature and the electron density determined from Stark broadening of characteristic X-ray lines originating from the region of peak emission. The free parameters in the simulation were η_A, the fraction of laser energy absorbed by the thermal plasma and f, the factor by which the classical free streaming flux limit was reduced. Each given experimental parameter defines an area in f, η_A space in which consistent simulations are obtained. The overlap of these regions gives $\eta_A \simeq$ 2.5% and f ≃ 0.03 (22). This is depicted in figure 6.1.3

6.2   Existing work at 0.53μm

In (18) the reflectivity and front and rear ion emission from thin foils were measured at 1.06μm and 0.53μm as a function of foil thickness. In addition the hard X-ray (fast electron Bremsstrahlung) continuum was monitored. A characteristic foil thickness for each wavelength was determined above which the rear ion emission became significantly reduced with respect to the front and the reflectivity saturated. This was equated to the burn depth. The ion emission is a convolved diagnostic of burn depth since it is dependent to a large degree on fast electrons (with a large range compared with the burn depth). Also such a thin foil will be accelerated over many spot sizes in the duration of the pulse, enhancing two dimensional effects e.g. 'stretching' of the foil reducing its effective thickness. However a consistent burn depth was determined from each of the diagnostics, albeit rather larger (for 1.06μm) than in (22). The burn depth at 0.53μm was significantly increased (by almost a factor of 2) and there was more efficient laser light absorption. The results are summarised in figure 6.2.1.

Other workers (86) have observed more efficient coupling of laser energy at shorter wavelength and earlier discussion (sub-section 1.3) suggests an enhanced mass ablation rate. This would indicate that a shorter wavelength is desirable for fusion. In view of the above the layered target technique described in (22) (as above) has been applied in the case of 0.53μm illumination.

Laser intensity	d_T (μm)	d_{i1}(μm)	d_{i2}(μm)	d_x(μm)
ω				
$(2\text{–}4)\times10^{14}$ W/cm²	0.11	0.12	0.20	0.11
	$(0.22)^a$	$(0.22)^a$	$(0.22)^a$	
	$(0.32)^b$	$(0.67)^b$	$(0.43)^b$	
ω				
2×10^{15} W/cm²	0.22	0.17	0.32	0.15
	$(0.44)^a$	$(0.46)^a$	$(0.60)^a$	
	$(0.70)^b$	$(2.0)^b$	$(1.5)^b$	
2ω				
10^{15} W/cm²	0.43	0.30	0.50	0.35
	$(0.9)^a$	$(0.75)^a$	$(1.5)^a$	
	$(1.4)^b$	$(2.2)^b$	$(2.0)^b$	

[a] With flux limit number $f = 0.05$.

[b] With flux limit number $f = 1.0$.

Experimental values of characteristic foil thicknesses d_T, d_{i1}, d_{i2}, and d_x (in microns). The values in parentheses represent the corresponding results obtained in simulations without fast electrons.
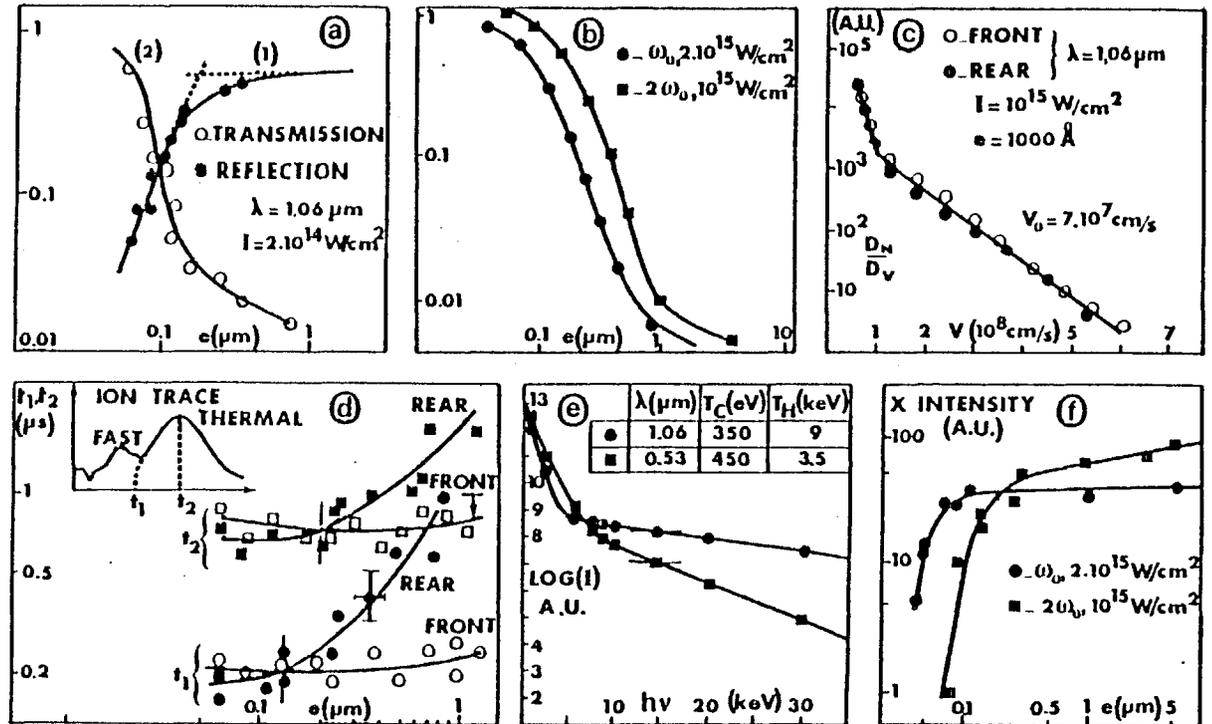
(a) Reflection coefficient (curve 1) and transmission coefficient (curve 2) variation vs foil thickness. (b) Transmission-coefficient variation with foil thickness at ω_0 and $2\omega_0$. (c) Front and rear ion-velocity spectra shown for two symmetric charge collectors (A.U. : arbitrary units). (d) Front and rear ion times of flight t_1 and t_2 vs foil thickness. $\lambda = 1.06\,\mu$m, $I = 2\times10^{14}$ W/cm², and distance to target 45 cm. (e) X-ray spectra at $1.06\,\mu$m ($I = 2\times10^{15}$ W/cm²) and at $0.53\,\mu$m ($I = 10^{15}$ W/cm²). (f) Relative intensity of x rays of 1–2-keV energy vs foil thickness for both wavelengths.

Figure 6.2.1   A summary of the experimental comparison of $1.06\,\mu$m and $0.53\,\mu$m illumination of (18)

6.3   The experiment

Targets as illustrated in figure 6.3.1 were irradiated with
$\sim$ 3J of 0.53μm illumination in an 80ps pulse. The focal diameter,
determined by spherical aberration,was 85μm. This was confirmed by
pin hole X-ray pictures. The intensity was thus $\simeq$ 7 x 10^{14}w.cm^{-2}.
The experimental set up was as described in sub-section 4.3. The essence
of the experiment was to monitor the relative strengths of Al and Si
X-ray emission as a function of Al overlay thickness. This was performed
for both plane (figure 6.3.1a) and spherical (figure 6.3.1b) targets.
The lines chosen for comparison were $Si(1^1S_0 - 3^1P_1)$ and $Al(1^1S_0 - 4^1P_1)$
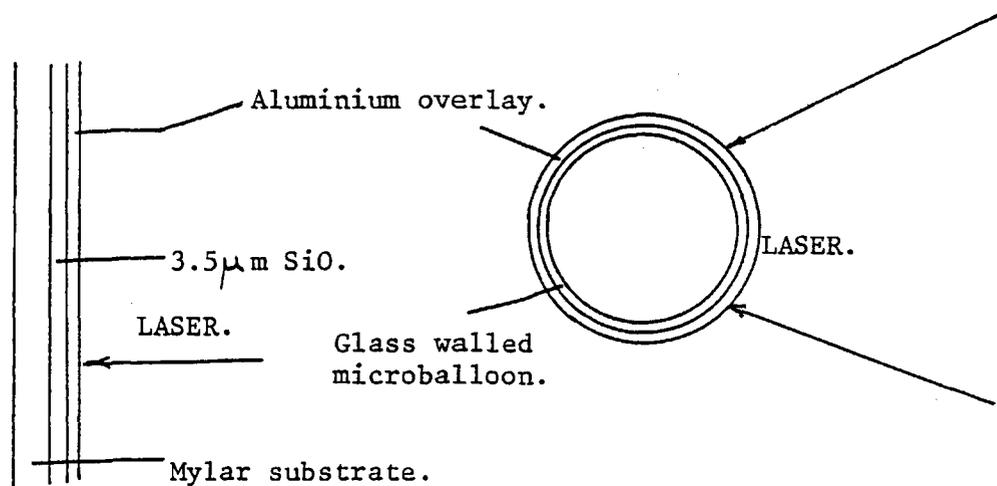
Figure 6.3.1   The spherical (a) and plane (b) targets used in the
0.53μm thermal transport experiment.

$Al(1\,^1S_o - 4\,^1P_1)$
(6.316 Å)

$Si(1\,^1S_o - 3\,^1P_1)$
(5.683 Å)

Shot number 06080379.

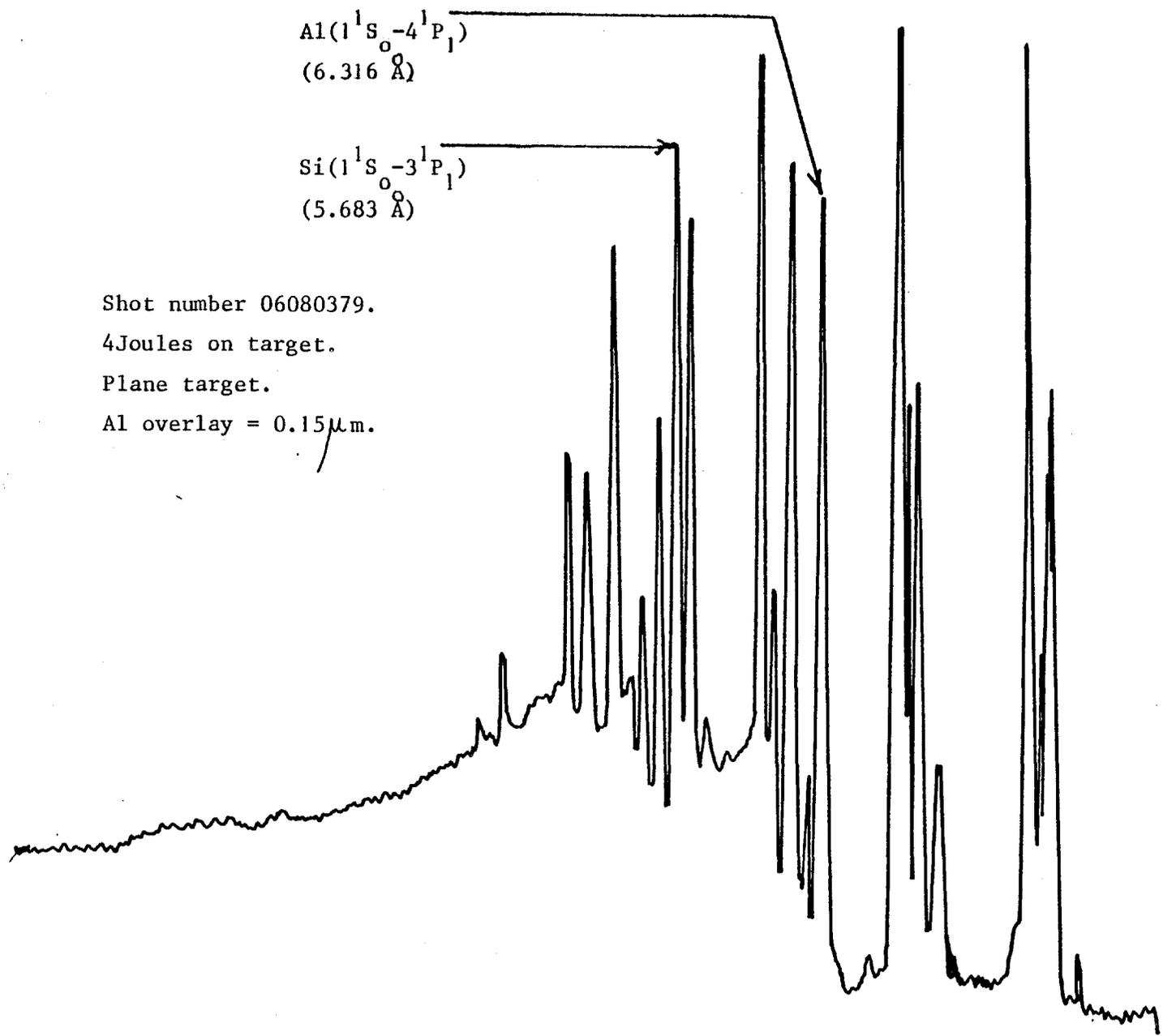4Joules on target.

Plane target.

Al overlay = 0.15 μm.

Figure 6.3.2 A typical microdensitometer tracing from the front spectrometer.

lying at 5.683Å and 6.314 Å respectively. The closeness of the lines eliminated any possible errors arising from differential absorption effects, the spectral film response and the reflectivity of the crystal.

Figure 6.3.3 The ratio of Si to Al emission vs Al overlay thickness

Al overlay thickness (μm)
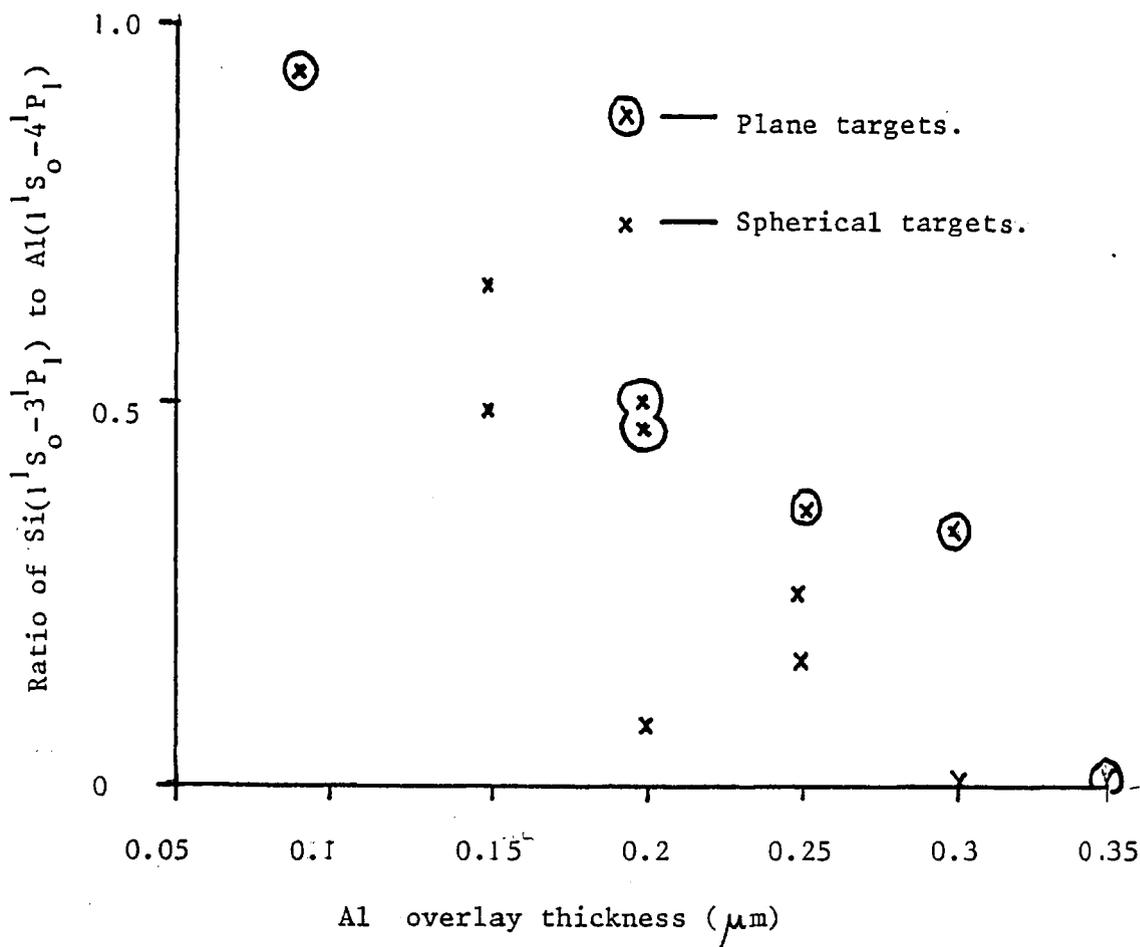
In this experiment the rear spectrometer, having a germanium crystal (2d = 4.00Å), monitored only the hydrogen and helium like recombination continuum for hν > 3.4keV. The front spectrometer, with a P.E.T. crystal (2d = 8.74Å) recorded the helium and hydrogen like spectra of Al and Si together with their recombination continua.

A microdensitometer tracing of a typical spectrum is shown in figure 6.3.2 together with target and laser details.

Targets as in figure 6.3.1, with Al overlays in the range 0.09μm to 0.4μm, were irradiated. An overlay thickness of 0.4μm was sufficient to completely supress Si emission in both plane and spherical targets. The Si/Al line ratio as a function of overlay thickness for plane and spherical targets is shown in figure 6.3.3 together with the intensity.

The temperature in the emitting region was determined from the slope of the Si recombination continuum. This continuum signal, converted into dimensionless units is plotted against $h\nu$ in figure 6.3.4. Also shown is the continuum produced by 1.06μm illumination on a similar target. The 0.53μm incident energy was 3 J whereas the 1.06μm energy was 20 J.
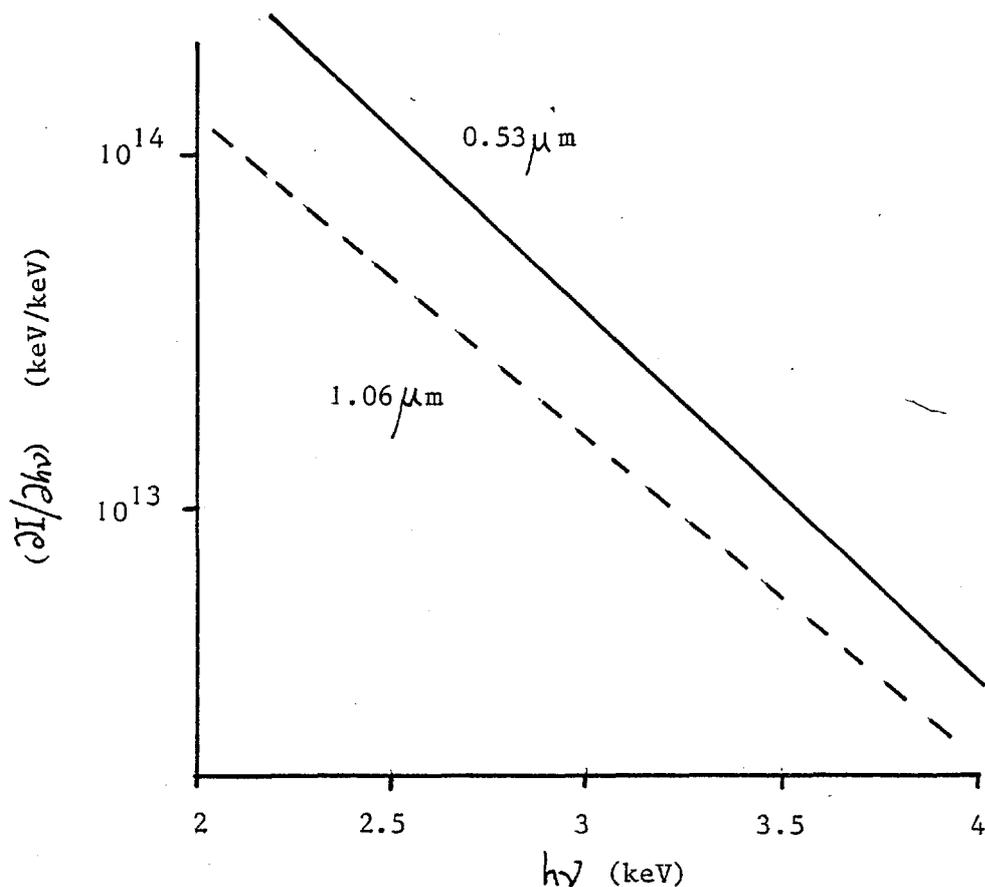
Figure 6.3.4 The absolute recombination continuum emission for 3 Joules of 0.53μm light and 20 Joules of 1.06μm light incident on aluminium.

The intensity of the X-ray continuum with 0.53μm illumination is much greater than with (more) 1.06μm illumination. This is a result of the greater burn depth leading to a larger emitting volume and the higher density associated with the shorter wavelength giving a higher X-ray emissivity.

The intensity of the 0.53μm illumination was $7 \times 10^{14} \text{wcm}^{-2}$ whereas at 1.06μm it was $2 \times 10^{15} \text{wcm}^{-2}$. In (87) the thermal continuum temperature as a function of irradiance is given for the same experimental set up but at 1.06μm. The temperature at $7 \times 10^{14} \text{wcm}^{-2}$ was $400 \pm 30\text{eV}$,

possibly slightly lower than the 420 ± 30eV observed at 0.53μm .

It is difficult to give a quantitative interpretation of the increased emission without the use of a numerical simulation because of the complicated density and temperature structure in the interaction region. However it is apparent that the increased emission will lead to a higher radiative preheat level in the target (see sub-section 6.5).

6.4   Comparison with numerical simulation

i)   The simulation

The hydrodynamic simulation Medusa was used to interpret the burn depth and thermal continuum measurements. The one-dimensional spherically symetric Lagrangian simulation uses a perfect gas equation of state and assumes full ionisation. For the purposes of this experiment, fast electron production and transport was omitted and the absorption of the incident light was-characterised by η_A, the fraction of the incident power dumped into the thermal plasma at the critical density surface.

Flux limited classical diffusion transport was used. Spitzer transport coefficients with arbitrary multiplying constants were assumed. The simulation was run in two modes, one in which the flux limit only was varied and the other in which both the flux limit and the thermal conductivity k were varied (by the same constant, f).

The experimental observables to which the simulation was fitted were the time integrated recombination continuum temperature and the ratio of Si to Al line emission. The simulation calculates these variables by assuming the upper levels to be in L.T.E. with the ground state of the next high stage of ionisation (22).

The free parameters of the simulation, η_A and f have different effects on the observables. At a fixed absorption, η_A, increasing the flux limit (i.e. reducing the heat flow) will reduce the thermal penetration depth, and hence the Si/Al line intensity ratio, and will increase the continuum temperature since the same energy is dumped into a lower mass of plasma. Increasing η_A at a fixed f, however, increases both the continuum temperature and the Si/Al line ratio, since a higher absorption will give a higher temperature and hence deeper thermal penetration. Thus consistent simulations are only obtained for particular values of f and η_A.

The thermal transport is described by the thermal conductivity, k , and the free streaming heat flux, Q_{max} . The heat flux is given by:

$$Q = \min \left(-k \nabla T_e , Q_{max} \right) \qquad \underline{6.4.1}$$

The free streaming limit or heat flux is the peak heat flux which can be carried by a distribtuion of electrons streaming at its thermal velocity:

$$Q_{max} = B \left(n_e k T_e \right) . \left(\frac{2 k T_e}{m_e} \right)^{1/2} \qquad \underline{6.4.2}$$

Where B is a constant of order unity, dependent on the electron distribution function.

In the simulation, to avoid a discontinuity, Q is taken as the harmonic mean of the two terms in equation $\underline{6.4.1}$.

As mentioned above the simulation was run in two modes, one (mode 1) in which:

$$Q = H.M. \left\{ -k \nabla T_e , f Q_{max} \right\} \qquad \underline{6.4.3}$$

and in the other (mode 2):

$$Q = H.M. \left\{ -f k \nabla T_e , f Q_{max} \right\} \qquad \underline{6.4.4}$$

A series of simulations was performed in each mode covering the range $\eta_A = 0.05$ to 0.25 and f = 1 to 1/100. This range of variables produced simulations covering the experimental results.

ii) Simulation results

To avoid 2 dimensional effects the shots onto microballoons were selected for comparison with the simulation. The experimental results are characterised by the continuum temperature, T_c, and the burn depth. The burn depth, t_B, was taken as the overlay thickness for which the Si/Al line intensity ratio was 0.5, this being the mid-point of the range

(a).

(b).
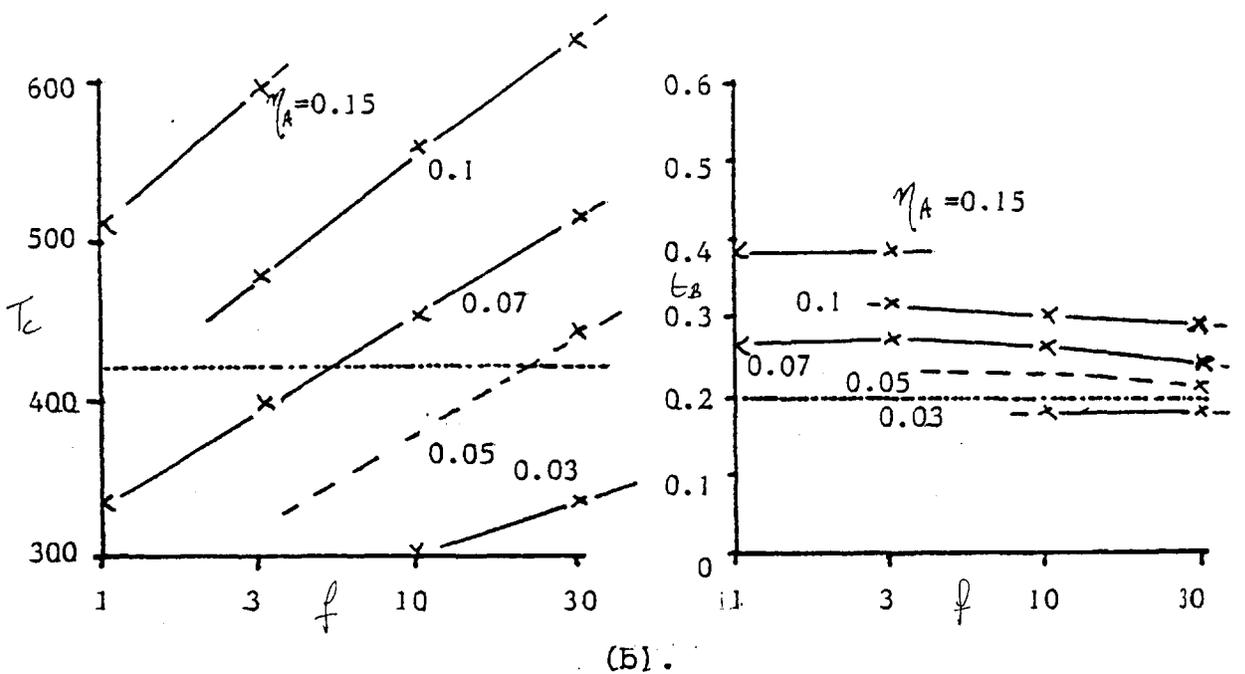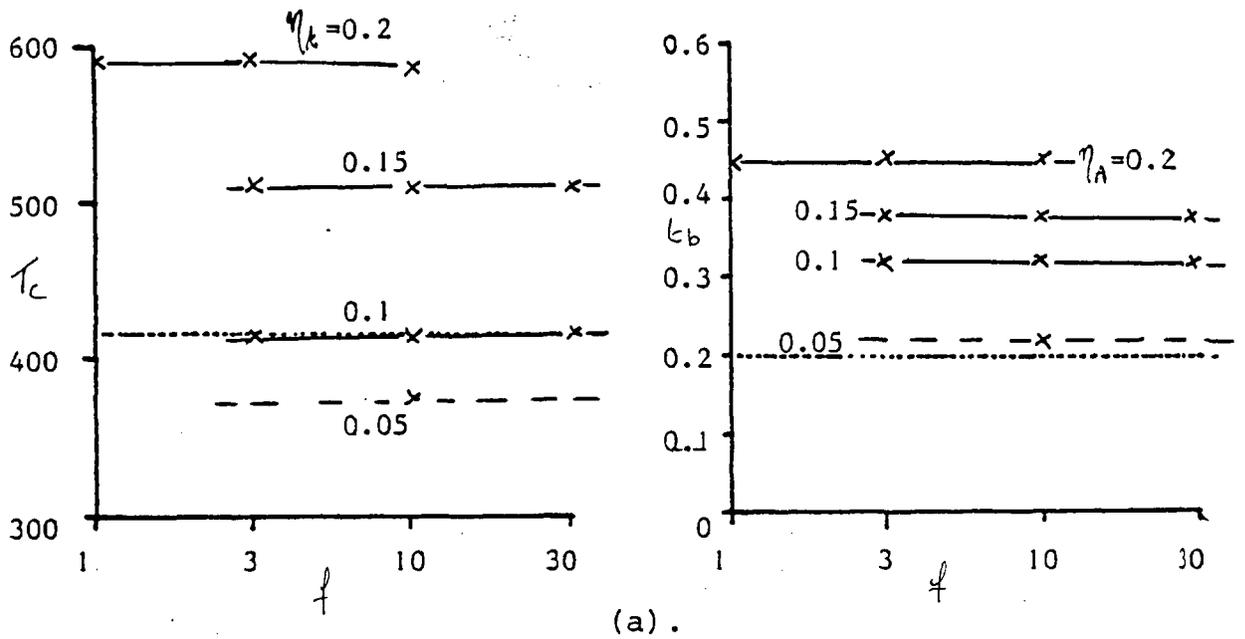
————————— - Experimental values of T_c and t_B.

——————————— - Simulation predictions.

— — — — — - Extrapolated simulation results.

Figure 6.4.1 The experimental continuum temperature and burn depth together with mode I (a) and mode II (b) simulation results.

of variation of the ratio. Figure 6.4.1 shows the experimental and simulation results in terms of T_c and t_B. Inspection shows that the burn depth is governed dominantly by η_A, and the temperature is dependent on both η_A and f. The mode 1 simulations were virtually independent of f in the range 1 to 1/30. This was because the maximum temperature gradient in the simulation was only able to drive a heat flux very much less than Q_{max}, i.e. the region of flux limitation was only reached for a very severe flux limit.

In mode 2 simulations, R was also varied and a greater dependence on f is evident in the simulation results.

It was found that only mode 2 simulations could be fitted to the experiment without the use of a very severe flux limit (i.e. f > 1/100). Figure 6.4.2 shows a matrix of the mode 2 simulations performed together with the 'allowed' regions defined by the experimental results.

Figure 6.4.2 The regions of good experiment/simulation agreement defined by the continuum temperature and burn depth

f^{-1}
(flux limit)

η_A (absorption)

Fitting by burn depth.

Fitting by continuum temp.

Region yielding consistent simulations.
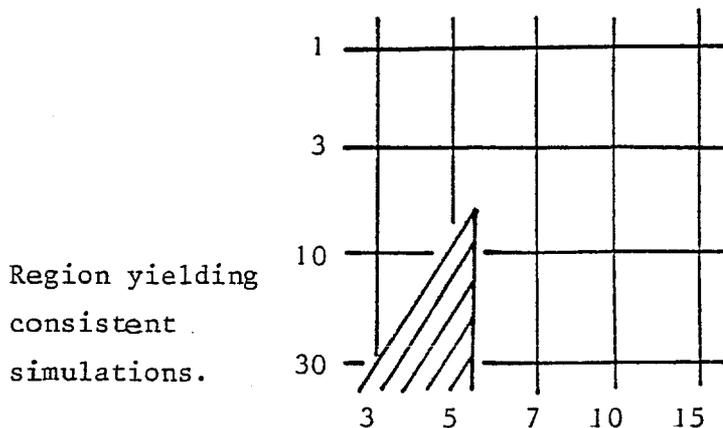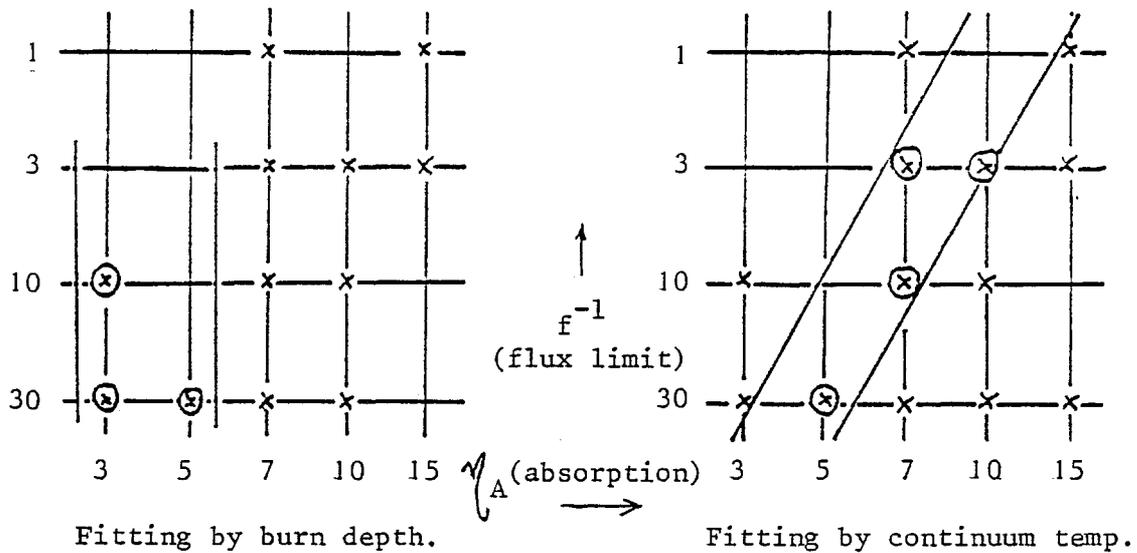
The absence of any significant dependence on f in the mode 1 simulations indicates that the flux is very much less than Q_{max}. The region of good fit in figure 6.4.2 is defined by f = 30 and η_A = 4 ± 1%. The thermal flux is evidently greatly inhibited even when the flux is very much less than Q_{max}. In this regime the electron mean-free-path is much less than the temperature gradient scale length so one would expect classical theory to be accurate. This suggests that some mechanism (e.g. turbulence) is responsible for a reduced mean free path and hence a low thermal conductivity.

The simulations performed in (18) required a large flux limit to approach the experimental results. A very large flux limit was required to reproduce the thermal penetration depth in foils and this was attributed to experimental 2-dimensional effects, lacking in the simulation. The absorption in the simulation was not a free parameter and was set at 10%. Our results suggest that this is rather high and this further explains the large predicted burn depth. The final conclusion that a flux limit comparable to the 1.06μm case exists with 0.53μm illumination compares favourably with our results although it is not clear if Q_{max} or Q_{max} and $\hat{R}$ were varied in the simulations.

6.5   Radiative preheat with 0.53μm illumination

As mentioned previously an enhanced thermal continuum signal is produced with 0.53μm illumination. This leads to significant radiative preheat (88) deep in the target. Indeed an attempt was made to observe fast electron preheat within the target by means of layered targets, however the radiation pumped Kα yield dominated so no useful conclusions could be drawn. This does not imply that the radiative preheat exceeded the fast electron preheat since radiation is far more efficient at K ionisation than electrons (see sub-section 2.3).

The pin diode array, as in sub-section 3.1, recorded Bremsstrahlung emission although the recording was rather irreproducible. The slope of the continuum gave T_H in the range 2 - 5 keV.

We will now roughly calculate the energy deposition within the target due to the continuum emission reported in sub-section 6.3. Let the continuum emission be $\partial I / \partial h\nu$ J.sr^{-1}keV^{-1}. It is assumed that the energy carried by the continuum at hν is deposited at a depth t such that:

$$t \cdot \frac{\mu_{h\nu}}{\rho} \cdot \rho = 1 \qquad 6\cdot5\cdot1$$

where $\mu_{h\nu}/\rho$ is the mass attenuation coefficient of the target material at photon energy $h\nu$. If the focal area is A then the energy deposition at a depth t is:

$$U = \frac{2\pi}{A} \cdot \frac{\partial I}{\partial t} = \frac{2\pi}{A} \cdot \frac{\partial I}{\partial h\nu} \cdot \frac{\partial h\nu}{\partial t} \qquad 6\cdot5\cdot2$$

Now the mass attenuation coefficient is well approximated by (89):

$$\frac{\mu_{h\nu}}{\rho} = \frac{C}{(h\nu)^3} \qquad 6\cdot5\cdot3$$

in an energy region free of absorption edges. Thus:

$$U = \frac{2\pi}{A} \cdot \frac{C\rho}{3(C\rho t)^{2/3}} \cdot \frac{\partial I}{\partial h\nu}\bigg|_{h\nu = (tC\rho)^{1/3}} \qquad 6\cdot5\cdot4$$

Typically, with $\sim 5J$ of green light incident on SiO, the continuum emission in the range 2-6 keV was $I_\nu \simeq 0.4 \exp(-h\nu /0.42)J.sr^{-1}. keV^{-1}$, where $h\nu$ is in keV, the pulse length was 80ps and the focal diameter was $85\mu m$. At a depth of $2\mu m$ in SiO equation 6.5.4, gives an energy deposition of $\simeq 10^6 Jcm^{-3}$ which is equivalent to $\sim 100ev$ per atom. This represents a significant preheat (see sub-section 7.3) however at a depth of $10\mu m$ the energy deposition has dropped to $\simeq 1eV$ per atom. These energy depositions are strongly dependent on the X-ray absorption characteristics of the target material, so to predict true radiation preheat levels a more elaborate calculation is required. However it is clear from the above that the effect is significant, especially in view of the very low adiabat required for a good implosion (7,8).

The same is true for $1.06\mu m$ illumination but the decreased continuum emission coupled with the greater fast electron preheat reduces the importance of radiation preheat.

6.6 Conclusion for 0.53μm illumination

In summary the shorter wavelength has been shown to result in a higher ablation pressure and a lower fast electron temperature than 1.06μm . The ablation pressure is roughly given by:

$$P_{AB} = \dot{M} \bar{v}_T \qquad \underline{6 \cdot 6 \cdot 1}$$

where $\dot{M}$ is the mass ablation rate per unit area and $\bar{v}_T$ is the thermal velocity of the ions. A burn depth of 0.1μm in Al for 1.06μm illumination at 2 x 10^{15}w.cm^{-2} gives P_{AB} = 1.3 Mbar. For 0.53μm illumination at 7 x 10^{14}w.cm^{-2} the burn depth was 0.25μm giving P_{AB} = 3.2 Mbar. In both cases the ablation plasma was assumed to be at 500eV.

This calculation is inaccurate in that it assumes that there is steady state ablation flow. The pulse length of 80ps is rather short for this to occur but since this is true for both 1.06μm and 0.53μm it is clear that the improvement at the shorter wavelength is considerable especially since the intensity is 1/3 that at 1.06μm and also pressure saturation would be expected to occur at a higher intensity than for 1.06μm .

There is some evidence (see figure 6.3.3) that the burn depth is greater in the spherical geometry irradiations.This could could be a feature of radial divergence in the spherical case leading to better penetration of the laser light to the critical density surface, also this could lead to better ablation again due to divergence effects.Whatever the cause it is evident that one must use similar geometries for experiment and simulation.

The lower fast electron temperature (as observed in (18)) indicates that the preheat range will be greatly reduced since r_A is roughly proportional to T_H^2. The coupling into preheat has unfortunately not been measured due to a poor choice of layered targets however the X-ray continuum reported in (18) suggests it is comparable to that at 1.06μm . Since the range is low the preheat pressure will be high, contributing to the ablation pressure, indeed the dividing line between the thermal

and suprathermal distributions is fine at such a low suprathermal
temperature.

CHAPTER 7

A DISCUSSION OF ABSORPTION MECHANISMS, ENERGY BALANCE AND THE
RELEVANCE OF THIS WORK TO INERTIAL CONFINEMENT SCHEMES

Various absorption mechanisms are described and in the light of the
pulse length and intensity scaling at $1.06\mu m$ it is concluded that with
short pulses at an intensity of $\sim 10^{15} w.cm^{-2}$ resonance absorption
dominates, becoming less important as the pulse length increases.

The energy balance between preheat, ablation and fast ions is
discussed and the results of the pulse length scaling experiment indicate
that preheat will be less of a problem than anticipated with long
pulses.

The observed enhanced thermal penetration rate at $0.53\mu m$ is
interpreted as resulting in a higher ablation pressure and hence more
efficient coupling into the target momentum. Together with the reduced
fast electron preheating this indicates that a laser compression scheme
is best driven by a short wavelength laser. However a possible application
of resistive inhibition is to screen the fuel from preheat in a long
wavelength fusion scheme in which fast electrons are the main driver.

7.1 Absorption mechanisms

i) Inverse Bremsstrahlung

Inverse Bremsstrahlung is the collisional damping of an E.M. wave
propogating in an underdense plasma. Incident electromagnetic energy
is converted into the kinetic energy of electrons quivering in the
oscillating electric field. This energy is turned to random, thermal
energy by collisions with the relatively slow moving ions. The absorption
coefficient per unit length (90) is:

$$\mu (cm^{-1}) = \frac{1.39 \times 10^{-15} \times n_e^2 . Z}{T_e^{3/2} \left(1 - \frac{n_e}{n_c}\right)^{1/2} n_c} \qquad 7.1.1$$

where T_e is in eV. The temperature dependence, coming directly from the collision frequency, serves as a cut-off on the heated plasma temperature since at high temperature μ becomes small. Moreover the scale length for the absorption mechanism, μ^{-1}, is large with respect to likely density gradient scale lengths in short pulse interactions (see equation 4.2.13.). In 100ps the plasma will have expanded to $\sim 10\mu m$, assuming $Z = 10$, $M_a = 20M_p$, $\lambda = 1.06\mu m$ and $T_e = 500eV$. The characteristic inverse Bremsstrahlung absorption distance for $n_e = n_c/2$ is $\sim 25\mu m$. When the density gradient scale length becomes sufficiently large for inverse Bremsstrahlung to be important then backscattering is high. Inverse Bremsstrahlung does not contribute greatly to the absorption of $1.06\mu m$ illumination at high intensity (i.e. $I \gtrsim 10^{14} w.cm^{-2}$).

ii) Resonance absorption

Resonance absorption occurs when p polarised light is incident obliquely on a plasma with a non zero density gradient. Incident energy is coupled to resonant plasma oscillations at the critical density surface, where the local electron plasma frequency equals the laser frequency. Large amplitude electrostatic oscillations build up. The spatial extent of the resonant region is determined by the density gradient scale length around critical. Energy is released from these oscillations either by collisional damping (linear resonance absorption) or (more importantly) when the peak electric field reaches a sufficiently high value that an electron can be accelerated through the resonant region within one cycle of the oscillation, thus aquiring a net velocity. This process is referred to as electron trapping or wave breaking and is a frequently occuring saturation mechanism in unstable plasma oscillations.

A linear theory of resonance absorption is given in (91). The absorption peaks at $\sim 50\%$ for an angle of incidence Θ such that (33):

$$\sin^2 \Theta \left(k_0 L \right)^{2/3} = 0.6 \qquad \underline{7.1.2}$$

where k_0 is the vacuum wave number and L the density gradient scale length. The absorption goes to zero as $\Theta \rightarrow 0$ (no normal component to the electric field) and as $\Theta \rightarrow \frac{\pi}{2}$ (the maximum distance of penetration into the density ramp is too far from critical for tunnelling to occur).

Various theories (11,12,92,93) predict scaling laws for the temperature of the heated electron distribution. All predict a dependence of the form:

$$T_H \propto \left(I \lambda^2 \right)^N \qquad \underline{7 \cdot 1 \cdot 3}$$

where N is in the range $\frac{1}{4}$ to $\frac{2}{3}$

In experimental conditions radiation will be incident over a range of angles and polarisations. This would be expected to smear out the angular dependence. Experimentally absorption <u>is</u> observed at normal incidence, however a peak at a specific non-normal angle of incidence is also seen (11,12).

The growth time for the resonance is of the order of $100/\omega_0$ (93) or about 0.05ps, very much shorter than typical pulse lengths.

The peak absorption is independent of L (91), however the angular width of the peak becomes narrower for large L. Since the overall absorption is averaged over a significant range of angles, a small L is vital for efficient absorption.

iii) <u>Parametric processes</u>

Electromagnetic radiation can be absorbed by the parametric coupling of the incident wave to two or more other modes existing in the plasma. The coupling occurs when there is an intense driver field at the sum or difference frequency of the driven modes (82). The driven modes can be electromagnetic, ion acoustic, electron acoustic or electrostatic. An example is the parametric decay instability in which a photon decays into an ion acoustic wave and an electron acoustic wave. Unfavourable instabilities are those which backscatter the incident radiation e.g. Raman and Brillouin scattering in which the incident photon couples to a backscattered photon of lower energy and a plasmon (electron acoustic wave) or an ion acoustic wave respectively. Those instabilities require large scale lengths to produce significant absorption. In order for the instability to becomes effective, it must grow significantly before it is convected away from the unstable region. This leads to a condition on the maximum density gradient above which the mode will not grow. In (94,95) it is concluded that steepening of

the density profile around critical will suppress the decay (81) and oscillating two stream (82) instabilities which must occur near critical. Typical interaction lengths for the backscatter instabilities are around 20 μm , less than those present in short pulse interactions.

iv) Absorption by ion acoustic turbulence

It has been proposed (83) that ion acoustic turbulence in the sub-critical plasma can lead to sufficiently large ion density fluctuations that significant absorption takes place. A large heat flux in this region leads to an opposing flux of low energy electrons to maintain charge neutrality. The distorted distribution function can drive unstable ion acoustic waves which enhance absorption. The mechanism requires an electron ion temperature ratio in excess of 5 (96) (more in an unmagnetised plasma) to avoid ion Landau damping of the unstable waves.

In the numerical calculations of (83) the heated electron distribution temperature behaves as:

$$T_H \propto I \qquad \qquad \underline{7 \cdot 1 \cdot 4}$$

with an assumed self-generated magnetic field of 1MG. In the calculations 20% resonance absorption was assumed, also the background ion acoustic turbulence level was assumed to be high near critical to overcome the problem in (96) that ~ 30 μm was required for the turbulence to build up. Such long scale lengths are not present in short pulse interactions.

v) Discussion

The observed preheat coupling dependence on pulse length is not consistent with absorption mechanisms favouring long density scale lengths. It has been experimentally observed that Raman and Brillouin scattering are significant only for long pulse lengths.(72,96). A similar behaviour is to be expected for the decay and the oscillating two stream instabilities. As pointed out previously, steepening of the density gradient at critical effectively stabilises both mechanisms (95).

Precise box calorimetry measurements of absorption by plane
targets (98) as a function of angle of incidence and polarisation
were interpreted in (28) as originating dominantly from resonance
absorption. The assumption of a moderately rippled critical density
surface was made (rms angle, $\bar{\phi}$ ~ 15°) in view of the small backscatter
fractions observed with a large f number (f/10) focussing lens.

The intensity scaling of the fast electron temperature has been
widely measured via the hard X-ray continuum and also by the layered
fluor target technique described here (3). Figure 7.1.1 shows
collected X-ray data (11) and the 'K$_\alpha$' temperature. Note that here
this pseudo temperature is altered by a suitable factor to enable
comparison with the N = 0 distribution assumed for the analysis of the
X-ray continuum data (see sub-section 4.1). The predicted scaling
laws for T_H of (11,12,92,93) for resonance absorption are shown,
together with the temperature from (83) assuming ion acoustic turbulénce.
The resonance absorption scaling laws fit the data most closely.

Simple analytic theories (11,12,92) for resonance absorption do not
yield the form of the heated distribution function. It is assumed for the
purposes of the calculation. In (11,12) a Maxwellian distribution is
assumed and in (92) a 'top-hat' distribution is assumed, in order to
determine the lowest energy of the hottest electron such that the distri-
bution function supports a given heat flux. The simulations of (38,92)
yield Maxwellian-like distributions, i.e. extending to high energy and
monotonically decreasing with increasing electron energy.

The growth rates for parametric instabilities are intensity depend-
ent.(82) so a marked scaling of the absorption by these mechanisms with
intensity is to be expected. A similar behaviour is observed with
Brillouin scattering, a closely related process (73). The absorption,
dominantly by ion-acoustic turbulence, in (83) scales weakly with intensity.
There was an assumed residual 20% absorption by resonance. This result
matches our measurements of preheat coupling efficienty which shows no
marked intensity dependence, however the reduction in preheat coupling with
increasing pulse length is not consistent with a process which requires
a long density gradient scale-length.

The intensity independence of the resonance absorption fraction (80)
(assuming a fixed density gradient scale length and angular spread at
critical) is in agreement with our measurements. Moreover in (28) it
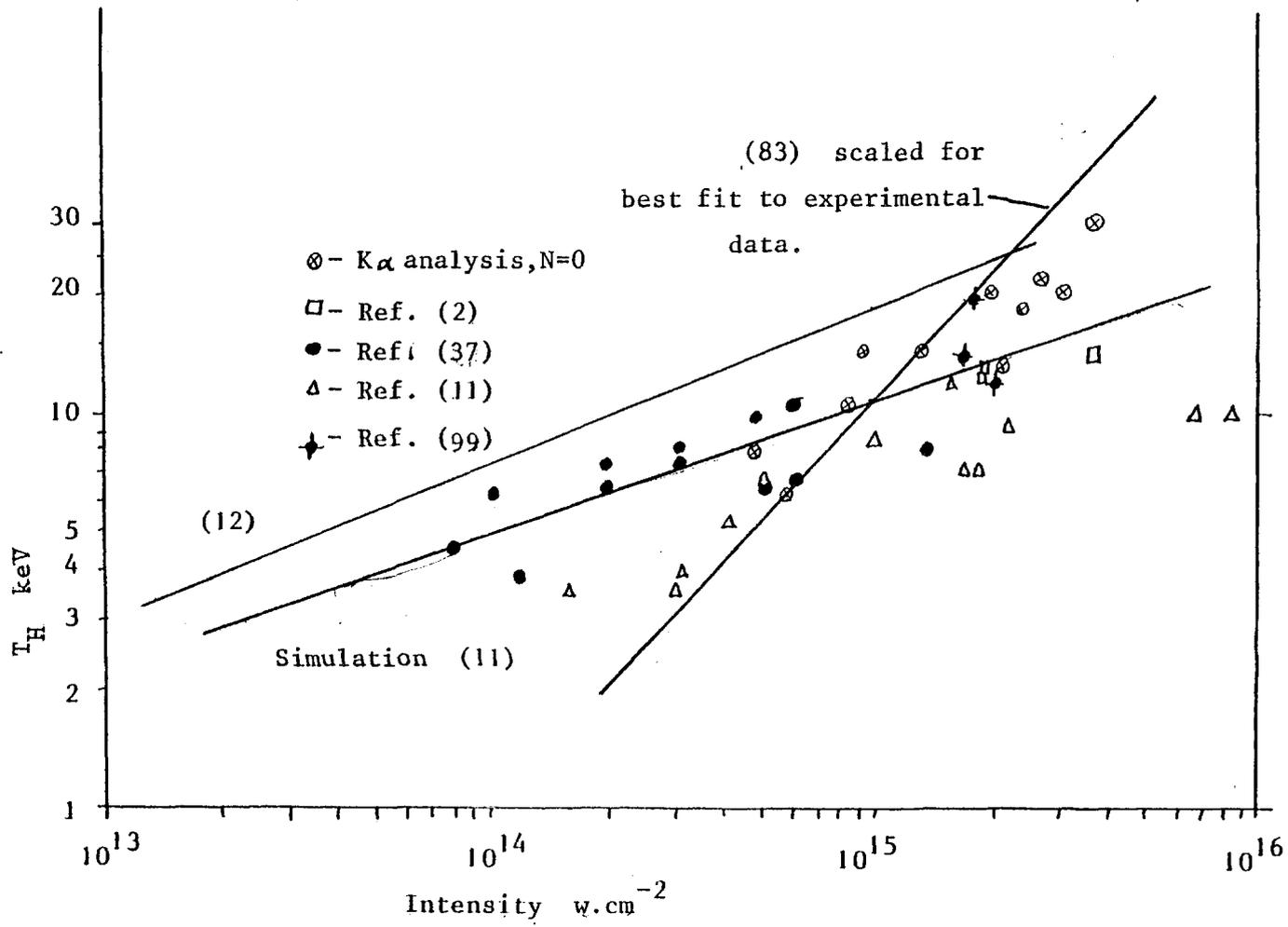was concluded that only 10% absorption was due to unspecified angle and

Figure 7.1.1 The suprathermal continuum temperature, K α temperature and the results of various fast electron scaling laws as a function of intensity.

polarisation independent processes, i.e. processes other than resonance absorption.

It has been observed that the fast electron temperature and hence the preheat is low for 0.53 μm illumination (18,86). Balance between the radiation pressure and plasma pressure for a fixed temperature at the critical density surface occurs at a fixed value of (1 λ^2). The critical density and hence pressure scale as λ^{-2} so profile steepening will be less pronounced at short wavelength. One would expect resonance absorption to be less effective at shorter wavelengths where there is less profile steepening. The observation of reduced preheat at 0.53 μm is consistent with resonance absorption being important at 1.06 μm.

As shown in sub-section 6.3, the absorption into the thermal plasma is higher at 0.53 μm than 1.06 μm . This is evident from the considerably larger burn depths and higher continuum emission observed with (less) 0.53 μm illumination. As pointed out above, longer density gradient scale lengths exist and also the critical density (proportioned to λ^{-2}) is four times higher than at 1.06 μm . Inverse Bremsstrahlung is density dependent via the collision frequency so the typical interaction length for 0.53 μm is 6 μm . (T_e = 500eV, Z = 10, $n_e = n_c/2$). Inverse Bremsstrahlung is thus important and we conclude that absorption mechanisms other than resonance play an increasingly important role at short wavelengths.

7.2 Energy balance

Calorimetry measurements (98,99) indicate a total absorption of 20 - 30% with short 1.06 μm pulses at an irradiance $\sim 10^{15}$w.cm^{-2}. Quantitative fast ion velocity spectra measurements (4) suggest $\sim$ 60% of the absorbed energy appears as fast ions. The theoretical model of (53) supports this.

With 100ps, 1.06 μm pulses at 0.5 - 4 x 10^{15}w.cm^{-2} we observe 7 $\pm$ 3 % of the incident energy as preheat. Measurements of burn depth and thermal temperature indicate that in 100ps at 10^{15}w.cm^{-2} the thermal front penetrates to $\sim$ 0.1 μm in aluminum and the temperature at the point of peak emission is $\simeq$ 500eV. The power density into the ablation process may be calculated from:

$$I_{AB} = \frac{\left\{\sum_{n=1}^{z} IP(n) + \frac{3}{2}(Z+1)kT_e\right\}. \delta t. \rho}{m_A \tau_{LASER}} \qquad 7.2.1$$

where δt is the burn depth , a fixed ablation temperature is assumed and there is full ionisation. A burn depth of $0.1\mu m$ in aluminium at 500eV and 10^{15}w.cm^{-2} gives an absorption of $\sim1.5\%$ into the thermal plasma. We would thus expect, with 25% absorption and 60% of that into fast ions (4, 99), that $\sim9\%$ of the indicent energy should appear as preheat.

At $0.53\mu m$ the overall absorption is higher (18,86) typically 30-50% at 10^{15}w.cm^{-2} with short pulses. In our experiments, the burn depth was measured to be $0.25\mu m$ with $\sim$3Joules of green light in 80ps in a $85\mu m$ spot at an average intensity of 7×10^{14}w.cm^{-2}. The assumption of a fully ionised ablation plasma at 500eV (again as measured at the point of peak emission) leads to an absorption of 8% into the thermal plasma (equation 7.2.1). In practice one would expect the ablation temperature to be higher than the 500eV observed in the peak emission region due to further heating of the low density plasma.

In the simulation the absorption is a free parameter, set by fitting to experiment. Previous work at $1.06\mu m$ (22) has fixed the absorption fraction at 2.5% (with a flux limit of 30). In the case of $0.53\mu m$ illumination, the best fit is obtained with an absorption of 4% (and a flux limit of 1/30).

The fast electron preheat in the case of $0.53\mu m$ proved undetectable by the layered fluor technique in this experiment. In retrospect this is not surprising. The absorption into preheat was seen to be independent of intensity. This explains the observation of (6) in which the spectrally integrated hard X-ray continuum was observed to depend on energy rather than intensity. At $0.53\mu m$ absorption mechanisms other than resonance are more active than at $1.06\mu m$ because of the higher density up to critical. An absorption of 10% (see figure 3.2.6) into preheat would thus be an upper limit with $0.53\mu m$ illumination. The hot electron temperature has been observed to be independent of I or λ at fixed $I\lambda^2$ (11,18) and theoretical models (11,12) also give this dependence. From the T_H scaling determined in sub-section 3.2, the expected temperature at 7×10^{14}w.cm^{-2} with $0.53\mu m$ is 3keV. Of the incident 3J a maximum of 0.3J will appear as preheat. The observed radiation pumped Kα yield swamps the yield pumped by this fast electron distribution.

Existing work (18) at $0.53\mu m$ using hard X-ray continuum data indicated that the fractional coupling is similar to $1.06\mu m$ although the range is reduced.

As discussed in sub-section 6.5, the thermal continuum emission with $0.53\mu m$ illumination is high. With $\sim$3J on target the continuum is typically

0.4 exp (-hν/0.42) J.sr^{-1} keV^{-1} where hν is in keV. This represents a total energy of 0.015 Joules carried by photons of $\lambda < 6$Å. Line emission will (roughly) double this energy to .03J, or 1% of incident. Radiative preheat is evidently becoming significant at short wavelength. Of couse in a fusion scheme one would choose an ablator to minimise this preheat, i.e. a low Z material, for which the recombination continuum is too soft to penetrate the target.

7.3   Inertial confinement and laser driven compression

The use of inertial confinement immediately sets requirements on target mass and driver energy . The thermonuclear energy production rate per unit volume is given by:

$$P = n_1 n_2 \overline{\sigma_{12} v} \, W \qquad 7.3.1$$

where n_1 and n_2 are the number densities of the reacting species, $\overline{\sigma_{12} v}$ is the cross-section for the reaction averaged over the (Maxwellian) velocity distribution of the ions and W is the energy released per reaction. The initial thermal energy density (neglecting the small ionisation energy) is:

$$U_{TH} = \tfrac{3}{2} nk(T_e + T_i) \qquad 7.3.2$$

where $n = n_1 + n_2$ is the total ion density. The overall gain of the system, M, is the fusion energy released divided by the driver energy. A fraction, $\mathcal{E}_D$ of the driver energy is coupled into thermal energy, E_{TH}. The fusion energy released is then:

$$E_{FUSION} = \left(\frac{M}{\mathcal{E}_D}\right) E_{THERMAL} \qquad 7.3.3$$

which gives:

$$n \, \mathcal{T} = \frac{M}{\mathcal{E}_D} \cdot \frac{12 \, k T_i}{W \, \sigma_{12} \upsilon} \qquad 7 \cdot 3 \cdot 4$$

where $\mathcal{T}$ is the confinement time, there are equal densities of the two species, no depletion of the reactants occurs during the reaction time and there is equilibration between electrons and ions, i.e. $T_i = T_e$.

Setting $(M/\mathcal{E}_D) = 2$ and choosing the D – T reaction gives the same condition for breakeven (i.e. $E_{FUSION} = E_{DRIVER}$) as that given by Lawson:

$$n \, \mathcal{T} \gg 10^{14} \, cm^{-3} \, s \qquad 7 \cdot 3 \cdot 5$$

In an inertial confinement scheme the confinement time is approximately the pellet radius divided by the sound speed, υ_s . The driver energy can be obtained from 7.3.1, 2 and 4, which for a solid spherical target is:

$$E_{DRIVER} = \frac{E_{THERMAL}}{\mathcal{E}_D} \cdot 4 \, \pi \left(\frac{M^3}{\mathcal{E}_D^4 \, n^2} \right) k T_i \left(\frac{12 \, k T \upsilon_s}{W \, \sigma_{12} \upsilon} \right)^3 \qquad 7 \cdot 3 \cdot 6$$

For the D – T reaction at solid density, with perfect coupling and unity gain, $(m = \mathcal{E}_D = 1)$ this implies $E_D = 1.6MJ$, with $\mathcal{T} \simeq 1ns$ (7). Practical consideration of coupling efficiency and overall gain increase this energy to a currently impractical figure. In (100) a more detailed calculation gave the minimum energy for breakeven as $\sim 10^9$ Joules, greatly increased due to hydrodynamic expansion during burn.

Equation 7.3.4 can be rewritten as:

$$m_i \upsilon_s \, n \, \mathcal{T} = \rho r = \frac{M}{\mathcal{E}_D} \cdot \frac{12 \, k T_i}{W \, \sigma_{12} \upsilon} \cdot m_i \upsilon_s \qquad 7 \cdot 3 \cdot 7$$

where ρ is the fuel density. The pellet mass and hence energy requirement

scales as ρr^3. For a fixed ρr, set by equation 7.3.7, the driver energy is greatly reduced at higher density, scaling as ρ^{-2}. It is thus desirable to compress the fuel in order to relax the demands on driver energy. The aim in laser fusion is to spherically implode a fuel containing target to $10^3 - 10^4$ times solid density. It is thought that this can reduce the driver energy to a practical level (1, 7). For the DT reaction:

$$D^+ + T^+ \rightarrow \alpha^{++} + n + 17\cdot6\,MeV \qquad 7\cdot3\cdot8$$
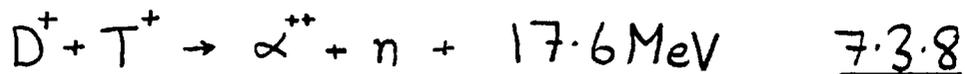
the ρr value required for breakeven is $\sim 1 gmcm^{-2}$ (7). Other less favourable fusion reactions are listed in (101).

Compression to such a high density requires a very large pressure, $\sim 10^6 Mbars$ at 10^3 times solid density in an ideal Fermi degenerate adiabatic compression (1,8).

The achievement of high pressure relies on the inward radial acceleration of the pellet mass by the relatively low ablation pressure over a large (cf final radius) distance such that the mass acquires a large specific kinetic energy, $\frac{1}{2}\rho v^2$. At peak compression the pressure is roughly given by this energy density:

$$P_f \approx \rho v^2 \qquad 7\cdot3\cdot9$$

which may be much larger than the ablation pressure. This pressure multiplication may be likened to a hammer blow. In a microballoon implosion, the pressure multiplication is related to the aspect ratio. A large aspect ratio implies a thin shell accelerated over a large distance leading to a high ρv^2 and hence final pressure. However it is thought that hydrodynamic instabilities, particularly the Rayleigh-Taylor instability will put an upper limit on the aspect ratio (19), so a high driving pressure is required.

The pressure exerted by the ablation process at $10^{15} w.cm^{-2}$ and $1.06 \mu m$ is ~ 10 Mbar. This pressure clearly has to be increased greatly, however the ablation pressure is seen to saturate for $I \gtrsim 10^{15} w.cm^{-2}$ (8) with $1.06 \mu m$ illumination. The only reasonable route to take for an ablative compression is to reduce the laser wave-

length. As seen in sub-section 6.3 a $0.53\mu m$, 80ps, 3 Joule pulse at
$5 \times 10^{14} w.cm^{-2}$ ablated more than twice the depth of material as a $1.06\mu m$,
100ps, 20 Joules pulse at $10^{15} w.cm^{-2}$. The thermal temperature was roughly
the same (420eV and 500eV respectively) so we may conclude that the momentum
carried by the ablated material and hence imparted to the target per incident
joule is greatly improved at $0.53\mu m$. This is an encouraging result with
regard to fusion.

The production of a high-energy short-wavelength laser pulse with
reasonable efficiency is an as yet unsurmounted technological problem.
The overall efficiency of a neoedymium glass laser is less than 1%. It may
be that a compromise must be struck between preheat and laser efficiency.
If this proves to be the case resistive inhibition may provide a means of
screening the fuel from preheat and maintaining a near Fermi degenerate
adiabat.

In Chapter 5 we saw how resistive inhibition can reduce the classical
preheat range by a factor of 2 - 3. This reduces the mass of material
required to protect the fuel core from preheat. At this stage it is
difficult to visualise a target design because of the unknown laser para-
meters. It has been proposed that a vacuum gap could provide a barrier to
preheat (102), and some complicated multiple-shell targets have been
designed. A low density foam could take the place of the vacuum gap and
also overcome the support problems of a multiple shell structure. However
the effect of an extensive low density layer on the hydrodynamic behaviour
of a compression is as yet unknown.

The application of resistive inhibition could render the exploding
pusher compression scheme viable. We will first consider the preheat
levels which are significant to an adiabatic compression.

The Fermi degenerate equation of state may be written as (8):

$$P_{FD} = .3.3 \rho^{5/3} \qquad\qquad 7.3.10$$

where P_{FD} is in Mbar, ρ in gcm^{-2}, the material is fully ionised and the
atomic mass equals twice the atomic number. Adiabatic compression from a
Fermi degenerate state results in a zero temperature rise (T = 0). The
pressure in an ideal gas, P_{IG}, with 3 degrees of freedom ($\gamma = 5/3$) under-

going an adiabatic compression from initial conditions P_o and ρ_o is:

$$P = P_o \left(\frac{\rho}{\rho_o} \right)^{5/3} \qquad 7.3.11$$

This is of similar form to 7.3.10. Close to the Fermi degenerate state we will take the total pressure as the sum of 7.3.10 and 11 in an adiabatic compression, $P_{TOT} = P_{IG} + P_{FD}$. A significant preheat level is one which doubles the final pressure at the desired (for fusion) final density, with respect to the Fermi degenerate pressure, i.e. $P_{IG} = P_{FD}$. The specific enthalpy of the fuel provided by preheat before the compression such that $P_{IG} = P_{FD}$ is:

$$H = \frac{\gamma}{\gamma - 1} \cdot \frac{P_{FD}}{\rho_o} \qquad 7.3.12$$

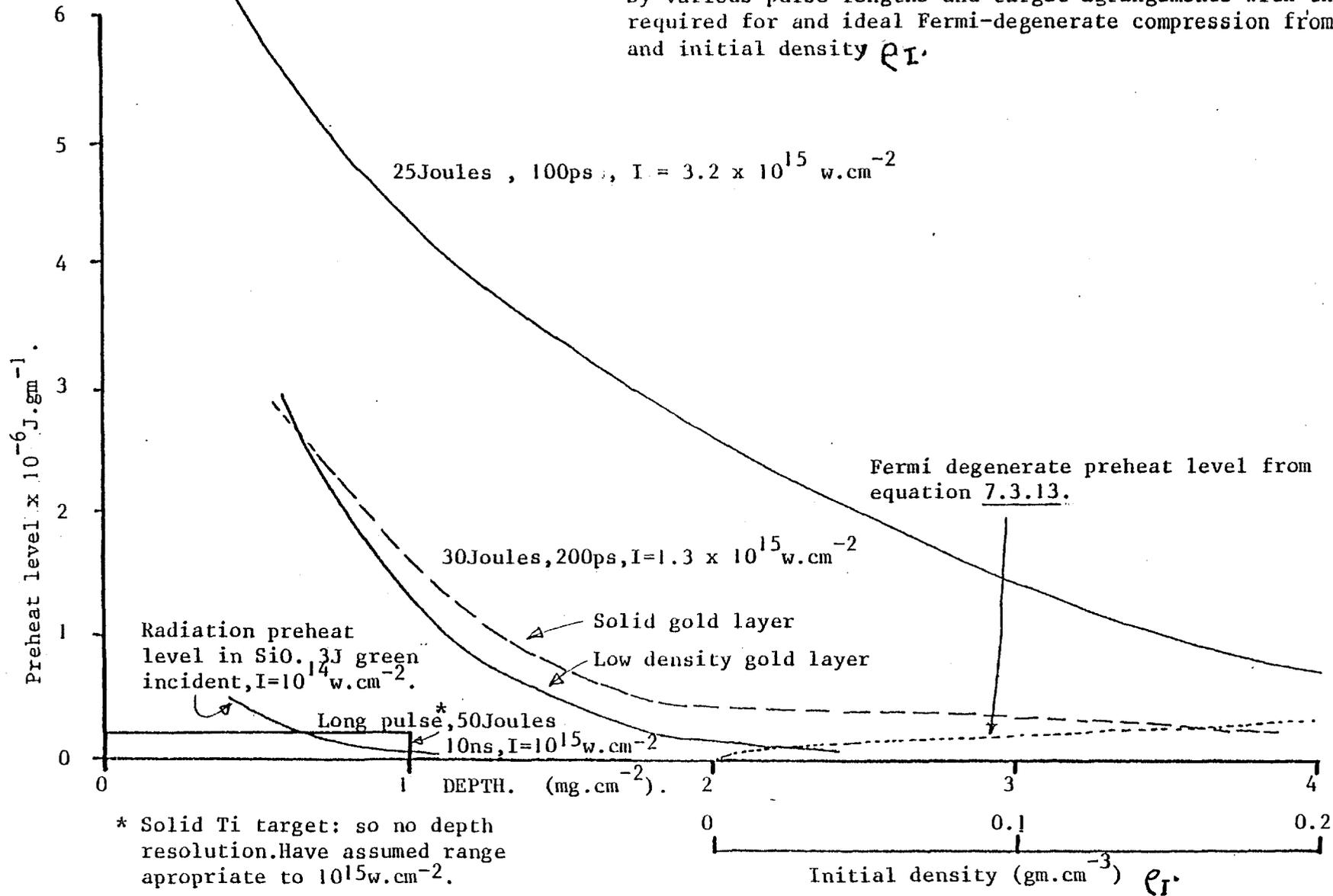where H, P_{FD} and ρ_o are in consistent units. Numerically this may be written as:

$$H = \rho_o^{2/3} \ 7.8 \times 10^5 \ J.gm^{-5/3}cm^{-2/3} \qquad 7.3.13$$

If the fuel is initially at solid density, (0.2 gcm^{-3} for solid DT) then this preheat level is 2.7 x $10^5 J.gm^{-1}$. Figure 7.3.1 shows the energy deposition per unit mass in the case of solid, low density and long pulse experiments as a function of depth in target. The radiative preheat level reported in Chapter 6 is also shown. The 'Fermi degenerate preheat level' is plotted as a function of initial density, ρ_o, in $gm.cm^{-3}$. This is the preheat level below which an ideal Fermi degenerate adiabatic compression is possible.

In the case of 150ps pulses (as in the low density gold experiments) the area mass density required to screen the fuel against preheat at $10^{15}w.cm^{-2}$ is ~4 mgm cm^{-2} for solid gold and ~2 mgm cm^{-2} with approximately half the mass being low density gold. It is reasonable to suppose that a target consisting solely of low density gold would further reduce this range. By optimisation of gold layer thickness, laser intensity and pulse length it could be possible to reduce the target mass required for preheat screening to the extent that an adiabatic exploding pusher experiment would be possible, however at this stage it is not

Figure 7.3.1 A comparison of the preheat levels produced by various pulse lengths and target arrangements with that required for and ideal Fermi-degenerate compression from and initial density ρ_I.

25Joules , 100ps , $I = 3.2 \times 10^{15}$ w.cm^{-2}

Fermi degenerate preheat level from equation 7.3.13.

30Joules,200ps,$I=1.3 \times 10^{15}$w.cm^{-2}

Solid gold layer

Low density gold layer

Radiation preheat level in SiO. 3J green incident,$I=10^{14}$w.cm^{-2}.

Long pulse*,50Joules 10ns,$I=10^{15}$w.cm^{-2}

Preheat level x 10^{-6}J.gm^{-1}.

DEPTH. (mg.cm^{-2}).

* Solid Ti target: so no depth resolution.Have assumed range apropriate to 10^{15}w.cm^{-2}.

Initial density (gm.cm^{-3}) ρ_I.

possible to say how the low density material would respond to a very
high fast electron flux as would be encountered at the target surface.
Simulations indicate that there is an optimum energy deposition per unit
area for inhibition. Below this deposition the inhibiting electric field,
$\eta \, j_H$, is reduced since j_H is reduced. With a higher deposition the high
temperature produced in the gold reduces η such that ηj_H, the electric
field, decreases, even though j_H is higher. In the experiment a larger
inhibition was observed than predicted. Optimistically the optimum
deposition is also higher and a suitable laser-target experiment
utilising resistive inhibition could be devised.

The observation that the preheat level drops with pulse length is
very important. If the long pulse had had a pure top-hat temporal
profile then for the first 100ps no difference between long and short
pulses would exist. The preheat level observed with a long pulse is
less than would be expected if for the first 100ps the behaviour was the
same as with a short pulse, we may therefore conclude that the long
rise-time of the pulse is responsible at least in part for the reduced
preheat. In an ideal isotropic compression (20) a temporally taylored
pulse would be used to minimise shock-heating. Such a pulse would
necessarily be slowly rising. Fast electron production would only be
expected to occur when the ponderomotive force was sufficient to
steepen the density profile (92). It is likely that an ablative
compression fusion scheme would operate at a wavelength shorter than
$1.06 \mu m$, especially in the light of recent advances in efficient
frequency multiplication (103). The reduction in the importance of
the ponderomotive force at short wavelength suggests that fast electron
preheat will not be a problem.

The application of resistive inhibition is most likely to be useful
in fusion schemes at long wavelength, especially at $10.6 \mu m$ where a
high laser efficiency is possible. Such a scheme would specifically
use resonance absorption as the principle absorption mechanism and
would rely on resistive inhibition to keep the target mass, and hence
energy requirement, low.

7.4   Conclusions

The diagnostic technique of layered fluor $K\alpha$ spectroscopy has
been developed and applied in a variety of laser target situations.
The shortcomings of previous work, particularly radiation pumping of
the $K\alpha$ emission and saturation due to ionisation, have been identified,

quantitatively observed and eliminated.

The absolute magnitude and range of fast electron preheating in high intensity laser-target interactions have been measured. The form and intensity scaling of the preheating distribution function have been diagnosed and the applicability of the Bethe-Bloch electron energy deposition formula verified in solid density targets.

The reduction of preheat with increasing pulse length has been observed and has been identified as a feature of a long incident illumination rise-time. It has been concluded that resonance absorption plays a dominant role with short pulses at $1.06 \mu m$, becoming less effective as the pulse length increases. It has been shown that with a 1ns pulse at $10^{15} wcm^{-2}$ the preheat level is consistent with a Fermi degenerate adiabatic compression of solid DT.

The preheat reduction mechanism of resistive inhibition has been demonstrated to significantly reduce the preheat range in low density gold. A Monte-Carlo numerical simulation has shown a significant departure from Spitzer resistivity in the heated low density gold layer. It is suggested that this results from persistent density structure in the low density gold.

Transport experiments with 80ps, $0.53 \mu m$ laser pulses have yielded the thermal conductivity and absorption in the thermal plasma. A significantly higher absorption and larger burn depth are interpreted as resulting in a higher ablation pressure. Hard X-ray continuum measurements indicate a lower fast electron temperature and the pulse length variation of preheat at $1.06 \mu m$ leads to the conclusion that preheat will not be a problem in a short wavelength fusion scheme. The radiative preheat resulting from the enhanced continuum emission at $0.53 \mu m$ has been observed via the radiative pumping of $K \alpha$ emission.

APPENDIX 1

CALCULATION OF INTENSITY FROM THE SPECTRA

i)   Energy in a line

Let the line profile be described by $\partial I/\partial h\nu$ J.sr^{-1}keV^{-1}.
The total energy in the line is then:

$$E = 4\pi \int_{LINE} \frac{\partial I}{\partial h\nu} \, dh\nu \qquad\qquad \underline{A\cdot 1\cdot 1}$$

A general configuration for a flat crystal spectrometer is as shown in figure A.1.1.

For a given photon energy, $h\nu$, the reflectivity of the crystal is $R(h\nu,\Theta)$. The Bragg reflection integral, R_c, is defined as the integral of R over all angles:

$$R_c = \int_0^{\pi} R(h\nu, \Theta) \, d\Theta \qquad\qquad \underline{A\cdot 1\cdot 2}$$

Consider the emission from the source in the energy interval $h\nu \rightarrow h\nu + \delta h\nu$. At a position x on the film the intensity will be:

$$dI = \frac{\partial I}{\partial h\nu} \, R(h\nu, \Theta(x)) \, \frac{\cos(\Theta + \Theta_F)}{r^2} \, dh\nu \qquad \underline{A\cdot 1\cdot 3}$$

If the sensitivity of the film is F.S. (Joules. ND^{-1}cm^{-2}) then the total area under the recorded line due to $h\nu \rightarrow h\nu + dh\nu$ will be:

$$d\left\{\int \int ND \, dx\right\} = \int \frac{dI \, dx}{FS} = \frac{1}{FS} \cdot \frac{\partial I}{\partial h\nu} \cdot \frac{\cos(\Theta + \Theta_F)}{r^2} \int R(h\nu, \Theta) \, dx \, dh\nu$$

$$= \frac{1}{FS} \cdot \frac{\partial I}{\partial h\nu} \cdot \frac{\cos(\Theta + \Theta_F)}{r^2} \, R_c \frac{dx}{d\Theta} \, dh\nu = \frac{\partial I}{\partial h\nu} \cdot \frac{R_c}{FSr} \, dh\nu$$

$$\underline{A\cdot 1\cdot 4}$$

Integrating over the entire spectrum gives the emitted energy in terms of the recorded area as:

$$E = \int ND\, dx \cdot \frac{FS\, r}{R_c} \quad J.sr^{-1} \qquad A \cdot 1 \cdot 5$$

If there is X-ray attenuating material between the source and the film then the total energy becomes:

$$E = \int ND\, dx \cdot \frac{FS\, r}{T\, R_c} \qquad A \cdot 1 \cdot 6$$

where T is the X-ray transmission of the (N) intervening materials, given by:

$$T = \exp\left\{ -\sum_{n=1}^{N} t_n \mu_n / \rho \right\} \qquad A \cdot 1 \cdot 7$$

$t_,$, ρ_n, and $\frac{\mu}{\rho}_n$ being the thickness, density and mass attenuation coefficient of material n.

If the X-ray signal being recorded originates throughout a layer of X-ray attenuating material (as in a K_α line) then there will be self absorption. If the emission is produced uniformly throughout a layer of parameters t, ρ and μ/ρ as defined above, then the original emission will be attenuated by:

$$T' = \frac{1 - \exp(-t\rho\mu/\rho)}{t\rho\mu/\rho} \qquad A \cdot 1 \cdot 8$$

If a slit is being used to enable spatial resolution then the sensitivity is further reduced. Let Γ_{ss} be the source to slit distance, Γ_{SF} be the optical slit to film distance, W_{SOURCE} be the source width (assumed uniform) and W_{SLIT} be the slit width. The signal recorded on the film is then attenuated by:

$$T'' = \frac{W_{SLIT}}{W_{SOURCE}} \cdot \frac{\Gamma_{ss} + \Gamma_{sF}}{\Gamma_{sF}} \qquad A \cdot 1 \cdot 9$$

If $W_{SLIT} \geqslant W_{SOURCE} \cdot \dfrac{\Gamma_{SF}}{\Gamma_{SS} + \Gamma_{SF}}$ then $T'' = 1$, and the spectrometer is space integrating.

The total energy in a line becomes:

$$E = \frac{1}{T\,T'\,T''} \cdot \int ND\,dx \cdot \frac{FS\,\Gamma}{R_c} \qquad A.1.10$$

ii) Intensity of continuum

Let the continuum emission be $\dfrac{\partial I}{\partial h\nu}$ J.sr^{-1}keV^{-1}.

The geometry is the same as in figure A.1.1. Consider emission in the range $h\nu \rightarrow h\nu + dh\nu$. Further consider an element of film of length dx such that all the energy in $dh\nu$ reaching the film falls in dx. The integrated exposure over dx will then be:

$$\int I\,dx = \frac{\partial I}{\partial h\nu} dh\nu \frac{R_c}{\Gamma} \quad J.\,cm^{-1} \qquad A.1.11$$

Now allow $dh\nu$ to increase until the dispersion of the spectrometer just allows the emission to fill dx, i.e.:

$$dh\nu = \frac{\partial h\nu}{\partial x} \cdot dx \qquad A.1.12$$

Then, if $\partial I/\partial h\nu$ is only slightly varying over the range $dh\nu$ the exposure over dx will be uniform:

$$\int I\,dx = FS.ND.dx = \frac{\partial I}{\partial h\nu} \cdot \frac{R_c}{\Gamma} \cdot \frac{\partial h\nu}{\partial x} dx \qquad A.1.13$$

The dispersion, $\partial h\nu / \partial x$ is trivially obtained from $n\lambda = 2d\sin\theta$, $h\nu$ (keV) $= 12.4/\lambda$ (Å) and $dx/d\theta = \Gamma /\sin(\theta + \theta_F)$ to give:

$$\frac{\partial I}{\partial h\nu} = \frac{ND\ FS\ \Gamma^2\ \lambda^2}{R_c\ 12.4.\ 2d.\ \cos\theta.\ \sin(\theta + \theta_F)} \qquad A.1.14$$

Consideration of previous discussion on absorption and spatial resolution modify this to:

$$\frac{\partial I}{\partial h\nu} = \frac{ND.FS.\ r^2\ \lambda^2}{T.T'.T''.R_c.12.4.2d.\cos\Theta.\sin(\Theta+\Theta_F)}$$

$$\underline{A.1.15}$$

iii) <u>Sensitivity</u>

The ultimate sensitivity of the spectrometer is governed by several factors, principally;

   i)   Inherent noise on film

  ii) Filtering

 iii) Crystal being used (by changing r and R_c)

A 100 μm diameter source is magnified to $\sim$ 200 μm on the film (in the spectral direction) the magnification being $1/\cos(\Theta + \Theta_F)$. The smallest reliably recordable ND in Kodirex is 0.03 which gives a value for the integrated area under a line of 6×10^{-4} ND.cm.

Taking as an example the MKII spectrometer with a PET crystal recording the K K_α line the emitted energy required to produce this exposure on Kodirex with negligable filtering is $8 \times 10^{-7} J.sr^{-1}$. However fogging problems arising from fast particle emission will necessitate the use of filtering which will reduce the sensitivity to $\sim 2 \times 10^{-6} J.sr^{-1}$.

The sensitivity is increased with the use of a germanium crystal since Γ is reduced. The spectral range of the spectrometer is moved to shorter wavelength. Figure A.1.2 indicates the approximate range over which each spectrometer may be operated together with the spectral range available at a given setting.

Spectrometer	PET	Germanium
I	2.5Å - 8.3Å(5.0Å)	1.1Å - 3.8Å (2.3Å)
II	3.3Å - 7.5Å(4.0Å)	1.5Å - 3.4Å (1.8Å)
III	3.0Å - 8.0Å(3.5Å)	1.4Å - 3.7Å (1.6Å)

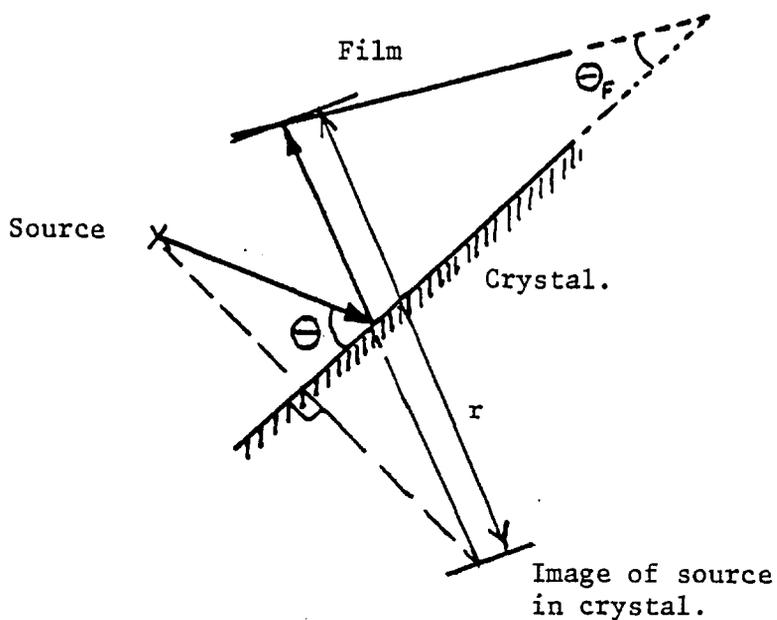<u>Figure A.1.2</u> The spectral range of each spectrometer

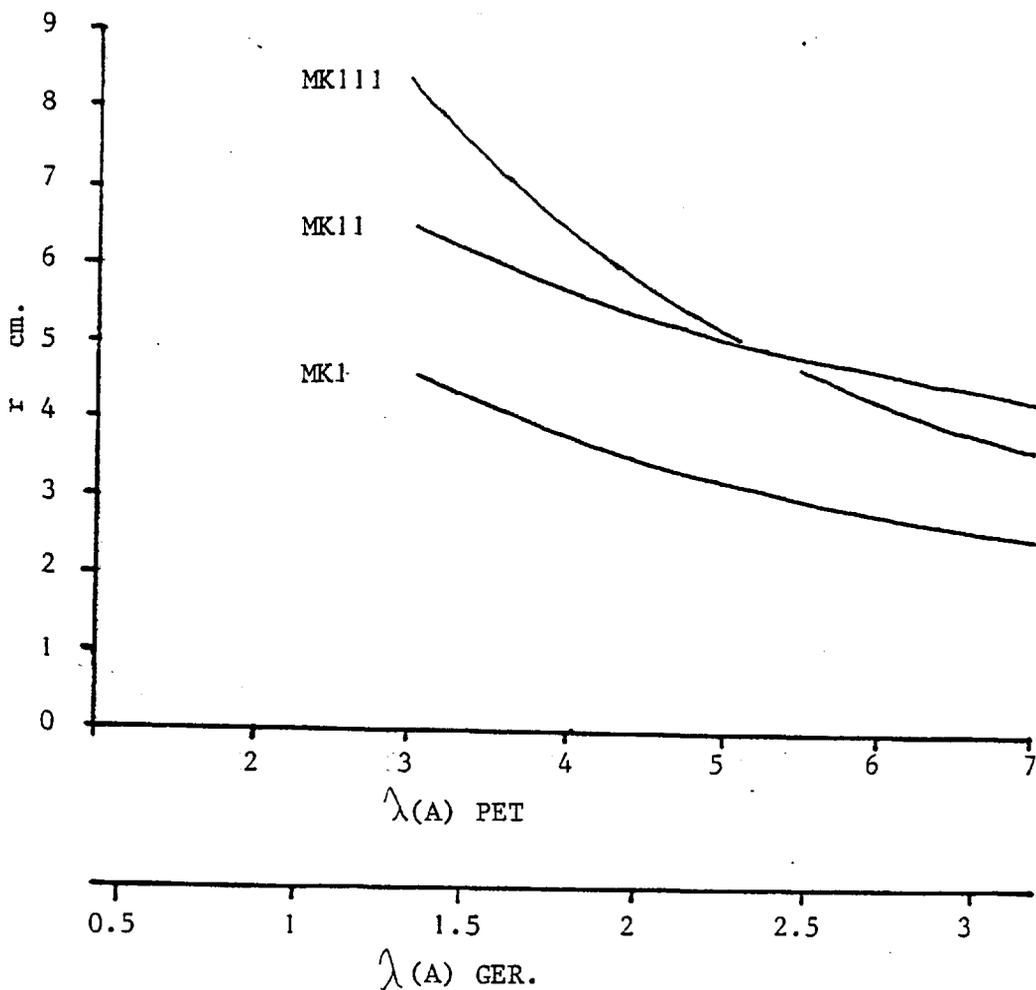**Figure A.1.1** The general configuration of a crystal spectrometer

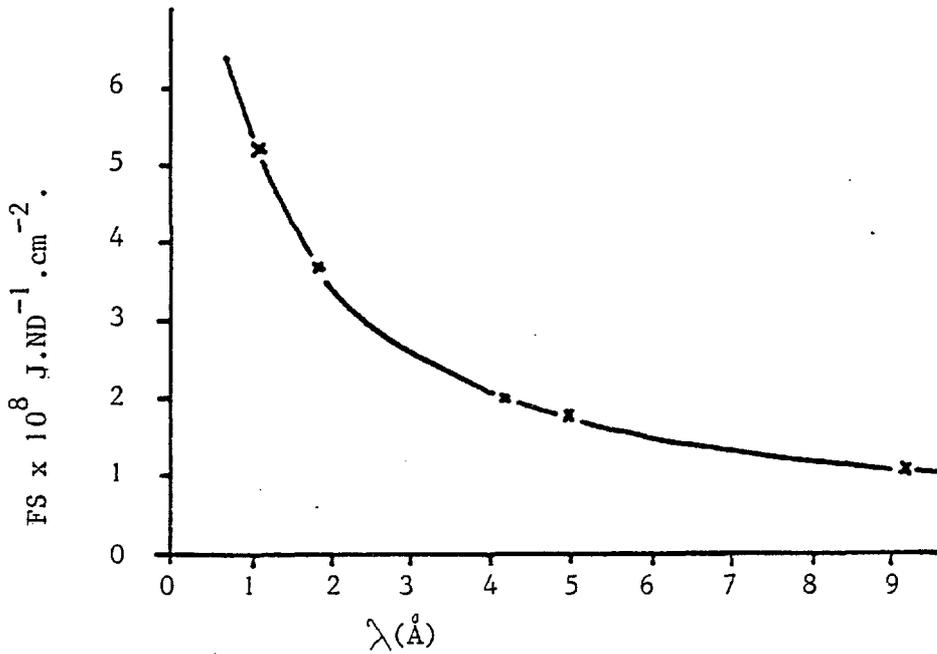**Figure A.1.3** The source-film distance as a function of wavelength.

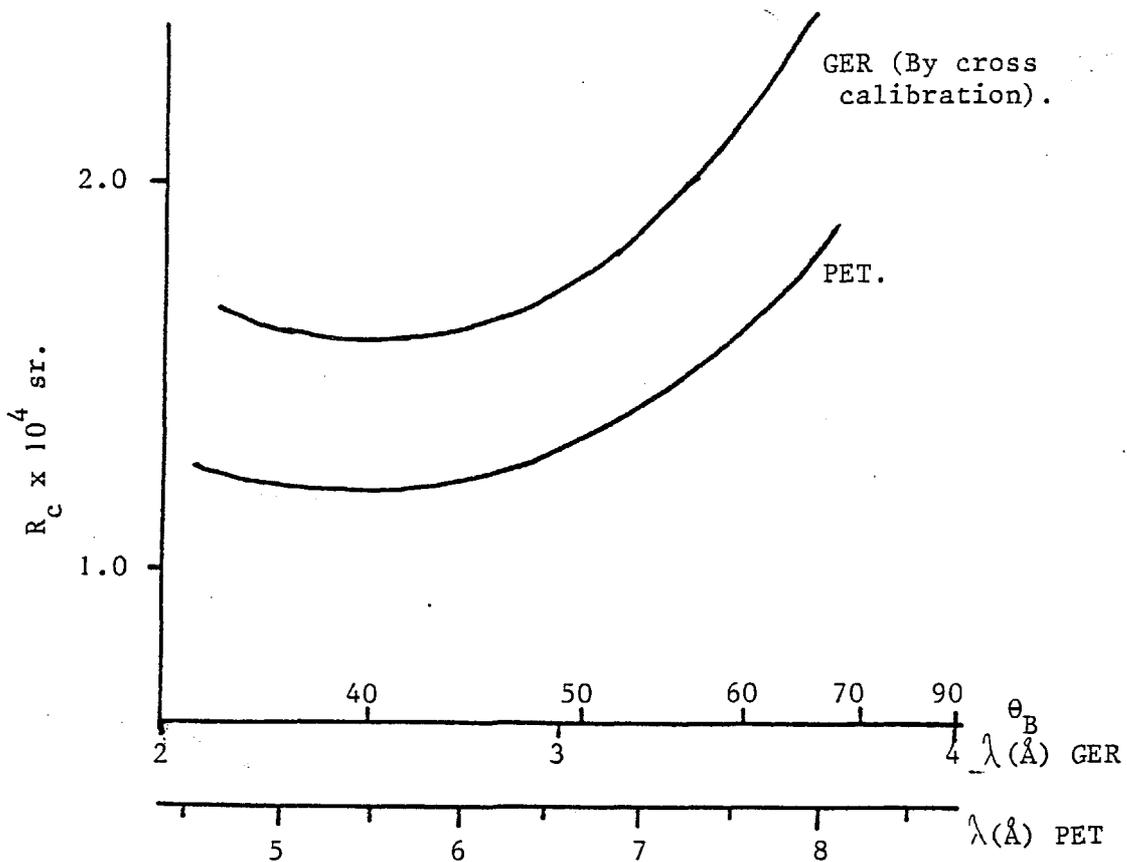Figure A.1.4 The sensitivity of Kodirex as a function of wavelength in the linear response region(57)

Figure A.1.5 The Bragg reflection integral for PET and germanium

The source - film distance Γ_{SF} is not unique since the position of the spectrometer with respect to the source is variable. However each spectrometer has a nominal zero position so the source - film distance as a function of wavelength is plotted in figure A.1.3 for this position (i.e. source 5mm from slit and set on a level with the horizontal centre line).

The sensitivity of Kodirex as a function of wavelength is shown in figure A.1.4, obtained from (57).

For a recorded ND > 1 a non-linear correction to the exposure was employed;

$$ND_{COR.} = 2 \cdot 6^{(ND-1)} \qquad \text{A.1.16}$$

The P.E.T. crystal has been absolutely calibrated at Leicester University and the Bragg reflection integral as a function of wavelength is reproduced in figure A.1.5.

The germanium crystal was cross-calibrated with the P.E.T. crystal at two wavelengths and the angular variation of R_c assumed the same as P.E.T. to obtain the dotted curve shown in figure A.1.5.
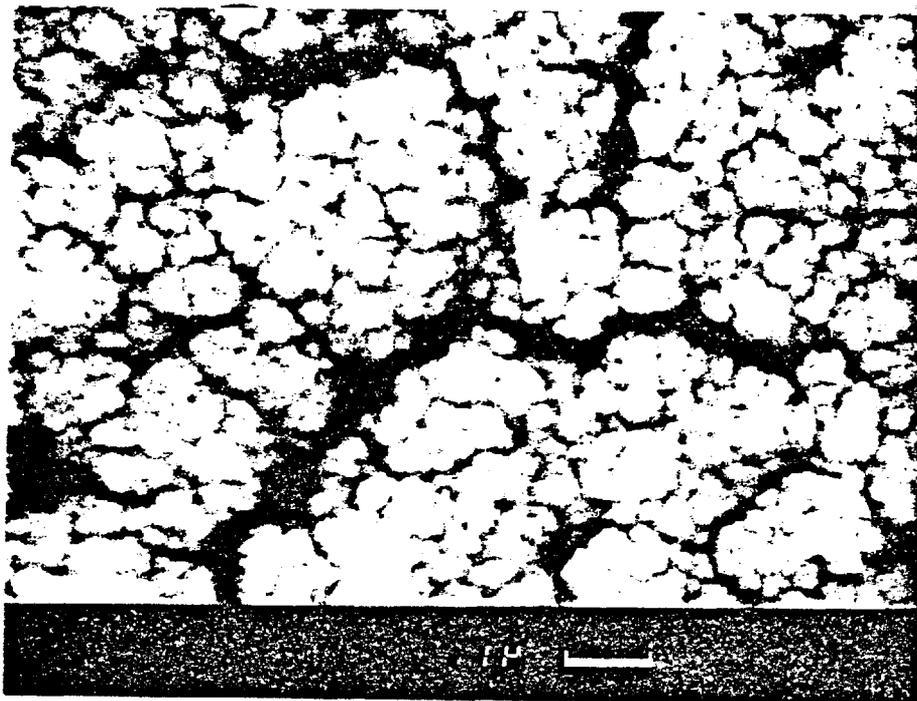
Figure A.2.1 An SEM micrograph of low density gold
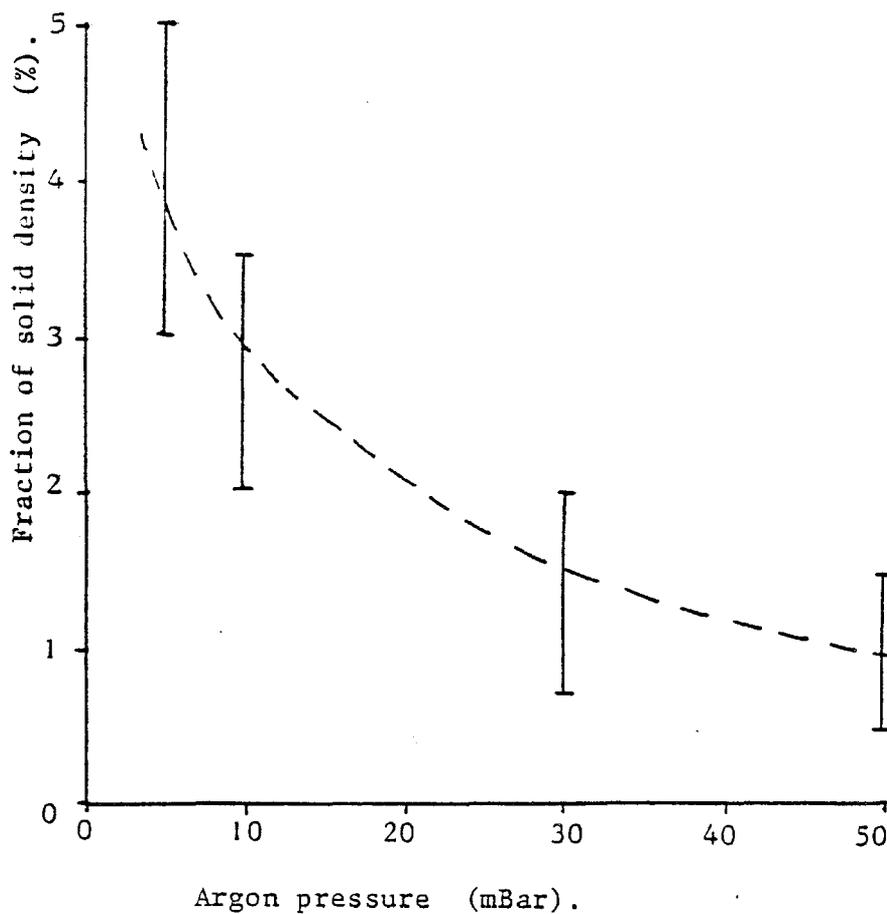

Argon pressure (mBar).

Figure A.2.2 The variation of the density of low density
gold with background pressure

APPENDIX II

FABRICATION OF LOW DENSITY GOLD LAYERS

In general low density films or 'smokes' can be produced by thermal evaporation of the material in a background atmosphere of some inert gas e.g. argon. (104).

The material is layed down in a layer resembling cotton wool when viewed through an S.E.M., with the density structure being on a few micron scale-length. Figure A.2.1 shows S.E.M. micrographs of a typical gold layer. The density is ~ 1% solid density and the layer was produced with a background atmosphere of 40 mBar argon.

The density of the layer is a strong function of the background pressure. It is also (less) dependent on the coating rate and the source-target distance.

In the case of gold the material is carried by convection currents within the background gas so it is important that the target be placed directly above the source. The rising plume of gold is clearly visible.

The source employed was a standard tungsten 'basket' filament, pre-wetted with gold. The target was positioned 80mm above the source. The coating rate was such that with a background pressure of 50mBar a 100μm thick layer was deposited in 5 mins. At this rate the filament appeared bright-red to white hot.

A very approximate guide to density vs pressure is shown in figure A.2.2. The source distance is 80mm and the coating rate set by having the same current as above (= 40Amps for the particular baskets being used).

Final density measurements were made with a scanning electron microscope to measure the thickness (see figure A.2.1) and a chemical balance (accurate to 0.02 mgm) to measure the mass of films of known area. In general two targets were made side by side. The thickness of gold on each target was measured and the mass of gold on one was determined by weighing before and after removal of the gold layer. The density on each was assumed the same, this haveing been previously tested.

REFERENCES

1)   J. Nuckolls, L. Wood, A. Thiessen, G. Zimmerman, Nature, 239
      139 (1972).

2)   K.A. Brueckner, Nuclear Fusion, 17, 1257 (1977).

3)   J.D. Hares, J.D. Kilkenny, M.H. Key and J.G. Lunney,
      Phys. Rev. Lett., 42, 1216, (1979).

4)   P.M. Campbell et al, in "Proc of the VI International Conf. on
      Plasma Physics and Controlled Nuclear Fusion Research"
      Birchtesgaden, West Germany, 1976 International Atomic Energy
      Agency, Vienna (1977) Vol. 1.

5)   V.W. Slivinsky, H.N. Kornblum, H.D. Shay, J. App. Phys., 46,
      1976 (1975).

6)   F.C. Young, Phys. Rev. Lett., 33, 747 (1974).

7)   K.A. Brueckner, S.A. Jorna, Rev. Mod. Phys., 46, 325 (1974).

8)   M.H. Key, "Lectures on the physics of the superdense region"
      20th Scottish Universities Summer School in Physics, Laser Plasma
      Interactions, St. Andrews, RL-80-020 (1980).

9)   C. Fauquinon, F. Floux, Phys. Fluids, 13, 386 (1970).

10)   A. Caruso, R. Gratton, Plasma Phys., 10, 867 (1968).

11)   D.W. Forslund, J.M. Kindel, K. Lee, Phys. Rev. Lett., 39, 284,
      (1977).

12)   K. Estabrook, W.L. Kruer, Phys. Rev. Lett., 40, 42 (1978).

13)   D.J. Bond, J.D. Hares, J.D. Kilkenny, Phys. Rev. Lett., 45, 252
      (1980).

14)   B. Ahlborn, M.H. Key, Rutherford Lab. Report RL-79-033 (1979).

15)   E.K. Storm et al, Phys. Rev. Lett., 40, 1570 (1978).

16)   M.D. Rosen, J.H. Nuckolls, Phys. Fluids, 22, 1393 (1979).

17)   J. Delettrez, et al, Bull. Am. Phys. Soc., $\underline{24}$, 945 (1979)

18)   F. Amiranoff, R. Fabbro, E. Fabre, C. Garban, J. Virmont,
        M. Weinfeld, Phys. Rev. Lett., $\underline{43}$, 522 (1979).

19)   K.A. Brueckner, S. Jorna, R. Janda, Phys. Fluids, $\underline{17}$, 1554 (1974).

20)   R.E. Kidder, Nuc. Fusion, $\underline{14}$, 797 (1974).

21)   J. Murdoch, Ph.D Thesis, University of London, Nov. 1979.

22)   Rutherford Lab. Central Laser Facility Annual Report 1979,p4.3,
        RL-79-036.

23)   J.S. Pearlman, J.J. Thomson, C.E. Max, Phys. Rev. Lett., $\underline{38}$,
        1397 (1977).

24)   S.J. Gitomer, D.B. Henderson, Phys. Fluids, $\underline{22}$, 364 (1979).

25)   J.J. Thomson, C.E. Max, K. Estabrook Phys. Rev. Lett., $\underline{35}$, 663
        (1975).

26)   D.R. Gray, J.D. Kilkenny, M.S. White, P. Blyth, D. Hull, Phys. Rev.
        Lett., $\underline{39}$, 1270 (1977).

27)   W.M.Mannheimer, Phys. Fluids, $\underline{20}$, 265 (1977).

28)   J.J. Thomson, W.L. Kruer, A.B. Langdon, C.E. Max, W.C. Mead, Phys.
        Fluids, $\underline{21}$, 707 (1978).

29)   R.S. Craxton, M.G. Haines, Phys. Rev. Lett., $\underline{35}$, 1336 (1975).

30)   P.M. Campbell, R.R. Johnson, F.J. Mayer, L.V. Powers, D.C. Slater,
        Phys. Rev. Lett., $\underline{39}$, 274 (1977).

31)   L.M. Wickens, J.E. Allen, P.T. Rumbsy, Phys. Rev. Lett., $\underline{41}$, 243
        (1977).

32)   H.A. Bethe, Ann. Phys. Leipzig $\underline{5}$, 325 (1930).

33)   G.J. Pert, Plasma Physics, $\underline{20}$, 175 (1978).

34)   W. Wagli, T.P. Donaldson, Phys. Rev. Lett., $\underline{40}$, 875 (1975).

35)   J.E. Balmer, T.P. Donaldson, Phys. Rev. Lett., $\underline{39}$, 1084 (1977).

36)   R.A. Cairns, Plasma Physics, $\underline{20}$, 991 (1978).

37) R.A. Haas et al, Phys. Rev. Lett., 39, 1533 (1977).

38) K.M.S. Fusion, inc., Annual Report, KMSF-U884 (1978).

39) B. Bezzerides, S.J. Gitomer, D.W Forslund, Phys. Rev. Lett., 44, 651 (1980).

40) C.M. Armstrong, B.H. Ripin, F.C. Young, R. Decoste, R.R. Whitlock, S.E. Bodner, J. App. Phys., 50, 8 (1979).

41) M.J. Berger, S.M. Seltzer, "Tables of Energy Losses and Ranges of Electrons and Possitrons", NASA SP-3012 (1964).

42) N.F. Mott, H.S.W. Massey, "The Theory of Atomic Collisions", Clarendon, Oxford. (1933).

43) L.V. Spencer, "Energy Dissipation by Fast Electrons", NBS Monograph 1, U.S. GPO Washington DC (1959).

44) N.A. Dyson, "X-rays in Atomic and Nuc. Phys.", Longman (1973).

45) A.P. Thorne, "Spectrophysics", Chapman and Hall Science Paperbacks, London (1974).

46) M. Green, V. E. Cosslett, Proc. Phys. Soc., 78, 1206 (1961).

47) G. Wentzel, Z. Phys., 43, 524 (1927).

48) W. Bambynek, et al. Rev. Mod. Phys. 44, 716 (1972).

49) R.W. Fink et al, "Inner Shell Ionisation Phenomena and Future Applications", CONF-720404, USAEC, 80 (1973).

50) Handbook of Spectroscopy, Vol. 1, C.R.C. Press, Ohio (1974).

51) D.T. Attwood, IEEE, J. Quant. Elec., QE-14, 909 (1978).

52) P. Mulser, R. Sigel, S. Witkowski, Physics Reports, 6, 187 (1973).

53) K.A. Brueckner, R.S. Janda, Nuc. Fusion, 17, 1265 (1977).

54) M. Green, V.E. Cosslet, J. Phys. D. Ser. 2, 425 (1968).

55) D. Brown, J. Gilfrich, J. App. Phys., 42, 4044, 1971.

56) R. Castaing, J. Descamps, J. Phys. Rad., 16, 304 (1955).

57) M.C. Hobby, N.J. Peacock, J. Phys.E, 6, 184 (1973).

58) L.L. House, Astrophys. J. Suppl., 18, 21 (1969).

59) Ya. B. Zel'dovich and Yu. P. Raiser, Physics of Shock Waves and High Temp. Hydro. Phenomena p.201. Academic Press (1966).

60) K.B. Mitchell, R.P. Godwin, J. App. Phys., 49, 3851 (1977).

61) B. Yaakobi, T.C. Bristow, Phys. Rev. Lett., 38, 350 (1977).

62) H.R. Griem, "Plasma Spectroscopy", McGraw-Hill, New York (1964).

63) B.I. Bennet, J.D. Johnson, G.I. Kerley, G.T. Rood, L.A.S.L. report no. LA-7130 (Feb. 1978).

64) R.W.P. McWhirter in "Plasma Diagnostic Techniques", Academic Press (1965).

65) J.C. Stewart, K.D. Pyatt Jr., Astrophys. J., 144, 1203 (1966).

66) Y. Matsukawa, Japanese J. App. Phys., 16, 311 (1977).

67) D.R. Ingliss, E. Teller, Astrophys. J., 90, 439 (1939).

68) J.D. Lawson, "The Physics of Charged Particle Beams", p. 125, Clarendon Press, Oxford (1977).

69) N.N. Ceglio, J.T. Larsen, Phys. Rev. Lett., 44, 579 (1980).

70) N.A. Ebrahim et al, Phys. Rev. Lett., 43, 1995 (1980).

71) L. Spitzer, R. Harm, Phys. Rev., 89, 977 (1953).

72) B.H. Ripin, E. A. McLean, App. Phys. Lett., 34, 809 (1979).

73) C. Yamanaka, T. Yamanaka, T. Sasaki, J. Mizui, H.B. Kang, Phys. Rev. Lett., 32, 1038 (1974).

74) University of Rochester, L.L.E. Review, Dec. 1979 - Feb. 1980, Vol. II.

75) B. Arad et al, Phys. Rev. Lett., 44, 326 (1980).

76) J. Virmont, R. Pellat, A. Mora, Phys. Fluids, 21, 567 (1978).

77) J.A. Stamper, Phys. Fluids, 18, 735 (1975).

78) S. Goudsmit, J.L. Saundersen, Phys. Rev., 57, 24 (1940).

79). D. Pines, D. Bohm, Phys. Rev., 85, 338 (1952).

80). P. Hoong-Yee, M.D. Rosen, Phys. Rev. Lett., 42, 236 (1979).

81) D.F. DuBois, M.V. Goldman, Phys. Rev., 164, 207 (1967).

82) K. Nishikawa, J. Phys. Soc. Japan, 24, 916 (1968).

83) W.M. Mannheimer, D.G. Colombant, Phys. Fluids, 21, 1818 (1978).

84) W.C. Meed, R.A. Haas, W.L. Kruer, D.W. Phillion, H.N. Kornblum, J.D. Lindt, D.R. MacQuigg, V.C. Rupert, Phys. Rev. Lett., 37, 489 (1976).

85) J. Christiansen, D. Ashby, K.V. Roberts, Comp. Phys. Comm., 7, 271 (1974).

86) A. Maaswinkel, K. Eidmann, R. Sigel, Bull. Am. Phys. Soc., 23, 766 (1978).

87) J.G. Lunney, PhD Thesis, Queens University Belfast, (1980).

88) Rutherford Lab. C.L.F. Annual Report 1980, Sec. 7.2.7, RL-80-026.

89) B.L. Henke, R. White, B. Lundberg, J. App. Phys., 28, 98 (1957).

90). J.M. Dawson, Phys. Fluids, 12, 875 (1969).

91) N.G. Denisov, Sov. Phys. JETP 4, 544 (1957).

92) R.L. Morse, C.W. Nielson, Phys. Fluids, 16, 909 (1973).

93) K.G. Estabrook, E.J. Valeo, W.L. Kruer, Phys. Fluids, 18, 1151 (1975).

94) F.W. Perkins, J. Flick, Phys. Fluids, 14, 2012. (1971).

95) H.H. Klein, W.M. Mannheimer, E. Ott, Phys. Rev. Lett., 31, 1187 (1973).

96) W.M. Manheimer, D.G. Colombant, B.H. Ripin, Phys. Rev. Lett., 38, 1135 (1977).

97) W.L. Kruer, K. Estabrook B.F. Lasinski, A.B. Langdon, Phys. Fluids, 23, 1326 (1980).

98) K.R. Manes, V.C. Rupert, J.M. Auerback, P. Lee, J.E. Swain, Phys. Rev. Lett., 39, 281 (1977).

99) K.M.S. Fusion, inc., Annual Report, KMSF-U884 (1978).

100) M.S. Chu, Phys. Fluids, 15, 413 (1972).

101) F.F. Chen, "Introduction to Plasma Physics" Plenum (1974).

102) K. Lee, D.W. Forslund, J.M. Kindel, L.E. Lindman, Nuc. Fusion, 19, 1447 (1979).

103) Optical Spectra, p. 18 (May 1980).

104) L. Holland, "Vacuum Deposition of Thin Films", Chapman and Hall (1963).

Measurement of Fast-Electron Energy Spectra and Preheating in Laser-Irradiated Targets

J. D. Hares and J. D. Kilkenny

Blackett Laboratory, Imperial College, London, United Kingdom

and

M. H. Key[(a)] and J. G. Lunney

Department of Pure and Applied Physics, Queen's University, Belfast, Northern Ireland

Fast electrons produced by the irradiation of plane-layered targets with 20-J, 100-ps, 10^{15}-W·cm^{-2}, neodymium-laser pulses have been diagnosed by the $K\alpha$ emission which they cause at various depths in the targets. The fast-electron energy spectrum and absolute energy deposition (target preheat) are measured.

When high-intensity laser radiation is incident on a solid it is well known that the resulting plasma has both a thermal (cold) and a hot component in its electron velocity distribution and that a large fraction of the absorbed laser energy couples into the hot electrons.[1-3] Fast ions are accelerated by the hot electrons, and the temperature of the hot electrons T_H has been inferred from the ion-velocity spectrum.[4] A substantial fraction of the hot-electron energy is transferred to the ions, and the remainder is deposited in the target causing preheating of the solid, x-ray continuum emission and K line emission. The hard-x-ray (5–50 keV) continuum slope has been widely used to estimate the hot-electron temperature.[1,3,5] However, the experimental method is not amenable to spatial resolution, and the total energy inferred in the hot electrons in sensitive to the model electron distribution function.[6]

We report the first experiments using $K\alpha$ radiation from laser-produced plasmas to measure the magnitude of preheating of the solid by hot electrons, with radiation-induced $K\alpha$ emission and saturation of the $K\alpha$ emission due to ionization eliminated. The range and degree of the preheating, and the form of the hot-electron velocity distribution are also measured. Direct measurement of this preheating has not previously been obtained and is of importance for laser-fusion target design.

Earlier work[7,8] has attributed $K\alpha$ emission to fast electrons and in a detailed study[9] their range and effective temperature were deduced for 10.6-μm radiation at 3×10^{13} W cm^{-2}. Target preheating was estimated in Ref. 8, but consideration of ionization effects below suggest that the conclusions drawn from the experiment were invalid.

$K\alpha$ radiation can arise from electron- or radiation-produced K-shell ionization. Radiative K-shell ionization is very efficient if the photon en-

ergy $h\nu$ is slightly greater than E_K the K-shell ionization potential. The low-energy x-ray recombination continuum from laser-produced plasmas has the form $I(\nu) = I_0 \exp(-h\nu/kT_c)$ where the cold-electron temperature T_c is ~0.5 keV in the present experiment. Thus to reduce radiation pumping E_K must be much greater than kT_c. In contrast, electrons are inefficient in K-shell ionization. The instantaneous ratio[10] of K-shell ionization to total energy deposition by an electron of energy E may be written as

$$R(E) \sim 3.0 \times 10^{-2} \ln(E/E_K)/\ln(4E/\overline{E}_i)$$

for potassium, where the mean excitation energy $\overline{E}_i$ is 240 eV. For $E > 15$ kV, $R(E)$ is nearly constant at $\overline{R} \simeq 1\%$. The $K\alpha$ yield is then $\omega' \overline{R} U$ where U is the energy deposited by electrons, and ω' is the fluorescence yield times the $K\alpha$ photon energy divided by E_K (0.15 for Ca).

As U increases, the ionization causes only a small shift in the wavelength of the $K\alpha$ line until an electron is removed from the L shell,[11] when

$$U \equiv U_s = N_a \left\{ \sum_{n=1}^{Z-10} E_i{}^n + 1.5k[(\overline{Z} - 10)T_e + T_i] \right\},$$

where $E_i{}^n$ is the ionization potential of ionization stage n and N_a is the number of fluor atoms under the focal area. The saturation energy yield of the "unshifted" $K\alpha$ line is simply $U_s \overline{R} \omega'$.

Previous work with neon[8] has ignored this saturation effect.[12] We estimate the saturation energy of the electron-pumped neon $K\alpha$ in Ref. 8 to be 5×10^{-7} J (for 10^{14} atoms) compared with the reported observed yield of 2×10^{-4} J.

The saturation and radiation pumping effects suggest using a fluor whose Z is appreciably larger than 10, but not so large that E_K is comparable with kT_H. In the work below, Ca and K ($E_K = 4.04$ and 3.62 keV, respectively) were used and kT_H was 11 keV. A 20-J, 100-ps neodymium
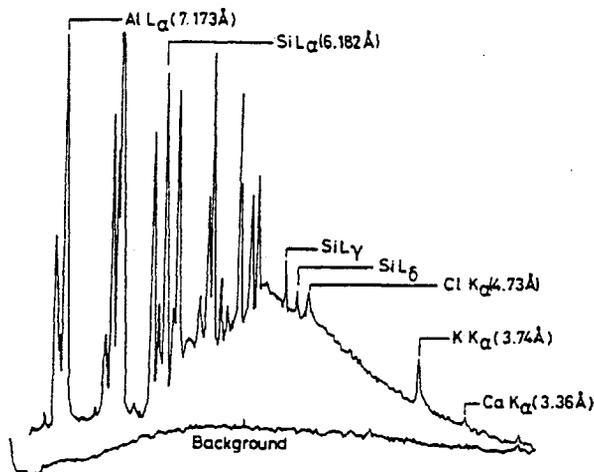
FIG. 1. A typical microdensitometer tracing from the front spectrometer. The Ca $K\alpha$ line appears much more brightly on the rear spectrometer, where it suffers no target absorption.

laser was normally incident on various plane-layered targets. The targets were positioned 150 μm away from the optimum focus of a $f/1$ lens. X-ray pinhole pictures indicated a focal spot of 100 μm, which corresponds to photographic measurements of the equivalent image plane. The layers were 0.1-μm Al; 1.0-μm SiO; 3.0-μm KCl; 2.5-, 12.5-, 25-, or 50-μm variable-thickness Mylar; and 2.5-μm CaF_2. The laser was incident on the Al. The top two layers of Al and SiO isolated the $K\alpha$ fluors from the ablation plasma, whose burnthrough depth for 100-ps pulse was only 0.1 μm. The Ca and K $K\alpha$ radiation was excited by electrons: The Cl with lower E_K was appreciably pumped by soft x-ray radiation. Time-integrated x-ray spectra were recorded by two miniature flat pentaerythritol crystal spectrometers. The reflectivities of the crystals have been measured.[13] All the $K\alpha$ emission lines

were recorded by a spectrometer behind the targets. A spectrometer in front of the target recorded the K and Cl $K\alpha$ lines, the attenuated Ca $K\alpha$ line, and the soft-x-ray plasma emission.

A typical microdensitometer trace from the front spectrometer is shown in Fig. 1. Three $K\alpha$ lines, the plasma continuum, and the Si and Al plasma emission lines are shown. The Ca and K $K\alpha$ intensities for different Mylar thicknesses are shown in Fig. 2. As expected, with increasing Mylar thickness the number of electrons energetic enough to penetrate to the activate the rear fluor decreases and thus the $K\alpha$ yield decreases with increasing depth in target.

The saturation and radiation effects referred to above were experimentally demonstrated. Figure 3 shows the $K\alpha$ line profile from the K at the front, in which the energy deposition is highest. The line clearly has shifted components.[11] The energy in the "unshifted" component is $(1.4 \pm 0.1) \times 10^{-5}$ J sr^{-1}, whereas the energy in the shifted components is $(0.8 \pm 0.3) \times 10^{-5}$ J sr^{-1}: For K $K\alpha$ $U_s = 1.0 \times 10^{-5}$ J sr^{-1} for the 100-μm-diam, 3-μm-deep emitting volume of KCl, in fair agreement with the experimental data.

To show the effect of radiation-induced $K\alpha$ emission, a 25-μm Mylar target with KCl on the rear was irradiated with a larger focal spot and hence lower flux density. There was no K $K\alpha$ yield observed, because the hot-electron temperature was too low. However, the Cl $K\alpha$ yield was $(1.3 \pm 0.1) \times 10^{-6}$ J sr^{-1}. The soft-x-ray recombination emission was the same as for the 100-μm focal spot, and was measured to have $I_0 = (6.0 \pm 1.0) \times 10^{-5}$ J sr^{-1} eV^{-1} and $kT_e = 0.5 \pm 0.1$ keV. The calculated Cl $K\alpha$ yield induced by this recombination emission was 1.7×10^{-6} J sr^{-1}, again in fair agreement with experiment. In this calculation proper account was taken of target geometry and reabsorption. The predicted radia-
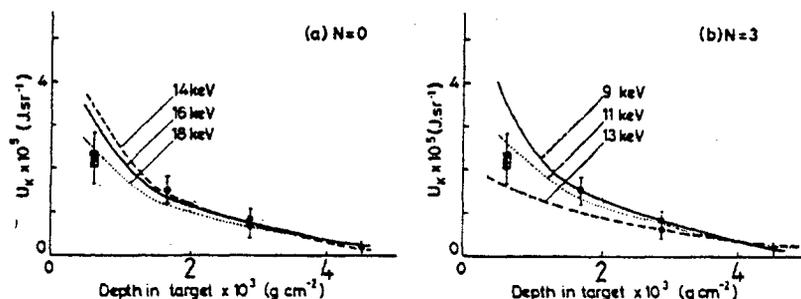

FIG. 2. Experimental and theoretical $K\alpha$ energies as a function of the average depth of the fluor layer in the target. Experimental energies are corrected for target absorption. Values of kT_H used for the theoretical curves are shown.
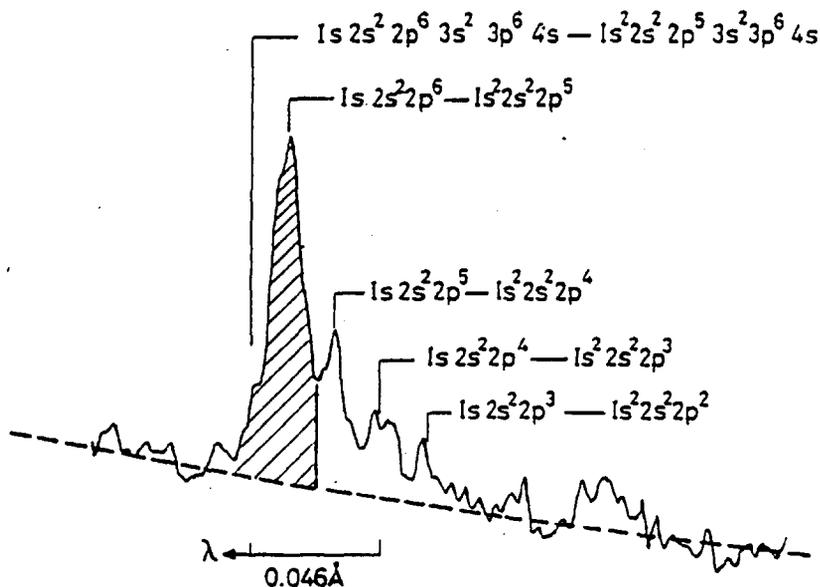
FIG. 3. An expanded microdensitometer tracing of a K $K\alpha$ line showing the short-wavelength shifted components. The indicated transitions from Ref. 11 should be compared with the observed peaks. "Unshifted" components are shaded.

tion pumped K $K\alpha$ yield is only 0.3×10^{-6} J sr^{-1} which is small compared with the lowest observed value of 2×10^{-6} J sr^{-1}.

The energy spectrum of the fast electrons was obtained from calculations of the $K\alpha$ yield of monoenergetic electrons using Ref. 14. To check this calculation, especially at low energy, an electron beam was used to calibrate duplicate targets. The beam supplied 0.1 μA at 15 to 50 kV into a 300-μm spot. The x-ray crystal spectrometer was used to record the various $K\alpha$

yields, for a known deposited charge. From the calibration and calculation the $K\alpha$ yields $Y(E)$ in J sr^{-1} electron^{-1} as a function of electron energy were obtained and are shown in Fig. 4. The agreement of the two adds confidence to our absolute measurement.

From the yields $Y(E)$ for monoenergetic electrons the yields for a distribution function $n(E)$ of electrons passing into the targets were predicted from $\int_0^\infty n(E)Y(E)dE$. With $n(E)=AE^{N/2}\exp(-E/kT_H)$, yields for $N=0$ and $N=3$ were calculated
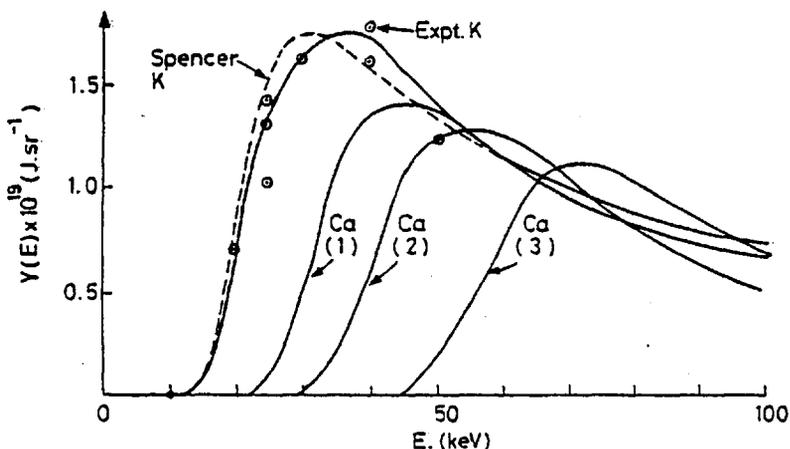

FIG. 4. The $K\alpha$ yield per electron as a function of incident electron energy for each of the different fluor layers. Curves 1, 2, and 3 refer to Mylar thicknesses of 2.5, 12.5, and 25.0 μm, respectively. The dotted line is the calculated yield for the front K layer and the points are from the electron-beam calibration. The good agreement should be noted. The solid lines are the yields used, derived from theory and the calibration.

TABLE I. Total energy deposition in fluor compounds.

Fluor layer (Mylar thickness)	Depth in target (mg cm^{-2})	Deposited energy (J)	Deposited energy density (J cm^{-3})
KCl (top)	0.56	0.40	1.4×10^7
CaF$_2$ (2.5 μm)	1.58	0.24	1.0×10^7
CaF$_2$ (12.5 μm)	2.81	0.12	5.1×10^6
CaF$_2$ (25 μm)	4.50	0.04	1.7×10^6

and are shown in Fig. 2. The factors A and kT_H are determined by fitting the predicted yields to the experimental yields. The case $N = 3$ fits the data best with $kT_H = 11 \pm 2$ keV. The slope of the hard-x-ray continuum between 10 and 20 keV also indicates a temperature of 12 ± 2 keV, which is comparable with collected data[1] at 2×10^{15} W cm^{-2}.

Choosing $N = 3$, the fit to the experimental results gives $A = (9.4 \pm 2.0) \times 10^{11}$ electrons keV$^{-2.5}$, $kT_B = 11.0 \pm 2.0$ keV. The total energy in this distribution which is passing into the target is $\int_0^\infty n(E)E\,dE = 2.2 \pm 0.4$ J. However, the calculation of the energy deposited into the target is insensitive to the assumed distribution function, provided that the distribution is fitted to the observed yields. This is because $R(E)$ is almost constant and a simple division of the energy in the $K\alpha$ line by ω/R gives the total energy deposited in the fluor. A more accurate calculation of energy deposition has been made using the $N = 3$ distribution and the results are shown in Table I.

Finally, we remark that the fast-electron energy deposition that we observe is broadly consistent with the expected overall energy balance. Of the 20 J onto the target, about 7 J should be absorbed.[3] About 60% of the absorbed energy should reappear as fast ions.[2] We observe the bulk of the remainder as preheat. One might

speculate that this observed 2.2-J deposition of energy by hot electrons suggests that any inhibition of the hot-electron transport is not very significant.

(a) Present address: Science Research Council, Rutherford, Laboratory, Chilton, Oxon, United Kingdom.

[1] D. W. Forslund, J. M. Kindel, and K. Lee, Phys. Rev. Lett. 39, 284 (1977).

[2] P. M. Cambell et al., in Proceedings of the Sixth International Conference on Plasma Physics and Controlled Nuclear Fusion Research, Birchtesgaden, West Germany, 1976 (International Atomic Energy Agency, Vienna, 1977), Vol. I.

[3] E. K. Storm et al., University of California Radiation Laboratory Report No. UCRL 50021-76, 1977 (unpublished), pp. 5.85–5.126.

[4] L. M. Wickens, J. E. Allen, and P. T. Rumsby, Phys. Rev. Lett. 41, 243 (1978).

[5] J. W. Shearer et al., Phys. Rev. A 6, 764 (1972).

[6] K. A. Brueckner, Nucl. Fusion 17, 1257 (1977).

[7] A. Zigler, H. Zmora, and J. L. Sczwab, Phys. Lett. 63A, 275 (1977).

[8] B. Yaakobi, I. Pelah, and J. Hoose, Phys. Rev. Lett. 37, 836 (1976).

[9] K. B. Mitchell and R. P. Godwin, J. Appl. Phys. 49, 3851 (1977).

[10] Handbook of Spectroscopy (C.R.C. Press, Ohio, 1974), Vol. I.

[11] L. L. House, Astrophys. J., Suppl. Ser. 18, 21 (1969).

[12] B. Yaakobi, private communication.

[13] Rutherford Laboratory Central Laser Facility Annual Report No. RL-78-039, 1978 (unpublished).

[14] L. V. Spencer, Energy Dissipation by Fast Electrons, National Bureau of Standards Monograph No. I (U. S., GPO, Washington, D. C., 1959).

Demonstration of Resistive Inhibition of Fast Electrons from Laser-Produced Plasmas in Low-Density Gold Targets

D. J. Bond, J. D. Hares, and J. D. Kilkenny

Blackett Laboratory, Imperial College, London, SW7 2BZ, England

A numerical model is used to show that the range of suprathermal electrons from laser-produced plasmas can be significantly reduced by the electric field needed to drive a return current of cold electrons. Direct experimental evidence of a reduction of preheat by at least a factor of 3 is presented for targets containing a low-density gold layer.

It is now well established that when high-intensity light is incident on solid targets, a considerable fraction of the laser energy is converted into suprathermal electrons with a temperature T_H much greater than that of the thermal plasma.[1-3] Some of the energy of these electrons heats the target to comparatively large depths. Experiments with 1.06-μm lasers on layered targets containing K fluors[4] have measured the range of these suprathermal electrons and found that the range was consistent with the hard x-ray measurement of temperature and the Bethe-Bloch formula[5] for energy loss with scattering included. Preheat would have to be minimized for an ablative compression, and the use of a vacuum gap[6] might be one way of optimizing a *target* to prevent preheat. In this Letter we demonstrate an alternative target design for reducing the preheat range by including a high-resistivity, low–volume-density material within the target. The effect is explained simply; it is confirmed by a numerical simulation and by direct experimental measurements.

Consider a laser beam incident on a semi-infinite plane target. A fraction of the absorbed laser power is converted into suprathermal elec-

trons flowing into the target carrying a current density j_H, which is typically 10^{10} A cm^{-2}.[4] The very-high-energy deposition rapidly ionizes the target which becomes a high–electron-density ($N_e \sim 10^{23}$ cm^{-3}), low–electron-temperature ($T_e \sim 200$ eV) plasma of resistivity η. Because such a plasma has a very small skin depth for the time scale of the laser pulse, a return current j_c must flow so that

$$ j_H + j_c = 0 . $$

The resistive electric field, $E = \eta j_c = -\eta j_H$, decelerates the suprathermal electrons, converting a part of their energy into Ohmic heating, ηj_c^2. If the collisional range of the suprathermal electrons is r_a (mass per area) and the target density is ρ then in the absence of electric field inhibition the suprathermal electrons will go a distance r_a/ρ, and the electrostatic potential a distance r_a/ρ into the target will be $\sim \eta j_H r_a/\rho$. However if $\eta j_H r_a/\rho \gtrsim kT_H/e$ the resistive electric field will appreciably impede the suprathermal electrons. The potential within the target is estimated in Table I for solid-density gold and for gold at 1% of its solid density (0.2 g cm^{-3}), with $j_H = 10^{10}$ A cm^{-2} for 100 ps as suggested by experi-

TABLE I. Estimates of the potential within the target for the density of solid gold and for 1% of that density.

Density	Target thickness X (μm)	Current density j_H (A cm^{-2})	Resistivity η (LTE and Spitzer) (Ω cm)	Potential $j_H \eta X$ (V)
Solid	0.5	10^{10}	8×10^{-5}	40
1% Solid	50	10^{10}	4×10^{-4}	2×10^4

ment.[4] The resistivity is calculated for local thermodynamic equilibrium (LTE)[7] and Spitzer resistivity.[8] It is clear that in normal gold, the target potential is negligible compared with the electron energy, whereas in low-density gold the target potential will be large and thus the supra-thermal electrons will be inhibited by the resistive electric field. The three factors in low-density gold which enhance this inhibition are (i) the large stopping distance r_a/ρ at low density, (ii) the high state of ionization (~30) achieved for small temperature rise in gold, and (iii) the larger LTE state of ionization at lower electron density for a given T_e.

To predict the effect of the resistive electric field we have used a Monte Carlo calculation with a self-consistent electric field. Hydrodynamics and thermal and radiation transport are neglected. The transport of the fast electrons at any one time is solved iteratively by a time-independent Monte Carlo transport calculation in slab geometry. The scattering is represented by a random Rutherford scattering from Fermi-screened nu-

FIG. 1. Computational results for solid and low-density targets. At the rear of the low-density target ~50% of the deposition is due to $\vec{J} \cdot \vec{E}$ heating by the return current.

clei and Debye-shielded ions. In between the scattering events, electrons follow parabolic trajectories representing the effect of the resistive field. A new electric field is determined from Ohm's law with a resistivity given by the equation of state for the local energy deposition and Ohmic heating up to that time, and $j_c = -j_H$ is determined from the transport calculation. The electron transport is then iterated to find a consistent E and j_H. The collisional energy deposition is calculated with use of the continuous slowing-down approximation accounting for bound electrons[5] and plasma electrons.[9]

The calculation was used to simulate typical experimental parameters. Experiments at $I = 3 \times 10^{15}$ W cm^{-2} indicate that the fast-electron energy spectrum is of the form $f(u) = u^{3/2} \exp(-u/kT_H)$ with $T_H = 14$ keV, with 8% of the incident energy in this distribution. Figure 1 shows that in the solid-density gold targets the resistive field has a negligible effect, whereas for low-density gold the range is reduced because of the resistive electric field.

To confirm the effect, an experiment was performed with tracer layers to detect fast electrons by the $K\alpha$ radiation they produced.[4] Targets were normally irradiated with 20-J, 90-ps, 1.05-μm laser pulses focused with an $f/1$ lens to a 100-μm-diam spot, at an intensity of 2.8×10^{15} W cm^{-2}. The targets consisted of 1.5 μm Al, 3 μm KCl, gold, and 3 μm CaF$_2$, and were fabricated by evaporating the various layers onto the aluminum substrate. The gold layer was deposited at various densities. Solid gold layers were made by vacuum evaporation; low-density layers (~1% solid density) were made by slowly evaporating the gold in an atmosphere of 50 mbar of argon, thus creating voids in the gold. The targets were constructed in pairs of similar area mass density but with solid- and ~0.6% solid-density gold. The area density of the low-density targets was determined by weighing and measuring their depth with a scanning electron microscope. The struc-
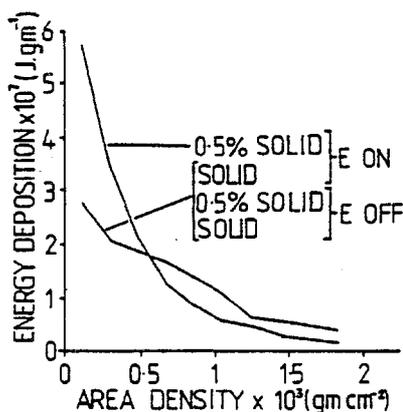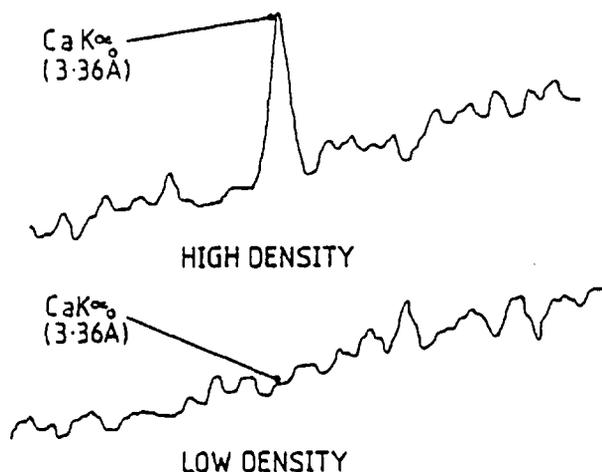
FIG. 2. Microdensitometer tracings in the region of the calcium $K\alpha$ line for a typical pair of targets with ~1 mg cm^{-2} of high- and low-density gold. The sensitivity is the same in both cases. The potassium $K\alpha$ yield measured by the front spectrometer was slightly higher for the low-density case.
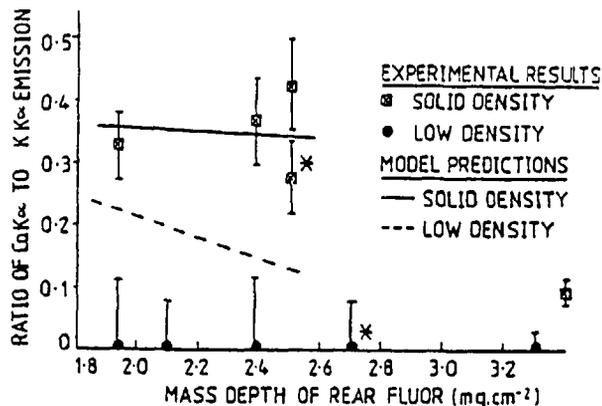

FIG. 3. Ratio of rear to front $K\alpha$ emission for pairs of targets with high- and low-density gold. The pair shown in Fig. 2 is represented by stars. The predicted inhibition is shown and is less than the observed inhibition.

ture of the low-density gold is of a submicron scale length. Expansion velocities are sufficiently high that it becomes uniform before the peak of the laser pulse.

The laser was incident on the aluminum which provided a flat and well-characterized ablation plasma. The Ca in CaF$_2$ and K in KCl acted as fast-electron detectors by the $K\alpha$ emission that was induced in them.[4] The gold acted as a variable-density electron filter. However, as shown below, the depth within the target of the gold reduced the resistive inhibition effects.

The $K\alpha$ emission was recorded by two miniature flat-crystal spectrometers. One spectrometer, at the front of the target, recorded the K $K\alpha$ emission and the Al plasma radiation. The other, at the rear, recorded the Ca $K\alpha$ emission.

A typical tracing of the Ca $K\alpha$ line for low- and high-density gold of the same area density is shown in Fig. 2. With low-density gold there is no observable $K\alpha$ line. The yields either side of the gold are shown in Fig. 3. For one shot 0.05 μm of KCl was deposited on the front of the target. From the attenuation of the heliumlike resonance lines, the area density of the gold was confirmed. It is clear that low-density gold reduces the $K\alpha$ yield, and therefore the energy deposition by fast electrons, by at least a factor of 3 over the same area density of high-density gold.

The $K\alpha$ yields predicted by the Monte Carlo calculation are also shown in Fig. 3. The inhibition predicted for low-density gold is small compared with the case in Fig. 1, because of the large amount of material that electrons have to pass through before they reach the gold. The predicted inhibition in Fig. 3 is also less than observed experimentally. This is probably due to defects in the model, the most noticeable being the application of the Spitzer formula to a low-lnΛ (~2) partially stripped plasma where the minimum impact parameter is less than or about the size of the atoms. The modeling was repeated with increased coefficients of resistivity. A factor-of-3 increase in resistivity brought the low-density Ca $K\alpha$ yields just inside the experimental error bars.

In conclusion we have shown both theoretically and experimentally that specific fast-electron energy deposition can be greatly increased by the use of a suitable low-density target material. This effect could be advantageous in ablative type compressions. For targets with high- and low-density layers of similar area mass density, a large irradiance may be used with the low-density target before preheat becomes important.

The experiment described in this Letter was performed at the Rutherford Laboratory Central Laser Facility.

[1]D. W. Forslund, J. M. Kindel, and R. Lee, Phys.

Rev. Lett. 39, 284 (1977).

[2]P. M. Campbell *et al.*, in *Proceedings of the Sixth International Conference on Plasma Physics and Controlled Nuclear Fusion Research, Berchtesgaden, West Germany, 1976* (International Atomic Energy Agency, Vienna, 1977), Vol. 1.

[3]E. K. Storm *et al.*, University of California Radiation Laboratory Report No. UCRL 50021-76, 1977 (unpublished), pp. 5.85–5.126.

[4]J. D. Hares, J. D. Kilkenny, M. H. Key, and J. G.

Lunney, Phys. Rev. Lett. 42, 1216 (1979).

[5]H. A. Bethe, Ann. Phys. (Leipzig) 5, 325 (1930).

[6]K. Lee, D. W. Forslund, J. M. Kindel, and L. E. Lindman, Nucl. Fusion 19, 1447 (1979).

[7]Ya. B. Zel'dovich and Yu. P. Raizer, in *Physics of Shock Waves and High Temperature Hydrodynamic Phenomena*, edited by W. D. Hayes and R. F. Probstein (Academic, New York, 1967), p. 201.

[8]L. Spitzer and R. Harm, Phys. Rev. 89, 977 (1953).

[9]D. Pines and D. Bohm, Phys. Rev. 85, 338 (1952).